UNIVERSITY OF SOUTHAMPTON

FACULTY OF ENGINEERING, SCIENCE AND MATHEMATICS

Optoelectronics Research Centre

Engineered optical materials by ultrafast laser nanostructuring

by

Rokas Drevinskas

Thesis for the degree of Doctor of Philosophy

2016

Creativity is intelligence having fun.

–Albert Einstein

Acknowledgements

I would like to express my gratitude to the numerous individuals whose help and support assisted my professional growth during my recent years and contributed to my work presented in this thesis.

First I want to thank my Bachelor and Master degrees supervisors Arūnas Ramanavičius and Ramūnas Valiokas, who introduced me to the research field of nanotechnology and material science. Special thanks are addressed to my PhD supervisor Peter G. Kazansky for leading my doctoral project and showing full trust in my work. I acknowledge all the help and support from our research group members Aabid Patel, Aušra Čerkauskaitė, Jingyu Zhang, Mindaugas Gecevičius, Martynas Beresna, and Costantino Corbari. Many thanks to Yu. P. Svirko, A. A. Lipovskii, Y. Bellouard, and A. G. Kazanskii research groups for productive collaborations. Certainly, great appreciation is given to the Engineering and Physical Sciences Research Council (EPSRC) for funding my work.

Finally, I want to thank my parents, brother and faithful friends, for helping me to fill my spare time with things other than research.

UNIVERSITY OF SOUTHAMPTON

ABSTRACT

FACULTY OF ENGINEERING, SCIENCE AND MATHEMATICS

Optoelectronics Research Centre

Thesis for the degree of Doctor of Philosophy

ENGINEERED OPTICAL MATERIALS BY ULTRAFAST LASER NANOSTRUCTURING

Rokas Drevinskas

This thesis is focused on ultrafast laser induced modification in optical materials including transparent dielectrics, high-index semiconductors, and glass-metal nanocomposites. Under certain conditions, ultrafast laser direct writing through a nonlinear light-matter interaction enables a high-precision nanostructuring. This type of the modification exhibits form birefringence and/or dichroism enabling the fabrication of polarization sensitive optical elements. The main activities involved in the research are the optimization of light-mater interaction processes, engineering the optical properties of materials, design and fabrication of optical elements, and implementation of engineered optics into the multidisciplinary fields. The pioneering steps were taken towards a practical exploitation of femtosecond laser imprinted space-variant optical elements and development of a novel scheme for optical trapping. As a result, a set of novel optical components with high efficiency, high phase density and low losses were successfully developed and demonstrated, including optical dichroic elements, polarization gratings, arrays of polarization micro-lenses and micro converters, and computer generated Fourier holograms. A novel type of optical tweezers with tunable orbital angular momentum was also designed and developed, which has attracted attention from the beam-shaping and optical micro-manipulation communities. The record high topological charge torque with high-precision control of trapped micron-size objects was achieved. Practical laser imprinted optical elements in materials other than fused silica were demonstrated. A number of optical elements were realized in amorphous silicon thin-films. It was demonstrated that the laser-induced periodic thin-film structures exhibit giant birefringence and was implemented in space-variant polarization and phase manipulations. Surface texturing with 30 nm resolution was demonstrated by potassium hydroxide wet etching and ultrafast laser nanostructuring of silica, leading to the fabrication of dichroic glass-metal patterns. Other laser material processing approaches such as single and double pulse irradiation of crystalline silicon, or irradiation of optical materials with tightly focused cylindrical vector beams were implemented. The femtosecond laser shaping of silver nanoparticles embedded in soda-lime glass was studied. The developed approach can be employed to control the anisotropy of the glass-metal nanocomposites.

DECLARATION OF AUTHORSHIP

I, *Rokas Drevinskas*

declare that this thesis and the work presented in it are my own and has been generated by me as the result of my own original research.

Engineered optical materials by ultrafast laser nanostructuring

I confirm that:

1. This work was done wholly or mainly while in candidature for a research degree at this University;
2. Where any part of this thesis has previously been submitted for a degree or any other qualification at this University or any other institution, this has been clearly stated;
3. Where I have consulted the published work of others, this is always clearly attributed;
4. Where I have quoted from the work of others, the source is always given. With the exception of such quotations, this thesis is entirely my own work;
5. I have acknowledged all main sources of help;
6. Where the thesis is based on work done by myself jointly with others, I have made clear exactly what was done by others and what I have contributed myself;
7. Parts of this work have been published (or will be published) as:

Paper A

R.Drevinskas, M.Gecevičius, M.Beresna, Y.Bellouard, P.G.Kazansky, *Tailored surface birefringence by femtosecond laser assisted wet etching*, *Optics Express* Vol. 3(2), 1428-1437 (2015)

Paper B

R.Drevinskas, P.G.Kazansky, *Dichroic Surfaces Engineered by Ultrafast Laser Assisted Wet Etching* (manuscript in preparation)

Paper C

M.Gecevičius, R.Drevinskas, M.Beresna, P.G.Kazansky, *Single beam optical vortex tweezers with tunable orbital angular momentum, Applied Physics Letters* Vol. 104(23), 231110 (2014)

Paper D

R.Drevinskas, P.G.Kazansky, *High-performance geometric phase elements in silica glass* (manuscript in preparation)

Paper E

J.Zhang, R.Drevinskas, M.Beresna, P.Kazansky, *Polarization sensitive anisotropic structuring of silicon by ultrashort light pulses*, *Applied Physics Letters* Vol.107, 041114 (2015)

Paper F

R.Drevinskas, M.Beresna, M.Gecevičius, M.Khenkin, A.G.Kazanskii, I.Matulaitienė, G.Niaura, O.I.Konkov, E.I.Terukov, Y.P.Svirko, P.G.Kazansky, *Giant birefringence and dichroism induced by ultrafast laser pulses in hydrogenated amorphous silicon, Applied Physics Letters* Vol. 106(17), 171106 (2015)

Paper G

R.Drevinskas, M.Beresna, J.Zhang, A.G.Kazanskii, P.G.Kazansky, *Ultrafast laser-induced metasurfaces for geometric phase manipulation*, *Advanced Optical Materials,* Vol.5, 1600575 (2017)

Paper H

R.Drevinskas, J.Zhang, M.Beresna, M.Gecevicius, A.G.Kazanskii, Yu.P.Svirko, P.G.Kazansky, *Laser material processing with tightly focused cylindrical vector beams*, *Applied Physics Letters* Vol.108, 221107 (2016)

Paper I

R.Drevinskas, M.Beresna, O.Deparis, P.G.Kazansky, *Laser assisted modification of poled silver-doped nanocomposite soda-lime glass, MATEC Web of Conferences* Vol.8, 02008 (2013)

Paper J

S.Chervinskii, R.Drevinskas, D.V.Karpov, M.Beresna, A.A.Lipovskii, Y.P.Svirko, P.G.Kazansky, *Revealing the nanoparticles aspect ratio in the glass-metal nanocomposites irradiated with femtosecond laser, Scientific Reports* Vol.5, 1-10 (2015)

Own Contribution. The Author of this thesis has taken the main responsibility, as a corresponding Author, for the preparation and writing of the papers A, B, C, D, E, F, G, H, and I. In all papers, the development and analysis of results have been conducted in collaborations with the co-Authors. The experimental measurements in Papers A, B, D, F, G, I, have been carried out only by the Author of this thesis while the experimental measurements in Papers C, E, H, J have been carried out equally by the first two Authors in collaboration with the co-Authors. The numerical effective medium approximation (EMA) calculations in Paper J were made by D.V. Karpov and Yu.P.Svirko.

Signed: .....

Date: .....

Table of Contents

List of Figures

Definitions and Abbreviations

$\vec{E}$	Electric field
$\vec{E}_0$	Amplitude of electric field
$\vec{D}$	Electric displacement
$\vec{H}$	Magnetic field
$\vec{B}$	Magnetic induction
$\vec{J}$	Current density
ρ_{ext}	External charge density
σ	Conductivity
$\vec{P}$	Polarization
P_{nl}	Nonlinear polarization
M	Magnetization
ε_0	Electric permittivity in free space
μ_0	Magnetic permeability in free space
ε	Complex electric permittivity of material
χ	Susceptibility tensor
t	Time
k_0	Wave number in vacuum
k	Complex wave number in material
α	Absorption coefficient
ω	Angular frequency of light
ω_p	Angular frequency of plasma
c	Speed of light in free space
λ	Wavelength of light
n	Complex refractive index of material
n_0	Linear refractive index
n_{nl}	Nonlinear refractive index coefficient
κ	Extinction coefficient
I	Laser intensity
I_0	Initial laser intensity
ϖ	Spot size
ϖ_0	Spot size at the waist
Z_R	Rayleigh range
$R(z)$	Radius of curvature

$\xi(z)$	Gouy phase shift
M^2	Qualitative beam parameter
E_p	Pulse energy
P	Average power
f	Laser repetition rate
P_p	Peak power
τ	Pulse duration
I_p	Peak intensity
F_p	Peak fluence
P_{cr}	Critical power for self-focusing
P_{in}	Input peak power
m	Electron mass
e	Electron charge
N	Plasma (electron) density
E_g	Bandgap energy of the material
E_k	Kinetic energy
E_{int}	Internal energy
K	Number of photons
$\hbar$	Reduced Planck constant
P_{PI}	Photoionization rate
σ_K	Multi-photon absorption coefficient
γ	Keldysh parameter
ω_p	Plasma frequency
Γ	Damping or relaxation constant
v_F	Fermi velocity
ν	Frequency of light
n_e	Extraordinary refractive index
n_o	Ordinary refractive index
k_B	Boltzmann constant
A	Azimuth of the slow-axis
θ	Angle of wave plate
ϕ	Geometric phase
φ	Phase retardation
η	Efficiency
D	Linear dichroism
A	Extinction

p	Dipole moment
α_p	Polarizability
σ_{ext}	Extinction cross section
ς	Filling factor
NA	Numerical aperture
FDTD	Finite-difference time-domain
SHG	Second-harmonic generation
SEM	Scanning electron microscope
VP-ESEM	Variable pressure/environmental scanning electron mode
SPP	Surface plasmon polariton
SPR	Surface plasmon resonance
GMN	Glass-metal nanocomposites
GPOE	Goemetric phase optical elements
ULN	Ultrafast laser nanostructured(-ing)
MGA	Maxwell Garnett approach
KOH	Potassium hydroxide
HF	Hydrofluoric acid
OAM	Orbital angular momentum
LIPSS	Laser induced periodic surface structures
LSFL	Low spatial frequency LIPSS
HSFL	High spatial frequency LIPSS

Chapter 1: Introduction

1.1 Motivation

Modern optical systems applied to key optical markets such as mobile and optical communications, healthcare, security, lightning and photovoltaics require complex optical materials to satisfy demand for enhanced performance at a reduced installation space. Despite the decades long expertise in fabrication of optical components, precision and quality still remains a challenging problem; material processing technologies are approaching its limits in terms of ability to produce functional materials with controlled compositional and structural consistency. The main idea of this work is to remove the barriers in product development and go beyond the state-of-the-art by applying ultrafast laser nanostructuring for engineering of optical materials.

The processing of optical materials by lasers has become a fast growing field of research. The very first investigations of the laser induced material modifications followed immediately after the invention of the laser in the early 1960s. Further development of laser systems allowed focusing powerful high quality laser beams into a diffraction limited spot leading to unprecedented optical intensities. As a result, the laser became a unique and versatile tool for engineering materials. The first lasers delivering sub-picosecond pulses were demonstrated in early 1970s with the advance in mode locking techniques and organic dye lasers. However, these laser sources lacked stability and power and thus were limited to applications in spectroscopy. The 1990s saw the revolution of ultrafast laser technology. The invention of new mode locking mechanisms, namely Kerr-lens mode locking [1] and semiconductor saturable absorber mirrors [2], allowed the generation of stable pulse trains from solid state laser systems, which gave stability and power scalability.

This was followed by the first demonstrations of femtosecond laser processing in the bulk of transparent materials made by K. Hirao group, which demonstrated the development of waveguiding structures written inside silica glass [3]. Later, the direct-write ultrafast laser nanostructuring technique was implemented in the engineering of various materials such as semiconductors, metals and transparent dielectrics [4]. The control of dichroic properties of Ag-doped nanocomposite glasses using femtosecond laser irradiation was introduced by Kaempfe in 1999 [5]. Later on, many studies reported the identification of femtosecond laser induced periodic surface [4,6] and bulk [7,8] structures with subwavelength periodicity. A decade ago, it was shown that such a periodic assembly of nanostructures behaves as a uniaxial birefringent material with the optical axis oriented parallel to the direction of laser beam polarization [9]. As a result, these nanostructures spatially varied by ultrafast laser direct writing and could serve as a perfect

candidate for designing high-performance polarization sensitive elements such as dichroic and geometric phase optical elements, challenging conventional optics (Figure 1-1). Furthermore, the technique could be extended to any transparent high-index material that supports laser induced nanostructuring, and could be effectively exploited for the integration into multi-functional optical systems. Highly flexible thin-films, or highly durable transparent solids could be implemented on demand.

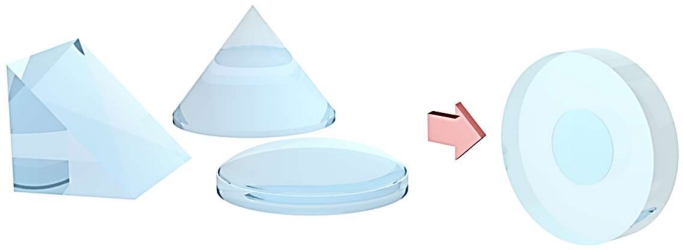

Figure 1-1. Conventional optics and its alternative – printed flat optics – realized in transparent medium by the means of geometric phase.

The key advantage of using ultrashort pulses for direct laser writing, as opposed to longer pulses, is that they can rapidly deposit energy in solids with high precision. The light is absorbed and the optical excitation ends before the surrounding lattice is perturbed, which results in highly localized nanostructuring without collateral material damage [10,11]. The technology allows fabricating any tailored phase optical element within thickness of material, and with spatial resolution as high as sub-100 nm, limited only by the translation stages. Smooth phase profiles can be produced as no phase wrapping is required. The optical elements are printed in a single step procedure. No moulding or polishing, which is typically for the conventional optics fabrication, is required. The manufacturing does not need expensive clean rooms in contrast to the diffractive optics fabrication.

In particular, the major motivation of this work was to advance the performance (i.e. increasing density and significantly reducing losses), of laser imprinted optical elements operating with objects as small as a few hundreds of nanometres. This would allow integrating printed optics into three dimensional photonic platforms, and would expand the range of applications beyond the beam shaping and pave the way towards their integration into material processing, telecommunications, nanophotonics, etc.

Briefly, this work was focused on engineering of various optical materials, including silica glass, glass-metal nanocomposites, crystalline silicon, amorphous silicon, by ultrafast laser nanostructuring. Applying the acquired knowledge along with full control of laser system, the polarization sensitive materials with precisely tunable optical properties were fabricated. Finally

the designed high-performance elements, which can be implemented in various applications, could push the frontiers of laser material processing to unprecedented precision and potentially develop a novel family of devices feeding into the future of photonics.

1.2 Thesis overview

The doctoral thesis has been written in a 'Three-Paper' format. It starts with the five chapters, and ends with the appended published and publishable papers. **Chapter 1: Introduction** provides a brief historical overview of the laser material processing and indicates the main motivation of the thesis based on a technological perspective of ultrafast laser nanostructuring. A brief overview of the thesis is also given. **Chapter 2: Ultrafast laser modification of transparent materials** provides the basics of light propagation in a transparent medium. Linear and nonlinear interaction, spot size and peak intensity calculations, ionization mechanisms governing the ultrashort pulse interaction with transparent materials and its subsequent permanent modification are reviewed. **Chapter 3: Engineered optical materials** firstly defines the form birefringence, dichroism and geometric phase. Later three sub-sections are focused on the laser induced nanogratings in silica, laser induced periodic surface structures in various materials including metals, semiconductors and dielectrics, and photomodification of metal-glass nanocomposites. The brief review on mechanisms, optical/structural properties and implementations is given. **Chapter 4: Summary of Papers** gives a summary of all appended papers, and **Chapter 5: Conclusions** concludes the thesis and gives the detailed package of future work.

Below is the list of appended manuscripts with its corresponding brief overviews.

Paper A. *Tailored surface birefringence by femtosecond laser assisted wet etching.* The main idea of this work was to study wet etching of ultrafast laser nanostructured silica glass. As a result, surface silica nanogratings were fabricated with its tailored optical properties.

Paper B. *Dichroic Surfaces Engineered by Ultrafast Laser Assisted Wet Etching.* This work was continuation of Paper B. The fabricated surface nanogratings incorporated with the metal thin-films or nanostructures were realized as a dichroic elements.

Paper C. *Single beam optical vortex tweezers with tunable orbital angular momentum.* Here a novel type of optical tweezers with tunable orbital angular momentum were designed and developed. The ultrafast laser nanostructured silica was used as a key element generating optical vortex beams.

Paper D. *High-performance geometric phase elements in silica glass.* This paper summarizes the ultrafast laser nanostructuring of silica glass done over the last several years of my research. The fabrication of high-performance printed flat optics was reported.

Paper E. *Polarization sensitive anisotropic structuring of silicon by ultrashort light pulses.* Here we demonstrate polarization sensitive structuring of silicon, which occurs only after the second pulse, while the first pulse always produces isotropic structures. The seeding effect is considered.

Paper F. *Giant birefringence and dichroism induced by ultrafast laser pulses in hydrogenated amorphous silicon.* This paper summarizes the nanostructuring of amorphous silicon thin-films done over the last several years of my research. For the first time, it was demonstrated that the laser induced periodic surface structures could exhibit giant birefringence.

Paper G. *Ultrafast laser-induced metasurfaces for geometric phase manipulation.* The research reported in this paper is based on the continuation of Paper F. The giant birefringence observed in laser induced periodic thin-film structures was implemented in space-variant polarization manipulations. Number of metasurfaces with various phase profiles were designed.

Paper H. *Laser material processing with tightly focused cylindrical vector beams.* The main idea of this work was to show experimentally and theoretically that the longitudinal component of electric field is not efficient for engineering of high-refractive index materials. The ultrafast laser nanostructured silica elements were used to generate cylindrical vector beams.

Paper I. *Laser assisted modification of poled silver-doped nanocomposite soda-lime glass.* Here is a brief report on initial experiments done on photomodification of metal-glass nanocomposites. The CODIXX AG sample, pristine and poled, was irradiated with femtosecond pulses; the further optical characterization was performed.

Paper J. *Revealing the nanoparticles aspect ratio in the glass-metal nanocomposites irradiated with femtosecond laser.* The further experiments on photomodification of metal-glass nanocomposites were elaborated. The work proposes the precise tunability of nanoparticles aspect ratio that could be achieved by controlling the processing conditions.

Chapter 2: Ultrafast laser modification of transparent materials

In this chapter I will shortly review the light-mater interaction in transparent materials. Tightly focused ultrashort pulses can reach intensities high enough to induce breakdown even in materials which are transparent to the wavelength of light. This can happen due to nonlinear processes, and can lead to different types of modification such as defect generation, positive refractive index change, nanostructuring and/or voids-like damage.

2.1 Fundamentals of light propagation in a medium

The interaction of light with microscopic objects could be described using classical theory. We start with Maxwell's equations for the macroscopic electromagnetic field:

$$\nabla \times \vec{H} = \frac{\partial \vec{D}}{\partial t} + \vec{J} \tag{2-1}$$

$$\nabla \times \vec{E} = -\frac{\partial \vec{B}}{\partial t}, \tag{2-2}$$

$$\nabla \cdot \vec{D} = \rho_{\text{ext}}, \tag{2-3}$$

$$\nabla \cdot \vec{B} = 0, \tag{2-4}$$

where $\vec{E}$ is the electric field, $\vec{D}$ the electric displacement, $\vec{H}$ the magnetic field, $\vec{B}$ the magnetic induction, $\vec{J}$ current density and ρ_{ext} the external charge density. Linear relationship between the current density and electric field is expressed via conductivity σ by:

$$\vec{J} = \sigma \vec{E}. \tag{2-5}$$

All macroscopic fields are connected via the polarization $\vec{P}$ and the magnetization $\vec{M}$:

$$\vec{D} = \varepsilon_0 \vec{E} + \vec{P} = \varepsilon_0 \varepsilon \vec{E}, \tag{2-6}$$

$$\vec{H} = \frac{1}{\mu_0} \vec{B} - \vec{M}, \tag{2-7}$$

where ε is the relative permittivity or dielectric constant of material, ε_0 and μ_0 are the electric permittivity and magnetic permeability in vacuum, respectively. In most cases the system is

non-magnetic, so $\vec{M} = 0$. Introducing the susceptibility tensor χ, from Eq. (2-6) where $\varepsilon = 1 - \chi$, we get polarization,

$$\vec{P} = \varepsilon_0 \chi \vec{E}, \tag{2-8}$$

that is expressed by the Taylor series:

$$\vec{P} = \varepsilon_0 \chi^{(1)} \vec{E} + \varepsilon_0 \chi^{(2)} \vec{E}\vec{E} + \varepsilon_0 \chi^{(3)} \vec{E}\vec{E}\vec{E} + \cdots. \tag{2-9}$$

The first term shows the linear polarization while the higher terms indicate the weight of the nonlinear $\vec{P}_{nl}$ term. Combining Eq. (2-5)-(2-9) and (2-1)-(2-4) we derive the expression for the electromagnetic wave:

$$\nabla \times \nabla \times \vec{E} + \mu_0 \sigma \frac{\partial \vec{E}}{\partial t} + \varepsilon_0 \mu_0 \left(1 + \chi^{(1)}\right) \frac{\partial^2 \vec{E}}{\partial t^2} + \mu_0 \frac{\partial^2 \vec{P}_{nl}}{\partial t^2} = 0. \tag{2-10}$$

If the system is linear, the last term can be neglected. In that case, we see that the polarization of the medium for a certain field is influenced only by its dielectric constant.

The wave equation (2-10) without a nonlinear term in one dimension can be solved with a plain electromagnetic wave, propagating in a medium:

$$\vec{E} = \vec{E}_0 \exp(ikz - i\omega t), \tag{2-11}$$

where $\vec{E}_0$ is the amplitude of the electric field and *k* is a complex wave vector that might be expressed by $\vec{k} = \vec{k}' + i\vec{k}''$. From Eq. (2-11) we see that the imaginary part is responsible for the damping of the field and the real part is combined with the absolute phase of the electromagnetic field. The absorption coefficient can be written as:

$$\alpha = 2k''. \tag{2-12}$$

Simplifying the electromagnetic wave equation (2-10) by neglecting the nonlinear term and treating the system as homogeneous with no external charges ($\nabla \times \nabla \times \vec{E} = \nabla\nabla \cdot \vec{E} - \nabla^2 \vec{E} = -\nabla^2 \vec{E}$ and $\nabla \cdot \vec{E} = 0$) and substituting the electric field propagation equation (2-11), we have:

$$k^2 = \omega^2 \mu_0 \varepsilon_0 \varepsilon(\omega) = \frac{\omega^2}{c^2} \varepsilon(\omega), \tag{2-13}$$

where $c = 1/\sqrt{\mu_0 \varepsilon_0}$, From here, we get the relation between the dielectric function and the conductivity:

$$\varepsilon(\omega) = \varepsilon' + i\varepsilon'' = \left(1 + \chi^{(1)}(\omega)\right) + i \frac{\sigma(\omega)}{\varepsilon_0 \omega}, \tag{2-14}$$

where dielectric function, conductivity and linear susceptibility are all complex. In that case, the complex refractive index is:

$$n(\omega) = n' + in'' = \sqrt{\varepsilon(\omega)}, \tag{2-15}$$

where the real part is responsible for the phase (refractive index) and imaginary part for the absorption, and we get:

$$\varepsilon' = n'^2 + n''^2, \tag{2-16}$$

$$\varepsilon'' = 2n'n'', \tag{2-17}$$

$$\alpha(\omega) = \frac{2\omega}{c}\mathrm{Im}\sqrt{\varepsilon(\omega)} = \frac{2\omega}{c}\sqrt{\varepsilon''}, \tag{2-18}$$

$$n'(\omega) = \mathrm{Re}\sqrt{\varepsilon(\omega)}. \tag{2-19}$$

The imaginary part is usually called the extinction coefficient ($n'' = \kappa$ and $n(\omega) = n + i\kappa$) and indicates the absorption by medium. The exponential attenuation of the intensity of the field is linked to the absorption coefficient and the length x of the medium in Beer's law:

$$I(x) = I_0 e^{-\alpha x}. \tag{2-20}$$

Here we described the homogeneous system, which includes only a single medium complex refractive index. For more complicated systems with at least one interface of two different mediums, several complex refractive indices should be considered.

2.2 Gaussian beam, spot size and peak intensity

The most common beam shapes used in laser optics can be approximated by a Gaussian beam. The electric field is given by:

$$E(r,z) = E_0\left(\frac{\varpi_0}{\varpi(z)}\right)\exp\left(-\frac{r^2}{\varpi^2(r)}\right)\exp\left(-ikz - ik\frac{r^2}{2R(z)} + i\xi(z)\right), \tag{2-21}$$

where E_0 is the electric field amplitude, ϖ_0 is the spot size (radius) at the waist, k is the wave vector, defined by $k = 2\pi n_0/\lambda$. The function $\varpi(z)$ is the spot size (radius) at which the field amplitude drops by $1/e$, and defines the spot size variation as a function of the distance from the beam waist,

$$\varpi(z) = \varpi_0\sqrt{1 + \left(\frac{z}{Z_R}\right)^2}, \tag{2-22}$$

where $Z_R = \pi n_0 \omega_0^2/\lambda$ is the Rayleigh range. The radius of curvature is defined by:

$$R(z) = z\left(1 + \left(\frac{Z_R}{z}\right)^2\right), \tag{2-23}$$

and the phase change close to the beam waist, referred to as the Gouy shift, is defined by:

$$\xi(z) = \operatorname{atan}\left(\frac{z}{Z_R}\right). \tag{2-24}$$

Also, real laser systems generate beams slightly deviated from the ideal Gaussian beam. The parameter used to describe closeness of a generated beam to a theoretical beam is known as the M-squared value, M^2, and typically has a value of less than 1.2 for current laser systems.

The important feature of a Gaussian beam is that it does not change its intensity distribution upon the free space propagation. Also, it preserves its shape as it passes through an optical system consisting of simple lenses. This is particularly important for material processing as no additional beam shape control needs to be considered. Thus, the spot size of a Gaussian beam in the focus is:

$$\varpi_0 = \frac{\lambda M^2}{\pi NA} = 0.32\,\lambda M^2/NA, \tag{2-25}$$

where $NA = n\sin(\theta)$ is the numerical aperture of the focusing lens. The spot size for homogeneous illumination by non-coherent radiation is $\varpi_0 = 0.61\,\lambda M^2/NA$, seemingly bigger for equal numerical aperture. However, it should be noted that focusing a Gaussian beam will require the clear aperture of optics to be larger than that of the beam in order to avoid beam aperturing.

For relatively long laser pulses, the peak power can be measured directly. However for short pulses, the power is calculated from the pulse duration, τ, and the pulse energy, $E_p = P/f$, where P is the measured average power and f is the laser repetition rate. The conversion depends on the temporal shape of the pulse, and typically for Gaussian-shaped pulses the peak power is:

$$P_p \approx 0.94\frac{E_p}{\tau}, \tag{2-26}$$

and the peak intensity in the focal spot is:

$$I_p = 2\frac{P_p}{\pi\varpi_0^2}, \tag{2-27}$$

which is two times higher than it is calculated for the laser beam with a top-hat intensity profile. Additionally, the laser induced damage threshold is frequently expressed in units of laser peak fluence:

$$F_p = 2\frac{E_p}{\pi\omega_0^2}, \tag{2-28}$$

which indicates the highest fluence value occurring within the laser beam profile.

In general, the precise characterization of the laser beam including its spot size, peak power and peak intensity are of high importance in any laser material processing experiment. Although the discussed equations are simple and widely used, the nonlinear processes arising under the high laser intensities make the task difficult and in most cases inaccurate.

2.3 Nonlinear propagation

For high laser intensities, the nonlinear term of polarization $\vec{P}_{nl}$ can not be neglected any more. If we have two frequencies ω_1, ω_2 interacting in the second order nonlinear medium, we get the sum of frequencies. The polarization for the generated frequency, ω_3, is:

$$\vec{P}_i^{\omega_3=\omega_1+\omega_2} = \varepsilon_0 \chi_{ijk}^{\omega_3=\omega_1+\omega_2} \vec{E}_j^{\omega_1} \vec{E}_k^{\omega_2}, \tag{2-29}$$

$$\vec{P}_i^{\omega_3=\omega_1-\omega_2} = \varepsilon_0 \chi_{ijk}^{\omega_3=\omega_1-\omega_2} \vec{E}_j^{\omega_1} \vec{E}_k^{\omega_2}, \tag{2-30}$$

where the medium must possess broken centrosymmetry. It means that the change of the sign of the electric field must change the sign of polarization and not affect the amplitude. In order to get efficient second harmonic generation, the system requires tphase-matching; the fundamental wave vector must match the generated wave vector ($\Delta k = k^{2\omega} - 2k^{\omega} = (2\omega/c) \cdot (n^{2\omega} - n^{\omega}) = 0$).

The third order nonlinearity term of the material polarization can be observed in any medium, and is responsible for the Kerr effect, self-focusing, third-harmonic generation, stimulated Brillouin and Raman scattering, two photon absorption etc. Most of these effects become very critical during the interaction of intense ultrashort laser pulses with any medium. For the centrosymmetric medium, where the second order nonlinearity is neglected, polarization is:

$$\vec{P} = \varepsilon_0 \chi^{(1)} \vec{E} + \varepsilon_0 \chi^{(3)} \vec{E}\vec{E}\vec{E}. \tag{2-31}$$

From the Eq. (2-6) and (2-19) we express the dielectric function and refractive index as:

$$\varepsilon = \frac{\varepsilon_0 E + P}{\varepsilon_0 E} = 1 + \chi^{(1)} + \chi^{(3)}|E|^2, \tag{2-32}$$

$$n = n_0 + \frac{\chi^{(3)}|E|^2}{2n_0} = n_0 + n_{nl} I, \tag{2-33}$$

where $I = \varepsilon_0 c n_0 E^2/2$ is the laser intensity, and $n_0 = \sqrt{1+\chi^{(1)}}$ and $n_{nl} = 3\chi^{(3)}/4\varepsilon_0 c n_0^2$ are the linear and nonlinear terms of the refractive index, respectively. For low intensities, the refractive index is independent of the intensity. However, when the intensity is increased, to the point where the electric field starts to perturb the electron clouds around the nuclei, the refractive index starts to depend on the intensity (Figure 2-1).

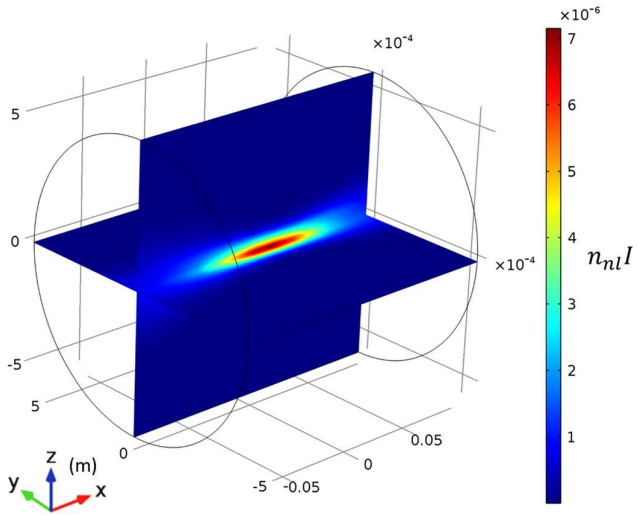

Figure 2-1. Induced refractive index change in silica glass by the Gaussian beam (λ = 1030 nm) with peak intensity of 6 GW/cm^2. *X*-axis defines the refractive index variation as a function of the distance from the beam waist ($\varpi_0 = 100 \times \lambda$) of collimated beam. Nonlinear refractive index coefficient is set to ~2.5×10^{-16} cm^2/W [12]. Calculations were performed based on reference [13].

Also, cubic nonlinear susceptibility evokes the damping in the medium due to multi-photon absorption. Similar to the refractive index, the absorption coefficient depends on the intensity of the electromagnetic field.

Moreover, there are multiple other processes that occur in the material when irradiated by high laser intensities causing carrier excitation and subsequent material permanent damage, and will be briefly discussed in the following sections.

2.4 Self-focusing and defocusing

For high laser intensities, the laser beam with a Gaussian intensity profile leads to spatial variations of the non-zero nonlinear refractive index (optical Kerr effect) with the highest value at the centre of the beam (Figure 2-1). Thus, the induced refractive index profile acts as a lens or a waveguide that may cause effects such as self-focusing and self-phase modulation. The phenomenon is important from a laser engineering and processing perspective, as the modification of the beam must be incorporated into the design.

When the power of a laser pulse is increased, self-focusing becomes stronger until it balances with diffraction and a filament is formed. If the peak power of the laser pulse exceeds the critical power for self-focusing,

$$P_{cr} = \frac{3.77\lambda^2}{8\pi n_0 n_{nl}}, \tag{2-34}$$

the collapse of the pulse to a singularity is predicted. Thus, the intensity of the short pulses inside transparent dielectrics can be significantly larger than its initial values (Figure 2-2), causing the damage of optical components or modification of optical material before the geometrical focus.

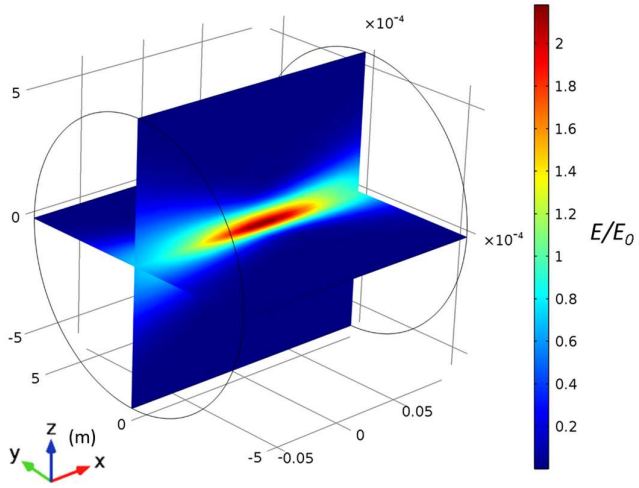

Figure 2-2. Self-focusing of Gaussian beam (λ = 1030 nm) with peak intensity of 6 GW/cm^2 propagating in silica glass. *X*-axis defines the E/E_0 variation as a function of the distance from the beam waist ($\varpi_0 = 100 \times \lambda$) of collimated beam. Nonlinear refractive index coefficient and critical power are set to ~2.5×10^{-16} cm^2/W [12] and ~4 MW, respectively. The magnitude of electric field increases as the self-focusing takes place. Calculations were performed based on reference [13].

Self-focusing of a collimated Gaussian beam is observed if the radiation power is greater than the critical power. In such a situation the Kerr nonlinearity continuously dominates over the

transverse diffraction. The scenario is changed when the beam is focused by a lens. Two regimes might be distinguished: for tight focusing the lens-focusing is dominated and the Kerr nonlinearity could be neglected, and for loose focusing the self-focusing is dominated. The boundary between these two regimes can be determined by [14,15]:

$$\sqrt{\frac{P_{in}}{P_{cr}}} = 0.852 + \sqrt{0.0219 + 0.1347 \times \left(\frac{\left(\frac{k\varpi_0}{2}\right)^2 - \left(\frac{n}{NA}\right)^2 + 1}{\left(\frac{n}{NA}\right)^2 - 1} \right)}, \tag{2-35}$$

When near the boundary obtained for a given spot size ω_0 of the collimated beam before the lens (or before the medium with n) both self-focusing and lens-focusing play a role. For example, if numerical aperture of the focusing lens is less than 0.01, self-focusing is likely to occur at input powers close to critical (Figure 2-3). If the numerical aperture is higher than 0.1, in order to get self-focusing, the input power has to be much higher than critical ($P_{in} > 10P_{cr}$) (Figure 2-3). However, the calculations does not account for plasma generation, and also loses its validity when the incident power is much larger than the critical power ($P_{in} > 100P_{cr}$).

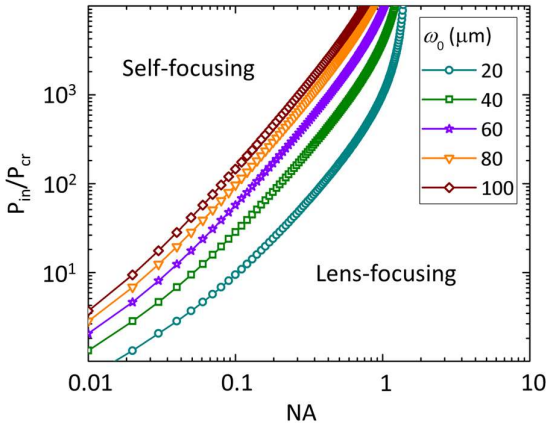

Figure 2-3. Self-focusing versus lens-focusing. Close to the boundary obtained for a given spot size (ϖ_0) of the beam at the plane of lens, both self-focusing and lens-focusing play a role. The calculations performed for fused silica at λ = 1030 nm. Typically the critical power in silica is around 4 MW.

On the other hand, when the laser beam is self-focused, the intensity increases and eventually reaches the medium ionization threshold. The generated plasma density (N) contributes a negative refractive index change [16],

$$n = n_0 - \frac{N}{2n_0 N_c}, \tag{2-36}$$

where $N_c = \omega^2 \varepsilon_0 m/e^2$ is defined as the characteristic plasma density with its frequency equal to the laser frequency, m and e are the electron mass and charge, respectively. As a result, the

plasma generation cancels the positive refractive index change and causes the subsequent defocusing.

2.5 Photoionization

Any interaction of an electromagnetic field with a target material can lead to structural modification. Therefore, both the linear and nonlinear properties of the medium are changed. The modification can be significant even far away from the fundamental absorption, where due to the high intensities of the light the multi-photon absorption caused by nonlinear processes takes part. This type of induced modification of a material is known as *laser assisted photoionization*. To achieve this in dielectrics, electrons must be transferred from the valence band to the conduction band.

At low intensities, photoionization can only occur if the energy of the absorbed photon is higher than the binding energy, E_g, of an electron. The direct excitation of electrons via the electromagnetic field is known as *multi-photon ionization (MPI)* (Figure 2-4(a)). In the MPI process, K photons of energy $\hbar\omega$ are absorbed and the energy balance is:

$$E_k + E_{int} = K\hbar\omega - E_g, \tag{2-37}$$

where E_k is kinetic energy of the ejected electron and E_{int} is the internal rotational/vibrational energy of the system directly after the ionization process. Thus, the minimum number K of photons needed for the MPI process is:

$$K\hbar\omega \geq E_g, \tag{2-38}$$

and the photoionization rate $P_{PI}(I) = \sigma_K I^K$ depends strongly on the laser intensity:

$$P_{PI}(I) = \sigma_K I^K, \tag{2-39}$$

where σ_K is the multi-photon absorption coefficient for K-photon absorption.

If the laser intensity increases, the electromagnetic field also increases and weakens the Coulomb potential between bonded electrons and atoms. During this deformation of the potential well, the tunnelling or over-the-barrier ionization is triggered (Figure 2-4(b,c)).

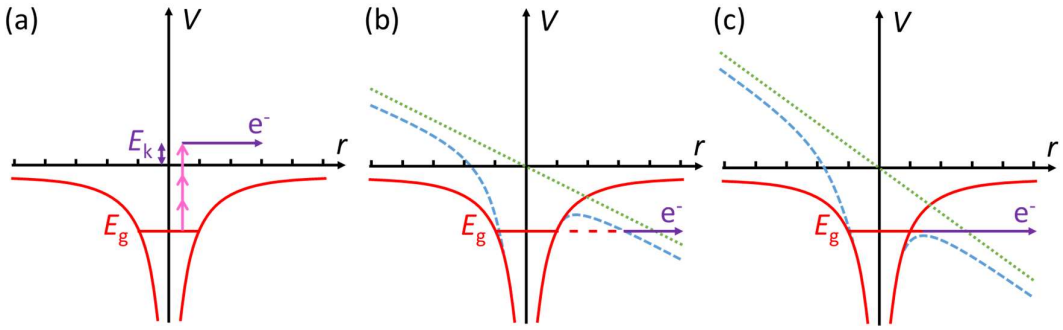

Figure 2-4. Schematic diagram of the ionization mechanisms in the nonlinear regime: (a) multi-photon ionization, (b) tunnelling ionization, and (c) over-the-barrier ionization. The red curves represent the original Coulomb potential and the dashed blue curves represent the distorted Coulomb potential by the external field, while the sloped green dotted line is the laser field potential. The solid red lines shows the energy of the least bound electron in the field-free case. The tunnelling path is indicated by the red dashed line.

As a result, the probability of the modification depends on the medium, laser frequency and intensity, and is governed by the Keldysh parameter [17]:

$$\gamma = \frac{\omega}{e}\sqrt{\frac{mcn\varepsilon_0 E_g}{I}}, \tag{2-40}$$

where ω is laser frequency, m and e are electron reduced mass and charge, I laser intensity, c is speed of light, n is refractive index of medium and E_g is binding energy of electron, which corresponds to the energy gap between the valence and conduction bands of the irradiated medium (e.g. 9 eV for silica glass, >1.5 eV for amorphous silicon, 1.1 eV for crystalline silicon). So, assuming $\hbar\omega < E_g$, the value of the Keldysh parameter identifies the origin of the ionization, where $\gamma < 1$ (high intensity and/or low frequency) indicates the tunnelling or over-the-barrier ionization, and $\gamma > 1$ (high frequency and rather low intensity) shows the nonlinear multi-photon response of the system.

For strong laser fields, one can expect ionization mechanisms such as tunnelling ionization or over-the-barrier ionization to dominate. The multi-photon picture does not hold anymore and the photoionization rates for various excitation wavelengths tend to merge revealing an independence on the photon energy, as i shown in Figure 2-5.

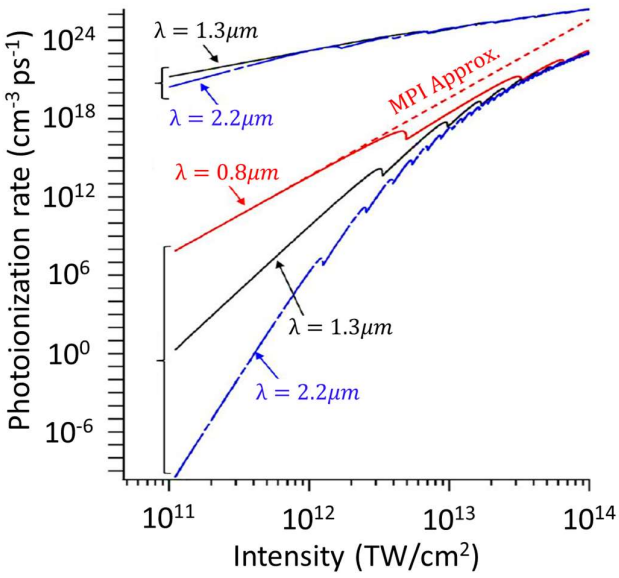

Figure 2-5. Photoionization rate as a function of laser intensity estimated by the Keldysh formulation for λ = 0.8 μm (red), λ = 1.3 μm (black) and λ = 2.2 μm (blue – dash-dotted). The calculations are performed assuming a band gap of 9 eV and 1.1 eV corresponding respectively to that of SiO2 and Si. For the case of fused SiO2 at 0.8 μm, the correspondence of the model with the well-established multi-photon approximation was checked (red dashed line) [17,18].

2.6 Free-carrier absorption and Avalanche ionization

An electron being excited to the conduction band of a wide bandgap dielectric material can absorb several laser photons sequentially, moving itself to higher energy states where free carrier absorption is efficient (Figure 2-6). In this case, the photons are absorbed in a broad band, where the absorption is linear for high plasma densities. Thus, the complex refractive index related to the dielectric function, i.e. permittivity of the free electrons, can be shown by:

$$\varepsilon(\omega) = 1 - \frac{\omega_p^2}{\omega^2 + i\Gamma\omega} = 1 - \omega_p^2 \left(\frac{\tau^2}{\tau^2\omega^2 + 1} + i \frac{\tau}{\omega(\tau^2\omega^2 + 1)} \right), \tag{2-41}$$

where $\omega_p = \sqrt{Ne^2/m\varepsilon_0}$ is the plasma frequency, expressed via the free electron density, electric permittivity, electron mass and charge, and Γ is denoted as a damping constant, also known as the relaxation or electron scattering rate, and is related to the electron mean free path l by $\Gamma = v_F/l = 1/\tau$, where v_F is the Fermi velocity and τ is the scattering time being typically from a fraction of a femtosecond to several tens of femtoseconds depending on the conduction electron energy. The imaginary part of the dielectric function, which is responsible for the light absorption, is:

$$\varepsilon'' = \frac{\omega_p^2 \tau}{\omega(\tau^2\omega^2+1)}. \quad (2\text{-}42)$$

When the electron density generated by photoionization reaches high values, e.g. $\omega_p \approx \omega$, $N \approx 10^{21}$ cm^{-3}, with an expected electron scattering time $\tau \leq 23\ fs$ [19,20], a large fraction of the remaining femtosecond laser pulse can be absorbed. Thus, avalanche ionization takes place, when the free-carrier absorption is followed by impact ionization (Figure 2-6).

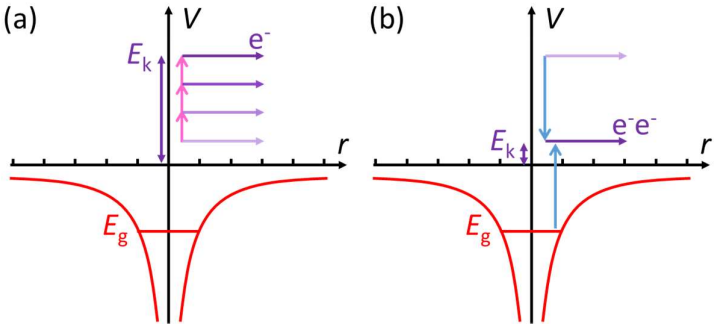

Figure 2-6. Schematic diagram of the free-carrier absorption and avalanche ionization mechanism. The three electron absorbs energy through free-carrier absorption acquiring sufficient energy to knock-out another electron from the valence to conduction band.

As long as the laser field is present, the electron density in the conduction band grows accordingly:

$$dN/dt = \eta_{av} N, \quad (2\text{-}43)$$

where η_{av} is the avalanche ionization rate. In very general terms, avalanche ionization requires seeding electrons in the conduction band of the material. These initial electrons could be provided either by thermally excited carriers, through easily ionized impurities or defect states, or by carriers that are directly excited by multi-photon or tunnelling ionization during the early stages of pulse propagation (Figure 2-7).

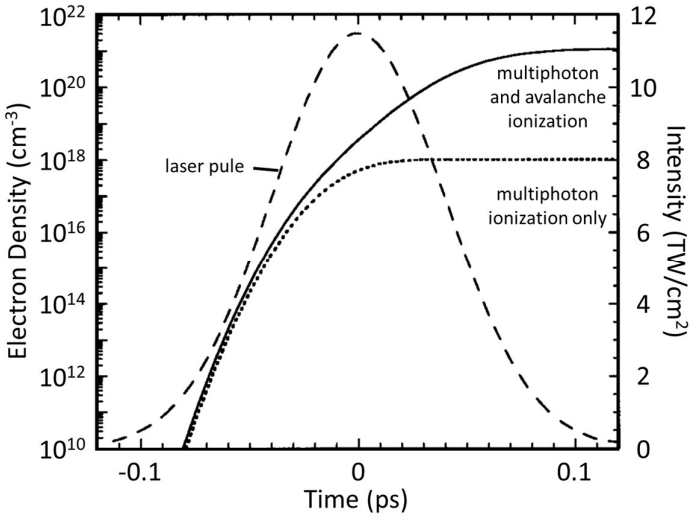

Figure 2-7. Electron densities produced by multi-photon ionization alone and in combination with avalanche ionization, plotted along with the Gaussian pulse shape. Seed electron are produced by multi-photon ionization at the peak of the pulse, after which an avalanche produced a critical density [21,22].

In summary, to ensure the accurate study of ultrashort laser pulses induced modification in a wide band-gap transparent solids, the nonlinear processes such as photoionization and impact ionization, self-focusing and defocusing, scattering and recombination etc., should be always considered. For example, permanent damage is typically related to the critical plasma concentration, while some experimental results put this assumption under dispute [20], indicating that the overall process is important. On the other hand, some effects strongly depend on the experimental configurations and could be easily neglected, e.g. self-focusing during the surface modification.

2.7 Permanent material modification

When sufficient energy is absorbed and delivered to the material, permanent modification occurs. In particular, this depends on the processing conditions and involves processes such as self-trapped excitons and defect formation, electron-phonon coupling and the subsequent refractive index change, nanostructuring and damage.

Through the nonlinear ionization processes discussed in the previous section, the electron is moved from the valence band to the conduction band, leaving a hole in the valence band. The excited electron and hole may be bound together by Coulomb attraction, which is referred to as an exciton [23]. Such electron-hole states are typically formed by an inelastic scattering of the

excited electrons or by direct resonant absorption (Figure 2-8). Consequently, free excitons may relax generating self-trapped excitons [24].

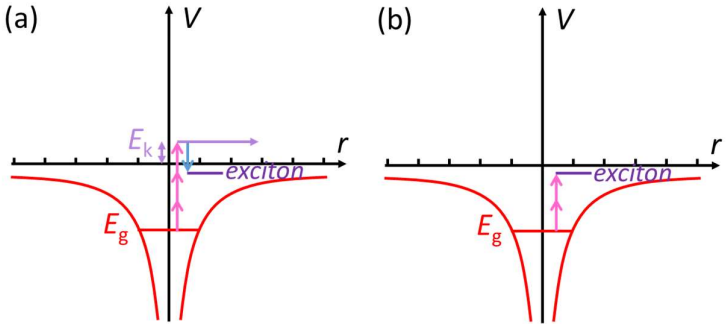

Figure 2-8. Schematic illustration of exciton level and two basic routes for exciton generation: (a) inelastic scattering of the multi-photon excited electrons, and (b) direct resonant absorption of multiple photons.

The relaxation of excitons to defects occurs a few tens of picoseconds after laser excitation, where the self-trapping process is accompanied by a strong distortion of the lattice. In the case of silica glass, weakening of Si–O–Si bonds yield an oxygen displacement from the equilibrium position in the tetrahedral, leading to a formation of silicon and oxygen dangling bonds [19], presented in Figure 2-9. This is one of the processes, in addition to material densification, resulting to a refractive index change in a wide band-gap silica materials. Structurally amorphous silica tetrahedra in the bulk can be shown as ≡Si–O–Si≡ with the defects induced by femtosecond pulses [25–29]: oxygen deficiency centers ODC(I) and ODC(II), which are four valent (≡Si-Si≡) and divalent (=Si^0) silicon atoms with its characteristic absorption at 160 nm and 250 nm, respectively; *E'* (≡$Si^{\bullet}$) is an asymmetric relaxed oxygen vacancy with an unpaired electron localized in a sp^3-like orbital of a single Si atom with its characteristic absorption at 210 nm; and oxygen excess center, referred to as a nonbridging oxygen hole centre NBOHC (≡Si–$O^{\bullet}$), is oxygen dangling bond with its characteristic luminescence at 650 nm. As a result of the intense ultrashort laser pulses, the defects generated from the self-trapped excitons increase drastically, leading to the potential of macroscopic structural damage in the material. Moreover, there is no doubt that these structural changes influence the ongoing multi-pulse modification of the material by producing absorption centres for the subsequent material ionization.

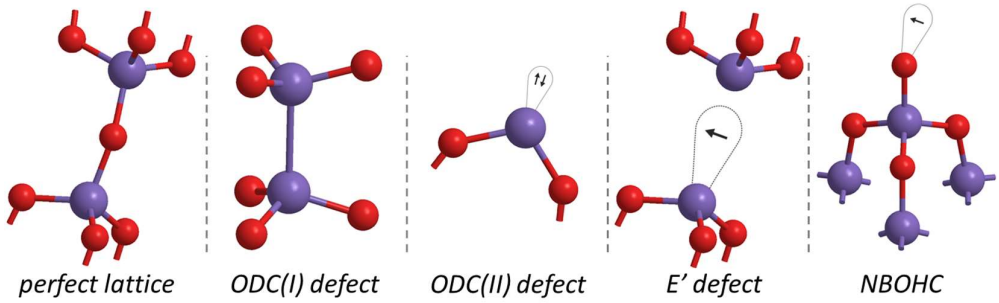

Figure 2-9. Structural models of perfect SiO_2 lattice and most common laser induced defects: ≡Si–Si≡ (Si rich ODC(I)); $=Si^0$ (ODC(II)); $≡Si^{\bullet}$ (E') and $≡Si–O^{\bullet}$ (NBOHC). Purple spheres – silicon; red spheres – oxygen. Structural models were reproduced on the basis of ref. [25–29].

The permanent modification of transparent materials strongly depends on the laser pulse duration, as it is a very nonlinear process and depends on a rapid build-up of conduction electrons. Free-carriers, excited through the processes discussed in the previous section and summarized in Figure 2-10 and Figure 2-11, distribute the absorbed energy via a carrier-carrier scattering over 10-100 fs and via a carrier-phonon scattering over < 10 ps. Thus, the lattice thermalization takes place around 10 ps. If the laser pulse duration is of the same timescale, a substantial amount of energy will be transferred to the lattice [30], while part of the excited states will be removed via the carrier recombination and diffusion processes. As a result, when the free carriers and lattice are at the equilibrium temperature, the material is at the same phase as it would be heated by conventional means [11]. The material modification dominated by thermal diffusion with the threshold scaled as the square root of the pulse duration $(\sim\sqrt{\tau})$ takes place (Figure 2-12). Material ablation, melting, evaporation and subsequent resolidification may occur with a strong tension gradient located around the irradiated regions [11].

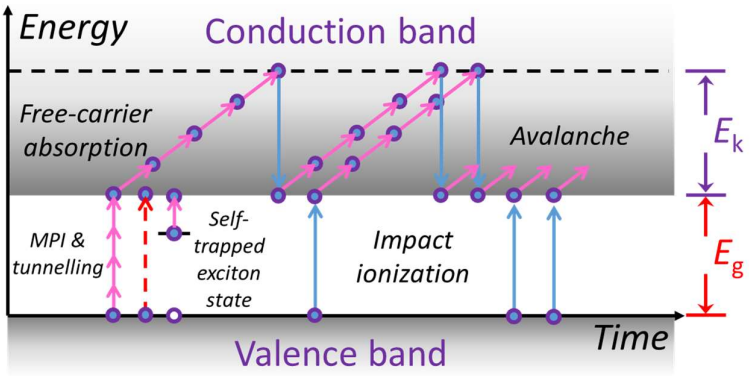

Figure 2-10. Schematic illustration of carrier excitation process in time.

For laser pulses shorter than several picoseconds, the energy absorption processes occur earlier than the energy transfer to the lattice [21]. As a result, the modification threshold deviates from the thermal diffusion relation $\sim\sqrt{\tau}$, as it is shown in Figure 2-12 [21,22]. It is widely discussed that the electrons reach high temperatures keeping the lattice in the cold state during the irradiation time. The subsequent shock-like deposition of energy from electrons to the lattice, after the pulse is gone, causes the ablation or structural change of material [19]. Thus, the energy deposition is localized, reducing the heat affected zone and collateral damage [10,11].

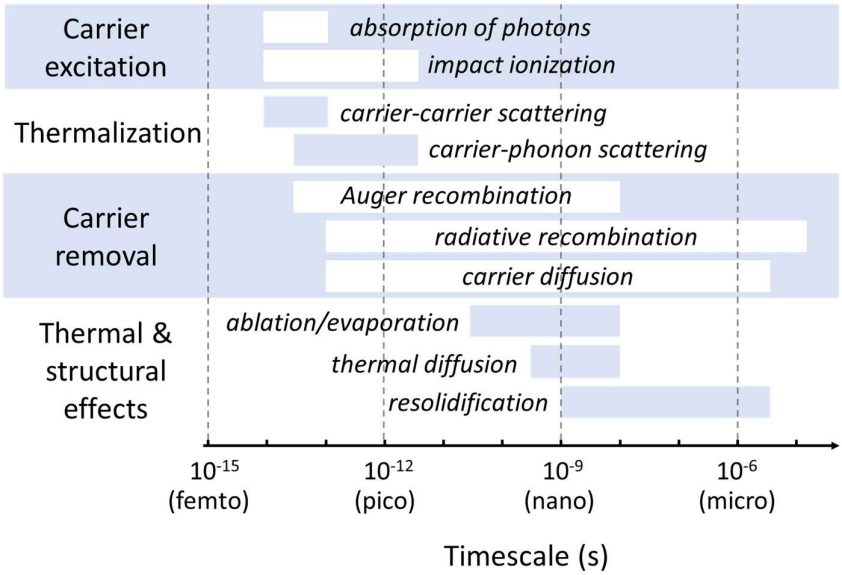

Figure 2-11. Timescales of various electron and lattice processes in laser excited solids. Each bar represents an approximate range of characteristic time over a range of carrier densities from 10^{17} cm^{-3} to 10^{22} cm^{-3} [10,11,31].

In order to ablate the atoms from a solid, energy higher than its binding energy must be delivered. When the Fermi energy (approx. binding energy) is exceeded, the electrons are ejected creating the electric field caused by charge separation and pull the ions out of the material. At the same time the ponderomotive force of the EM field moves electrons deeper into the material accelerating the ions [32]. Such material ablation processes occur under femtosecond laser pulses when the thermal effects are neglected.

However, despite the extensive studies aimed to determine the mechanisms of femtosecond laser induced modification [10,11,19–21,33], the processes are still not fully understood. Critical or sub-critical plasma densities, thermal or non-thermal processes, defect-free or defect-accumulated, fast thermal cooling and micro-explosions, melting and vaporization etc., still are hot topics of discussion.

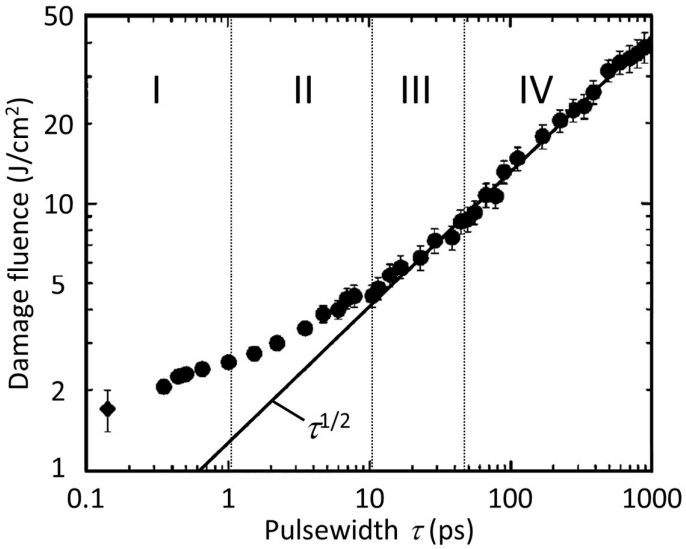

Figure 2-12. Pulse width dependence of threshold damage fluence for fused silica at 1053 nm (•) and 825 nm (♦) [21,22]. The corresponding pulse width leads to (I) strong non-equilibrium ($T_{electron} >> T_{lattice}$) medium with dominant multi-photon and avalanche ionization; (II) electron-lattice thermalization (carrier-carrier and carrier-phonon scattering) during the pulse propagation; (III) increasing lattice heat with the resultant damage threshold dominated by thermal diffusion $\left(\sim\sqrt{\tau}\right)$; (IV) melting and boiling as the multi-photon ionization is not sufficient to seed avalanche.

Various types of modification inside transparent solids as a function of laser fluence and pulse duration can be produced. Under femtosecond laser irradiation of bulk silica glass, at low pulse energies a smooth positive refractive index change is observed [3,34]. At higher pulse energies subwavelength gratings, referred to as nanogratings [7,8] are observed. At high pulse energies voids-like damage [35] have been reported. These three regimes can be clearly distinguished employing laser pulses shorter than 300 fs [36,37] (Figure 2-13). Even at longer pulses, slightly perturbed nanogratings appear at relatively low fluencies, right above the permanent modification threshold. All three modification types have found high interest from scientific communities and are widely implemented in various fields including fabrication of waveguide lasers in doped glasses and crystals [38,39], polarization sensitive elements [40,41], optical data storage [42,43].

Similar modification regimes are observed on virtually any type of media including metal, semiconductor, dielectric solids and thin films [4,6,44–54], multicomponent [55] and porous [56–58] glasses. Under the pulse energies slightly below or above the damage threshold, the material nanostructuring, amorphization, crystallization, oxidation, ablation, melting etc. can be induced. The flexibility of this technique in terms of materials and ability to implement 3D geometries with

subwavelength precision turned it into an ideal low-cost platform for rapid prototyping, which could be explored in multiple fields.

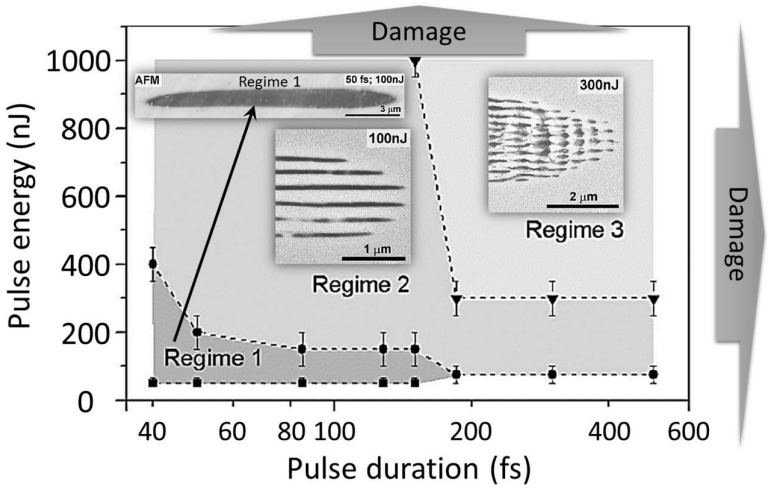

Figure 2-13. Threshold pulse energies for different regimes of femtosecond laser induced modification in silica glass. Regime 1 corresponds to smooth refractive index modification. Regimes 2 and 3 correspond to nanogratings formation. Inset atomic force and scanning electron microscopy images of structures induced by 50 fs and 100 nJ (Regime 1), 185 fs and 100 nJ (Regime 2), 500 fs and 300 nJ (Regime 3) [36].

Chapter 3: Engineered optical materials

The main objective of this thesis is material anisotropy induced by ultrafast laser irradiation. In this chapter I will provide the basic concept of the form birefringence, dichroism and geometric phase, and I will focus on the literature review of shaping of metal nanoparticles and fabrication of volume and surface periodic structures. Although the mechanisms of ultrafast laser nanostructuring is still not clear, the brief discussion on the studies done by other groups including the identification of structural and optical properties, and the subsequent implementations will give a better understanding of the processes taking place.

3.1 Form birefringence and dichroism

Gratings with a period smaller than the wavelength of the incident light are known as a subwavelength grating, and is often referred to as nanogratings. The light wave in such subwavelength structure behave the same way as that in an anisotropic material, and the phenomenon is known as form birefringence [59–61]. The form birefringence can reach much higher values than natural anisotropic crystals, and is usually designed by controlling the periodicity and duty cycle of the nanogratings. Propagation of optical waves in such periodic media can thus be described by the effective refractive indices coming from the effective-medium theory [59]. This means that the electric field oscillating along (*TE* mode) and perpendicular (*TM* mode) to the layered medium obtain a different amount of phase shift.

For a specific periodic system, the Bloch wave analysis [59] can be employed to analyse the *TE* and *TM* waves propagating in the medium. The eigenmodes of propagation are the Bloch waves expressed as:

$$E = E_K(y)\exp(-i\beta z - iKy + i\omega t), \tag{3-1}$$

where β and K are the *z* and *y* components of the Bloch wave vector, with K corresponding to the wave vector of the periodic structure. The dispersion relation between λ and K for the *TE* and *TM* waves propagating in media with refractive indices n_1 and n_2 of the corresponding layers *a* and *b* with periodicity of $\Lambda = a + b$ (see Figure 3-1) is given by [59]:

$$TE\colon \cos(K\Lambda) = \cos(k_{1y}a)\cos(k_{2y}b) - 0.5\left(\frac{k_{2y}}{k_{1y}} + \frac{k_{1y}}{k_{2y}}\right)\sin(k_{1y}a)\sin(k_{2y}b), \tag{3-2}$$

$$TM\colon \cos(K\Lambda) = \cos(k_{1y}a)\cos(k_{2y}b) - 0.5\left(\frac{n_1^2k_{2y}}{n_2^2k_{1y}} + \frac{n_2^2k_{1y}}{n_1^2k_{2y}}\right)\sin(k_{1y}a)\sin(k_{2y}b), \tag{3-3}$$

with

$$k_{1y,2y} = \sqrt{\left(\frac{2\pi n_{1,2}}{\lambda}\right)^2 - \beta^2}, \tag{3-4}$$

$$\beta = \frac{2\pi}{\lambda} n_{o,e}, \tag{3-5}$$

where $n_{o,e}$ are the related ordinary and extraordinary (i.e. effective) indices of refraction for *TE* and *TM* waves, respectively.

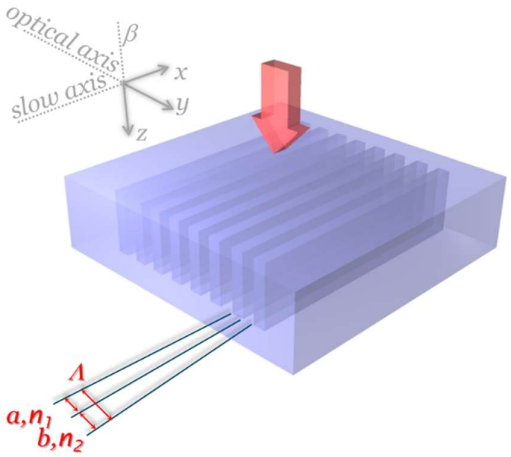

Figure 3-1. The light wave (β) propagation along the lamella-like structures. Optical and slow axes of the designed birefringent element are perpendicular and parallel to the grating planes, respectively. The periodicity of such structure is defined as $\Lambda = a + b$, where *a* and *b* corresponds to the width of materials with refractive indices of n_1 and n_2.

When the periodicity of nanogratings is much smaller than the wavelength of the incident light, the lowest order approximation $\{O[(\Lambda/\lambda)^2]\ \text{expansion}\}$ of Eqs. (3-2) and (3-3) can be used [62], leading to:

$$TE: \frac{K^2}{n_0^2} + \frac{\beta^2}{n_0^2} = \left(\frac{2\pi}{\lambda}\right)^2, \tag{3-6}$$

$$TM: \frac{K^2}{n_0^2} + \frac{\beta^2}{n_e^2} = \left(\frac{2\pi}{\lambda}\right)^2, \tag{3-7}$$

with the resulting effective refractive indices defined by:

$$\frac{1}{n_e^2} = \frac{a}{\Lambda}\frac{1}{n_1^2} + \frac{b}{\Lambda}\frac{1}{n_2^2}, \tag{3-8}$$

$$n_o^2 = \frac{a}{\Lambda} n_1^2 + \frac{b}{\Lambda} n_2^2. \quad (3\text{-}9)$$

Then, the form birefringence of such structures is related to the nanograting properties by:

$$n_0^2 - n_e^2 = \frac{ab\left(n_1^2 - n_2^2\right)^2}{\Lambda\left(an_2^2 + bn_1^2\right)}. \quad (3\text{-}10)$$

The layered medium, with $\Lambda \ll \lambda$, optically behaves as a uniaxial material with the birefringence being always negative, i.e. $\Delta n = n_e - n_o < 0$. Also, from Eq. (3-8) and (3-9) the periodic medium do not depend on the wavelength of light, except on the intrinsic material dispersion of n_1 and n_2. However, if the periodicity is comparable to the wavelength, the approximations become invalid. Thus, the dispersion of the periodic structure has to be considered adding a higher order approximation [63,64], and the accurate estimate of Eq.(3-10) is written as:

$$n_0^2 - n_e^2 = 4\frac{ab}{\Lambda^2}\left[(n_2 - n_1)^2 + \frac{(b-a)(n_2 - n_1)^3}{\Lambda n_2}\right] + O((n_2 - n_1)^4). \quad (3\text{-}11)$$

As a result, the phase retardation of transmitted light can be directly determined by the thickness (d) of the nanogratings and its possessed form birefringence:

$$\varphi = d \cdot (n_o - n_e). \quad (3\text{-}12)$$

In addition, artificial electromagnetic media based on metallic or polar dielectric nanostructures, with a non-zero imaginary part of the refractive index, by coupling light to free electrons or phonons can control the amplitude of the light waves. If the anisotropy is introduced, the polarization sensitive transmission, also known as differential extinction or dichroism, can be observed.

The polarization microscopy can be used for birefringent or dichroic sample characterization as a contrast enhancing tool. The traditional polarization microscope is represented in Figure 3-2. The transmitted intensity of light is measured when the polarizer before the sample is fixed at -45° with respect to the nanograting orientation, while the polarizer after the sample is fixed at -45° (parallel) or 45° (crossed). The retardance dispersion $\varphi(\lambda)$ is then defined by:

$$\varphi(\lambda) = \operatorname{acos}\left(\frac{I_{parallel} - I_{crossed}}{I_{parallel} + I_{crossed}}\right) \times \frac{\lambda}{2\pi} = \Delta(\lambda) \times \frac{\lambda}{2\pi}. \quad (3\text{-}13)$$

The ratio of the transmitted light intensity polarized perpendicular and parallel to the orientation of nanostructures ($I_{\perp sample}/I_{\parallel sample}$) expressed in absorption units, i.e. dichroism, can be defined as follows:

$$D = A_{\perp} - A_{\parallel} = -log\left(\frac{I_{\perp\,\mathrm{sample}}}{I_{\parallel\,\mathrm{sample}}}\right), \tag{3-14}$$

where $A_{\perp}$ and $A_{\parallel}$ are the extinction spectra for two different polarizations.

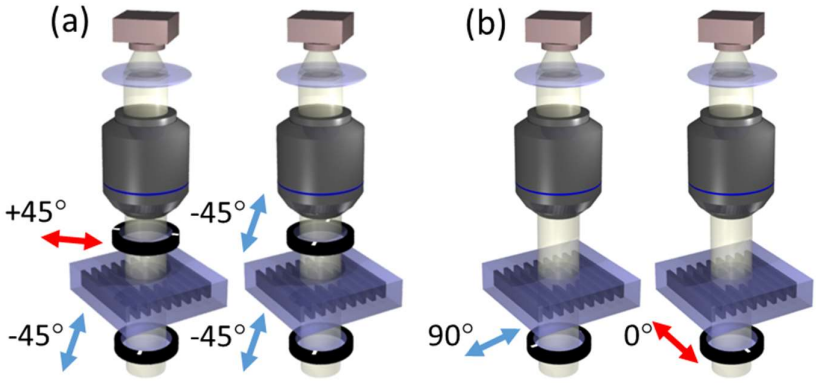

Figure 3-2. Schematic configurations of (a) retardance and (b) dichroism spectra measurement set-up. The phase retardation is calculated from the transmittance of light measured when the linear polarizer before the sample was fixed at -45° with respect to the nanogratings orientation while the linear polarizer after the sample was fixed at 45° (parallel) or −45° (cross-polarized). For the dichroism characterization, the transmittance of light polarized parallel (0°) and perpendicular (90°) to the orientation of nanogratings is measured.

The previously described anisotropy measurement system can be used only if the orientation of the nanogratings is known. For more complex samples, this problem can be solved with the PolScope microscope [65], which is essentially the same polarization microscope with polarizer and analyser (Figure 3-3). In the PolScope system, a linear polarizer is replaced with a circular polarizer simplifying the further extraction of data and excluding the possibility of undefined measurements when the polarization plane is oriented along the slow or fast optical axis. The analyser with a liquid crystal universal compensator, which is made of variable retarder plates (LCA and LCB) and a linear polarizer, are used. The PolScope also requires monochromatic light, thus the circular polarizer is combined with an interference filter. The intensity recorded by the detector is:

$$\begin{aligned} I(\alpha,\beta,x,y) = \frac{1}{2} I_0(x,y) \\ \cdot [1 \\ + \cos\alpha \sin\beta \cos\varphi(x,y) \\ - \sin\alpha \sin\beta \cos 2A(x,y) \sin\varphi(x,y) \\ + \cos\beta \sin 2A(x,y) \sin\varphi(x,y)] + I_{min}(x,y). \end{aligned} \tag{3-15}$$

Here I_0 is the distribution of light intensity after the sample, I_{min} is the distribution of the depolarized background arising from the imperfections of the polarizers. The α and β are the retardance values for LCA and LCB retarders, respectively. Finally, the characterization of sample with its intrinsic retardance $\varphi(x,y)$ and azimuth of the slow axis direction $A(x,y)$ are performed by measuring a series of intensity images for various α and β values, and extracting the $\varphi(x,y)$ and $A(x,y)$ values [65].

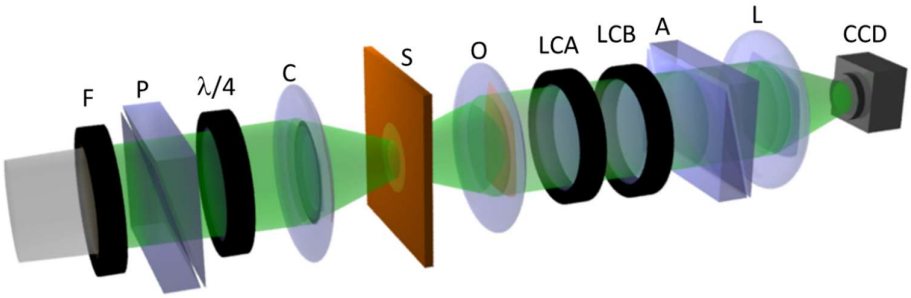

Figure 3-3. Schematic of typical birefringence characterization system PolScope. The optical set-up is based on a traditional light microscope and an analyser for circular polarized light: band-pass filter for 546 nm (F); linear polarizer (P); quarter-wave plate (λ/4); condenser lens (C); specimen (S); objective lens (O); polarization state analyser made of liquid crystal devices LCA and LCB, and analyser (A); imaging lens (L) and camera detector (CCD) [65].

3.2 Geometric-phase optics

Conventional optics such as lenses, mirrors, etc. manipulate the phase via an optical path difference by controlling thickness d or refractive index $n = (n_e + n_o)/2$ of a material (Figure 3-4). Thus, the dynamic phase term can be expressed as:

$$\phi(x,y) = \frac{2\pi}{\lambda} n(x,y) d(x,y). \tag{3-16}$$

Despite decades long expertise in fabrication of optical elements, precision and quality still remains a challenging problem. Moreover, in an increasing number of cases it is desirable to create arbitrary vectorial beams, where the polarization is varied in space [66].

Recently, a promising type of optic has emerged exploiting space-variant polarization-state manipulations for controlling light. Here, the wave front is modified by introducing a spatially varying anisotropy and is a result of the geometric phase known also as Pancharatnam-Berry phase. The calculation of the space-variant Pancharatnam-Berry phase is based on the rule proposed by Pancharatnam [67] for comparing the phases of two light beams in different

states of polarization as the argument of the vectorial projection between the two polarization states. Pancharatnam showed that a cyclic change in the state of polarization of the light is accompanied by a phase shift determined by the geometry of the cycle as represented on the Poincaré sphere [68]. As a result, space-variant polarization-state manipulations are accompanied by a phase shift that results from the geometric phase [69,70]. For the most general case, the geometric phase occurs when polarization and phase are changed simultaneously but very slowly (adiabatically), and eventually brought back to the initial configuration. For example, when circularly polarized light is transmitted through a wave plate, an absolute phase shift results, which is equal to twice the rotation angle of the wave plate optical axis. Here, the phase front is modified by introducing a spatially varying anisotropy:

$$\phi(x,y) = 2A(x,y), \tag{3-17}$$

where A is the local azimuth of the slow-axis (or optical axis) of a space-variant anisotropic material. This allows continuous optical phase shifts and without phase resets (Figure 3-4), in contrast to the conventional elements, wherein the phase profiles are encoded as discrete optical path variations in the refractive index or thickness, limiting its performance. The phase reset in dynamic phase elements result in unwanted diffracted light, reducing efficiency and introducing artefacts. The absence of such discontinuities in geometric phase optics allows to achieve high-fidelity and continuous phase shifts with a high conversion efficiency. In particular, phase profiles of any optical component can be achieved solely by means of the geometric phase with efficiencies reaching 100%.

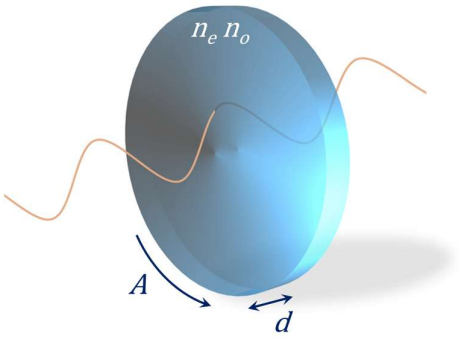

Figure 3-4. Light wave propagation along the optical element. Thickness *d* and refractive index $n = (n_o + n_e)/2$ variation in space produces dynamic phase shift, and spatial variation of azimuth of the slow-axis (or optical axis) of anisotropic material results into geometric phase shift.

Spectral behaviour of the geometric phase optics is generally independent of the phase profile, and determined almost entirely by the properties of the material or structure itself. As a result, spectra may range from very achromatic to highly chromatic [71]. Also, geometric phase shifts are polarization selectable. If the input light is a conjugate of two orthogonal circular polarizations, it will be coupled into the separate waves with positive and negative geometric phase shifts. Thus, by adjusting the input polarization, the special control of light beam will be achieved [72].

Although geometric phase optics is a promising alternative for manipulating light, it still stumbles on the lack of an adequate technology for cost-efficient fabrication of flexible and durable optical elements. A large number of space-variant polarization elements were implemented as spatially oriented dielectric or metal gratings [40,73–78], polarization-sensitive materials such as azobenzene-containing materials [79], and liquid-crystal devices [80–85]. The fabrication methods mainly depend on standard nanolithography techniques with the predefined materials such as silicon or noble metals. Thus, the efficiency is limited by plasmonic absorption, antenna scattering and structure density. However, only the recent alternative demonstrations of photo-aligned transparent dielectrics such as liquid crystals and silica show the potential to leverage the field of geometric phase optics. The typical fabrication set-up for direct-write ultrafast laser nanostructuring of silica is shown in Figure 3-5. Cost-efficient and high-precision direct-write techniques with flexible target materials, conversion efficiencies higher than 90%, and negligible optical absorption will definitely challenge the limitations of conventional optics.

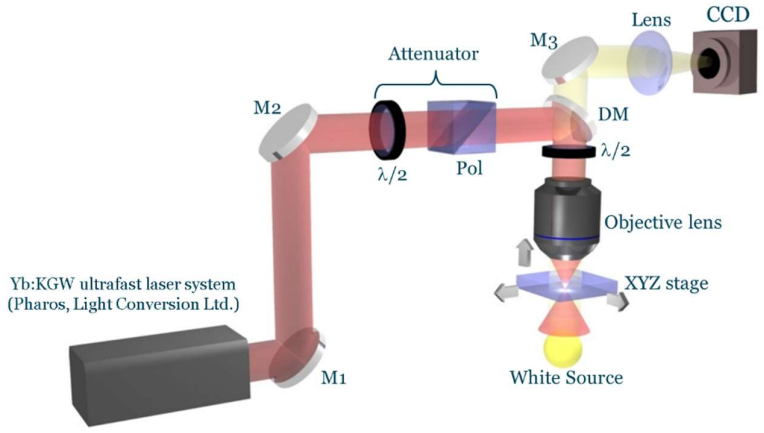

Figure 3-5. Typical experimental set-up for direct-write ultrafast laser nanostructuring of transparent solids. Power and polarization of focused pulses are controlled via half-wave plates mounted on rotation stages and synchronized with the ultrafast laser system and XYZ translation stages. The fabrication process is always monitored with camera detector.

3.3 Laser induced periodic surface structures

First observation of laser induced periodic surface structures (LIPSS) dates back to the 60's, when Birnbaum reported ripple formation on the surface of semiconductors [86]. Since then, this phenomena was observed on virtually any type of media including metals, semiconductors and dielectrics [4,44–47]. The phenomenon turned out to be rather universal and the ripples could be formed with wavelengths ranging from the mid-infrared to the blue end of the visible spectrum and from continuous wave operation to femtosecond laser systems. Example of TiN surface structure formed by femtosecond pulses is shown in Figure 3-6.

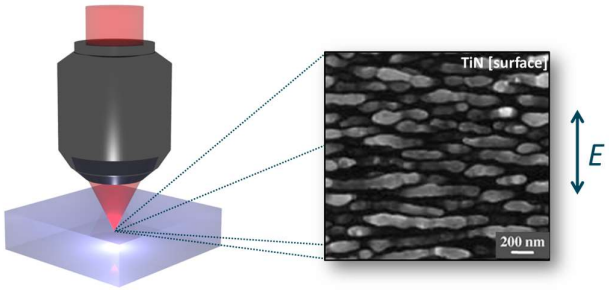

Figure 3-6. Periodic surface structures formed on TiN surface by 100 linearly polarized ultrashort laser pulses with 130 fs pulse duration, 800 nm wavelength, repetition rate of 2 Hz, and fluence of 0.3 J/cm^2, focused via a plano convex lens with F = 60mm [6].

For normal incidence, the period of surface structures was known to be close to the wavelength of the light and oriented perpendicular to the laser beam polarization [87]. For oblique incidence and *TM* polarization (electric field is oriented parallel to the plane of incidence) the ripples occur with one of two possible periods [88]

$$\Lambda = \frac{\lambda}{1 \pm \sin\theta}, \tag{3-18}$$

where θ is the angle of the incident of laser beam, and the negative or positive signs correspond to the forward and backward scattering, respectively. If the laser beam is moved with respect to the sample, the ripples can coherently extend over the scanned area.

Lately, ultrashort laser pulses were observed to induce two types of periodic surface structures [89]: above single pulse damage threshold – ripples with a period close to the wavelength ($\sim\lambda$), and below single pulse damage threshold – subwavelength ripples with periods down to 30 nm $(\lambda/10)$ [90,91]. Here, the period was found to be dependent on the number of pulses and the subsequent carrier density [49,91,92], where the final subwavelength structure is formed only after tens or even thousands of pulses.

It is generally accepted that low-spatial frequency LIPSS (LSFL), having a spatial period close to the laser wavelength, are formed due to optical interference of the incident laser light with a surface electromagnetic waves generated at the interface of materials. At certain carrier densities (~2×10^{21}–1×10^{22} cm^{-3}), the combination of LIPSS theory [93] with a Drude model shows that the excitation of surface plasmon polaritons (SPPs) and its interference with the femtosecond laser pulse take place [92,94–97]. The surface wave driven periodic modulation of the electromagnetic field along the laser polarization gives anisotropy in the following modification processes. It is assumed that the further steps are governed by the fast (non-thermal) and slow (thermal) phase transitions [11,98–106]. Under a short pulse irradiation, due to the high peak intensities the excitation of a large fraction of electrons from bonding to anti-bonding states destabilizes the lattice and leads to an instantaneous melting within a sub-picosecond timescale. On the other hand, upon pulse durations longer than the carrier-phonon coupling time, the efficient energy transfer from optically excited electron-hole plasma to the crystal lattice is ensured. So after an excitation lasting several picoseconds, the carrier-lattice thermalization and subsequent lattice melting occurs. Once the solidification process starts within nanoseconds after the excitation, the liquefied phase crystallizes into the LSFL pattern. The early stage LSFL upon a subsequent pulse irradiation modulates SPP phase-matching conditions and reduces the periodicity of the final pattern.

In contrast, the high-spatial frequency LIPSS (HSFL) have spatial periods significantly smaller than the irradiation wavelength and are usually observed for irradiation with ultrashort laser pulses predominantly for below band-gap excitation of transparent materials and hundreds to thousands of laser pulses per irradiation spot. However, the origin of the HSFL is still quite controversially discussed in the literature [6,94,96,107,108]. Within the interpretations proposed in previous studies [11,109], the early stage laser induced unstable nanostructures, during the relaxation of a highly non-equilibrium surface, self-organize into HSFL patterns.

As a result, the nanostructuring in a single-step process provides a practical way of designing functional surfaces towards the controlled optical [110], mechanical and chemical [111] material properties, which could be used for various applications such as colorizing and dewetting shown in Figure 3-7. Even so, the optical anisotropy of LIPSS has never been the main object of study, and only the periodic volume nanogratings induced in glass were explored in the field of light manipulation [40], and will be briefly discussed in the following section.

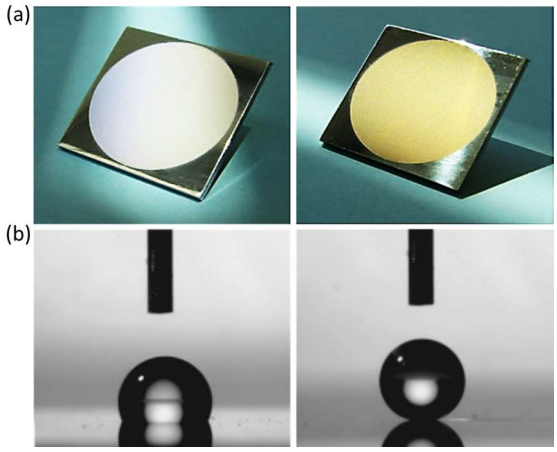

Figure 3-7. Practical applications of laser induced periodic surface structures. (a) Images show that the same laser processes aluminium sample exhibits various colours depending on the view angle [110].(b) Water droplets on flat (left) and processed (right) silicon surface treated with fluorosilane [111].

3.4 Self-organized nanogratings in silica glass

Under certain conditions, the interaction of femtosecond pulses with silica is known to induce self-assembled nanostructures with lamellae-like oxygen deficient regions oriented perpendicular to the incident beam polarization [7,8], shown in Figure 3-8. A decade ago, Bricchi et al. demonstrated that such thermally stable nanostructures due to the sub-wavelength periodicity behave as a uniaxial birefringent material where the optical axis is parallel to the orientation of laser polarization [9,112]. Here the negative birefringence of $\Delta n \approx -4 \times 10^{-3}$, and of the same order as the natural birefringence of uniaxial crystals such as quartz, ruby and sapphire, was reported. The recent works suggested these regions being a composition of parallel planar nanocracks [63] or nanoporous planes filled with decomposed SiO_2 and oxygen [113] with silica nanocrystals of several nanometres size embedded in the defect-rich nanogratings planes [114].

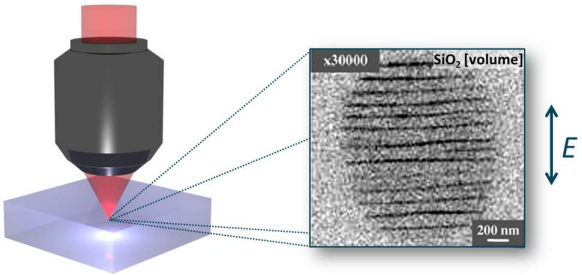

Figure 3-8. Periodic structures formed in silica glass by ultrafast laser system operating at wavelength of 800 nm and delivering pulses of 150 fs at repetition rate of 200 kHz. Train of pulses with energy of 1 μJ was focused inside silica via 0.95 NA objective [7].

Despite many hypotheses to explain the mechanism of the peculiar self-organization, the formation of the periodic nanostructures remains under debate bringing the ideas of seeding processes governed by the randomly distributed inhomogeneity [7,115–120]. Recently, the single isolated nanoplane was achieved in porous silica prepared from the phase-separated alkali-borosilicate glass [56,58,57]; and combining the experimental results with the concept of the surface plasma wave excitation, the significance of the seed structure was identified. Additionally, the constructive interference of scattered light was proposed to explain the extreme shortening down to sub-100 nm of the nanogratings period. This relates very well to the effects observed in surface ripple formation, when the period is found to be dependent on the number of pulses [121].

The initial model for nanograting formation was based on the interference of the bulk electron plasma longitudinal wave, propagating in the plane of light polarization, with the incident light [7]. The early coupling is triggered by inhomogeneities induced along with the motion of free carriers. Thus, the periodic structure resulted due to the interference, enhancings the coupling and generates a periodic modulation of the plasma concentration ($>10^{21}$ cm^{-3}). As a result, this modulation is further frozen within the material structure. Conversely, the model does not work in the case of subcritical plasma concentrations. Later, this model was adjusted by assuming two-plasmon decay [122]. The two-plasmon decay is the parametric process in which the incident photon is separated into two plasmons, i.e. two electron plasma waves. The interference between two plasmons of the same frequency propagating in opposite directions produce periodic subwavelength modulations (Cherenkov mechanism of momentum conservation). The characteristic generation of the 3/2 harmonic may be observed due to the decay process. Although the model is valid for plasma concentrations lower than critical ($\sim10^{20}$ cm^{-3}), experimentally this was never confirmed by independent research groups.

Nanoplasma formation was the other model implemented to explain the nanogratings formation [63,115]. In very general terms, the generation of defect inside silica matrix is followed by the formation of inhomogeneous plasma. Under the multipulse regime, the plasma spots evolve into spherically shaped nanoplasma. Due to the local field enhancement at the boundaries, the polarization sensitive growth of initially spherical nanoplasma will occur. When the electron concentration is below the critical, the electric field is enhanced at the equator leading to nanoplane formation. The final pattern leads to the period of $\lambda/2n$. However, if the plasma concentration is too high, the dominant enhancement at poles would be initiated, and nanogratings would not be produced. Recently, the nanoplasmonic model has been elaborated by introducing the randomly distributed inhomogeneities in fused silica [119]. Within the increase of the seed concentration, two types of nanoplanes oriented perpendicular to the polarization were

identified. If the nanospheres are widely separated, the low spatial frequency nanoplanes with the period of $> \lambda/n$ are formed, and attributed to the interference of the incident and the inhomogeneity scattered light waves. For high concentrations of nanospheres, the mechanism changes drastically as the mutual enhancement induced by the multiple scattering from nanoplasmas becomes dominant. Thus, the nanoplasmas develop from random inhomogeneities into the highly ordered high spatial frequency pattern, with the characteristic period of $\lambda/2n$. In fact, the periodicity may decrease drastically with the further increase of inhomogeneities, until the nanoplanes merge, i.e. generated plasma uniformly distributes over the irradiated region. Indeed this model could be adapted explaining not only volume nanogratings, but also surface ripples.

As an alternative, the model based on attractive interaction and self-trapping of exciton–polaritons, was suggested to explain the periodicity of nanogratings in the direction of light propagation [123]. The two dispersion branches of exciton–polaritons are excited simultaneously by multi-photon absorption. As a result, the interference of propagating exciton–polaritons produces the polarization grating. After the relaxation process ($<$ ps) to indirect states decoupled from light, the excitons can be trapped freezing the grating pattern formed by the exciton-polariton interaction with light [124]. The process is followed by the generation of molecular oxygen and nanoporous structure that originate the formation of nanogratings.

The ultrafast laser nanostructuring in silica is strongly dependent on the nonlinear processes, thus this makes the technique extremely flexible in terms of materials and ability to implement three-dimensional geometries with subwavelength precision. As a result, this turned it into an ideal low-cost platform for product engineering. The induced modifications served as a perfect candidate for designing numerous optical elements such as Fresnel zone plates [125], lens-based spin filters [72], polarization gratings [40], polarization, special beam and high-order laser mode converters [40,126–128], explored in the fields of beam shaping and manipulation (Figure 3-9). Also, multi-dimensional optical data storage has been demonstrated [42,123,129–131].

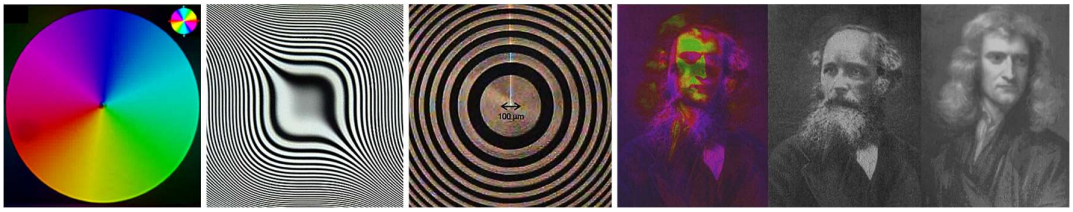

Figure 3-9. Practical implementations of ultrafast laser nanostructured silica glass: (left to right) radial polarization and Airy beam converters, Fresnel zone plate, multi-dimensional optical memory [40,123,125–129,132].

Another interesting property of the laser modified glass is highly selective wet etching [133,134]. The etchant such as hydrofluoric acid or potassium hydroxide efficiently tackles the stress affected and Si-rich porous structure, while the pristine SiO_2 matrix remains unetched. This was successfully implemented for fabrication of microfluidic channels (Figure 3-10), mechanical flexures, and preforms for molds [135–138]. Together with positive refractive index change, the technique can be used designing lab-on-a-chip platforms [139–141].

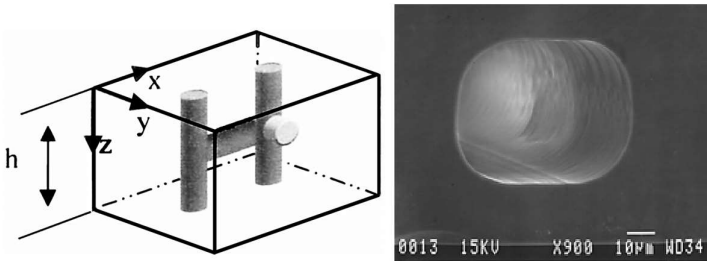

Figure 3-10. Direct-write three-dimensional microfabrication inside a volume of silica glass. The functional micro-fluidic channels and tunnels are realized by ultrafast laser nanostructuring and highly selective chemical wet etching [137,142].

Currently liquid crystals being versatile and flexible materials are the most popular choice for realization of optical devices operating on the geometrical phase [80–83]. However, liquid crystals have such limitations as low durability, with typical damage threshold of 0.2 J/cm^2, low thermal stability and high absorption in infrared, >1700 nm. As an alternative, various methods for passive spatial light modulation have been suggested utilising segmented linear polarizers, quartz based waveplates and photolithographically produced subwavelength gratings [73,143,144]. However, most of the fabrication techniques are lacking of spatial fabrication resolution, as well as are cost and time inefficient, leaving the room for ultrafast laser nanostructuring to be explored.

3.5 Photomodification of glass-metal nanocomposites

Ensembles of modified metal nanoparticles embedded in transparent media are of interest due to their intrinsic anisotropy [145] that results in linear and nonlinear dichroism and birefringence [146]. Conventionally, such anisotropic glass-metal nanocomposites (GMNs) are fabricated by stretching glass slabs containing spherical nanoparticles [147]. In particular, this technique is used in commercially available dichroic polarizers, which employ glasses containing elongated silver or copper nanoparticles [148]. However, modern functional devices require control of the birefringence and dichroism with sub-micron spatial resolution when the shape of the nanoparticles varies over the substrate in a prescribed fashion at distances comparable with

the wavelength. These devices could be of interest for optical encoding, multidimensional data storage and fabrication of complex, polarization-sensitive spectral masks. The required space-selective shaping of metal nanoparticles can be achieved via irradiating GMNs with intense laser [149,150] or ion beams [151,152], as shown in Figure 3-11.

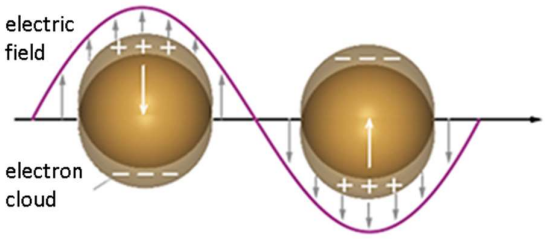

Figure 3-11. Electronic oscillations in metal nanoparticles affected by external electric field.

The first paper showing the ultrashort laser induced elongation of silver nanoparticles appeared in 1999, published by Kaempfe [5]. To explain the mechanism, the Coulomb model was used, which was suggested even earlier for the metal particles photo-fragmentation, by Kamat et al., in 1998 [153] and recently by others works [154–156]. Many studies have been done trying to clarify the mechanisms, optimize the conditions, and apply modifications in data storage or optical component fabrication [146,149,153,157–160], which is very well summarized for Ag-doped glasses in Podlipensky's thesis [161].

In very general terms, the modification of metal nanoparticles depends on the intensity of the ultrashort laser pulses, where surface plasmon resonance (SPR) is crucial because of the electric field enhancement around the particle. Excitation of metal clusters near the SPR frequency leads to the non-thermal distribution of conduction electrons in the metal (Figure 3-11). Using intense laser pulses, up to 0.5 TW/cm^2 for Ag NPs in glass [161], the SPR induces the electron emission from the metal surface into the glass. The dense electron plasma situated in the glass in the direction of the laser polarization is formed. While electrons are emitted, the metal becomes positive, i.e. ionized, inducing the electric field caused by charge separation. Metal ions (Me^+) are ejected around the particle forming an ionic shell. The temperature lower than the glass transition temperature must be ensured to maintain the limited mobility of metal ions in order to get the defined shape. Ions close to the plasma are reduced because of free electrons in the surrounding lattice. Such an effect causes the elongation of particles in the direction of polarization (Figure 3-12). If we have very strong pulse intensities ~2 TW/cm^2 for Ag NPs in glass [161], high density plasma is formed at the interface poles oriented parallel to the polarization. Here the ablation of particle and the shock stress induced due to the expansion of the host glass are induced. Thus, the particle is physically elongated in the direction perpendicular to the polarization (Figure 3-12). Both models described above can be valid only for particles doped in the homogeneous lattice

and pulses shorter than picoseconds, when the conventional thermal effects are neglected. For ultrafast laser induced metal shaping, within the first 100 fs the dominant is photon-electron interaction; 100 fs ÷ 10 ps – electron-lattice relaxation occurs; around 100 ps we have cooling to the surrounding medium [162]. The behaviour of the system might change because of the surface plasmon coupling effects, or non-symmetric contact with the lattice (surface structures), where the energy flow might be localized. Even with short pulses the thermal energy can be accumulated in the lattice and the viscosity of the metal can be changed altering the shape of the particles. In that case the doped particles are much more stable because of the uniform surrounding.

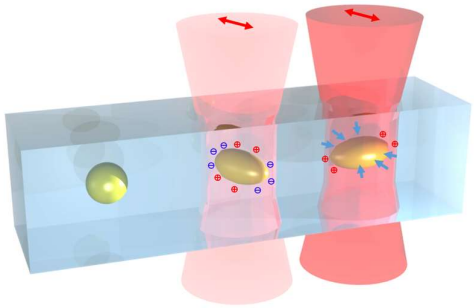

Figure 3-12. Laser assisted shape transformation of metal nanospheres embedded inside a slab of glass in the case of irradiation by linearly polarized ultrashort laser pulses at low and high intensities (left to right). Blue arrows indicate the expansion of host material; red arrows indicate the orientation of polarization of incident light. Blue and red circles represent the ejected electrons and metal ions, respectively. The simplified sketch was reproduced on the basis of ref. [163].

The laser modified metal nanoparticles can be directly studied by linear absorption as the non-propagating oscillations of conduction electrons coupled to the light evokes localized surface plasmons (LSP) (Figure 3-11). Such oscillations occur in the systems where surface carriers are trapped at least in two dimensions. The least complicated and most used system is spherical metallic nanoparticles surrounded by the insulating medium. If the particle diameter is much smaller than the wavelength of the electromagnetic field, a simple quasi-static approximation is applied (Rayleigh theory). It means that the electromagnetic field in the particle is constant and the system can be treated as electrostatic. It should be noted that the quasi-static approximation gives a solution only for one dipole, while the Mie solution to Maxwell's equations would consider a multipole extension.

In the electrostatic approximation, within the potential calculations [164], the particle dipole moment can be expressed as

$$p = \varepsilon_0 \varepsilon_m \alpha_p E_0 = 4\pi\varepsilon_0 \varepsilon_m r^3 \frac{\varepsilon-\varepsilon_m}{\varepsilon+2\varepsilon_m} E_0, \quad (3\text{-}19)$$

where ε_m is dielectric function of surrounding medium, $\varepsilon = \varepsilon' + i\varepsilon''$ is the dielectric function of metal particle, r is the radius of the particle and the polarizability is

$$\alpha_p = 4\pi r^3 \frac{\varepsilon-\varepsilon_m}{\varepsilon+2\varepsilon_m}, \quad (3\text{-}20)$$

which shows the ability of the metal particle to be polarized in the external field. If we have a metal particle in any insulator medium, the detection of an extinction of such a small particle is quite complicated because of the high scattering of the surrounding medium. However, it is shown that the extinction and scattering of the particles is enhanced at the dipole plasmon resonance condition [165,166], and the extinction cross section for V volume particle can be defined by

$$\sigma_{ext} = 9V \frac{\omega}{c} \varepsilon_m^{3/2} \frac{\varepsilon''}{[\varepsilon'+2\varepsilon_m]^2+\varepsilon''^2}, \quad (3\text{-}21)$$

and the Eq. (2-20) could be written as $I(x) = I_0 e^{-C\sigma x}$, where C is the concentration of particles. For most insulating mediums only the real part of dielectric constant ε_m is considered. Both metal and insulator dielectric constants are dependent on the incident light frequency.

For metals the dispersion is well defined by Drude equation (2-41) corrected by adding the permittivity $\varepsilon_{core} = \varepsilon_{core}' + \varepsilon_{core}''$ responsible for the interband transitions of the core electrons, and corresponds to the high frequency permittivity. Thus, we get Drude-Sommerfeld expression for the metal dispersion:

$$\varepsilon(\omega) = \varepsilon_{core} + 1 - \frac{\omega_p^2}{\omega^2+i\Gamma\omega}, \quad (3\text{-}22)$$

Looking at the Eq.(3-21), the resonance has to satisfy the condition of:

$$[\varepsilon' + 2\varepsilon_m]^2 + [\varepsilon'']^2 = \text{minimum}, \quad (3\text{-}23)$$

where we get the maximized extinction cross section, knowing that the surrounding medium has only the real part, and the real part of the metal dielectric function is negative:

$$\varepsilon' = -2\varepsilon_m. \quad (3\text{-}24)$$

Combining Drude-Sommerfeld and the resonance condition, we get the expression of the frequency of LSP for the metal sphere in the electrostatic field:

$$\omega_{LSP}^2 = \frac{\omega_p^2}{\varepsilon'_{core}+1+2\varepsilon_m} - \Gamma^2. \quad (3\text{-}25)$$

In real life, the symmetry of the nanoparticles is distorted, therefore, the factor of nonsphericity must be taken into account. Ellipsoidal clusters with different dimensions *r* for axes *xyz* have separated SPR conditions, with the polarizability:

$$\alpha_{x;y;z} = r_x r_y r_z \frac{4\pi}{3} \cdot \frac{\varepsilon-\varepsilon_m}{\varepsilon_m+[\varepsilon+\varepsilon_m]L_{x;y;z}}, \quad (3\text{-}26)$$

where *L* is a depolarization factor of the spheroid for each axis ($0 < L < 1$), and for spherical particle it is $L_x=L_y=L_z=1/3$. Another problem in the real system is the fill factor which creates the gradient metal cluster matrix. Although it is hard to correctly include the multipolar interactions, Maxwell-Garnett theory describes the position of localized plasmon resonance quite well, taking into account the filling factor of particles [167]. For such a system the main point is to evaluate the dielectric functions. In that case, the effective dielectric function must be introduced with the inclusion of the filling factor ς:

$$\varepsilon_{\text{eff}} = \varepsilon_m \frac{(\varepsilon+2\varepsilon_m)+2\varsigma(\varepsilon-\varepsilon_m)}{(\varepsilon+2\varepsilon_m)-\varsigma(\varepsilon-\varepsilon_m)}. \quad (3\text{-}27)$$

As already mentioned before, the theoretical description of the system meets some lack of factors which can be crucial for more realistic complex systems.

Chapter 4: Summary of Papers

Paper A: *Tailored surface birefringence by femtosecond laser assisted wet etching*

Fabrication of surface nanogratings by ultrafast laser nanostructuring, lapping/polishing, and wet etching of silica glass is demonstrated. Using potassium hydroxide at room temperature as a highly selective etchant of modified glass, the nanogratings with periodicity of ~300 nm and duty cycle of roughly 10% of the etched nano-planes are revealed. Such birefringent structures show the polarization dependent linear increase in retardance reaching threefold value within 25 hours. The dispersion control of birefringence by the etching procedure led to the fabrication of the chromatic to achromatic wave plate elements over the entire visible spectral range. By implementing the high-vacuum and variable pressure environmental scanning electron microscopy, and thermal annealing procedure, the mechanism of the enhanced etching selectivity based on the laser induced densification of silica structure and formation of ≡Si–Si≡ defects is complemented by a strong correlation with the laser induced $=Si^0$ (ODC (II)), $\equiv Si^{\bullet}$ (E′) defects.

Paper B: *Dichroic Surfaces Engineered by Ultrafast Laser Assisted Wet Etching*

The work presented in this paper is the continuation of the research done in Paper A. Highly selective wet etching of ultrafast laser nanostructured silica glass is used to fabricate surface nanogratings, that could be implemented as a host substrate for metal thin-film deposition and self-organization of metal nanostructures. The resulting linear dichroism defined by the orientation of the host nanogratings and tuned by the chemical etching time is shown.

Paper C: *Single beam optical vortex tweezers with tunable orbital angular momentum*

Within the work reported in this paper the pioneering steps towards a practical exploitation of femtosecond laser imprinted space-variant optical elements and development of a novel scheme for optical trapping were taken. The high precision torque control of trapped micron-size objects using single beam optical vortex tweezers with tunable orbital angular momentum was demonstrated. Specifically, the fabricated polarization converter, also referred to as S-waveplate, with the initial polarization state varying from linear to circular, was used to gradually control the torque transferred to the trapped silica beads without changing the trapping potential.

Paper D: *High-performance geometric phase elements in silica glass*

The main idea of the manuscript is to summarize the work done on printing and optimization of geometric phase elements in silica glass. In particular, within this work the phase profiles of various optical components including gratings, vortex retarders, computer generated holograms were achieved with low optical losses, high diffraction efficiency and high phase density. Thus, due to the high thermal and chemical stability of silica elements, the optical trapping with a total

average laser power of 5 W was demonstrated, which would be impossible with alternative beam shaping elements such as liquid crystals based devices.

Paper E: *Polarization sensitive anisotropic structuring of silicon by ultrashort light pulses*

In Paper E, the structuring of crystalline silicon surface by linearly polarized single and double pulse femtosecond laser irradiation was presented. After the first pulse the wavelength-size symmetric crater-shaped structure is generated, which was successfully implemented for designing wavefront sensors. However, the interaction of linearly polarized second pulse with the symmetric crater-shaped structure induces the anisotropy in the near-field pattern and causes the polarization sensitive deformation of structure. Thus, the work shown in this paper is a good indication that the multipulse regime or seeding are necessary for the polarization sensitive printing.

Paper F: *Giant birefringence and dichroism induced by ultrafast laser pulses in hydrogenated amorphous silicon*

In this paper, for the first time it was shown that the laser induced periodic thin-film structures exhibit giant birefringence and dichroism. Form birefringence of $\Delta n \approx -0.6$ induced in amorphous silicon was reported, which is two orders of magnitude higher than commonly observed in uniaxial crystals and ultrafast laser nanostructured silica glass. The studies identifying the optical and structural properties of irradiated amorphous silicon thin-films were performed.

Paper G: *Ultrafast laser-induced metasurfaces for geometric phase manipulation*

The work presented in Paper G is the continuation of the research done in Paper F. The giant birefringence observed in laser induces periodic thin-film structures was implemented in space-variant polarization manipulations. A number of geometrical phase optical elements such as polarization gratings, lenses, converters and/or Fourier holograms were realized in amorphous silicon thin-films.

Paper H: *Laser material processing with tightly focused cylindrical vector beams*

The main idea of this work is to prove experimentally that the longitudinal field associated with radial polarization is inefficient for the flat surface modification of high-index materials. Therefore, the comprehensive modification study of silica glass, crystalline silicon, and amorphous silicon thin-films, irradiated by tightly focused cylindrical vector beams with azimuthal and radial polarizations, were performed. Both simulations and experiments have shown that the longitudinal component is supressed at the interface of high-index contrast materials. In order to enhance such modification, roughness of the surface or number of laser pulses have to be increased.

Paper I: *Laser assisted modification of poled silver-doped nanocomposite soda-lime glass*

The homogenization of silver nanoparticles embedded in soda-lime glass by thermal poling is demonstrated. Thus, the narrowing of localized plasmon resonance band is observed and subsequently used to spectrally identify the photomodification of nanoparticles by linearly polarized ultrashort laser pulses. Dichroism four times larger than in non-poled sample was reported.

Paper J: *Revealing the nanoparticles aspect ratio in the glass-metal nanocomposites irradiated with femtosecond laser*

In this paper the controlled shaping of silver nanoparticles embedded in soda-lime glass was reported. Employing the experimental absorption spectra for *s*- and *p*-polarizations and comparing it with the modelling based on Maxwell Garnett approximation modified for spheroidal inclusions, the mean aspect ratio of the re-shaped silver nanoparticles as a function of the laser fluence was identified.

Chapter 5: Conclusions

Almost two decades ago, it was shown that using femtosecond laser pulses, nanostructures oriented perpendicular or parallel to the incident light polarization can be induced inside transparent materials. Such structures behave as an anisotropic material, where two components of the electric field have different propagation constants caused by the different effective medium. Such phenomenon originates the extraordinary optical and structural properties of engineered materials that can be applied in many fields including integrated optics, optoelectronics, telecommunications and healthcare. However, it is very important to achieve the high control over the processes of ultrafast laser nanostructuring in order to make the technique practical.

My PhD project was focused mainly on optimization and applications of femtosecond laser nanostructuring of transparent materials including dielectrics, semiconductors and glass-metal nanocomposites. The activities involved in my research were (1) understanding the fundamentals of light-mater interaction, (2) engineering and optimizing the optical properties (birefringence, dichroism, etc.) of materials by laser direct writing, (3) design and fabrication of polarization sensitive optical elements, and (4) implementation of fabricated optics into the multidisciplinary fields such as flat optics, material processing, optical trapping, etc. As a result, a set of high-performance optical components were successfully developed and demonstrated, including glass-metal dichroic elements, polarization gratings, arrays of polarization micro-lenses and micro-converters, computer generated Fourier holograms etc. I also designed and developed a novel type of optical tweezers with tunable orbital angular momentum reaching a record high topological charge, which has attracted attention from the beam-shaping and optical micro-manipulation communities, and has resulted in multiple conference and journal papers. Over the last three years this has become a new research direction for our group. Throughout this work, I was involved with and actively pursued collaborations with research groups from University of Eastern Finland, Eindhoven University of Technology, St. Petersburg Academic University, M.V.Lomonosov Moscow State University, and many others.

5.1 Challenges

The ultimate goal is to produce a printable anisotropic material, combining the benefits of durability and optical quality of inorganic crystals with the feasibility of liquid crystals, which would revolutionize the design and manufacturing of high-end optical components. The printing technology would then be used to fabricate beam shaping optics for telecommunications, laser

material processing, optical micro-manipulation, holography, stimulated emission depletion microscopy, optical components for polarization imaging, etc. Eventually we would be able to print high performance optics at a fraction of production time and cost of the conventional technologies.

Currently most of optical devices operating on the geometrical phase are fabricated from the anisotropic materials, e.g. liquid crystals or quartz, which show the optical transmission and conversion efficiency up to 99.9%. However, liquid crystals have such shortcomings as low durability, i.e. typical damage threshold is around 0.2 J/cm^2, low thermal stability, and high absorption in infrared (>1700 nm). As a result, liquid crystals cannot be used in the infrared for emerging telecom or silicon photonics applications. As an alternative, various methods for passive spatial light modulation have been suggested utilising segmented linear polarizers, polymer or quartz based waveplates and photo-lithographically produced subwavelength gratings. However, only basic configurations of segmented quartz waveplates can be implemented due to a limited number and relatively big size of segments, which results in diffraction losses and require additional spatial filtering. Furthermore, the manufacturing of the segmented elements requires costly high precision and time consuming assembly procedures.

Alternatively, ultrafast laser nanostructuring serves as a perfect candidate for manufacturing geometric phase optics. The technology allows fabricating any tailored phase optical element, e.g. Airy beam or polarization vortex converters, within <0.1-100 micron thickness of material. Smooth phase profiles can be produced, as no phase wrapping is required. The optical elements are printed in a single step procedure. No moulding or polishing, which is typically for the conventional optics fabrication, is required. The manufacturing does not need expensive clean rooms in contrast to the diffractive optics fabrication. The same technology can be exploited for waveguide optics and free space optics fabrication.

Thus, it is technologically attractive to use the ultrafast laser direct writing, which offers feasibility and rapid prototyping of optical elements at reduced costs. However, the mechanisms, which lead to the induced modification in the bulk material, are still not well understood. It is known that the process is strongly compromised by plasma scattering and self-focusing, which clamps laser intensity. The lack of control over these processes leads to slow writing speed and uneven nanostructures resulting in excessive scattering in the fabricated optical elements. Here we can identify the key challenges towards the practical use of the technology:

1. ***Materials.*** The technology has to be applicable to various types of materials from solids to thin-films, and from transparent dielectrics to semiconductors and metals. So far only a few demonstrations including bulk high-silica and thin-film silicon materials have been

realized. The flexibility is necessary in order to integrate the printed optics into complex photonic platforms. For example, the nanostructures are directly written in silica glass, which is key optical material due to its wide transparency range from the UV to the near IR, high strength and outstanding thermal and chemical stability. The laser induced damage threshold is around *26 J/cm^2* (*1-on-1, 1064 nm, 3.5 ns, 10 Hz*), which corresponds to the intensity of ~*7 GW/cm^2* (peak power ~2 GW and average power ~100 W). It is also the material of choice in optical communication meaning that the same technology can be used for functionalizing optical fibres.

2. ***Losses.*** Optical scattering is one of the key factors limiting the technology to be implemented in high power applications. Because of imperfections of induced nanostructures, typically as much as 10-50% of the incident light is scattered in visible spectral range.
3. ***Broadband performance.*** Another challenge for the geometrical phase based optical technology is to achieve achromatic behaviour for the spectral range over 400 nm. This would allow implementing optics for visible spectrum without introducing chromatic aberration, which is one of the main optical flaws.
4. ***Phase density.*** The sophisticated phase elements require manufacturing of complex high phase density patterns. However, when the azimuth density of imprinted nanogratings is below π/10 (rad/μm), the beam is perturbed during the material modification process causing the subsequent anisotropic polarization effects. As a result, the laser induced birefringence is not spatially homogeneous. This effect causes the decrease of the conversion efficiency of imprinted optics, as well as originates the mode impurity in the generated beams.
5. ***Time/cost efficiency.*** Currently up to thousands of pulses are required to induce stable self-organized nanostructure, i.e. to record the single dot of information, what significantly slows down the fabrication process. From several to tens of hours are required to fabricate a single optical element by the technique. The ability to control self-assembly process by seeding and efficient energy deposition would allow to induce nanostructures with several pulses (burst of pulses) increasing data writing speed by one to three orders of magnitude.

As a result, the new scientific and technological solutions are essential to make femtosecond laser printing of optics available to the market.

5.2 Future work

In addition to the first demonstrations of ultrafast laser printed flat optics for controlled beam-shaping and optical micro-manipulations [168,169], recently our research group has demonstrated the optical data storage technique which could potentially preserve huge amounts of digital data for billions of years [42]. Due to the high interest shown by public and scientific communities, most of my future work will be related to the geometric-phase optics and optical data storage imprinted in transparent materials.

In the next several years an extensive research program is planned on the fundamental physics of ultrashort laser pulse excitation of bulk transparent materials aiming to reveal new mechanisms and exotic states in material transformation. Although our previous research developments logically bring us to the necessity of using sub-100 fs pulses, we enter unexplored land where some of our predictions may fail while obtained fundamental facts may occur beyond our expectations. Hence, the future work is of high risk and, at the same time, promises considerable advances in the fundamental knowledge and technological applications.

The primary tasks will be developing and characterizing materials with on-demand properties exploiting ultrashort laser pulse induced self-assembled nanostructures and exotic phases. For such experiments, ultrashort laser pulse irradiation regimes are predicted to be most favourable as they suppress restoration of laser disintegrated matter toward its initial structure due to low-enthalpy bond scissoring. This will push matter to reconstruct its structure in a divergent chemical path and one may expect emerging new nano-sized material properties.

The near future will be devoted for the elaboration of a three-dimensional point spread function engineering (3D PSFE) technique, which involves polarization and intensity control in the focus of the laser beam. The main purpose of PSFE is to control spatial distribution of intensity and polarization for localization of material modification.

The most important part of the future work will be demonstrating the capabilities of ultrashort laser pulses combined with 3D PSFE for advancing the quality of induced nanostructures.

Currently hundreds of pulses are required to induce self-organized nanostructure i.e. to record the information. We will analyse the influence of the glass physical properties (melting temperature, thermal diffusivity, absorption) on the nanogratings formation process. This analysis will enable the tailoring of the chemical composition and structure of glasses including nanoporous silica to reduce the required number of pulses. As part of the task, different dopants of silica glass will be analysed in the context of nanograting formation. We also expect to enhance nanograting formation by inducing oxygen deficiency centers in the glass matrix, which according

to our recent study could act as a precursor for the nanostructure formation. Transparent glass-ceramics with a composition close to one of the fresnoite crystalline phase will be investigated. This glass-ceramic shows improved brittleness damage resistance several times and a great potential for improvement of imprinted elements durability.

We also plan on establishing pump-probe experiments. The ultrashort pump pulses will be used to seed electrons and defects to facilitate nanogratings formation. The ability to control self-assembly processes by ultrashort laser pulses (seeding and efficient energy deposition) will allow to induce nanostructures with several pulses (burst of pulses) increasing writing speed by multiple orders of magnitude.

Recent experiments suggest that micro-explosions could happen before the NGs formation, and the subsequent seeding of structure formation could be triggered. We anticipate the control of micro-explosions could help to increase the speed of nanogratings formation. Additional spatio-temporal tailoring of laser pulses will allow to localize excitation of plasma and increase production of densified material. Such modifications can be also used for three-dimensional optical data storage in highly durable materials such as sapphire.

A series of experiments is planned on shaping nanogratings on surfaces by the means of the 3D PSFE technique. For this aim, we will use amorphous silicon thin-films. By creating different polarization patterns in the beam, we intend to obtain nanostructures in complex patterns.

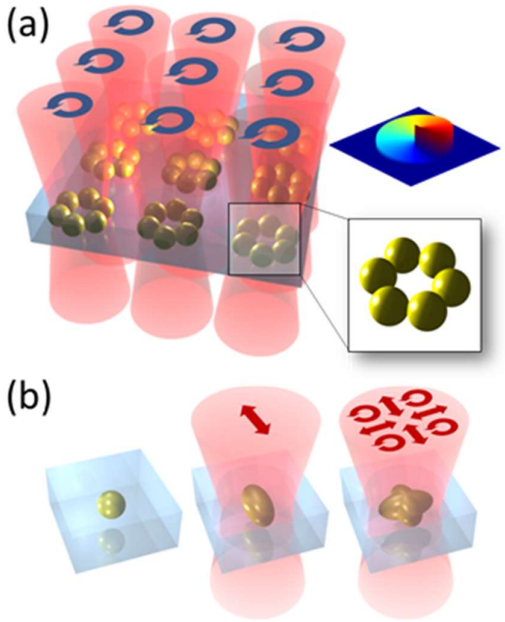

Figure 5-1. Schematics of potential tailoring of nanoparticles in metal-doped glasses. (a) NPs rings array fabrication by irradiating with parallel optical vortex beams. (b) Nanoparticle sculpting: from linear to spatially variant polarization.

Using both ultrashort laser pulses and longer pulses, it is expected to achieve unprecedented control over the spatial distribution of the precipitated metal NPs inside metal-doped glasses (Au, Ag, Cu), and the control over the plasmonic properties of obtained NPs and NP arrays. Two examples of planned experiments are shown in Figure 5-1. First, with vortex laser beams, we intend to generate NP ring arrays. Second with a spatially variant polarization, initially spherical particles will be formed into a desired shape, and implemented for multiplexed high-density optical data storage.

The system for massive parallel data recording will be developed (Figure 5-2). To increase the number of dots per laser exposure, hundreds of beam spots will be used for modifying a spinning fused silica disc. Instead of placing in a square matrix as in previous setups, the spots will be positioned along a straight line in order to fit the rotation disc. Within the future projects it is expected to achieve writing speed of tens to hundreds MB/s.

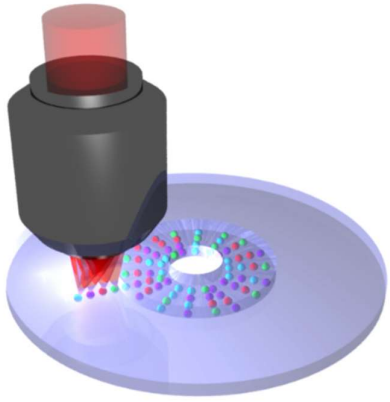

Figure 5-2. Single shot parallel data writing realized in rotation geometry.

Plenty of work will be done to explore new recording dimensions for a rewritable highly-stable optical storage media inside transparent solids beyond five dimensions whose achieving is a typical problem of conventional phase transition based memories. The optimization of parameters (spatial and temporal) of ultrashort pulses will be used to maximize the transmission and repeatability of induced nanogratings. This will achieve >1 TB/cm^3 density of optical recording.

We will collaborate with the consortium Part-Time Scientists (Robert Bohme, CEO Founder) and AUDI (Berlin, Germany) in the Google Lunar XPRIZE project to record an eternal time capsule with our technology and deliver it to the Moon in 2018. Many other collaborations are in progress.

The advantages of the ultrafast laser printing technique will be exploited to demonstrate novel photonic devices for high resolution optical microscopy and high power laser material processing. Spatial control of the nanograting period achieved by spatial chirp of ultrashort laser pulses will be explored for implementation of dielectric metasurfaces with space-variant anisotropy. The

parameters including pulse energy, writing speed, beam profile, etc. will be controlled by re-configuring the already developed setup in order to optimize the fabrication process. Additionally, we will be able to generate 2nd, 3rd and 4th harmonics or tune the laser wavelength with a non-collinear optical parametric amplifier. Spatial light modulator, polarization converters and conventional optics might be adapted to the system to manipulate the laser beam profile. The flexibility and high precision of translation stages with a resolution of < 100 nm will permit exploitation of various complex phase designs and integration in three-dimensional (multi-layered) optical elements. Laser assisted wet etching will be used in order to fabricate the micro-fluidic systems. The optimization process of nanostructuring will be performed by monitoring the laser induced structures with a scanning electron microscope and optical transmission microscope. The imprinted elements will be optically characterized and/or visualized with the VIS/NIR micro-spectrometer and the quantitative birefringence measurement system. The final goal is to achieve >99% transmittance, >99% diffraction efficiency, >3rad/um phase density and increase writing speed by 100 times (beyond 10 cm/s). As a result, light manipulation will be obtained by an engineered three-dimensional transparent slab materials with multi-layered graded refractive index profiles, where refractive index will be controlled by the period and orientation of subwavelength structures (Figure 5-3).

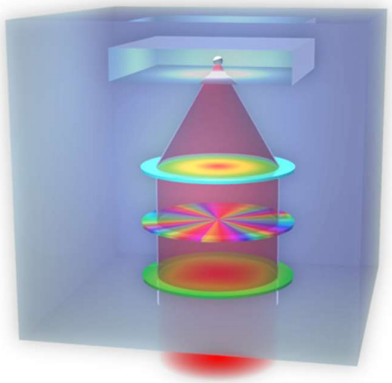

Figure 5-3. Multi-layered flat optics imprinted inside a single slab of glass.

Using this technology I will be able to reduce the bandwidth of birefringent elements to 25 nm and demonstrate a wavelength selective multi-layered mode converter integrated into complex optoelectronic systems, e.g. STED (stimulated emission depletion) microscopy, simultaneous spatial and temporal focusing (SSTF), OAM (orbital angular momentum) based telecommunication and micro-manipulation devices, holography. This will allow a significant simplification for popular microscopy techniques leading to a low cost nano-photolithography and high resolution imaging. An all-fiber polarization sensitive imaging system will be demonstrated based on laser nanostructured multi-core fibers or fiber bundles. Such a system could be exploited in endoscopy for in-situ optical detection of cancerous tissues, which are known to exhibit distinctive features

in polarized light. The spatio-temporally shaped light pulses will be used to produce the precipitation of nano-crystalline silicon in amorphous thin films for printing flexible printed optics, which can be exploited for consumer electronics.

Honors & Awards

2016 **Leader of Tomorrow** (handpicked top 100 under 30)

46th St Gallen Symposium, St. Gallen, Switzerland

2015 **Incubic/Milton Chang Student Travel Grant**

CLEO 2015, San Jose, US

2014 **Joint first prize winner of Brilliance in Research competition**

Optoelectronics Research Centre, University of Southampton, UK

List of Publications

14+ JOURNAL PAPERS (9 CORRESPONDING AUTHOR)

22+ CONFERENCE PAPERS (9 GIVEN TALKS)

JOURNAL PAPERS:

[1] **R.Drevinskas**, P.G.Kazansky

Dichroic Surfaces Engineered by Ultrafast Laser Assisted Wet Etching

Manuscript in preparation

[2] **R.Drevinskas**, P.G.Kazansky

High-performance geometric phase elements in silica glass

Manuscript in preparation

[3] **R.Drevinskas**, M.Beresna, J.Zhang, A.G.Kazanskii, P.G.Kazansky

Ultrafast laser-induced metasurfaces for geometric phase manipulation

***Advanced Optical Materials,* Vol.5, 1600575 (2017)**

[4] **R.Drevinska**s, J.Zhang, M.Beresna, M.Gecevicius, A.G.Kazanskii, Y.P.Svirko, P.G.Kazansky

Laser material processing with tightly focused cylindrical vector beams

***Applied Physics Letters* Vol.108, 221107 (2016)**

[5] J. Zhang, A. Čerkauskaitė, **R. Drevinskas**, A. Patel, M. Beresna, P. G. Kazansky

Eternal 5D data storage by ultrafast laser writing in glass

***Proc. of SPIE* (invited) Vol. 9736, 97360U (2016)**

[6] S.S.Fedotov, **R.Drevinskas**, S.V.Lotarev, A.S.Lipatiev, M.Beresna, A.Čerkauskaitė, V.N.Sigaev, P.G.Kazansky

Direct writing of birefringent elements by ultrafast laser nanostructuring in multicomponent glass

***Applied Physics Letters* Vol.108, 071905 (2016)**

[7] S.Chervinskii, **R.Drevinskas**, D.V.Karpov, M.Beresna, A.A.Lipovskii, Y.P.Svirko, P.G.Kazansky

Revealing the nanoparticles aspect ratio in the glass-metal nanocomposites irradiated with femtosecond laser

***Scientific Reports* Vol.5, 1-10 (2015)**

[8] **R.Drevinskas**, M.Beresna, M.Gecevičius, M.Khenkin, A.G.Kazanskii, I.Matulaitienė, G.Niaura, O.I.Konkov, E.I.Terukov, Y.P.Svirko, P.G.Kazansky

Giant birefringence and dichroism induced by ultrafast laser pulses in hydrogenated amorphous silicon

***Applied Physics Letters* Vol. 106(17), 171106 (2015)**

[9] **R.Drevinskas**, M.Gecevičius, M.Beresna, Y.Bellouard, P.G.Kazansky
Tailored surface birefringence by femtosecond laser assisted wet etching
***Optics Express* Vol. 3(2), 1428-1437 (2015)**

[10] J.Zhang, **R.Drevinskas**, M.Beresna, P.Kazansky
Polarization sensitive anisotropic structuring of silicon by ultrashort light pulses
***Applied Physics Letters* Vol.107, 041114 (2015)**

[11] M.V.Khenkin, D.V.Amasev, A.O.Dudnik, A.V.Emelyanov, P.A.Forsh, A.G.Kazanskii, **R.Drevinskas**, M.Beresna, P.G.Kazansky
Effect of Laser Wavelength on Structure and Photoelectric Properties of a-Si: H Films Crystallized by Femtosecond Laser Pulses
***Journal of Nanoelectronics and Optoelectronics* Vol. 9(6), 728-733 (2015)**

[12] M.Gecevičius, **R.Drevinskas**, M.Beresna, P.G.Kazansky
Single beam optical vortex tweezers with tunable orbital angular momentum
***Applied Physics Letters* Vol. 104(23), 231110 (2014)**

[13] M.Gecevičius, M.Beresna, **R.Drevinskas**, P.G.Kazansky
Airy beams generated by ultrafast laser-imprinted space-variant nanostructures in glass
***Optics Letters* Vol. 39(24), 6791-6794 (2014)**

[14] **R.Drevinskas**, M.Beresna, O.Deparis, P.G.Kazansky
Laser assisted modification of poled silver-doped nanocomposite soda-lime glass
***MATEC Web of Conferences* Vol.8, 02008 (2013)**

CONFERENCE PAPERS:

[1] R.Drevinskas, M.Beresna, J.Zhang, A.Patel, A.Cerkauskaite, A.G.Kazanskii, P.G.Kazansky
Geometric Phase Holograms Imprinted by Femtosecond Laser Nanostructuring
***CLEO* San Jose, CA 5-10 June 2016 SW4L.2**

[2] P. G. Kazansky, A. Čerkauskaitė, R. Drevinskas, J. Zhang
Eternal 5D optical data storage in glass (invited)
***SPIE Optics and Photonics* San Diego, CA 28 Aug 2016**

[3] J. Zhang, A. Čerkauskaitė, **R. Drevinskas**, A. Patel, M. Beresna, P. G. Kazansky
Eternal 5D data storage by ultrafast laser writing in glass (invited)
***SPIE LASE* San Francisco, CA 16-18 Feb 2016 9736-29**

[4] P.G.Kazansky, M.Beresna, M.Gecevičius, J.Zhang, **R.Drevinskas**, A.Patel, A.Čerkauskaitė, A.S.Lipatiev, A.G.Okhrimchuk, V.N.Sigaev
Advances in Femtosecond Laser Nanostructuring in Glass: From Printed Geometrical Phase Optics to Eternal Data Storage
***Advanced Solid State Lasers Conference* Berlin 4-9 Oct 2015 AW1A.4**

[5] M.Beresna, **R.Drevinskas**, Zhang J., M.Gecevičius, P.G.Kazansky
Engineering anisotropy in glass with ultrafast laser assisted nanostructuring
Frontiers in Optics **San Jose, CA 18-22 Oct 2015 FTu5E.2**

[6] **R.Drevinskas**, M.Beresna, M.Gecevičius, M.Khenkin, A.G.Kazanskii, O.I.Konkov, Y.P.Svirko, P.G.Kazansky
Femtosecond Laser Printed Microoptics in Hydrogenated Amorphous Silicon
European Conference on Lasers and Electro-Optics **Munich 21-25 Jun 2015 CK_14_4**

[7] **R.Drevinskas**, M.Gecevičius, M.Beresna, P.G.Kazansky
Femtosecond Laser Nanostructuring for High-Topological Charge Vortex Tweezers with Continuously Tunable Orbital Angular Momentum
European Conference on Lasers and Electro-Optics **Munich 21-25 Jun 2015 ECBO_2_3**

[8] M.Beresna, **R.Drevinskas**, A.S.Lipatiev, S.S.Fedotov, S.V.Lotarev, V.N.Sigaev, P.G.Kazansky
Functional Birefringent Elements Imprinted by Femtosecond Laser Nanostructuring of Multi-Component Glass
European Conference on Lasers and Electro-Optics **Munich 21-25 Jun 2015 CM_6_3**

[9] **R.Drevinskas**, M.Beresna, M.Gecevičius, A.G.Kazanskii, O.I.Konkov, Y.P.Svirko, P.G.Kazansky
Radially polarized optical vortex micro-converters imprinted by femtosecond laser nanostructuring in amorphous silicon
CLEO **San Jose, CA 10-15 May 2015 AM2K.3**

[10] **R.Drevinskas**, M.Gecevičius, M.Beresna, P.G.Kazansky
High-topological charge vortex tweezers with continuous control of orbital angular momentum by ultrafast laser machining
CLEO **San Jose, CA 10-15 May 2015 STu1L.2**

[11] **R.Drevinskas**, M.Beresna, M.Gecevičius, M.Khenkin, A.G.Kazanskii, O.I.Konkov, P.G.Kazansky
Polarization sensitive printing by ultrafast laser nanostructuring in amorphous silicon
CLEO **San Jose, CA 10-15 May 2015 SF2I.4**

[12] S.Chervinskii, **R.Drevinskas**, M.Beresna, A.A.Lipovskii, P.G.Kazansky
Glass-metal nanocomposite modification by femtosecond laser irradiation
Northern Optics & Photonics 2015 (NOP '15) **Lappeenranta, Finland 2-4 Jun 2015 Poster**

[13] S.Chervinskii, **R.Drevinskas**, M.Beresna, A.A.Lipovskii, P.G.Kazansky
Dichroic Reflectance and Transmittance of Glass-Metal Nanocomposite Modified by Femtosecond Laser Irradiation
XII International Conference on Nanostructured Materials (NANO '14) **Moscow, Russia 13-18 Jul 2014 Poster**

[14] M.Beresna, A.G.Kazanskii, A.V.Emelyanov, P.A.Forsh, M.V.Khenkin, E.I.Terukov, M.Gecevičius, **R.Drevinskas**, P.G.Kazansky
Amorphous hydrogenated silicon modified by femtosecond laser radiation for photovoltaics
Sixth International Conference on Optical, Optoelectronic and Photonic Materials and Applications (ICOOPMA '14) **Leeds, UK 27 Jul - 1 Aug 2014**

[15] J.Zhang, **R.Drevinskas**, M.Beresna, M.Gecevičius, P.G.Kazansky
Silicon microreflector created by single ultrafast laser pulse
CLEO **San Jose 8-13 Jun 2014 JTh2A.138**

[16] J.Zhang, **R.Drevinskas**, M.Beresna, M.Gecevičius, P.G.Kazansky
Polarization-sensitive cat's eye structuring of silicon by ultrashort light pulses
CLEO **San Jose 8-13 Jun 2014 STh1J.3**

[17] M.Gecevičius, **R.Drevinskas**, M.Beresna, P.G.Kazansky
Optical tweezers with tunable orbital angular momentum
CLEO **San Jose 8-13 Jun 2014 JTh2A.32**

[18] **R.Drevinskas**, M.Gecevičius, M.Beresna, Y.Bellouard, P.G.Kazansky
Nanotexturing of glass surface by ultrafast laser assisted wet etching
CLEO **San Jose 8-13 Jun 2014 AM1L.2 (Invited)**

[19] **R.Drevinskas**, M.Beresna, O.Deparis, P.G.Kazansky
Laser assisted modification of poled silver-doped nanocomposite soda-lime glass
Progress in ultrafast laser modifications of materials (PULMM) **Corsica 15-20 Apr 2013**

[20] A.Patel, M.Gecevičius, **R.Drevinskas**, M.Beresna, P.G.Kazansky
Unambiguous evidence of two plasmon decay during ultrafast laser writing in glass
European Conference on Lasers and Electro-Optics **Munich 12-16 May 2013 CM_4_3**

[21] A.Patel, M.Gecevičius, **R.Drevinskas**, M.Beresna, P.G.Kazansky
3/2 harmonic generation - the clue to the mechanism of ultrafast laser nanostructuring
CLEO **San Jose, CA Jun 9-14 2013 CM2M.2**

[22] P.G.Kazansky, M.Beresna, M.Gecevičius, J.Zhang, A.Patel, **R.Drevinskas**, A.Kazanskii
Recent progress in ultrafast laser nanostructuring: from two-plasmon decay to longitudinal field puzzle
Nonlinear Optics **Kohala Coast, Hawaii, USA Jul 21-26 2013 NF2A.4**

Bibliography

1. D. E. Spence, P. N. Kean, and W. Sibbett, "60-fsec pulse generation from a self-mode-locked Ti:sapphire laser," Opt. Lett. **16**, 42–44 (1991).

2. U. Keller, D. a Miller, G. D. Boyd, T. H. Chiu, J. F. Ferguson, and M. T. Asom, "Solid-state low-loss intracavity saturable absorber for Nd:YLF lasers: an antiresonant semiconductor Fabry-Perot saturable absorber," Opt. Lett. **17**, 505–507 (1992).

3. K. M. Davis, K. Miura, N. Sugimoto, and K. Hirao, "Writing waveguides in glass with a femtosecond laser," Opt. Lett. **21**, 1729–1731 (1996).

4. J. Bonse, J. Krüger, S. Höhm, and A. Rosenfeld, "Femtosecond laser-induced periodic surface structures," J. Laser Appl. **24**, 042006 (2012).

5. M. Kaempfe, T. Rainer, K. J. Berg, G. Seifert, and H. Graener, "Ultrashort laser pulse induced deformation of silver nanoparticles in glass," Appl. Phys. Lett. **74**, 1200 (1999).

6. J. Bonse, H. Sturm, D. Schmidt, and W. Kautek, "Chemical, morphological and accumulation phenomena in ultrashort-pulse laser ablation of TiN in air," Appl Phys A-Mater **71**, 657–665 (2000).

7. Y. Shimotsuma, P. Kazansky, J. Qiu, and K. Hirao, "Self-Organized Nanogratings in Glass Irradiated by Ultrashort Light Pulses," Phys. Rev. Lett. **91**, 247405 (2003).

8. P. Kazansky, H. Inouye, T. Mitsuyu, K. Miura, J. Qiu, K. Hirao, and F. Starrost, "Anomalous Anisotropic Light Scattering in Ge-Doped Silica Glass," Phys. Rev. Lett. **82**, 2199–2202 (1999).

9. E. Bricchi, B. G. Klappauf, and P. G. Kazansky, "Form birefringence and negative index change created by femtosecond direct writing in transparent materials," Opt. Lett. **29**, 119–121 (2004).

10. R. R. Gattass and E. Mazur, "Femtosecond laser micromachining in transparent materials," Nat. Photonics **2**, 219–225 (2008).

11. S. K. Sundaram and E. Mazur, "Inducing and probing non-thermal transitions in semiconductors using femtosecond laser pulses," Nat. Mater. **1**, 217–224 (2002).

12. Z. Wu, H. Jiang, L. Luo, H. Guo, H. Yang, and Q. Gong, "Multiple foci and a long filament observed with focused femtosecond pulse propagation in fused silica," Opt. Lett. **27**, 448–450 (2002).

13. COMSOL, "Self-Focusing," https://www.comsol.com/model/download/198897/models.woptics.self_focusing.pdf.

14. C. Corbari, A. Champion, M. Gecevičius, M. Beresna, Y. Bellouard, and P. G. Kazansky, "Femtosecond versus picosecond laser machining of nano-gratings and micro-channels in silica glass," Opt. Express **21**, 3946–3958 (2013).

15. A. Couairon and A. Mysyrowicz, "Femtosecond filamentation in transparent media," Phys. Rep. **441**, 47–189 (2007).

16. Y. R. Shen, *The Principles of Nonlinear Optics* (Wiley, 1984).

17. Keldysh L. V., "Ionization in the field of a strong electromagnetic wave," Sov. Phys. JETP **20**, 1307–1314 (1965).

18. S. Leyder, D. Grojo, P. Delaporte, M. Lebugle, W. Marine, N. Sanner, M. Sentis, and O. Utéza, "On the wavelength dependence of femtosecond laser interactions inside band gap solids," in A. Heisterkamp, P. R. Herman, M. Meunier, and S. Nolte, eds. (2013), p. 861113.

19. S. S. Mao, F. Quéré, S. Guizard, X. Mao, R. E. Russo, G. Petite, and P. Martin, "Dynamics of femtosecond laser interactions with dielectrics," Appl. Phys. A Mater. Sci. Process. **79**, 1695–1709 (2004).

20. L. Sudrie, A. Couairon, M. Franco, B. Lamouroux, B. Prade, S. Tzortzakis, and A. Mysyrowicz, "Femtosecond Laser-Induced Damage and Filamentary Propagation in Fused Silica," Phys. Rev. Lett. **89**, 186601 (2002).

21. B. C. Stuart, M. D. Feit, S. Herman, A. M. Rubenchik, B. W. Shore, and M. D. Perry, "Optical ablation by high-power short-pulse lasers," J. Opt. Soc. Am. B **13**, 459 (1996).

22. B. C. Stuart, M. D. Feit, A. M. Rubenchik, B. W. Shore, and M. D. Perry, "Laser-Induced Damage in Dielectrics with Nanosecond to Subpicosecond Pulses," Phys. Rev. Lett. **74**, 2248–2251 (1995).

23. M. Ueta, H. Kanzaki, K. Kobayashi, Y. Toyozawa, and E. Hanamura, *Excitonic Processes in Solids* (Springer Berlin Heidelberg, 1986).

24. Y. Toyozawa, *Relaxation of Elementary Excitations* (Springer Berlin Heidelberg, 1980).

25. M. Beresna, M. Gecevičius, M. Lancry, B. Poumellec, and P. G. Kazansky, "Broadband anisotropy of femtosecond laser induced nanogratings in fused silica," Appl. Phys. Lett. **103**, 131903 (2013).

26. L. Skuja, "Optically active oxygen-deficiency-related centers in amorphous silicon dioxide," J. Non. Cryst. Solids **239**, 16–48 (1998).

27. A. Zoubir, C. Rivero, R. Grodsky, K. Richardson, M. Richardson, T. Cardinal, and M. Couzi, "Laser-induced defects in fused silica by femtosecond IR irradiation," Phys. Rev. B - Condens. Matter Mater. Phys. **73**, 1–5 (2006).

28. L. Skuja, K. Kajihara, M. Hirano, and H. Hosono, "Oxygen-excess-related point defects in glassy/amorphous SiO2 and related materials," Nucl. Instruments Methods Phys. Res. Sect. B Beam Interact. with Mater. Atoms **286**, 159–168 (2012).

29. H.-B. Sun, S. Juodkazis, M. Watanabe, S. Matsuo, H. Misawa, and J. Nishii, "Generation and Recombination of Defects in Vitreous Silica Induced by Irradiation with a Near-Infrared Femtosecond Laser," J. Phys. Chem. B **104**, 3450–3455 (2000).

30. C. Schaffer, A. Brodeur, and E. Mazur, "Laser-induced breakdown and damage in bulk transparent materials induced by tightly focused femtosecond laser pulses," Meas. Sci. Technol. **12**, 1784–1794 (2001).

31. J. P. Callan, "Ultrafast Dynamics and Phase Changes in Solids Excited by Femtosecond Laser Pulses," (2000).

32. E. G. Gamaly, A. V Rode, V. T. Tikhonchuk, and B. Luther-Davies, "Ablation of solids by femtosecond lasers : ablation mechanism and ablation thresholds for metals and dielectrics," Phys. Rev. A (2001).

33. C. B. Schaffer, A. Brodeur, and E. Mazur, "Laser-induced breakdown and damage in bulk transparent materials induced by tightly focused femtosecond laser pulses," Meas. Sci. Technol. **12**, 1784–1794 (2001).

34. K. Miura, J. Qiu, H. Inouye, T. Mitsuyu, and K. Hirao, "Photowritten optical waveguides in various glasses with ultrashort pulse laser," Appl. Phys. Lett. **71**, 3329 (1997).

35. E. N. Glezer, M. Milosavljevic, L. Huang, R. J. Finlay, T. H. Her, J. P. Callan, and E. Mazur, "Three-dimensional optical storage inside transparent materials," Opt. Lett. **22**, 422 (1997).

36. C. Hnatovsky, R. S. Taylor, P. P. Rajeev, E. Simova, V. R. Bhardwaj, D. M. Rayner, and P. B. Corkum, "Pulse duration dependence of femtosecond-laser-fabricated nanogratings in fused silica," Appl. Phys. Lett. **87**, 014104 (2005).

37. S. Onda, W. Watanabe, K. Yamada, K. Itoh, and J. Nishii, "Study of filamentary damage in synthesized silica induced by chirped femtosecond laser pulses," J. Opt. Soc. Am. B **22**, 2437 (2005).

38. R. Osellame, S. Taccheo, G. Cerullo, M. Marangoni, D. Polli, R. Ramponi, P. Laporta, and S. De Silvestri, "Optical gain in Er-Yb doped waveguides fabricated by femtosecond laser pulses," Electron. Lett. **38**, 964–965 (2002).

39. A. G. Okhrimchuk, A. V Shestakov, I. Khrushchev, and J. Mitchell, "Depressed cladding, buried waveguide laser formed in a YAG:Nd3+ crystal by femtosecond laser writing," Opt. Lett. **30**, 2248–2250 (2005).

40. M. Beresna, M. Gecevičius, and P. G. Kazansky, "Polarization sensitive elements fabricated by femtosecond laser nanostructuring of glass," Opt. Mater. Express **1**, 783–795 (2011).

41. M. Gecevičius, M. Beresna, R. Drevinskas, and P. G. Kazansky, "Airy beams generated by ultrafast laser-imprinted space-variant nanostructures in glass," Opt. Lett. **39**, 6791–6794 (2014).

42. J. Zhang, M. Gecevičius, M. Beresna, and P. G. Kazansky, "Seemingly unlimited lifetime data storage in nanostructured glass," Phys. Rev. Lett. **112**, 033901 (2014).

43. E. N. Glezer, M. Milosavljevic, L. Huang, R. J. Finlay, T.-H. Her, J. P. Callan, and E. Mazur, "Three-dimensional optical storage inside transparent materials," Opt. Lett. **21**, 2023–2025 (1996).

44. D. C. Emmony, R. P. Howson, and L. J. Willis, "Laser mirror damage in germanium at 10.6 um," Appl. Phys. Lett. **23**, 598–600 (1973).

45. Z. Guosheng, P. M. Fauchet, and A. E. Siegman, "Growth of spontaneous periodic surface structures on solids during laser illumination," Phys. Rev. B **26**, 5366–5381 (1982).

46. H. M. Van Driel, J. E. Sipe, and J. F. Young, "Laser-induced periodic surface structure on solids: A universal phenomenon," Phys. Rev. Lett. **49**, 1955–1958 (1982).

47. R. J. Nemanich, D. K. Biegelsen, and W. G. Hawkins, "Aligned, coexisting, liquid and solid regions in laser-annealed Si," Phys. Rev. B **27**, 7817–7820 (1983).

48. B. Gaković, M. Trtica, D. Batani, T. Desai, P. Panjan, and D. Vasiljević-Radović, "Surface modification of titanium nitride film by a picosecond Nd:YAG laser," J. Opt. A Pure Appl. Opt. **9**, S76–S80 (2007).

49. G. Miyaji and K. Miyazaki, "Origin of periodicity in nanostructuring on thin film surfaces ablated with femtosecond laser pulses," **16**, 16265–16271 (2008).

50. M. Hashida, Y. Miyasaka, Y. Ikuta, S. Tokita, and S. Sakabe, "Crystal structures on a copper thin film with a surface of periodic self-organized nanostructures induced by femtosecond laser pulses," Phys. Rev. B - Condens. Matter Mater. Phys. **83**, 2–6 (2011).

51. M. V. Khenkin, D. V. Amasev, A. O. Dudnik, A. V. Emelyanov, P. A. Forsh, A. G. Kazanskii, R. Drevinskas, M. Beresna, and P. Kazansky, "Effect of Laser Wavelength on Structure and Photoelectric Properties of a-Si:H Films Crystallized by Femtosecond Laser Pulses," J. Nanoelectron. Optoelectron. **9**, 728–733 (2015).

52. P. Karpinski, V. Shvedov, W. Krolikowski, and C. Hnatovsky, "Laser-writing inside uniaxially birefringent crystals: fine morphology of ultrashort pulse-induced changes in lithium niobate," Opt. Express **24**, 7456 (2016).

53. Y. Shimotsuma, T. Sei, M. Mori, M. Sakakura, and K. Miura, "Self-organization of polarization-dependent periodic nanostructures embedded in III–V semiconductor materials," Appl. Phys. A **122**, 159 (2016).

54. S. Mori, "Nanogratings Embedded in Al2O3-Dy2O3 Glass by Femtosecond Laser Irradiation," J. Laser Micro/Nanoengineering **11**, 87–90 (2016).

55. S. S. Fedotov, R. Drevinskas, S. V. Lotarev, A. S. Lipatiev, M. Beresna, A. Čerkauskaite, V. N. Sigaev, and P. G. Kazansky, "Direct writing of birefringent elements by ultrafast laser nanostructuring in multicomponent glass," Appl. Phys. Lett. **108**, (2016).

56. Y. Liao, Y. Shen, L. Qiao, D. Chen, Y. Cheng, K. Sugioka, and K. Midorikawa, "Femtosecond laser nanostructuring in porous glass with sub-50 nm feature sizes.," Opt. Lett. **38**, 187–9 (2013).

57. Y. Liao, W. Pan, Y. Cui, L. Qiao, Y. Bellouard, K. Sugioka, and Y. Cheng, "Formation of in-volume nanogratings with sub-100-nm periods in glass by femtosecond laser irradiation," Opt. Lett. **40**, 3623 (2015).

58. Y. Liao, J. Ni, L. Qiao, M. Huang, Y. Bellouard, K. Sugioka, and Y. Cheng, "High-fidelity visualization of formation of volume nanogratings in porous glass by femtosecond laser irradiation," Optica **2**, 329 (2015).

59. A. Yariv and P. Yhe, *Optical Waves in Crystals* (Wiley, 1984), pp. 165–174.

60. M. Born and E. Wolf, *Principles of Optics* (Pergamon Press, 1980), p. 705.

61. H. Kikuta, Y. Ohira, and K. Iwata, "Achromatic quarter-wave plates using the dispersion of form birefringence," Appl. Opt. **36**, 1566–1572 (1997).

62. C. Gu and P. Yeh, "Form birefringence dispersion in periodic layered media," Opt. Lett. **21**, 504 (1996).

63. R. Taylor, C. Hnatovsky, and E. Simova, "Applications of femtosecond laser induced self-organized planar nanocracks inside fused silica glass," Laser Photonics Rev. **2**, 26–46 (2008).

64. C. Gu and P. Yeh, "Form birefringence dispersion in periodic layered media," Opt. Lett. **21**, 504 (1996).

65. M. Shribak and R. Oldenbourg, "Techniques for fast and sensitive measurements of two-dimensional birefringence distributions," Appl. Opt. **42**, 3009–3017 (2003).

66. E. Wolf, *Progress in Optics* (Elsevier B.V., 2005), p. 481.

67. B. Y. S. Pancharatnam, "Generalized theory of interference, and its applications. Part I. Coherent pencils," Proc. Indian Acad. Sci. A **44**, 247–262 (1956).

68. C. Brosseau, *Fundamentals of Polarized Light: A Statistical Optics Approach* (Wiley, 1998), p. 424.

69. M. V Berry, "Quantal phase factors accompanying adiabatic changes," Proc. R. Soc. London Ser. A **392**, 45–57 (1984).

70. Z. Bomzon, V. Kleiner, and E. Hasman, "Pancharatnam-Berry phase in space-variant polarization-state manipulations with subwavelength gratings," Opt. Lett. **26**, 1424–1426 (2001).

71. R. Drevinskas, M. Gecevičius, M. Beresna, Y. Bellouard, and P. G. Kazansky, "Tailored surface birefringence by femtosecond laser assisted wet etching," Opt. Express **23**, 1428–1437 (2015).

72. Y. Ke, Y. Liu, J. Zhou, Y. Liu, H. Luo, and S. Wen, "Photonic spin filter with dielectric metasurfaces," Opt. Express **23**, 33079 (2015).

73. Z. Bomzon, G. Biener, V. Kleiner, and E. Hasman, "Space-variant Pancharatnam-Berry phase optical elements with computer-generated subwavelength gratings," Opt. Lett. **27**, 1141–1143 (2002).

74. E. Hasman, Z. Bomzon, A. Niv, G. Biener, and V. Kleiner, "Polarization beam-splitters and optical switches based on space-variant computer-generated subwavelength quasi-periodic structures," Opt. Commun. **209**, 45–54 (2002).

75. E. Hasman, V. Kleiner, G. Biener, and A. Niv, "Polarization dependent focusing lens by use of quantized Pancharatnam-Berry phase diffractive optics," Appl. Phys. Lett. **82**, 328–330 (2003).

76. N. Yu and F. Capasso, "Flat optics with designer metasurfaces," Nat. Mater. **13**, 139–150 (2014).

77. G. Zheng, H. Mühlenbernd, M. Kenney, G. Li, T. Zentgraf, and S. Zhang, "Metasurface holograms reaching 80% efficiency," Nat. Nanotechnol. **10**, 308–312 (2015).

78. S. Jahani and Z. Jacob, "All-dielectric metamaterials," Nat. Nanotechnol. **11**, 23–36 (2016).

79. T. Todorov, L. Nikolova, and N. Tomova, "Polarization holography 1: A new high-efficiency organic material with reversible photoinduced birefringence," Appl. Opt. **23**, 4309 (1984).

80. M. N. Miskiewicz and M. J. Escuti, "Direct-writing of complex liquid crystal patterns," Opt. Express **22**, 12691–12706 (2014).

81. J. Kim, Y. Li, M. N. Miskiewicz, C. Oh, M. W. Kudenov, and M. J. Escuti, "Fabrication of ideal geometric-phase holograms with arbitrary wavefronts," Optica **2**, 958 (2015).

82. P. F. McManamon, P. J. Bos, M. J. Escuti, J. Heikenfeld, S. Serati, H. Xie, and E. A. Watson, "A review of phased array steering for narrow-band electrooptical systems," Proceeding IEEE **97**, (2009).

83. L. Marrucci, C. Manzo, and D. Paparo, "Pancharatnam-Berry phase optical elements for wave front shaping in the visible domain: Switchable helical mode generation," Appl. Phys. Lett. **88**, 221102 (2006).

84. M. W. Kudenov, M. J. Escuti, E. L. Dereniak, and K. Oka, "White-light channeled imaging polarimeter using broadband polarization gratings," Appl. Opt. **50**, 2283–2293 (2011).

85. J. A. Davis, D. E. McNamara, D. M. Cottrell, and T. Sonehara, "Two-Dimensional Polarization Encoding with a Phase-Only Liquid-Crystal Spatial Light Modulator," Appl. Opt. **39**, 1549 (2000).

86. M. Birnbaum, "Semiconductor surface damage produced by Ruby lasers," J. Appl. Phys. **36**, 3688–3689 (1965).

87. A. Siegman and P. Fauchet, "Stimulated Wood's anomalies on laser-illuminated surfaces," IEEE J. Quantum Electron. **22**, 1384–1403 (1986).

88. Z. Guosheng, P. Fauchet, and A. Siegman, "Growth of spontaneous periodic surface structures on solids during laser illumination," Phys. Rev. B **26**, 5366–5381 (1982).

89. A. Borowiec and H. K. Haugen, "Subwavelength ripple formation on the surfaces of compound semiconductors irradiated with femtosecond laser pulses," Appl. Phys. Lett. **82**, 4462 (2003).

90. N. Yasumaru, K. Miyazaki, and J. Kiuchi, "Femtosecond-laser-induced nanostructure formed on hard thin films of TiN and DLC," Appl. Phys. A Mater. Sci. Process. **76**, 983–985 (2003).

91. J. Bonse, J. Krüger, S. Höhm, and A. Rosenfeld, "Femtosecond laser-induced periodic surface structures," J. Laser Appl. **24**, 042006 (2012).

92. J. Bonse, A. Rosenfeld, and J. Krüger, "On the role of surface plasmon polaritons in the formation of laser-induced periodic surface structures upon irradiation of silicon by femtosecond-laser pulses," J. Appl. Phys. **106**, 104910 (2009).

93. J. E. Sipe, J. F. Young, J. S. Preston, and H. M. Driel, "Laser-induced periodic surface structures. I. Theroy," Phys. Rev. B **27**, 1141–1154 (1983).

94. M. Huang, F. Zhao, Y. Cheng, N. Xu, and Z. Xu, "Origin of laser-induced near-subwavelength ripples: interference between surface plasmons and incident laser," ACS Nano **3**, 4062–4070 (2009).

95. J. Bonse, S. Baudach, J. Krüger, W. Kautek, and M. Lenzner, "Femtosecond laser ablation of silicon – modification thresholds and morphology," Appl. Phys. A **74**, 19–25 (2002).

96. J. Bonse, M. Munz, and H. Sturm, "Structure formation on the surface of indium phosphide irradiated by femtosecond laser pulses," J. Appl. Phys. **97**, (2005).

97. J. Bonse and J. Krüger, "Pulse number dependence of laser-induced periodic surface structures for femtosecond laser irradiation of silicon," J. Appl. Phys. **108**, 034903 (2010).

98. M. O. Thompson, J. Galvin, J. Mayer, P. S. Peercy, J. M. Poate, D. C. Jacobson, A. G. Cullis, and N. G. Chew, "Melting temperature and explosive crystallization of amorphous silicon during pulsed laser irradiation," Phys. Rev. Lett. **52**, 2360–2364 (1984).

99. C. V Shank, R. Yen, and C. Hirlimann, "Time-resolved reflectivity measurements of femtosecond-optical-pulse-induced phase transitions in silicon," Phys. Rev. Lett. **50**, 454–457 (1983).

100. P. Saeta, J.-K. Wang, Y. Siegal, N. Bloembergen, and E. Mazur, "Ultrafast electronic disordering during femtosecond laser melting of GaAs," Phys. Rev. Lett. **67**, 1023–1026 (1991).

101. D. von der Linde, K. Sokolowski-Tinten, and J. Bialkowski, "Laser – solid interaction in the femtosecond time regime," Appl. Surf. Sci. **109**, 1–10 (1997).

102. M. C. Downer and C. V Shank, "Ultrafast heating of silicon on sapphire by femtosecond Optical Pulses," Phys. Rev. Lett. **56**, 761–764 (1986).

103. Y. Siegal, E. N. Glezer, L. Huang, and E. Mazur, "Laser-induced phase transitions in semiconductors," Annu. Rev. Mater. **25**, 223–247 (1995).

104. I. L. Shumay and U. Hofer, "Phase transformations of an InSb surface induced by strong femtosecond laser pulses," Phys. Rev. B **53**, 878–884 (1996).

105. A. Rousse, C. Rischel, S. Fourmaux, I. Uschmann, S. Sebban, G. Grillon, P. Balcou, E. Forster, J. P. Geindre, P. Audebert, J. C. Gauthier, and D. Hulin, "Non-thermal melting in semiconductors measured at femtosecond resolution," Nature **410**, 65–68 (2001).

106. P. Stampfli and H. K. Bennemann, "Theory for the instability of the diamond structure of Si, Ge, and C induced by a dense electron-hole plasma," Phys. Rev. B **42**, 7163–7173 (1990).

107. F. Costache, S. Kouteva-Arguirova, and J. Reif, "Sub-damage-threshold femtosecond laser ablation from crystalline Si: surface nanostructures and phase transformation," Appl. Phys. A **79**, 1429–1432 (2004).

108. D. Dufft, a. Rosenfeld, S. K. Das, R. Grunwald, and J. Bonse, "Femtosecond laser-induced periodic surface structures revisited: A comparative study on ZnO," J. Appl. Phys. **105**, 034908 (2009).

109. J. Reif, F. Costache, M. Henyk, and S. V Pandelov, "Ripples revisited: non-classical morphology at the bottom of femtosecond laser ablation craters in transparent dielectrics," Appl. Surf. Sci. **197-198**, 891–895 (2002).

110. A. Y. Vorobyev and C. Guo, "Colorizing metals with femtosecond laser pulses," Appl. Phys. Lett. **92**, 2006–2009 (2008).

111. T. Baldacchini, J. E. Carey, M. Zhou, and E. Mazur, "Superhydrophobic surfaces prepared by microstructuring of silicon using a femtosecond laser," Langmuir **22**, 4917–4919 (2006).

112. E. Bricchi and P. G. Kazansky, "Extraordinary stability of anisotropic femtosecond direct-written structures embedded in silica glass," Appl. Phys. Lett. **88**, 111119 (2006).

113. J. Canning, M. Lancry, K. Cook, A. Weickman, F. Brisset, and B. Poumellec, "Anatomy of a femtosecond laser processed silica waveguide [Invited]," Opt. Mater. Express **1**, 998 (2011).

114. V. Oliveira, S. P. Sharma, P. Herrero, and R. Vilar, "Transformations induced in bulk amorphous silica by ultrafast laser direct writing," Opt. Lett. **38**, 4950–4953 (2013).

115. V. Bhardwaj, E. Simova, P. Rajeev, C. Hnatovsky, R. Taylor, D. Rayner, and P. Corkum, "Optically Produced Arrays of Planar Nanostructures inside Fused Silica," Phys. Rev. Lett. **96**, 057404 (2006).

116. R. Taylor, C. Hnatovsky, and E. Simova, "Applications of femtosecond laser induced self-organized planar nanocracks inside fused silica glass," Laser Photonics Rev. **2**, 26–46 (2008).

117. F. Liang, R. Vallée, and S. Chin, "Mechanism of nanograting formation on the surface of fused silica," Opt. Express **20**, 4389–4396 (2012).

118. M. Beresna, M. Gecevičius, P. G. Kazansky, T. Taylor, and A. V. Kavokin, "Exciton mediated self-organization in glass driven by ultrashort light pulses," Appl. Phys. Lett. **101**, 053120 (2012).

119. A. Rudenko, J.-P. Colombier, and T. E. Itina, "From random inhomogeneities to periodic nanostructures induced in bulk silica by ultrashort laser," Phys. Rev. B **93**, 075427 (2016).

120. F. Zimmermann, A. Plech, S. Richter, A. Tünnermann, and S. Nolte, "The onset of ultrashort pulse-induced nanogratings," Laser Photonics Rev. **8**, 1–8 (2016).

121. J. Bonse, J. Krüger, S. Höhm, and A. Rosenfeld, "Femtosecond laser-induced periodic surface structures," J. Laser Appl. **24**, 042006 (2012).

122. H. Misawa and S. Juodkazis, *3D Laser Microfabrication: Principles and Applications* (Wiley-VCH Verlag GmbH & Co. KGaA, Weinheim, 2006).

123. M. Beresna, M. Gecevičius, P. G. Kazansky, T. Taylor, and A. V. Kavokin, "Exciton mediated self-organization in glass driven by ultrashort light pulses," Appl. Phys. Lett. **101**, 053120 (2012).

124. P. Martin, S. Guizard, P. Daguzan, G. Petite, P. D'Oliveira, P. Meynadier, and M. Perdrix, "Subpicosecond study of carrier trapping dynamics in wide-band-gap crystals," Phys. Rev. B **55**, 5799–5810 (1997).

125. E. Bricchi, J. D. Mills, P. G. Kazansky, B. G. Klappauf, and J. J. Baumberg, "Birefringent Fresnel zone plates in silica fabricated by femtosecond laser machining," Opt. Lett. **27**, 2200 (2002).

126. M. Beresna, M. Gecevičius, P. G. Kazansky, and T. Gertus, "Radially polarized optical vortex converter created by femtosecond laser nanostructuring of glass," Appl. Phys. Lett. **98**, 201101 (2011).

127. M. Gecevičius and M. Beresna, "Airy beams generated by ultrafast laser-imprinted space-variant nanostructures in glass," Opt. Lett. **39**, 6791–6794 (2014).

128. Altechna, "S-waveplate (Radial Polarization Converter)," http://www.altechna.com/product_details.php?id=1048.

129. Y. Shimotsuma, M. Sakakura, P. G. Kazansky, M. Beresna, J. Qiu, K. Miura, and K. Hirao, "Ultrafast manipulation of self-assembled form birefringence in glass," Adv. Mater. **22**, 4039–4043 (2010).

130. J. Zhang, A. Čerkauskaitė, R. Drevinskas, A. Patel, M. Beresna, and P. G. Kazansky, "Eternal 5D data storage by ultrafast laser writing in glass," in *Laser-Based Micro- and Nanoprocessing X*, U. Klotzbach, K. Washio, and C. B. Arnold, eds. (2016), p. 97360U.

131. Y. He, Z. Liu, Y. Liu, J. Zhou, Y. Ke, H. Luo, and S. Wen, "Higher-order laser mode converters with dielectric metasurfaces," Opt Lett **40**, 5506–5509 (2015).

132. R. Berlich, D. Richter, M. Richardson, and S. Nolte, "Fabrication of computer-generated holograms using femtosecond laser direct writing," Opt. Lett. **41**, 1752 (2016).

133. S. Rajesh and Y. Bellouard, "Towards fast femtosecond laser micromachining of fused silica: The effect of deposited energy," Opt. Express **18**, (2010).

134. S. Kiyama, S. Matsuo, S. Hashimoto, and Y. Morihira, "Examination of Etching Agent and Etching Mechanism on Femotosecond Laser Microfabrication of Channels Inside Vitreous Silica Substrates," J. Phys. Chem. C **113**, 11560–11566 (2009).

135. F. Madani-Grasset and Y. Bellouard, "Femtosecond laser micromachining of fused silica molds," Opt. Express **18**, 21826 (2010).

136. A. Schaap and Y. Bellouard, "Molding topologically-complex 3D polymer microstructures from femtosecond laser machined glass," Opt. Mater. Express **3**, 1428 (2013).

137. Y. Bellouard, A. Said, M. Dugan, and P. Bado, "Fabrication of high-aspect ratio, micro-fluidic channels and tunnels using femtosecond laser pulses and chemical etching," Opt. Express **12**, 2120–2129 (2004).

138. B. Lenssen and Y. Bellouard, "Optically transparent glass micro-actuator fabricated by femtosecond laser exposure and chemical etching," Appl. Phys. Lett. **101**, 103503 (2012).

139. K. Sugioka and Y. Cheng, "Femtosecond laser processing for optofluidic fabrication," Lab Chip **12**, 3576 (2012).

140. R. M. Vazquez, R. Osellame, D. Nolli, C. Dongre, H. van den Vlekkert, R. Ramponi, M. Pollnau, and G. Cerullo, "Integration of femtosecond laser written optical waveguides in a lab-on-chip," Lab Chip **9**, 91–96 (2009).

141. M. Kim, D. J. Hwang, H. Jeon, K. Hiromatsu, and C. P. Grigoropoulos, "Single cell detection using a glass-based optofluidic device fabricated by femtosecond laser pulses," Lab Chip **9**, 311–318 (2009).

142. A. Marcinkevičius, S. Juodkazis, M. Watanabe, M. Miwa, S. Matsuo, H. Misawa, and J. Nishii, "Femtosecond laser-assisted three-dimensional microfabrication in silica," Opt. Lett. **26**, 277–279 (2001).

143. F. Gori, "Measuring Stokes parameters by means of a polarization grating," Opt. Lett. **24**, 584 (1999).

144. J. Ford, F. Xu, K. Urquhart, and Y. Fainman, "Polarization-selective computer-generated holograms," Opt. Lett. **18**, 456–458 (1993).

145. L. D. Landau and E. M. Lifshitz, *Electrodynamics of Continuous Media*, Volume 8 o (Pergamon Press, 1960).

146. G. Seifert, M. Kaempfe, K. J. Berg, and H. Graener, "Production of “ dichroitic ” diffraction gratings in glasses containing silver nanoparticles via particle deformation with ultrashort laser pulses," Appl. Phys. B **73**, 355–359 (2001).

147. A. Berger, W.-G. Drost, S. Hopfe, M. Steen, and H. Hofmeister, "Stress State and Twin Configuration of Spheroidal Silver Nanoparticles in Glass," in *Nanostructured and Advanced Materials for Applications in Sensor, Optoelectronic and Photovoltaic Technology* (Springer Netherlands, 2005), pp. 323–326.

148. G. Baraldi, J. Gonzalo, J. Solis, and J. Siegel, "Reorganizing and shaping of embedded near-coalescence silver nanoparticles with off-resonance femtosecond laser pulses," Nanotechnology **24**, 255301 (2013).

149. A. Podlipensky, A. Abdolvand, G. Seifert, and H. Graener, "Femtosecond laser assisted production of dichroitic 3D structures in composite glass containing Ag nanoparticles," Appl. Phys. A **80**, 1647–1652 (2005).

150. L. A. H. Fleming, G. Tang, S. A. Zolotovskaya, and A. Abdolvand, "Controlled modification of optical and structural properties of glass with embedded silver nanoparticles by nanosecond pulsed laser irradiation," **2861**, (2011).

151. A. Oliver, J. A. Reyes-Esqueda, J. C. Cheang-Wong, C. E. Román-Velázquez, A. Crespo-Sosa, L. Rodríguez-Fernández, J. A. Seman, and C. Noguez, "Controlled anisotropic deformation of Ag nanoparticles by Si ion irradiation," Phys. Rev. B **74**, 245425 (2006).

152. Y. K. Mishra, F. Singh, D. K. Avasthi, J. C. Pivin, D. Malinovska, and E. Pippel, "Synthesis of elongated Au nanoparticles in silica matrix by ion irradiation," Appl. Phys. Lett. **91**, 063103 (2007).

153. P. V Kamat, M. Flumiani, and G. V Hartland, "Picosecond Dynamics of Silver Nanoclusters. Photoejection of Electrons and Fragmentation," **5647**, 3123–3128 (1998).

154. D. Werner and S. Hashimoto, "Improved Working Model for Interpreting the Excitation Wavelength- and Fluence-Dependent Response in Pulsed Laser-Induced Size Reduction of Aqueous Gold Nanoparticles," J. Phys. Chem. C **115**, 5063–5072 (2011).

155. D. Werner, A. Furube, T. Okamoto, and S. Hashimoto, "Femtosecond Laser-Induced Size Reduction of Aqueous Gold Nanoparticles: In Situ and Pump - Probe Spectroscopy Investigations Revealing Coulomb Explosion," 8503–8512 (2011).

156. K. Yamada, Y. Tokumoto, T. Nagata, and F. Mafuné, "Mechanism of laser-induced size-reduction of gold nanoparticles as studied by nanosecond transient absorption spectroscopy," J. Phys. Chem. B **110**, 11751–6 (2006).

157. M. Kaempfe, G. Seifert, K. Berg, H. Hofmeister, and H. Graener, "Polarization dependence of the permanent deformation of silver nanoparticles in glass by ultrashort laser pulses," Eur. Phys. J. D **16**, 237–240 (2001).

158. A. Royon, K. Bourhis, M. Bellec, G. Papon, B. Bousquet, Y. Deshayes, T. Cardinal, and L. Canioni, "Silver clusters embedded in glass as a perennial high capacity optical recording medium," Adv. Mater. **22**, 5282–6 (2010).

159. A. Podlipensky, V. Grebenev, G. Seifert, and H. Graener, "Ionization and photomodification of Ag nanoparticles in soda- lime glass by 150 fs laser irradiation: a luminescence study," **109**, 135–142 (2004).

160. A. Stalmashonak, A. Unal, G. Seifert, and H. Graener, "Optimization of dichroism in laser-induced transformation of silver nanoparticles in glass," **7033**, 1–8 (2008).

161. A. V. Podlipensky, "Laser assisted modification of optical and structural properties of composite glass with silver nanoparticles," (2005).

162. S. Link, C. Burda, and B. Nikoobakht, "Laser-Induced Shape Changes of Colloidal Gold Nanorods Using Femtosecond and Nanosecond Laser Pulses," 6152–6163 (2000).

163. A. Stalmashonak, G. Seifert, and A. Abdolvand, *Ultra-Short Pulsed Laser Engineered Metal-Glass Nanocomposites*, SpringerBriefs in Physics (Springer International Publishing, 2013).

164. S. A. Maier, *Plasmonics. Fundamentals and Applications* (Springer Science, 2007), p. 223.

165. U. Kreibig and M. Vollmer, *Optical Properties of Metal Clusters* (Berlin: Springer, 1995).

166. Mie G., "Beitrage zur Optik truber Medien, speziell kolloidaler Metallosungen," Ann. Phys. **25**, 377–445 (1908).

167. J. I. Gittleman and B. Abeles, "Comparison of the effective medium and the Maxwell-Garnett predictions for the dielectric constants of granular metals," Phys. Rev. B **15**, 3273 (1977).

168. M. Gecevičius, R. Drevinskas, M. Beresna, and P. G. Kazansky, "Single beam optical vortex tweezers with tunable orbital angular momentum," Appl. Phys. Lett. **104**, 231110 (2014).

169. R. Drevinskas, M. Beresna, M. Gecevičius, M. Khenkin, A. G. Kazanskii, I. Matulaitienė, G. Niaura, O. I. Konkov, E. I. Terukov, Y. P. Svirko, and P. G. Kazansky, "Giant birefringence and dichroism induced by ultrafast laser pulses in hydrogenated amorphous silicon," Appl. Phys. Lett. **106**, 171106 (2015).

Paper A

R. Drevinskas, M. Gecevičius, M. Beresna, Y. Bellouard, and P. G. Kazansky

Tailored surface birefringence by femtosecond laser assisted wet etching

Optics Express 3(2), 1428-1437 (2015)

Tailored surface birefringence by femtosecond laser assisted wet etching

Rokas Drevinskas,[1,*] Mindaugas Gecevičius,[1] Martynas Beresna,[1] Yves Bellouard[2] and Peter G. Kazansky[1]

[1]*Optoelectronics Research Centre, University of Southampton, SO17 1BJ, United Kingdom*
[2] *Mechanical Engineering Department, Eindhoven University of Technology, P.O. Box 513, 5600 MB, Eindhoven, The Netherlands*
**rd1c12@orc.soton.ac.uk*

Abstract: Surface texturing is demonstrated by the combination of wet etching and ultrafast laser nanostructuring of silica glass. Using potassium hydroxide (KOH) at room temperature as an etchant of laser modified glass, we show the polarization dependent linear increase in retardance reaching a threefold value within 25 hours. The dispersion control of birefringence by the etching procedure led to achromatic behaviour over the entire visible spectral range. The mechanism of enhanced KOH etching selectivity after femtosecond laser exposure is discussed and correlated to the formation of various laser-induced defects, such as silicon-rich oxygen deficiency and color centers.

OCIS codes: (140.3390) Laser materials processing; (260.5430) Polarization; (260.1440) Birefringence.

References and links

1. R. R. Gattass and E. Mazur, "Femtosecond laser micromachining in transparent materials," Nat. Photonics **2**(4), 219–225 (2008).
2. Y. Shimotsuma, P. G. Kazansky, J. Qiu, and K. Hirao, "Self-organized nanogratings in glass irradiated by ultrashort light pulses," Phys. Rev. Lett. **91**(24), 247405 (2003).
3. R. Taylor, C. Hnatovsky, and E. Simova, "Applications of femtosecond laser induced self-organized planar nanocracks inside fused silica glass," Laser Photon. Rev. **2**(1-2), 26–46 (2008).
4. J. Canning, M. Lancry, K. Cook, A. Weickman, F. Brisset, and B. Poumellec, "Anatomy of a femtosecond laser processed silica waveguide [Invited]," Opt. Mater. Express **1**(5), 998 (2011).
5. V. Oliveira, S. P. Sharma, P. Herrero, and R. Vilar, "Transformations induced in bulk amorphous silica by ultrafast laser direct writing," Opt. Lett. **38**(23), 4950–4953 (2013).
6. M. Beresna, M. Gecevičius, and P. G. Kazansky, "Polarization sensitive elements fabricated by femtosecond laser nanostructuring of glass," Opt. Mater. Express **1**(4), 783–795 (2011).
7. J. Zhang, M. Gecevičius, M. Beresna, and P. G. Kazansky, "Seemingly unlimited lifetime data storage in nanostructured glass," Phys. Rev. Lett. **112**(3), 033901 (2014).
8. A. Marcinkevičius, S. Juodkazis, M. Watanabe, M. Miwa, S. Matsuo, H. Misawa, and J. Nishii, "Femtosecond laser-assisted three-dimensional microfabrication in silica," Opt. Lett. **26**(5), 277–279 (2001).
9. Y. Bellouard, A. Said, M. Dugan, and P. Bado, "Fabrication of high-aspect ratio, micro-fluidic channels and tunnels using femtosecond laser pulses and chemical etching," Opt. Express **12**(10), 2120–2129 (2004).
10. S. Juodkazis, K. Yamasaki, V. Mizeikis, S. Matsuo, and H. Misawa, "Formation of embedded patterns in glasses using femtosecond irradiation," Appl. Phys., A Mater. Sci. Process. **79**(4-6), 1549–1553 (2004).
11. C. Hnatovsky, R. S. Taylor, E. Simova, P. P. Rajeev, D. M. Rayner, V. R. Bhardwaj, and P. B. Corkum, "Fabrication of microchannels in glass using focused femtosecond laser radiation and selective chemical etching," Appl. Phys., A Mater. Sci. Process. **84**(1-2), 47–61 (2006).
12. M. Hörstmann-Jungemann, J. Gottmann, and D. Wortmann, "Nano- and microstructuring of SiO2 and sapphire with fs-laser induced selective etching," J. Laser Micro/Nanoeng. **4**, 135–140 (2009).
13. F. Venturini, M. Sansotera, R. M. Vazquez, R. Osellame, G. Cerullo, and W. Navarrini, "Micromanufacturing in fused silica via femtosecond laser irradiation followed by gas-phase chemical etching," Micromachines **3**(4), 604–614 (2012).
14. C. Corbari, A. Champion, M. Gecevičius, M. Beresna, Y. Bellouard, and P. G. Kazansky, "Femtosecond versus picosecond laser machining of nano-gratings and micro-channels in silica glass," Opt. Express **21**(4), 3946–3958 (2013).

#223680 - $15.00 USD Received 23 Sep 2014; revised 29 Oct 2014; accepted 17 Nov 2014; published 21 Jan 2015

15. C. Hnatovsky, R. S. Taylor, E. Simova, V. R. Bhardwaj, D. M. Rayner, and P. B. Corkum, "Polarization-selective etching in femtosecond laser-assisted microfluidic channel fabrication in fused silica," Opt. Lett. **30**(14), 1867–1869 (2005).
16. Y. Bellouard, A. Said, and P. Bado, "Integrating optics and micro-mechanics in a single substrate: a step toward monolithic integration in fused silica," Opt. Express **13**(17), 6635–6644 (2005).
17. Y. Hanada, K. Sugioka, H. Kawano, I. S. Ishikawa, A. Miyawaki, and K. Midorikawa, "Nano-aquarium for dynamic observation of living cells fabricated by femtosecond laser direct writing of photostructurable glass," Biomed. Microdevices **10**(3), 403–410 (2008).
18. S. Juodkazis, V. Mizeikis, and H. Misawa, "Three-dimensional microfabrication of materials by femtosecond lasers for photonics applications," J. Appl. Phys. **106**(5), 051101 (2009).
19. S. Ho, M. Haque, P. R. Herman, and J. S. Aitchison, "Femtosecond laser-assisted etching of three-dimensional inverted-woodpile structures in fused silica," Opt. Lett. **37**(10), 1682–1684 (2012).
20. Y. Bellouard, E. Barthel, A. A. Said, M. Dugan, and P. Bado, "Scanning thermal microscopy and Raman analysis of bulk fused silica exposed to low-energy femtosecond laser pulses," Opt. Express **16**(24), 19520–19534 (2008).
21. S. Rajesh and Y. Bellouard, "Towards fast femtosecond laser micromachining of fused silica: The effect of deposited energy," Opt. Express **18**(20), 21490–21497 (2010).
22. S. Juodkazis, Y. Nishi, and H. Misawa, ""Femtosecond laser-assisted formation of channels in sapphire using KOH solution," Phys," Status Solidi-R **2**(6), 275–277 (2008).
23. S. Kiyama, S. Matsuo, S. Hashimoto, and Y. Morihira, "Examination of etching agent and etching mechanism on femotosecond laser microfabrication of channels inside vitreous silica substrates," J. Phys. Chem. C **113**(27), 11560–11566 (2009).
24. S. LoTurco, R. Osellame, R. Ramponi, and K. C. Vishnubhatla, "Hybrid chemical etching of femtosecond laser irradiated structures for engineered microfluidic devices," J. Micromech. Microeng. **23**(8), 085002 (2013).
25. M. Hermans, J. Gottmann, and F. Riedel, "Selective, laser-induced etching of fused silica at high scan-speeds using KOH," J. Laser Micro/Nanoeng. **9**, 126–131 (2014).
26. M. Beresna, M. Gecevičius, M. Lancry, B. Poumellec, and P. G. Kazansky, "Broadband anisotropy of femtosecond laser induced nanogratings in fused silica," Appl. Phys. Lett. **103**(13), 131903 (2013).
27. D. J. Stokes, *Principles and practice of variable pressure/environmental scanning electron microscopy (VP-ESEM)* (John Wiley & Sons, Ltd, 2008).
28. A. Champion, M. Beresna, P. Kazansky, and Y. Bellouard, "Stress distribution around femtosecond laser affected zones: effect of nanogratings orientation," Opt. Express **21**(21), 24942–24951 (2013).
29. P. M. Dove, N. Han, A. F. Wallace, and J. J. De Yoreo, "Kinetics of amorphous silica dissolution and the paradox of the silica polymorphs," Proc. Natl. Acad. Sci. U.S.A. **105**(29), 9903–9908 (2008).
30. J. Gratz and P. Bird, "Quartz dissolution : theory of rough and smooth surfaces," Geochim. Cosmochim. Acta **57**(5), 977–989 (1993).
31. L. Skuja, "Optically active oxygen-deficiency-related centers in amorphous silicon dioxide," J. Non-Cryst. Solids **239**(1-3), 16–48 (1998).
32. H. Seidel, L. Csepregi, A. Heuberger, and H. Boumgortel, "Anisotropic etching of crystalline silicon in alkaline solutions," J. Electrochem. Soc. **137**(11), 3612–3626 (1990).
33. J. Kerr, *Handbook of chemistry and physics*, 81st ed. (CRC, 2000).
34. M. Gecevičius, M. Beresna, J. Zhang, W. Yang, H. Takebe, and P. G. Kazansky, "Extraordinary anisotropy of ultrafast laser writing in glass," Opt. Express **21**(4), 3959–3968 (2013).
35. H. Kikuta, Y. Ohira, and K. Iwata, "Achromatic quarter-wave plates using the dispersion of form birefringence," Appl. Opt. **36**(7), 1566–1572 (1997).
36. M. Gecevičius, M. Beresna, and P. G. Kazansky, "Polarization sensitive camera by femtosecond laser nanostructuring," Opt. Lett. **38**(20), 4096–4099 (2013).
37. N. Yu and F. Capasso, "Flat optics with designer metasurfaces," Nat. Mater. **13**(2), 139–150 (2014).

1. Introduction

Femtosecond laser assisted micro-machining through the nonlinear light-matter interaction attracts considerable interest due to its ability to produce three-dimensional devices in transparent media [1]. Under certain conditions, the interaction of femtosecond pulses with silica is known to induce self-assembled nanostructure with stripe-like oxygen deficient regions oriented perpendicular to the incident beam polarization [2]. The recent works suggested these regions being a composition of parallel planar nanocracks [3] or nanoporous planes filled with decomposed SiO_2 and oxygen [4] with silica nanocrystals of 4 nm size embedded in the defect-rich nanograting planes [5].

The sub-wavelength periodicity of ultrafast laser induced nanostructures behaves as a uniaxial birefringent material where the optical axis is parallel to the direction of laser polarization. The sign of birefringence is negative, according to planar form birefringence, with the typical value of -4×10^{-3} estimated in silica glass. For comparison, quartz is a

#223680 - $15.00 USD Received 23 Sep 2014; revised 29 Oct 2014; accepted 17 Nov 2014; published 21 Jan 2015

26 Jan 2015 | Vol. 23, No. 2 | DOI:10.1364/OE.23.001428 | OPTICS EXPRESS 1429

positive uniaxial crystal with the value of 9×10^{-3}. The birefringence resulting from self-assembled nanostructures in fused silica is exploited for the fabrication of numerous polarization sensitive optical elements ranging from diffraction gratings to polarization and optical vortex converters, and data storage [6,7].

More than a decade ago, it was demonstrated that the structure modification with ultrafast laser irradiation allows a highly selective wet etching process [8]. Generally, the etching is performed with diluted hydrofluoric acid (HF), which was successfully applied in fabrication of micro- channels, and tunnels [3,9–15] or more complex structures [8,16–19].

HF is a strong etchant even for pristine glass, therefore the etching rate and selectivity is mainly determined by the contrast in morphology of the laser modified, i.e. locally induced stress or nanocracks, and unmodified zones [3,20]. The typical HF based micro-fabrication gives the etching ratio up to 50 [21]. To enhance the selectivity, a promising alternative for HF is potassium hydroxide (KOH) [21–25]. The mechanism for femtosecond laser assisted KOH etching of fused silica is still under debate and a few studies can be found on the matter. It is suggested that KOH efficiently tackles laser induced Si-rich structures while the SiO_2 matrix remains almost unetched, giving the ratio up to 200 for micro-channel fabrication at high etchant temperatures (80°C) [23].

In this paper, we demonstrate that selective KOH etching reveals high contrast nanogratings without affecting the unmodified silica lattice and leads to the control of optical dispersion and enhancement of the retardance exhibited by the nanostructures.

2. Laser assisted KOH etching of fused silica

In order to investigate the laser assisted etching process, several millimetre long lines were written with a regeneratively amplified, mode-locked Yb:KGW based ultrafast laser system (Pharos, Light Conversion Ltd.) operating at 1030 nm at a 200 kHz-repetition rate. Two identical samples were prepared using pulse duration of 700 fs, a linear polarization oriented perpendicular to the writing direction, a writing speed of 0.2 mm/s and a pulse energy of 2.5 μJ. The laser beam was focused in the bulk of the silica substrate using a 0.16 NA-objective lens yielding a fluence of roughly 19 J/cm^2. After the laser irradiation, nanoplanes parallel to the laser beam propagation and perpendicular to the polarization plane were formed. To reveal the nanograting cross-section, the sample was lapped and polished.

Taking into account that laser-induced defects [oxygen deficiency centers (ODC II, = Si^0) and color centers (E', ≡$Si^{\bullet}$)] tend to annihilate at high temperatures [26], one sample was annealed at 900°C for one hour while the other was kept at room temperature. Both the annealed and non-annealed substrates were then immersed into a KOH (1 mol/L) solution at room temperature (RT, 20° C) for 24 hours.

Surface imaging during all fabrication steps was performed with a scanning electron microscope (SEM) (Zeiss Evo50 and Zeiss Evo ME15) operating in two modes: (1) high-vacuum secondary electron mode (SE) and (2) variable pressure environmental scanning electron mode (VP-ESEM or VPSE), collecting the luminescence signal by excitation-relaxation and electron-ion recombination of molecules in gaseous chamber [27].

VPSE mode enables high-resolution scanning without conductive coating and additional surface etching. In the microscope chamber, gas molecules are ionized via the interaction with primary, backscattered and secondary electrons. After a short time, on the nanosecond scale, the excited molecules relax to the neutral ground state, emitting photons. This transition is caused due to a short lifetime of the excited state and electron-ion recombination, when the electrons emitted from the specimen or generated in the gas cascade are captured by the ions. Due to a strong electric field in the chamber, ionized gas molecules are attracted to the sample and recombined with the surface electrons, mapping its insulator/conductor properties via a luminescence signal. The better insulator the sample is, the more electrons are built-up and are emitted [27]. As a result, the regions with more constrained electrons in the VPSE image appear brighter and vice versa.

#223680 - $15.00 USD Received 23 Sep 2014; revised 29 Oct 2014; accepted 17 Nov 2014; published 21 Jan 2015

As can be seen in Fig. 1 (a) and (c), after the twenty four hours annealing procedure, some part of the nano-structures visible in the VPSE image of non-annealed specimens disappeared. Indeed, images of non-annealed nanograting show the nanoplanes as dark regions surrounded by a white shell while their annealed counter-parts show only a white pattern. Considering the physical principle of the VPSE imaging mode, the observation points toward a localized increase of surface conductivity that disappear during the annealing process. Knowing that ODC (II) and E′ defects annihilate, we conclude that these oxygen deficient-regions are the main reason for the locally increased surface conductivity. It should be noted that bright shells surrounding etched-grooves are caused by the built-up of electrons showing its tendency to localize in the higher density at the surface edges which further supports a model of localized volume expansion in the nanogratings regions [28]. The same specimens were then coated with a 10 nm gold layers and imaged using the topography based SE mode (Figs. 1(b) and 1(d)). It shows that the width of the etched planes shrinks by a factor of 2 from ~30 nm to ~15 nm. In the case of the annealed specimen, we attribute the ongoing KOH etching to the dissolution of ≡Si–Si≡ bonds generated during laser exposure.

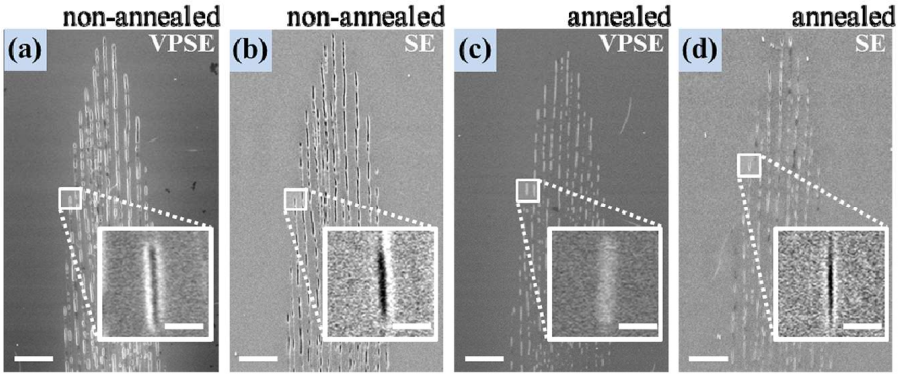

Fig. 1. SEM images of the cross sectioned single line nanograting, etched for 24 h: (a) non-annealed, imaged with VPSE mode; (b) non-annealed, imaged with SE mode; (c) annealed at 900°C for 1h, imaged with VPSE mode; (d) annealed at 900°C for 1h, imaged with SE mode. For SE mode samples were coated with a 10 nm-gold film. The insets show magnified defect-rich nanoplanes in laser modified silica. Scale bars are 2 μm for full images and 125 nm for insets.

Structurally, amorphous silica tetrahedra in the bulk consists of silica coordinated tetrahedras (≡Si–O–Si≡) with two- and three-fold coordinations with the surface [29,30]. In order to get a soluble complex, the dissolution of unmodified glass must be based on the termination of connection through the two or three Si–O backbond sites of the ≡Si–O–Si≡ groups to the neighbouring atoms. After the femtosecond laser irradiation the various types of defects are induced: Si-rich oxygen deficiency centers (≡Si–Si≡ or ODC I); oxygen deficiency centers (= Si^0 or ODC II); color centers (≡$Si^{\bullet}$ or E′) and non-bridging oxygen-hole centers (≡Si–$O^{\bullet}$ or NBOHC) [26,31]. In that case, the dissolution of laser modified glass is based on the termination of connection through the combination of zero to three Si–O and Si–Si backbond sites to the neighbouring atoms.

Considering pure crystalline silicon and silica glass composites, the etching selectivity at high temperatures (~100° C) gives values of about 100-300, while at RT the ratio increases by an order of magnitude giving the etching rate of 2-3 μm/h for silicon and ~0.8 nm/h for silica [32]. The dissolution reaction mechanism [32] for pure Si is:

#223680 - $15.00 USD Received 23 Sep 2014; revised 29 Oct 2014; accepted 17 Nov 2014; published 21 Jan 2015

$$
\begin{aligned}
&Si + 6OH^- + 2H_2O \\
&\rightarrow Si(OH)_4 + 2OH^- + 2H_2O + 4e^- \\
&\rightarrow SiO_2(OH)_2^{2-} + 4OH^- + 2H_2,
\end{aligned}
\tag{1}
$$

and for SiO_2 substrate, it is written:

$$
SiO_2 + 2OH^- \rightarrow SiO_2(OH)_2^{2-}, \tag{2}
$$

These equations describe the processes under high pH of silicate ($SiO_2(OH)_2^{2-}$) solutions (as well as orthosilicic acid ($Si(OH)_4$) for pure Si) in which potassium ions (K^+) take part only by affecting the potential distribution in the electrolyte [32]. Both chemical reactions, described in Eqs. (1) and (2), yield the same final products through different paths (breaking of two and three Si–O (799 kJ mol^{-1}) backbond sites for SiO_2 substrates and Si–Si (326 kJ mol^{-1} for native silicon and weaker for ≡Si–Si≡ defects) sites for Si substrates [33]).

For femtosecond laser-modified zones, we consider that the higher etching selectivity results from a combination of two effects, structural and morphological. On one hand, the femtosecond laser locally modifies the SiO_2 matrix introducing both backbond and dangling bond sites. On the other hand, the change in morphology directly affects the etching rate by increasing the surface area exposed to the etchant and therefore, available for chemical reaction. In the sequel, we use the high-selectivity of KOH etching to investigate birefringent surfaces.

3. Laser-induced surface birefringence

In these experiments, the silica glass was irradiated using the laser setup described before. The sample was modified with 300 fs and 700 fs pulses, polarized parallel (0°) and perpendicular (90°) to the writing direction. The writing speed was 1 mm/s with 0.5 µm interline distance and the laser pulse energy was in the range of 0.25–0.55 µJ. The laser beam was focused in the bulk of the substrate via a 0.35 NA objective lens providing a net fluence of 9–20 J/cm^2. For each set of parameters (polarization, pulse duration, and laser energy), 32 squares (of 100 µm-side dimension) were written at different depths (z-axis) starting from 75 µm and moving deeper by 1.5 µm steps (Fig. 2). A total of 512 squares were written.

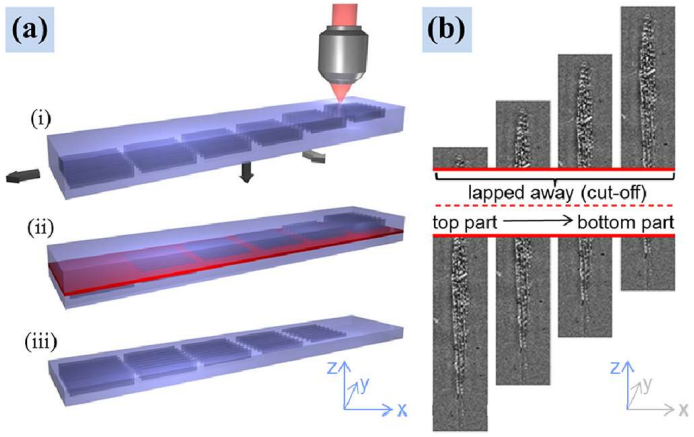

Fig. 2. (a) The sketch of laser-assisted fabrication of surface nanograting: (i) femtosecond laser writing inside a bulk glass, (ii) lapping and (iii) polishing. (b) Schematic diagram of the lapping, from the cross-sectioned single line nanograting point of view, showing the structure sectioning in z-axis direction.

#223680 - $15.00 USD Received 23 Sep 2014; revised 29 Oct 2014; accepted 17 Nov 2014; published 21 Jan 2015

26 Jan 2015 | Vol. 23, No. 2 | DOI:10.1364/OE.23.001428 | OPTICS EXPRESS 1432

For the laser processing conditions specified before, the 12 to 16 μm-long nanogratings were fabricated (z-axis direction). The top surface of the sample was lapped/polished (Logitech LP50) removing 80 ± 5 μm of the material. As a result, the uppermost squares were completely cut-off and the lower structures were sectioned at different depths revealing different cross-sections of the nanograting (Fig. 2 and Fig. 3). The lowest squares remained unaffected inside the bulk of the substrate. The etching of the nanograting exposed on the surface was carried out at room temperature (RT, 20° C) by immersing the sample into a KOH solution (1 mol/L), for a specific period of time, varying from 5 minutes to 1 hour. After each time period, the sample was dried for subsequent characterizations.

The modified areas were characterized with a quantitative birefringence measurement system (CRi Abrio mounted on an Olympus microscope BX51) operating at 546 nm wavelength. The dispersion of retardance was measured using a VIS-NIR birefringence measurement system (CRAIC also mounted on an Olympus microscope BX51). The polarizer before the sample was fixed at a 45° angle with respect to the nanograting orientation, while the polarizer after the sample was rotated either to 45° or to –45°. The spectral measurements of transmitted light intensity were taken for two configurations of the setup, the first one being when both polarizers are parallel, ($I_{parallel}$) and the second one when polarizers are perpendicular one to another ('cross polarized', $I_{crossed}$). The retardance dispersion R(λ) was then calculated as follows [26]:

$$R(\lambda) = a\cos\left(\frac{I_{parallel} - I_{crossed}}{I_{parallel} + I_{crossed}}\right)\cdot\frac{\lambda}{2\pi} = \Delta(\lambda)\cdot\frac{\lambda}{2\pi}. \qquad (3)$$

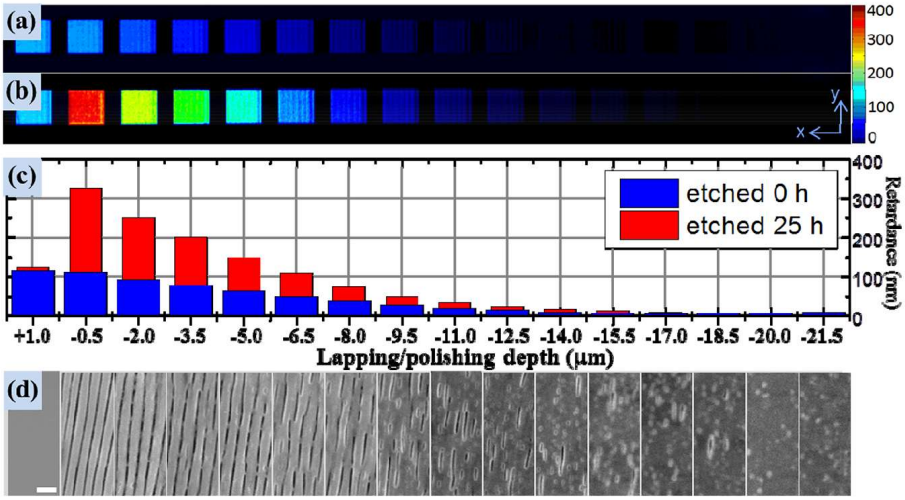

Fig. 3. The nanograting lapped/polished at different depths from Z = + 1.0 μm to Z = –21.5 μm, written with 300 fs, 0° polarization and 0.45 μJ pulse energy (see Fig. 2). The peak part of the nanograting is at the depth of Z = 0 μm. (a), (b) Retardance (in air, for λ = 546 nm) images before and after total 25 h etching, respectively, with the columns (c) indicating its values at different cut-off. Color scale: 0–400 nm. (d) VPSE SEM images of the sectioned and etched nanograting, where the cut-off values correspond to (a)–(c). Scale bar: 500 nm.

Within the first 60 min of the etching procedure, the retardance increase rate dropped almost by one order until it saturated and became constant over the rest time of the experiment (Figs. 4(a)–4(d)). The change of slope in the retardance growth after one hour is attributed to the initially high etching rate observed during the first hour. This increased etching rate can be explained by two factors: an easier access of the etchant to the modified, defects-rich, regions and the OH^--concentration decreasing in time. The second factor seems to be less dominant because continuous experiments without refreshing the etchant yield the same results as experiments performed with a continuous refreshing of the etchant. After total 25 hours of

#223680 - $15.00 USD Received 23 Sep 2014; revised 29 Oct 2014; accepted 17 Nov 2014; published 21 Jan 2015

26 Jan 2015 | Vol. 23, No. 2 | DOI:10.1364/OE.23.001428 | OPTICS EXPRESS 1433

etching, a three-fold retardance increase was observed for all experimental conditions with 0° incident beam polarization while a two-fold retardance increase was found for 90° polarization. In both cases, there is no indication of saturation, what suggests that further etching would lead to higher retardance level (Fig. 4). From the SEM-based analysis, we can see that the top 3 to 6 μm of the laser-induced structure contains highly-ordered nanopatterns (Fig. 3(d)) that provides a major contribution to the measured retardance value after the etching process (Figs. 3(a)–3(c)). Going down from the top to the bottom of the laser affected structures, the order and the continuity of nanoplanes are lost presumably due to an increase of the scattering. The uniform planes are fully replaced by randomly distributed porous structure at depth of 10 to 12 μm (Fig. 3(d)). For this reason, all the following results presented in this paper are related to the squares with the cut-off position – measured from the top of the laser induced zone - smaller than 1.5 μm.

Before the etching process, the retardance of laser induced nanogratings depends both on polarization and pulse duration. Pulses with 0.25 μJ-energy and 90°-polarization produce about 70% higher retardance values than with 0°-polarization without exhibiting a dependence on the pulse duration. Such a high difference in retardance is caused by the laser processing conditions close to the threshold for nanogratings formation (~0.2 μJ [6]). For the higher pulse energy, the retardance difference decreases with the appearance of a dependence on pulse duration. In the case of 0.45 μJ and 0.55 μJ pulse energies with 700 fs-pulse duration, the induced nanograting possesses up to ~40% higher retardance values than with 300 fs showing only a weak dependence on polarization state [34]. However, during the etching experiment the birefringence exhibits strong dependence on polarization giving ~50% higher retardance increase for 0° polarization (Figs. 4(a)–4(d)) and show only a weak dependence on pulse duration (Fig. 5(a)).

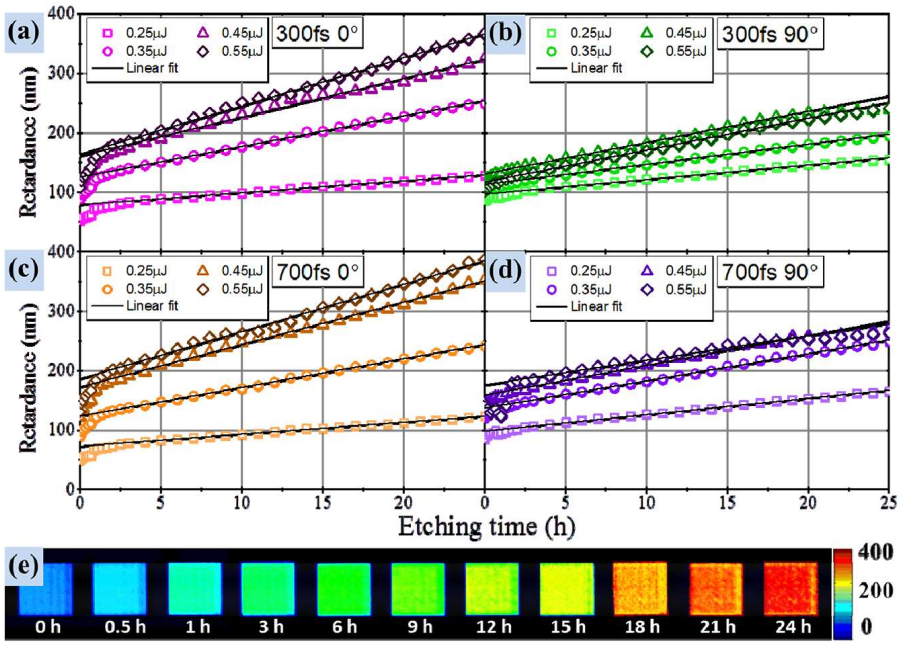

Fig. 4. (a)–(d) Retardance (in air, for λ = 546 nm) dependence on the etching time. Nanograting was written with 700 fs and 300 fs pulse duration, 0° and 90° polarization, energies ranging from 0.25 μJ to 0.55 μJ; lapped and polished at the top part of the structure. The linear fitting was performed. (e) Imaged retardance (in air, for λ = 546 nm) dependence on the etching time. Structure was written with 300 fs, 0° polarization and 0.45 μJ pulse energy. Color scale: 0–400 nm.

#223680 - $15.00 USD Received 23 Sep 2014; revised 29 Oct 2014; accepted 17 Nov 2014; published 21 Jan 2015

26 Jan 2015 | Vol. 23, No. 2 | DOI:10.1364/OE.23.001428 | OPTICS EXPRESS 1434

The retardance exhibited by the exposed nanograting was linearly increasing with the etching time. The growth rates extracted from the linear fits of the etching kinetics (Fig. 4) group into two polarization branches (Fig. 5(a)). At 0.25 μJ the rates are higher for 90° polarization while at 0.35–0.55 μJ the 0° polarization bypasses it.

The formation of irregularities and periodic ruptures observed for 0.45–0.55 μJ and 90° polarization is believed to be the key factor for the roughly two times lower retardance growth rates observed after the etching process (Fig. 5(b)). It is more efficient to maintain the grating homogeneity assembling it into the orientation perpendicular to the writing direction (0° polarization) where each new written line extends the nanoplanes.

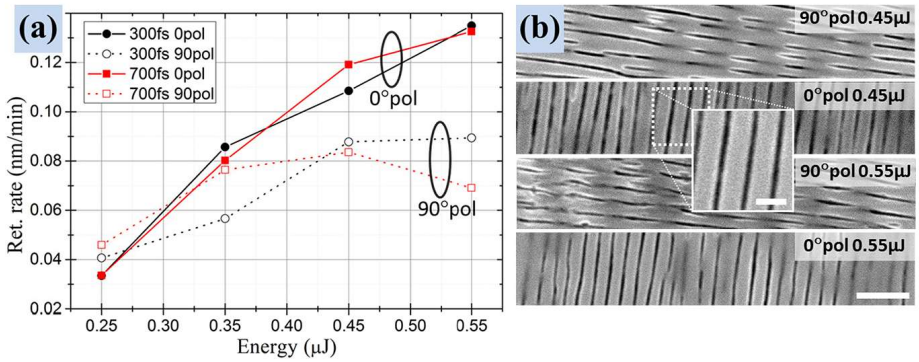

Fig. 5. (a) The etching induced retardance growth rate dependence on the laser modification conditions. The steady-state growth rates were extracted from the fitting curves, see Fig. 4. (b) VPSE SEM images of the surface nanograting written with 300 fs at various conditions and etched for 25 h. Inset shows the higher resolution zoomed in etched silica regions/nanoplanes. Scale bars: 1 μm and 300 nm (for inset).

The dispersion analysis revealed achromatic behaviour in the spectral range from 400 nm to 870 nm for the etched nanostructures induced with 0.45 μJ and 0.55 μJ pulse energies (Fig. 6(a)). In order to create achromatic birefringent device, the constant phase shift for all wavelengths must be ensured. Knowing that the element before the etching procedure was chromatic, we estimate that the retardance growth rate at 850 nm was almost two times larger than at 515 nm. After 25 h of etching, we get 1.2π–1.4π phase shift in the spectral range from 400 to 870 nm.

In general, the etching process offers a method to control the retardance of the surface elements by removing laser modified silica regions, i.e. when defect-rich nanoplanes are dissolved. Subsequent control of the retardance is achieved by filling the surface nanostructure with water. The dispersion variation from air to water medium indicates a $-3.22\cdot\pi$–$-3.30\cdot\pi$ phase shift per refractive index unit (RIU) with a refractive index resolution of $6\cdot10^{-3}$ (Fig. 6(b)). For a lower refractive index of the surrounding medium, a higher retardance is observed. In consequence, modified silica (defect-rich) regions before etching ("Bulk" line in Fig. 6(b)) have a lower refractive index than the water.

#223680 - $15.00 USD Received 23 Sep 2014; revised 29 Oct 2014; accepted 17 Nov 2014; published 21 Jan 2015

26 Jan 2015 | Vol. 23, No. 2 | DOI:10.1364/OE.23.001428 | OPTICS EXPRESS 1435

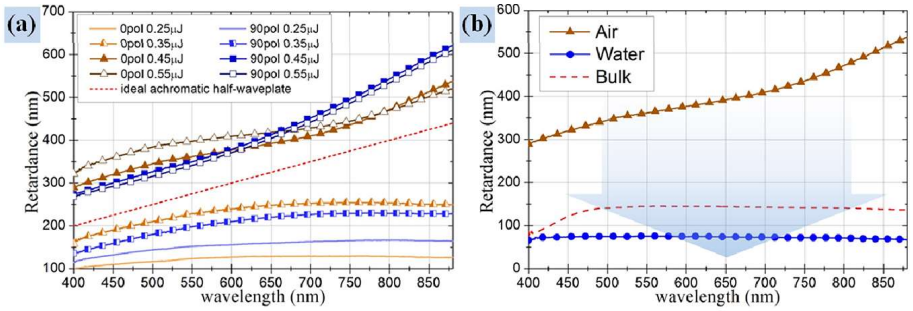

Fig. 6. Retardance (in air) dispersion of 25 h etched nanograting (a) written with 700 fs, energies from 0.25 μJ to 0.55 μJ and two polarizations states. (b) Retardance dispersion of nanograting filled with different refractive index medium: bulk – before etching (defect-rich silica); air – etched for 25 h and dried; water – etched for 25 h and immersed in water. The nanograting was written with 700 fs, 45 μJ pulse energy and 0° polarization. Blue arrow indicates the increase of medium's refractive index.

The qualitative analysis of the effective refractive indices change for TE and TM waves (n_{TE} and n_{TM}) was performed based on the so-called effective medium theory [35]

$$k_{1TE,1TM} = \sqrt{\left(\frac{2\pi n_1}{\lambda}\right)^2 - \beta_{TE,TM}^2}, \tag{4}$$

$$k_{2TE,2TM} = \sqrt{\left(\frac{2\pi n_2}{\lambda}\right)^2 - \beta_{TE,TM}^2}, \tag{5}$$

$$1 = \cos\left(a \cdot k_{1TE}\right)\cos\left(b \cdot k_{2TE}\right) - 0.5 \cdot \left(\frac{k_{2TE}}{k_{1TE}} + \frac{k_{1TE}}{k_{2TE}}\right)\sin\left(a \cdot k_{1TE}\right)\sin\left(b \cdot k_{2TE}\right), \tag{6}$$

$$1 = \cos\left(a \cdot k_{1TM}\right)\cos\left(b \cdot k_{2TM}\right) - 0.5 \cdot \left(\frac{n_1^2 k_{2TM}}{n_2^2 k_{1TM}} + \frac{n_2^2 k_{1TM}}{n_1^2 k_{2TM}}\right)\sin\left(a \cdot k_{1TM}\right)\sin\left(b \cdot k_{2TM}\right), \tag{7}$$

$$n_{TE,TM} = \frac{\lambda}{2\pi}\beta_{TE,TM}, \tag{8}$$

where n_1 and n_2 are the refractive indices of silica and variable medium (modified-silica, water or air), respectively defined with the duty cycle of $a/(a + b)$ (Fig. 7). The retardance can be determined by the structure depth (d) and the difference in the effective refractive indices:

$$R = d \cdot \left(n_{TE} - n_{TM}\right). \tag{9}$$

To simplify the calculations, we approximate laser induced nanogratings by an ideal cube shape with a constant order assembly along the entire depth of the structure (Fig. 7). Then, knowing the retardance value of the unetched nanograting, the total cube's depth (d) of 8 μm was estimated. The nanograting period (275 nm) and duty cycle (0.89) used in calculations were determined from the SEM analysis. Having all these parameters we could calculate retardance and refractive indices for layered medium by using Eqs. (4)–(9). The retardance values that are close to the experimentally measured ones, were obtained by reducing the refractive index of modified nanoplanes to $0.767 \cdot n_{silica}$. This correction factor takes into account the porous and defect-rich nature of the material forming the grooves.

#223680 - $15.00 USD Received 23 Sep 2014; revised 29 Oct 2014; accepted 17 Nov 2014; published 21 Jan 2015

26 Jan 2015 | Vol. 23, No. 2 | DOI:10.1364/OE.23.001428 | OPTICS EXPRESS 1436

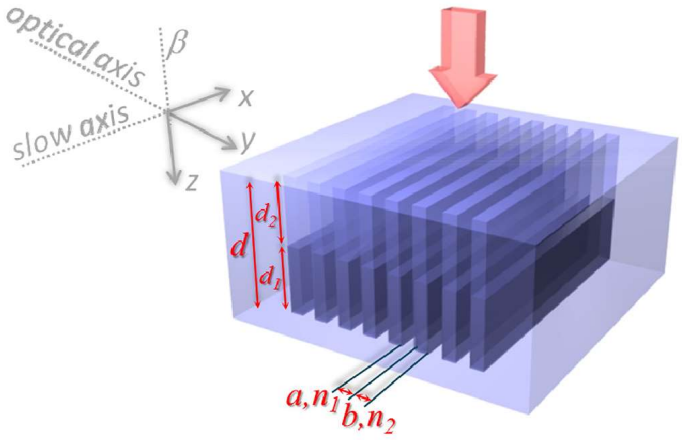

Fig. 7. The sketch of the light wave β (red arrow) propagating along the femtosecond laser induced nanograting in the silica glass. The optical axis of the fabricated birefringent element is perpendicular and the slow axis is parallel to the grating nanoplanes with thickness b and refractive index n_2; a and n_1 corresponds to the unmodified silica glass. The depth (d) of the nanograting is divided into unetched (d_1) and etched (d_2) parts.

Using the same modeling parameters, we analyzed the behavior of the etched nanograting filled with water. From the experimental results (Fig. 6(b)) we clearly see the chromatic retardance of ~75 nm. The corresponding calculations of modified-silica/silica (d_1, bn_2/an_1) and water/silica (d_2, bn_2/an_1) sandwiches indicate that water penetrates about 4.1 μm into the nanostructure and the water/silica part contributes only for ~9 nm of the total, 75 nm retardance.

Curiously, the calculations for air/silica produced a weak achromatic behavior and resulted in retardance much lower than observed in the experiments. We speculate that the achromatic properties of the structure are caused by the changing duty cycle and non-uniform/dispersive values of the effective refractive indices along the depth of the grating. The inconsistency between experiments and modeling in this particular case is attributed to these parameters that were not taken into account in the calculations.

4. Conclusions

We have demonstrated a fabrication method of birefringent surface elements in fused silica. Femtosecond laser-induced nanogratings written in the bulk of silica with 0° incident beam polarization exhibit up to a three-fold retardance increase after lapping/polishing and 25 h of KOH etching at room temperature. Scanning electron microscopy analysis before and after the annealing procedure indicates a strong relationship between a locally increased surface conductivity and laser-induced ODC (II) and E′ defects that accounts for the high etching selectivity between modified and unmodified silica zones. The removal of sub-wavelength periodicity stripe-like oxygen deficient regions by etching and replacement with the different medium gives a way to effectively control the refractive indices of TM and TE waves. This observation opens new opportunities for designing both, chromatic and achromatic wave plates that can be used for micro-optics applications such as polarization sensitive cameras [36], and flat optics [37].

Acknowledgments

We are grateful to Dr. Stuart Boden for useful discussions in the field of scanning electron microscopy.

#223680 - $15.00 USD Received 23 Sep 2014; revised 29 Oct 2014; accepted 17 Nov 2014; published 21 Jan 2015

Paper B

R. Drevinskas, and P. G. Kazansky

Dichroic Surfaces Engineered by Ultrafast Laser Assisted Wet Etching

Manuscript in preparation

Dichroic Surfaces Engineered by Ultrafast Laser Assisted Wet Etching

ROKAS DREVINSKAS,* AND PETER G. KAZANSKY

Optoelectronics Research Centre, University of Southampton, Southampton SO17 1BJ, United Kingdom
**R.Drevinskas@soton.ac.uk*

Abstract: Fabrication of polarization sensitive metal thin-films is demonstrated. First, surface nanogratings with periodicity of ~300 nm and duty cycle of roughly 10% of the etched nano-planes are designed by ultrafast laser assisted KOH wet etching of silica glass. Later, the nanostructured silica is implemented as a host substrate for metal thin-film deposition. The resulting linear dichroism defined by the orientation of host nanogratings is revealed. The control of plasmonic response as a function of chemical etching time of engineered silica nanogratings is demonstrated. Such silica substrates can be implemented for template-defined self-organization of materials such as liquid crystals, silicon thin-films, metal thin-films, etc. and show the potential to be realized not only in integrated optics and electronics but also sensing applications.

OCIS codes: (320.2250) Femtosecond phenomena; (350.3850) Materials processing; (050.1930) Dichroism

References and links

1. N. Yu and F. Capasso, "Flat optics with designer metasurfaces," Nat. Mater. **13**, 139–150 (2014).
2. N. Meinzer, W. L. Barnes, and I. R. Hooper, "Plasmonic meta-atoms and metasurfaces," Nat Phot. **8**, 889–898 (2014).
3. G. Zheng, H. Mühlenbernd, M. Kenney, G. Li, T. Zentgraf, and S. Zhang, "Metasurface holograms reaching 80% efficiency," Nat. Nanotechnol. **10**, 308–312 (2015).
4. J. Kim, Y. Li, M. N. Miskiewicz, C. Oh, M. W. Kudenov, and M. J. Escuti, "Fabrication of ideal geometric-phase holograms with arbitrary wavefronts," Optica **2**, 958 (2015).
5. R. R. Gattass and E. Mazur, "Femtosecond laser micromachining in transparent materials," Nat. Photonics **2**, 219–225 (2008).
6. S. K. Sundaram and E. Mazur, "Inducing and probing non-thermal transitions in semiconductors using femtosecond laser pulses," Nat. Mater. **1**, 217–224 (2002).
7. J. Bonse, J. Krüger, S. Höhm, and A. Rosenfeld, "Femtosecond laser-induced periodic surface structures," J. Laser Appl. **24**, 042006 (2012).
8. A. Y. Vorobyev and C. Guo, "Colorizing metals with femtosecond laser pulses," Appl. Phys. Lett. **92**, 2006–2009 (2008).
9. T. Baldacchini, J. E. Carey, M. Zhou, and E. Mazur, "Superhydrophobic surfaces prepared by microstructuring of silicon using a femtosecond laser," Langmuir **22**, 4917–4919 (2006).
10. J. Eichstädt, G. R. B. E. Römer, and a. J. J. Huis in 't Veld, "Towards Friction Control using laser-induced periodic Surface Structures," Phys. Procedia **12**, 7–15 (2011).
11. R. Drevinskas, M. Beresna, M. Gecevičius, M. Khenkin, A. G. Kazanskii, I. Matulaitienė, G. Niaura, O. I. Konkov, E. I. Terukov, Y. P. Svirko, and P. G. Kazansky, "Giant birefringence and dichroism induced by ultrafast laser pulses in hydrogenated amorphous silicon," Appl. Phys. Lett. **106**, 171106 (2015).
12. Y. Shimotsuma, P. Kazansky, J. Qiu, and K. Hirao, "Self-Organized Nanogratings in Glass Irradiated by Ultrashort Light Pulses," Phys. Rev. Lett. **91**, 247405 (2003).
13. P. Kazansky, H. Inouye, T. Mitsuyu, K. Miura, J. Qiu, K. Hirao, and F. Starrost, "Anomalous Anisotropic Light Scattering in Ge-Doped Silica Glass," Phys. Rev. Lett. **82**, 2199–2202 (1999).
14. M. Beresna, M. Gecevičius, and P. G. Kazansky, "Polarization sensitive elements fabricated by femtosecond laser nanostructuring of glass," Opt. Mater. Express **1**, 783–795 (2011).
15. M. Gecevičius, R. Drevinskas, M. Beresna, and P. G. Kazansky, "Single beam optical vortex tweezers with tunable orbital angular momentum," Appl. Phys. Lett. **104**, 231110 (2014).
16. M. Gecevičius, M. Beresna, R. Drevinskas, and P. G. Kazansky, "Airy beams generated by ultrafast laser-imprinted space-variant nanostructures in glass," Opt. Lett. **39**, 6791–6794 (2014).
17. S. Rajesh and Y. Bellouard, "Towards fast femtosecond laser micromachining of fused silica: The effect of deposited energy," Opt. Express **18**, (2010).
18. S. Kiyama, S. Matsuo, S. Hashimoto, and Y. Morihira, "Examination of Etching Agent and Etching Mechanism on Femotosecond Laser Microfabrication of Channels Inside Vitreous Silica Substrates," J. Phys. Chem. C **113**, 11560–11566 (2009).
19. R. Drevinskas, M. Gecevičius, M. Beresna, Y. Bellouard, and P. G. Kazansky, "Tailored surface birefringence by femtosecond laser assisted wet etching," Opt. Express **23**, 1428–1437 (2015).
20. P. Yeh, "A new optical model for wire grid polarizers," Opt. Commun. **26**, 289–292 (1978).
21. M. Xu, H. P. Urbach, D. K. G. de Boer, and H. J. Cornelissen, "Wire-grid diffraction gratings used as polarizing beam splitter for visible light and applied in liquid crystal on silicon," Opt. Express **13**, 2303 (2005).
22. T. W. Ebbesen, H. J. Lezec, H. F. Ghaemi, T. Thio, and P. A. Wolff, "Extraordinary optical transmission through sub-wavelength hole arrays," Nature **391**, 667–669 (1998).
23. T.-W. Chang, X. Wang, A. Hsiao, Z. Xu, G. Lin, M. R. Gartia, X. Liu, and G. L. Liu, "Bifunctional Nano Lycurgus Cup Array Plasmonic Sensor for Colorimetric Sensing and Surface-Enhanced Raman Spectroscopy," Adv. Opt. Mater. **3**, 1397–1404 (2015).
24. H. Sun, M. Yu, G. Wang, X. Sun, and J. Lian, "Temperature-Dependent Morphology Evolution and Surface Plasmon Absorption of Ultrathin Gold Island Films," J. Phys. Chem. C **116**, 9000–9008 (2012).
25. M. Kang, S.-G. Park, and K.-H. Jeong, "Repeated Solid-state Dewetting of Thin Gold Films for Nanogap-rich Plasmonic Nanoislands," Sci. Rep. **5**, 14790 (2015).
26. D. Gaspar, A. C. Pimentel, T. Mateus, J. P. Leitão, J. Soares, B. P. Falcão, A. Araújo, A. Vicente, S. A. Filonovich, H. Águas, R. Martins, and I. Ferreira, "Influence of the layer thickness in plasmonic gold nanoparticles produced by thermal evaporation," Sci. Rep. **3**, (2013).
27. A. Yariv and P. Yhe, *Optical Waves in Crystals* (Wiley, 1984).
28. H. Kikuta, Y. Ohira, and K. Iwata, "Achromatic quarter-wave plates using the dispersion of form birefringence," Appl. Opt. **36**, 1566–1572 (1997).
29. V. Ovchinnikov and A. Shevchenko, "Self-Organization-Based Fabrication of Stable Noble-Metal Nanostructures on Large-Area

Dielectric Substrates," J. Chem. **2013**, 1–10 (2013).
30. K.-S. Lee and M. A. El-Sayed, "Gold and Silver Nanoparticles in Sensing and Imaging: Sensitivity of Plasmon Response to Size, Shape, and Metal Composition," J. Phys. Chem. B **110**, 19220–19225 (2006).

1. Introduction

Designs of flat optics have attracted great interest for being a promising alternative to control light waves [1]. Although numerous lithography techniques enabling the manufacturing of high efficiency and low scattering optical elements with complex phase gradients have been reported [2–4], the technological flexibility remains a problem; it is still dictated by the material properties, and/or requires a long time to process. Here we propose an ultrafast laser nanostructuring assisted wet etching as an alternative method capable of fabricating anisotropic surfaces used as a substrate for metal thin-film deposition resulting in a dichroic optical elements.

The key advantage of using femtosecond pulses for direct laser writing, as opposed to longer pulses, is that they can rapidly deposit energy in solids with high precision. The light is absorbed and the optical excitation ends before the surrounding lattice is perturbed, which results in highly localized nanostructuring without collateral material damage [5,6]. The laser-induced periodic surface structures that can be realized on virtually any type of media including metals, semiconductors and dielectrics have been reported [7]. Despite a vast number of applications, including coloration [8], control of surface chemical and mechanical properties [9,10], the polarization sensitive transmission has never been the main topic of the research [11]. This could be related to morphology of structures which is always affected by the ablation process. Alternatively, the interaction of femtosecond laser pulses with transparent media in volume is known to induce highly ordered self-assembled nanogratings oriented perpendicular to the incident beam polarization [12,13]. The laser-induced periodic structure behaves as a uniaxial birefringent crystal, where the two orthogonal components of electric field (along and perpendicular the layered planes) have different optical path. The birefringence resulting from self-assembled nanostructures in fused silica is exploited for the fabrication of numerous polarization sensitive optical elements ranging from diffraction grating to polarization and optical vortex converters [14–16]. However, due to the negligible linear absorption of transparent materials, the implementation of such nanogratings as polarization sensitive optical elements was not proposed. To do so, another interesting property of laser modified glass of highly selective wet etching must be applied [17]. The mechanism for femtosecond laser assisted KOH etching of fused silica is still under debate and a few studies can be found on the matter. The KOH efficiently tackles rarefied silica nano-planes filled with Si-rich structure while the SiO2 matrix remains unetched. KOH etching with high selectivity reveals high contrast nanogratings and substantially enhances retardance exhibited by the nanostructure [19] Such engineered surface nanogratings integrated with noble metals or other highly absorbing medium is expected to behave as a strong dichroic optical element similar to wire grid polarizer [20]. The periodic structure takes part as a template for the deposited material.

If the period of nanogratings is sufficiently small compared to the wavelength, the structure behaves as if it were homogeneous and uniaxial material [20]. In the case of metal nanogratings, also referred to as wire grid polarizers, the movement of free electrons in the direction perpendicular to the orientation of wires is restricted as it is not along the wires, and usually related to polarization currents induced by incident light. Thus, it is expected that the light polarized parallel to the nanogratings will not feel the structure and will be transmitted or reflected in the same way as in isotropic metal films. And if the light is polarized perpendicular, the transmission is enhanced due to the localized free electrons. Specifically, the metal nanograting can be described as a homogeneous birefringent layer which behaves as a conductor for parallel polarization and behaves as an insulator for the perpendicular polarization. Although the anisotropic transmission of ideal geometry can be analyzed considering only the differences between the effective medium [20] or propagation constants of the guided modes [21] for the two polarizations, the complexity of real fabricated structures, e.g. polycrystalline nature of metal films, formation of nano-gaps, nano-islands, nano-rods etc., resulting into the intricate transmission behavior requires more complex approaches where the polarization sensitive modes coupled with the surface plasmons are discussed [22–26].

Here we demonstrate silica nanogratings fabricated by femtosecond laser assisted KOH etching. Further we use such nanogratings as a host substrate for metal thin-film deposition. In both cases, for uniform and nano-cracked films, the differential extinction spectra with opposite signs are measured. The differential extinction spectra of deposited metal film as a function of ultrafast laser assisted wet etching time of silica glass is demonstrated. The sensing experiments of bulk refractive index show the potential of such dichroic surface elements implementing not only in the field of integrated optics but also in surface enhanced sensing. However, it should be noted that in this work we do not focus on the processes of deposition and self-organization of metal films. The main target is to implement these metalic surfaces for the demonstration of silica nanogratings-defined extinction anisotropy; which in fact could be realized aligning various materials including liquid crystals, silicon thin-films, etc.

2. Materials and methods

Laser modification of fused silica glass was performed with regeneratively amplified, mode-locked Yb:KGW based ultrafast laser system (Pharos, Light Conversion Ltd.) operating at 1030 nm with a 200 kHz repetition rate. The sample was modified with the pulse duration of 300 fs, linear polarization parallel to the writing direction, 1 mm/s writing speed with 0.5 µm interline distance and the laser pulse energy of 0.45 µJ. The laser beam was focused in the bulk of the substrate via a 0.35 NA objective lens. Under these processing conditions 32 squares (100 µm × 100 µm) were written in different depths starting from 75 µm (the bottom of the structure) and going deeper every 1.5 µm. The top surface of the sample was lapped/polished (Logitech LP50) removing ~75–85 µm so that the uppermost squares would be cut-off completely and the lower structures would be sectioned in different depth (Fig. 1). KOH (1M concentration) etching of the surface nanograting was carried out at room temperature (RT) by immersing the sample into the solution for a specific period of time, for a maximum of 24 hours. The fabricated samples were coated with 30 nm thickness gold film deposited by sputter coater (208HR). The squares sectioned at the top of the structure, where the most uniform nanogratings are formed, were used for the further characterization.

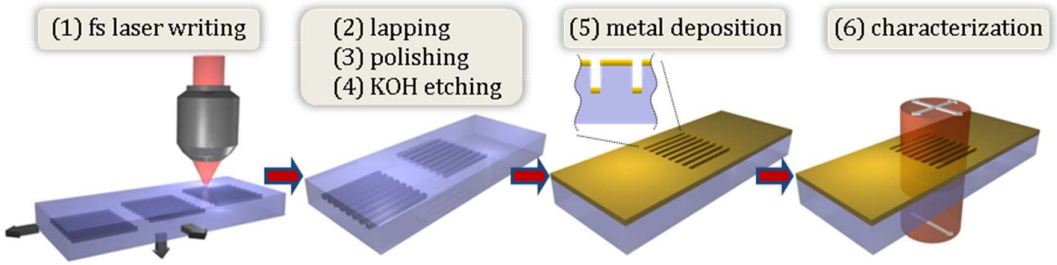

Fig. 1. Direct-write femtosecond laser nanostructuring assisted KOH etching of silica glass towards the fabrication of polarization sensitive surface elements.

The micro modified areas were optically characterized with a UV-VIS-NIR micro-spectrometer system (CRAIC; Olympus BX51) and quantitative birefringence measurement system (CRi Abrio; Olympus BX51). The spectral dependence of the metal thin-films on parallel and perpendicular polarizations was measured by inserting VIS linear polarizer before the sample. The imaging was carried out with an optical microscope (Olympus BX51) and scanning electron microscope (Zeiss Evo50; Zeiss Evo ME15).

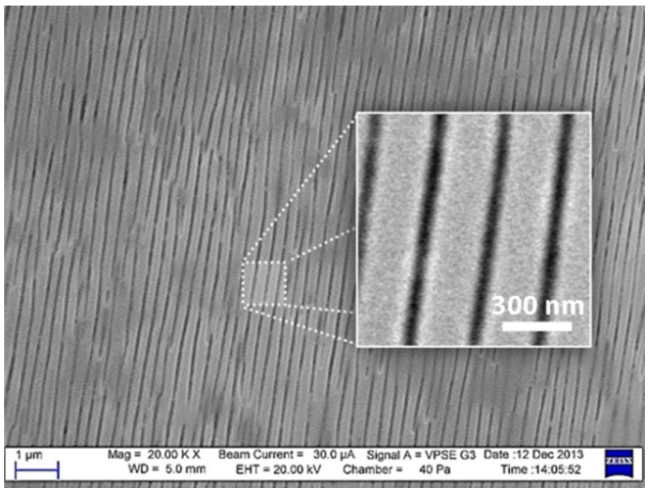

Fig. 2. VPSE SEM images of the surface nanogratings written inside silica glass, and revealed after the lapping/polishing and KOH etching for 24 h procedures. Inset shows the higher resolution zoomed-in etched silica nano-planes. Scale bars: 1 µm and 300 nm.

The high quality surface nanograting was formed in a three step procedure. After the laser irradiation, nano-planes parallel to the laser propagation and perpendicular to the polarization are formed. For the laser processing conditions mentioned above, the fabricated nanogratings are 10–15 µm long in the Z direction. But only the top 3–5 µm is packed in a highly-ordered pattern. During the lapping/polishing process, the written squares are cut-off at different heights opening the different parts of the nanogratings. As shown in Fig. 2, after 24 hours of KOH etching the nanogratings with periodicity of ~300 nm and duty cycle of roughly 10% of the etched nano-planes are formed. The depth of about 4 µm of the etched nano-planes was estimated by measuring the phase retardation of silica nanogratings before etching and after etching, and fitting the predicted geometry by the so-called effective medium theory [27,28].

3. Results and discussion

The extinction peaks measured in VIS spectral range are attributed to the surface plasmon resonance originated by self-assembled metal structures, similar reported in [24,26]. More specifically, gold deposited on the silica, due to the poor adhesion, is tend to form island-like nanoparticles structure [29]. If the amount of metal deposited on substrate is sufficient, the surface is fully covered (>10 nm) resulting into uniform polycrystalline thin-film. In this case the surface plasmons are delocalized and the transmission spectra of bulk metal are typically measured.

The ratio of transmitted light intensity polarized perpendicular and parallel to the nanogratings orientation ($I_{\perp sample}/I_{\parallel sample}$) expressed in absorption units, also referred to as differential extinction or dichroism, can be defined as follows:

$$D = A_{\perp} - A_{\parallel} = -log\left(\frac{I_{\perp\,\mathrm{sample}}}{I_{\parallel\,\mathrm{sample}}}\right), \quad (1)$$

where $A_{\perp}$ and $A_{\parallel}$ are the extinction spectra for two different polarizations. Because of the thin layer deposited, the fraction of light with both polarizations is transmitted, and both transmitted modes interacting with nanostructures can be observed in the extinction spectra. This causes the positive and/or negative peaks in spectra (Figs. 3 and 4).

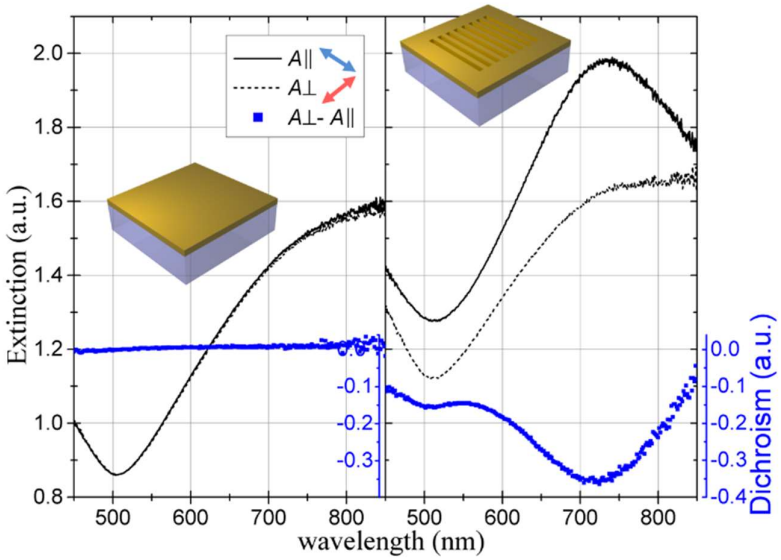

Fig. 3. Extinction (black) and linear dichroism (blue) spectra of 30 nm thickness gold film deposited on pristine (left) and nanostructured (right) silica substrate. The incident light was polarized parallel (black-dotted) and perpendicular (black-solid) to the orientation of nanogratings. Arrows indicate the orientation of polarization according to the nanogratings in the graphic insets.

After depositing 30 nm homogeneous gold film on silica nanogratings, we still observe the polarization sensitive excitation of surface plasmon resonance at around ~730 nm for parallel polarization (Fig. 3(right)). This is attributed to the anisotropic self-organization of metal film inside the etched nano-planes, i.e. the thin layer of metal is covering not only the top surface of nanogratings but also the inner surfaces (sidewalls and bottom surface) of the etched silica grooves. As a result, the peak of linear dichroism at around 730 nm with the value of -3.5 is observed, where the transmission of light polarized perpendicular to the nanogratings is higher.

By contaminating the surface with the etchant solution, i.e. directly weakening the adhesion similar reported in [29], nano-cracking of metal film deposited on a flat silica surface is observed showing strong resonance peak at around 570 nm (Fig. 4(left)). The measured extinction spectra indicates that the deposited metal is self-organized into randomly distributed nano-particles or nano-islands structure [24]. However, if the film is deposited on the silica nanogratings, the red and blue shifts with the peak positions at 525 nm and 590 nm are observed for the light polarized parallel and perpendicular to the nanogratings orientation, respectively (Fig. 4(right)). It is well know that the resonant feature of localized surface plasmon resonance is highly sensitive to the size and shape of nanostructures [30], thus we identify that the re-organization of the film (nano-cracking) into plasmonic element is defined by the surface morphology of silica glass. The positive dichroism with the maximum value of roughly 1.2 is achieved at 600 nm wavelength. Contrary to homogeneous film shown before, the light polarized parallel to the nanogratings orientation gives higher transmittance than the light polarized perpendicular.

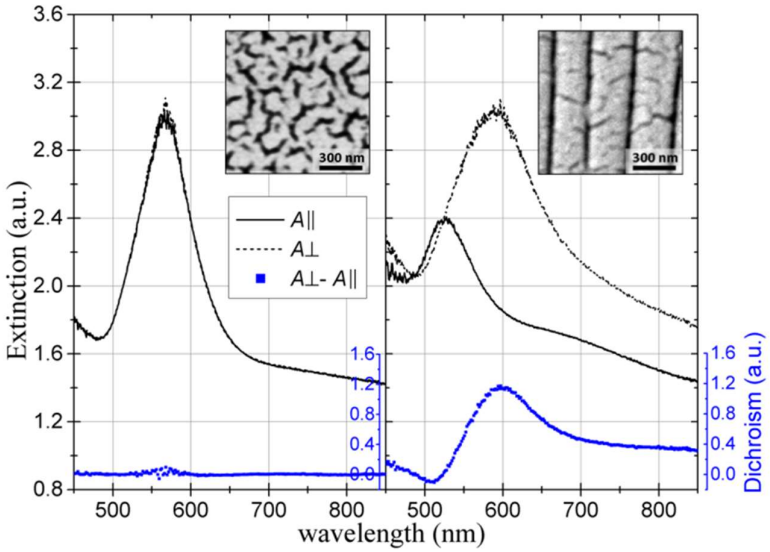

Fig. 4. Extinction (black) and linear dichroism (blue) spectra of 30 nm thickness nano-cracked gold film deposited on pristine (left) and nanostructured (right) silica substrate. The probing light was polarized parallel (black-dotted) and perpendicular (black-solid) to the orientation of nanogratings. Insets show the SEM images of the surface patterns; scale bar is 300 nm.

Characteristics of the fabricated surface nanogratings are dependent on many laser material processing parameters, e.g. pulse energy, pulse duration, laser repetition rate, focusing conditions, etc. [19]. Additionally, the post-processing of the laser nanostructured surfaces can be employed towards the engineering of optical properties of deposited materials. With the increase of KOH etching time up to 12 hours, the ratio of the transmitted parallel and perpendicular polarized light at 600 nm wavelength increases up to 25 times, as shown in Fig. 5.

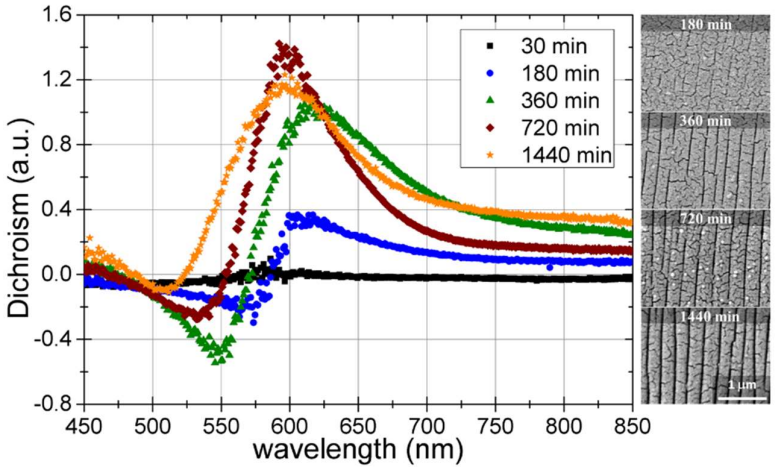

Fig. 5. Dichroism spectra of nano-cracked gold films deposited on nanostructured silica glass as a function of KOH etching time. SEM images on the right show the corresponding surface topographies resulted after 180, 360, 720 and 1440 minutes of the total etching time. Scale bar is 1 μm.

In Figure 5, SEM images confirm that the longer etching time is used, the deeper and wider grooves are formed which directly could affect the morphology of deposited films. The maximum width of ~30 nm and depth of ~4 μm were estimated. After 0.5 hours of etching, the resonance peaks at 580 nm with the 2.8 extinction was measured for two perpendicular polarizations. When the nanogratings are being etched more, these resonance peaks shift to the blue and red spectral range for parallel and perpendicular polarizations, respectively. After 3 hours of etching, peaks are at 580 nm and 595 nm with measured ~2.8 extinction for both polarizations; after 6 hours, at 553 nm and 595 nm with measured ~3 extinction for both polarizations; after 12 hours, at 547 nm and 591 nm with measured 2.8 and 3.5 extinction; and after 24 hours, at 525 nm and 590 nm with measured ~2.4 and ~3 extinction. So, after the total 24 hours of etching, the separation of resonance peaks in the extinction spectrum is maximized with of roughly 65 nm. However, the maximum extinction is measured after 12 hours. Thus the measured dichroism peaks out at 1.4 after 12 hours and decreases to 1.2 after 24 hours of etching (Fig. 5). This could be the result of relatively perfect geometry (depth/width) of silica nanogratings for the efficient light coupling with deposited metallic nanostructures.

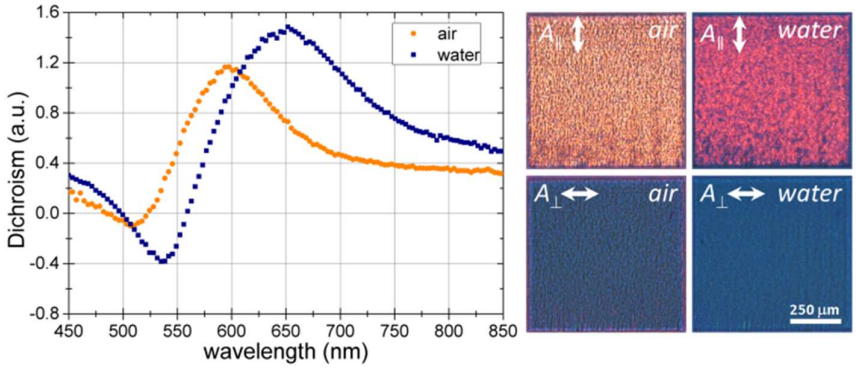

Fig. 6. Dichroism spectra (left) and optical transmission images (right) of nano-cracked gold films deposited on nanostructured silica glass as a function of immersion medium. Arrows indicate the orientation of linearly polarized incident light. Scale bar is 250 µm.

The dichroic element, made of silica nanogratings etched for 24 hours, was implemented for the bulk refractive index sensing experiments (Fig. 6). After immersing the metallic surface into the distilled water, the resonance peaks shifted from 525 nm to 544 nm and from 590 nm to 632 nm for parallel and perpendicular polarizations, respectively; and the extinction increased from 2.4 to 2.7 with the background drop from 1.75 to 1.48 (at 650 nm wavelength) for parallel polarization. As a result, the separation of resonance peaks in the extinction spectrum is increased from 65 nm to 88 nm. And if we estimate the sensitivity, i.e. the resonance shift per unit of refractive index (RIU), we get ~60 nm/RIU for parallel polarization, ~140 nm/RIU for perpendicular polarization, and ~170 nm/RIU for linear dichroism, where the maximum peak shifts from 600 nm to 650 nm (Fig. 6(left)). The resonance shift changes the color of fabricated element as it is shown in optical transmission images in Fig. 6(right).

4. Conclusions

In conclusion, we have demonstrated a multi-step fabrication technique for polarization sensitive plasmonic elements. The ultrafast laser nanostructuring assisted KOH etching was implemented to fabricate silica surface nanogratings. Further incorporation of silica nanogratings with the deposited thin gold films, have shown the strong separation of resonance frequencies for two different polarizations. This technique with the high precision laser-direct writing could be used to make templates for virtually any profile plasmonic patterns where the high polarization sensitivity is required.

Acknowledgments

The study has been supported by EPSRC (grant EP/M029042/1). The data for this work is accessible through the University of Southampton Institutional Research Repository (dx.doi.org/10.5258/SOTON/400341).

Paper C

M. Gecevičius, R. Drevinskas, M. Beresna, and P. G. Kazansky

Single beam optical vortex tweezers with tunable orbital angular momentum

Applied Physics Letters 104(23), 231110 (2014)

APPLIED PHYSICS LETTERS **104**, 231110 (2014)

Single beam optical vortex tweezers with tunable orbital angular momentum

Mindaugas Gecevičius, Rokas Drevinskas,[a] Martynas Beresna, and Peter G. Kazansky
Optoelectronics Research Centre, University of Southampton, Southampton SO17 1BJ, United Kingdom

(Received 12 April 2014; accepted 19 May 2014; published online 10 June 2014)

We propose a single beam method for generating optical vortices with tunable optical angular momentum without altering the intensity distribution. With the initial polarization state varying from linear to circular, we gradually control the torque transferred to the trapped non-absorbing and non-birefringent silica beads. The continuous transition from the maximum rotation speed to zero without changing the trapping potential gives a way to study the complex tribological interactions. © *2014 AIP Publishing LLC*. [http://dx.doi.org/10.1063/1.4882418]

The optical trapping of microscopic transparent objects has been demonstrated almost three decades ago.[1] Since it was shown that the gradient force can be used in three-dimensional manipulations, the technique has become attractive for numerous of fields in physical and biomedical sciences.[2–6] The light carries linear and angular momentum that can be transferred to the illuminated objects. Angular momentum of the beam is comprised of spin angular momentum (SAM)[7] and orbital angular momentum (OAM).[8] SAM is associated with the polarization of the light and is always intrinsic.[9] It can be used to rotate absorbing or birefringent particles around their axis.[10–13] OAM comes from the azimuthal phase variation of the beam. It was demonstrated that the beam with helical phase $\varphi = l\phi$, where φ is phase, ϕ is polar angle, and l is positive or negative integer number, possess well-defined OAM with $l\hbar$.[8] Such beams frequently referred to as optical vortices enable the rotation of transparent non-birefringent particles[14] and the rotation can be both extrinsic or intrinsic.[9] The ability to tune the angular momentum adds an extra degree of control to optical systems and has applications ranging from atomic manipulation[15,16] to quantum information processing.[17,18]

The transfer of total angular momentum to the trapped particles can be accomplished in several ways. Some methods involve beams without orbital momentum when the intensity distribution or the linear polarization of the beam is actively rotated in order to torque objects.[13,19,20] By changing the state of polarization, the average spin momentum of the photon is changed and therefore, the rotation speed of the particle can be controlled.[11,12,21] Furthermore, without introducing elliptical or linear polarizations, the transferred torque might be tuned by two counter-propagating waves of orthogonal circular polarization.[22–24]

The control of OAM is more complicated. The change of wavefront helicity affects the geometry of the beam: the higher $|l|$, the larger diameter of the beam. As a result, the angular momentum of the beam can be defined either by the shape of the beam or by the photon density, which makes the approach limited for the task that requires a constant gradient of the intensity and tunable angular momentum. OAM of the beam can be controlled using a spatial light modulator by generating and superimposing two optical vortices with opposite handedness[25] or generating fractional vortices.[26] However, the polarization of two vortices is the same and leads to an interference fringe pattern while in the partial vortices case, the beam does not have a symmetric donut shape. Other approaches introduce azimuthal phase gradients in holographic rings.[27] However, this method is limited to the range of rotation speed that is quantized and possesses azimuthal intensity gradient variations.

Here, we propose an alternative method of generating optical vortices with gradually controlled OAM, which does not have previously mentioned limitations. We used a superstructured half-wave plate polarization converter, referred to as the S-waveplate.[28] Such a converter is usually used to generate beams with radial/azimuthal polarization distributions. It is also known that such an optical element can be exploited to generate optical vortices.[28,29] In this Letter, we demonstrate the continuous control of an orbital angular momentum by controlling the spin angular momentum of the input light. We also show that it does not affect the shape of the beam and can be used as an optical tweezer with tunable torque.

The operation of the S-waveplate can be described by Jones calculus. The matrix for the S-waveplate is as follows:

$$M_S = \begin{pmatrix} \cos\phi & \sin\phi \\ \sin\phi & -\cos\phi \end{pmatrix}, \tag{1}$$

where ϕ is a polar angle in the polar coordinate system. If left-handed (right-handed) circularly polarized light is transmitted through the S-waveplate, right-handed (left-handed) circularly polarized right-handed (left-handed) optical vortex is generated

$$\vec{E}_{LV} = M_S \begin{pmatrix} 1 \\ -i \end{pmatrix} = e^{-i\varphi} \begin{pmatrix} 1 \\ i \end{pmatrix}. \tag{2}$$

A spatially variant phase factor in the exponential part indicates the presence of an optical vortex with the topological charge $|l| = 1$, where a sign of l depends on the handedness of the input polarization.

Each photon of circularly polarized light carries SAM of $S = s\hbar$, where $s = \pm 1$. In the case of optical vortices, the optical momentum is contributed by OAM with $L = l\hbar$. Positive l corresponds to right-handed optical vortex and negative to

[a]Author to whom correspondence should be addressed. Electronic mail: rd1c12@orc.soton.ac.uk

left-handed. The S-waveplate changes the incident photon spin momentum $-S$ to S and transfers orbital momentum L to the light.

The electric field of any linearly or elliptically polarized light can be expressed as the superposition of left- and right-handed circular polarizations. In the case of elliptically polarized light, at the output of the S-waveplate two optical vortices with opposite handedness circular polarization and opposite handedness of the helical phase are produced. The overall effect of the S-waveplate on the light can be expressed as

$$(\alpha|\uparrow\rangle + \beta|\downarrow\rangle)\,|0\rangle \xrightarrow{S\text{-}waveplate} \beta|\uparrow, R\rangle + \alpha|\downarrow, L\rangle, \tag{3}$$

where $|\uparrow\rangle$ and $|\downarrow\rangle$ are up and down spin states of light, $|\mathrm{R}\rangle$ and $|\mathrm{L}\rangle$ are right and left orbital state of light. Coefficients α and β describing the state of the orbital angular momentum are same as for the spin state of light entering the S-waveplate (Fig. 1(c)). The average OAM transferred to light depends on the angle of orientation of the quarter-wave plate

$$\langle L_{out}(\theta)\rangle = -\langle S_{in}(\theta)\rangle. \tag{4}$$

In the case of linearly polarized light when the spin momentum of the photons is zero, the output is radially or azimuthally polarized light with the zero orbital momentum.

Now, we need to determine the SAM relationship with the angle of the quarter-wave plate which transforms linearly polarized light to elliptically polarized light at the first part of the beam conversion. The electric field can be described as

$$\vec{E}_E = \alpha(\theta)\begin{pmatrix}1\\-i\end{pmatrix}E_0 + e^{i\Delta\Phi}\beta(\theta)\begin{pmatrix}1\\i\end{pmatrix}E_0, \tag{5}$$

where θ is the angle of the quarter-wave plate, $\Delta\Phi$ is the phase difference between two polarizations. The intensity is

$$I_E = A(\theta)I_0 + B(\theta)I_0. \tag{6}$$

After some algebraic operations done by multiplying Jones matrices of a linearly polarized electric field by a quarter-wave plate matrix (Q), left/right handed circular polarizer (L/R), and expressing the intensity of the final electric field, $A(\theta)$ and $B(\theta)$ are expressed by the simple trigonometric functions

$$A(\theta) = \frac{\sin(2\theta)+1}{2}; \quad B(\theta) = \frac{1-\sin(2\theta)}{2}. \tag{7}$$

Now, we can see the dependence of the spin value on the orientation of the quarter-wave plate. The elliptically polarized light transmitted through the S-waveplate produces the superposition of two optical vortices with the opposite topological charges. The amplitude ratio between two vortices will correspond to the ratio between opposite circular polarizations at the input with the elliptically polarized light. The average OAM of the photon transferred by the S-waveplate is

$$\langle L(\theta)\rangle = -\langle S\rangle = -\hbar(A(\theta) - B(\theta)) = -\sin(2\theta)\hbar. \tag{8}$$

As a result, the average OAM value per photon can be not just integer but any real number in the range $[-1\ 1]$ and can be controlled simply by rotating the quarter-wave plate.

In this system, the optical vortex along with the OAM also possesses the SAM. As the particles are transparent and non-birefringent, the rotation is not affected by the SAM. However, if only the OAM is required, the quarter–wave plate inserted in the optical path after the S-waveplate would eliminate the SAM from the beam.

Experimentally, the control of OAM was demonstrated with the optical trapping of fused silica beads (1 μm size) dispersed in aqueous solution. The experiment was performed with a regeneratively amplified diode pumped Yb:KGW

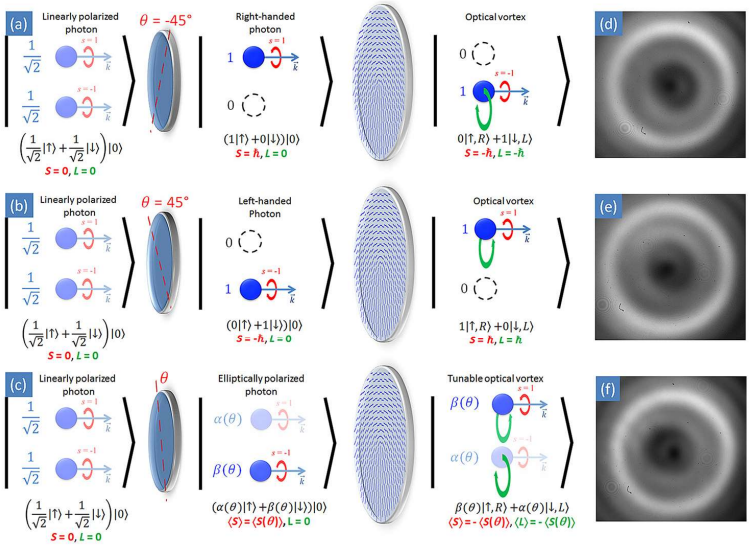

FIG. 1. The transformation of a photon transmitted through a quarter-wave plate and the S-waveplate. Linearly polarized photon passes through the quarter-wave plate (set at the angle θ) and acquires spin momentum depending on the θ value. (a) Light with spin momentum $S = \hbar$ and no OAM (right-handed circularly polarized light) transmitted through the S-waveplate changes spin momentum to $S = -\hbar$ and acquires $L = -\hbar$ (left–handed circularly polarized left-handed optical vortex). (b) Light with spin momentum $S = -\hbar$ (left-handed circularly polarized light) is transformed into the light with the spin momentum $S = \hbar$ and $L = \hbar$ (right-handed circularly polarized optical vortex). (c) Elliptically polarized light with spin momentum $\langle \mathrm{S}(\theta)\rangle$ acquires $\langle \mathrm{L}\rangle = -\langle \mathrm{S}(\theta)\rangle$ and $\langle \mathrm{S}\rangle = -\langle \mathrm{S}(\theta)\rangle$. The measured intensity profiles of left- and right-handed optical vortices (d), (e) and a radially polarized beam (f).

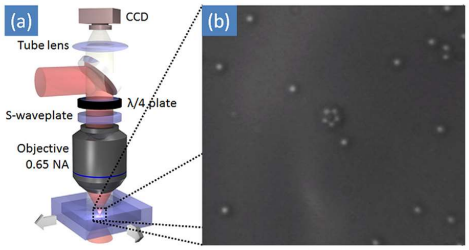

FIG. 2. (a) Experimental trapping setup. (b) The image of five fused silica beads assembled into a ring.

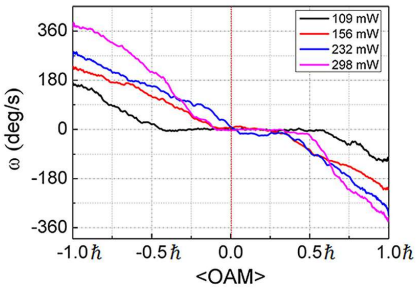

FIG. 4. Rotation speed of trapped beads dependence on the average orbital angular momentum of the photons.

(Yb-doped potassium gadolinium tungstate) femtosecond laser operating at $\lambda = 1030$ nm. The average power was attenuated by a combination of a half-wave plate and Glan polarizer. To avoid the damage of silica beads the power was kept below 300 mW. Additionally, the pulse duration was stretched from 270 fs to 14 ps and the repetition rate set to the maximum (500 kHz) approaching a quasi CW state. The polarization of the laser beam was controlled by the quarter-wave plate mounted on the motorized rotational stage. After the quarter-wave plate, the laser beam passed through the S-waveplate and was focused with a 20× microscope objective (0.65 NA) into the cell filled with colloidal silica beads (Fig. 2(a)). The imaging was implemented by illuminating the sample with white light and recorded using a digital camera (Fig. 2(b)).

The dependence of the torque transferred to silica beads on the OAM was characterized by rotating the quarter-wave plate with a constant angular speed of 0.5 deg/s. As the rotation speed of the quarter-wave plate was kept constant, at any given time the angle of the wave plate was known: $\theta(t) = 45° - 0.5°{\cdot}t$, where the OAM can be calculated from Eq. (8). The rotation speed of the ring was calculated by comparing the adjacent frames n and $n+1$ using the least squares method (Fig. 3). Adding the rotation angles between frames, the total rotation angle dependence on time was obtained and the dependence of the trapped beads rotation speed on the OAM and laser average power finally calculated (Fig. 4).

In the experiment, five SiO_2 beads were observed to arrange in a ring by the optical vortex produced by the S-waveplate. The lowest average power used for trapping silica beads was 109 mW. When the optical axis of quarter-wave plate was set to 45° the beads started rotating counter clockwise indicating the presence of the left handed optical vortex ($l = -1$) (Fig. 3(a)). As expected, the rotation direction could be changed by flipping the handedness of circular polarization (see Eq. (2)). Depending on the average power of the trapping beam the rotation speed of the beads' ring at $l = \pm 1$ varied from 90 deg/s to 360 deg/s. By changing the OAM value from $l = \pm 1$ to zero the rotation was continuously slowing down until it completely halted by the friction forces forming zero speed plateau (Fig. 4).

The overall dynamics of the rotation speed dependence on the OAM and laser average power reflects the behavior of the system in the presence of friction and inertia (Fig. 4). Additionally, the rotation is affected by imperfections of optical trap and irregularities of silica beads. Only at low OAM values all mentioned factors become significant producing strongly asymmetric zero speed plateau. The width of the plateau depends on the laser power as the higher photon density gives stronger OAM per beam at the same OAM per photon. The presence of the inertia and the system imperfections modulates the plateau introducing the dynamic and static asymmetries dependent on the direction of rotation. The observed asymmetry in rotation speed at the $l = -1$ and $l = +1$ decreases with the laser power increase when at the higher velocities the weight of the factors becomes less significant (Fig. 4).

In conclusion, we demonstrate single beam optical vortex tweezer with tunable orbital angular momentum.

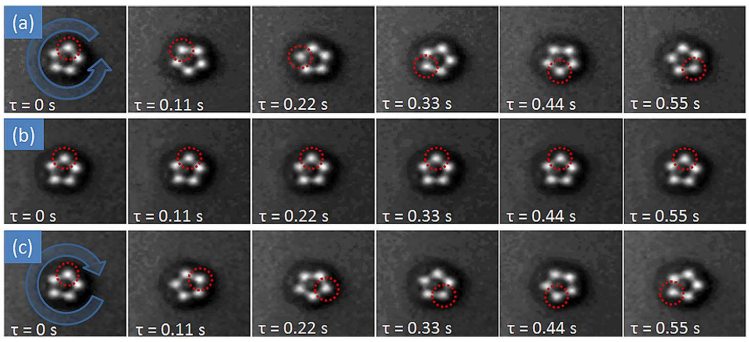

FIG. 3. The rotation of five trapped SiO_2 beads. (a) Particles rotate counter clockwise when polarization before the S-waveplate is right-handed circular. (b) Beads do not rotate when polarization before S-waveplate is linear. (c) Particles rotate clockwise when polarization before the S-waveplate is left-handed circular (Multimedia view) [URL: http://dx.doi.org/10.1063/1.4882418.1].

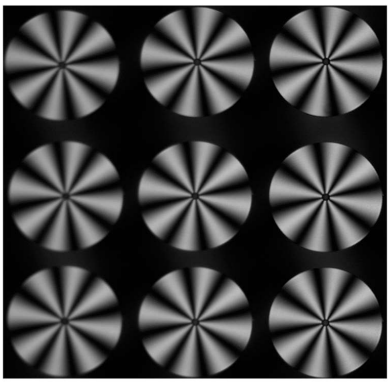

FIG. 5. The array of nine polarization converters. Cross-polarized microscope image shows that the topological charge of converters is four (eight lobes). Such converter can be used in generation of optical vortex with tunable OAM from $\langle L\rangle = -4\hbar$ to $\langle L\rangle = 4\hbar$. The diameter of the converters is 600 μm.

Changing the initial beam polarization, we continuously maximize or completely eliminate the rotation of silica beads ensuring the constant trapping potential. The observed asymmetry in rotation speed proposes a technique for measuring the interaction between trapped objects and its environment. Vortices with tunable OAM may allow precise control of particles rotation of any type materials and bio-objects such as DNA molecules measuring not only it is linear[3] but also rotational response to the system. Furthermore, micro-channel based fluidic systems can be implemented applying complex micro-converter arrays with the maximum achievable rotation speed controlled by the topological charge (Fig. 5).

Authors acknowledge valuable discussions with Etienne Brasselet from Université Bordeaux.

[1]A. Ashkin, M. J. Dziedzic, J. E. Bjorkholm, and S. Chu, Opt. Lett. **11**, 288 (1986).
[2]A. Ashkin, M. J. Dziedzic, and T. Yamane, Nature **330**, 769 (1987).
[3]S. Smith, Y. Cui, and C. Bustamante, Science **271**, 795 (1996).
[4]M. P. MacDonald, L. Paterson, K. Volke-Sepulveda, J. Arlt, W. Sibbett, and K. Dholakia, Science **296**, 1101 (2002).
[5]D. G. Grier, Nature **424**, 810 (2003).
[6]J. Berthelot, S. S. Aćimović, M. L. Juan, M. P. Kreuzer, J. Renger, and R. Quidant, Nat. Nanotechnol. **9**, 295–299 (2014).
[7]R. Beth, Phys. Rev. **50**, 115 (1936).
[8]L. Allen, M. W. Beikersbergen, R. J. C. Spreeuw, and J. P. Woerdman, Phys. Rev. A **45**, 8185 (1992).
[9]A. T. O'Neil, I. MacVicar, L. Allen, and M. J. Padgett, Phys. Rev. Lett. **88**, 053601 (2002).
[10]H. He, M. E. J. Friese, N. R. Heckenberg, and H. Rubinsztein-Dunlop, Phys. Rev. Lett. **75**, 826 (1995).
[11]N. B. Simpson, K. Dholakia, L. Allen, and M. J. Padgett, Opt. Lett. **22**, 52 (1997).
[12]M. E. J. Friese, T. A. Nieminen, N. R. Heckenberg, and H. Rubinsztein-Dunlop, Nature **394**, 348 (1998).
[13]E. Higurashi, R. Sawada, and T. Ito, Phys. Rev. E **59**, 3676 (1999).
[14]K. T. Gahagan and G. A. Swartzlander, Opt. Lett. **21**, 827 (1996).
[15]T. Kuga, Y. Torii, N. Shiokawa, T. Hirano, Y. Shimizu, and H. Sasada, Phys. Rev. Lett. **78**, 4713 (1997).
[16]K.-P. Marzlin, W. Zhang, and E. Wright, Phys. Rev. Lett. **79**, 4728 (1997).
[17]G. Molina-Terriza, J. Torres, and L. Torner, Phys. Rev. Lett. **88**, 013601 (2001).
[18]A. Vaziri, J.-W. Pan, T. Jennewein, G. Weihs, and A. Zeilinger, Phys. Rev. Lett. **91**, 227902 (2003).
[19]L. Paterson, M. P. MacDonald, J. Arlt, W. Sibbett, P. E. Bryant, and K. Dholakia, Science **292**, 912 (2001).
[20]A. T. O'Neil and M. J. Padgett, Opt. Lett. **27**, 743 (2002).
[21]M. Friese, J. Enger, H. Rubinsztein-Dunlop, and N. Heckenberg, Phys. Rev. A **54**, 1593 (1996).
[22]T. Galstyan and V. Drnoyan, Phys. Rev. Lett. **78**, 2760 (1997).
[23]E. Brasselet and T. Galstian, Opt. Commun. **186**, 291 (2000).
[24]M. Funk, S. J. Parkin, A. B. Stilgoe, T. A. Nieminen, N. R. Heckenberg, and H. Rubinsztein-Dunlop, Opt. Lett. **34**, 139 (2009).
[25]C. H. J. Schmitz, K. Uhrig, J. P. Spatz, and J. E. Curtis, Opt. Express **14**, 6604 (2006).
[26]S. Tao, X.-C. Yuan, J. Lin, X. Peng, and H. Niu, Opt. Express **13**, 7726 (2005).
[27]Y. Roichman, B. Sun, Y. Roichman, J. Amato-Grill, and D. Grier, Phys. Rev. Lett. **100**, 013602 (2008).
[28]M. Beresna, M. Gecevičius, and P. G. Kazansky, Opt. Mater. Express **1**, 783 (2011).
[29]E. Karimi, S. Slussarenko, B. Piccirillo, L. Marrucci, and E. Santamato, Phys. Rev. A **81**, 053813 (2010).

Paper D

R. Drevinskas, and P.G.Kazansky

High-performance geometric phase elements in silica glass

Manuscript in preparation

High-performance geometric phase elements in silica glass

Rokas Drevinskas, and Peter G. Kazansky

Optoelectronics Research Centre, University of Southampton, Southampton, SO17 1BJ, United Kingdom

Rokas Drevinskas: R.Drevinskas@soton.ac.uk
Peter G. Kazansky: pgk@soton.ac.uk

Corresponding author: Rokas Drevinskas R.Drevinskas@soton.ac.uk, +44 23 8059 3924

ABSTRACT

We demonstrate direct-write ultrafast laser nanostructuring of silica glass resulting in space-variant dielectric metasurfaces embedded in bulk with continuous phase profiles of nearly any optical components achieved solely by the means of geometric phase. Complex designs of half-wave retarders with 90% transmission at 532 nm and >95% transmission at >1 μm, including polarization gratings with efficiency nearing 90% and computer generated holograms with phase gradient of ~0.8π rad/μm, were fabricated. We also demonstrate a vortex half-wave retarder generating single beam optical vortex with tunable orbital angular momentum of up to ±100ħ. The damage threshold of silica elements being as high as $LIDT_{1\text{-on-}1}$ = 26.25 ± 3.15 J/cm² (1064 nm, 3.5 ns, 10 Hz) enables simultaneous optical manipulation of large number of micro-objects using high-power laser beams. Thus, the continuous control of torque without altering the intensity distribution was implemented in optical trapping demonstration with a total of 5 W average power, which is otherwise impossible with alternate beam shaping devices. In principle, the direct-write technique can be extended to any transparent material that supports laser assisted nanostructuring, and can be effectively exploited for the integration of printed optics into multi-functional optoelectronic systems.

Keywords: Femtosecond phenomena; Materials processing; Form birefringence.

INTRODUCTION

Conventional optics manipulates the properties of light via optical path difference by controlling thickness or refractive index of material. Despite decade–long expertise in fabrication of optical components, precision and quality still remains a challenging problem. The recent advances in flat optics have challenged the limitations of conventional optics by implementing ultrathin planar elements that instead of rely on dynamic phase manipulates light waves via subwavelength-spaced phase shifters with spatially varying phase response.[1,2] Various phase profiles of nearly any optical components ranging from lenses, gratings and vortex-phase plates to elements capable of bending the light in unusual ways have been demonstrated using plasmonic metasurfaces,[3,4] or dielectric gradient metasurfaces[5–9] referred to as geometric phase (Pancharatnam-Berry phase[10–12]) optical elements and realized by space-variant polarization manipulations.[13]

One of the approaches for designing geometric phase elements is to exploit the transparent dielectrics which originate form birefringence. Thus the desired phase pattern of the wave is directly encoded in the optical axis orientation, and is equal to twice the rotation angle of the local retarder. However, despite the numerous techniques enabling the manufacturing of high-efficiency elements,[6,14–18] the limited technological flexibility and low material durability, e.g. liquid crystals with damage threshold of 0.2 J/cm², prevents these elements from being widely integrated in consumer electronics or high-power laser applications. Here we propose a direct-write ultrafast laser nanostructuring of silica glass as an alternative method capable of fabricating geometric phase optics. The key advantage of using femtosecond pulses for direct laser writing, as opposed to longer pulses, is that they can rapidly deposit energy in solids with high-precision. The light is absorbed and the optical excitation ends

before the surrounding lattice is perturbed, which results in highly localized nanostructuring without collateral material damage.[19,20]

A decade ago, the formation of self-organized subwavelength periodicity structures, referred to as nanogratings, in the bulk of silica glass after irradiation with ultrashort light pulses was observed.[21,22] Such a periodic assembly behaves as a uniaxial birefringent material with optical axis oriented parallel to the polarization of incident laser beam. The birefringence value of these thermally stable nanostructures is negative ($\Delta n \approx -4\times10^{-3}$) and of the same order as the natural birefringence of uniaxial crystals such as quartz, ruby and sapphire.[23] As a result, these modifications serve as a perfect candidate for designing phase optics. A number of optical elements including Fresnel zone plates,[24] dynamic phase holograms,[25–29] polarization diffraction gratings and polarization converters[7,30] have been demonstrated. In this work we leverage the potential implementations of silica nanogratings as the geometric phase manipulating elements.

We fabricate complex designs of half-wave retarders with up to 90% transmission in visible spectral range, polarization gratings with efficiencies as high as 90%, computer generated holograms with phase gradients of ~0.8π rad/μm, and vortex retarders generating orbital angular momentum of up to $\pm100\hbar$. The highly durable silica nanostructures enable the demonstration of simultaneous optical manipulation of large number of micro-objects using high-power laser beams.

ENGINEERED MATERIALS AND METHODS

Our experiments were carried out with a ytterbium doped potassium gadolinium tungstate (Yb:KGW) based mode-locked regenerative amplified femtosecond laser system PHAROS (Light Conversion Ltd.) operating at a wavelength of 1030 nm with the pulse duration fixed at 300 fs to 600 fs. The laser beam was focused with a 0.16 NA to 1.2 NA objective lens 300 μm below the surface of a fused silica substrate, which was mounted onto a XYZ linear air-bearing translation stage (Aerotech Ltd.). Laser repetition rate and sample translation speed varied from 20 kHz to 200 kHz and 0.02 mm/s to 2 mm/s ensuring the pulse density higher than 1×10^5 pulses/mm.

Typically, silica nanogratings with periodicity of ~300 nm and duty cycle of roughly 10% of the nano-planes oriented perpendicular to the polarization are formed. The thickness of structures diverges from several microns to tens of microns depending on the numerical aperture of the objective used for printing. Then the retardance is defined as $\varphi = h(n_e - n_o)\,2\pi/\lambda = h\Delta n\,2\pi/\lambda$, where h is the thickness, n_e, n_o – extraordinary and ordinary effective refractive indices, and λ is the probing wavelength. Multiple layers of scanned lines with the interline distance of 1 μm using fixed pulse energy were printed in order to achieve the target phase retardation. The pulse energies used in experiments were kept below 2 μJ.

Local orientation of nanogratings, i.e. the azimuth of slow-axis of laser induced form birefringence, $A(x,y)$ (Fig. 1(a)), was continuously controlled by rotating the half-wave plate, $\theta(x,y)$, mounted on the motorized rotational stage before the objective lens. The local azimuth of slow-axis of imprinted element is expressed as,

$$A(x,y) = 2\theta(x,y) - \pi/2, \tag{1}$$

where the orientation of the half-wave plate corresponds to the orientation of the polarization of the incident linearly polarized laser beam used for silica modification, and the azimuth-offset of $\pi/2$ occurs due to the nanogratings orientation, which is always perpendicular to the incident polarization. As a result, phase profiles of complex geometric phase (GP) elements were imprinted; and the circularly polarized light transmitted through the elements experiences the relative phase change equal to $\phi(x,y) = \pm 2A(x,y)$, where the sign is defined by the handedness of the input polarization.

The imprinted elements were optically characterized with the VIS/NIR micro-spectrometer CRAIC (integrated in Olympus BX51) and the quantitative birefringence measurement system CRi Abrio (integrated in Olympus BX51) operating at 546 nm wavelength. Nd:YAG cw laser (Spectra-Physics) frequency-doubled to 532 nm and supercontinuum fiber laser (Fianium) emitting a broad optical spectrum in the range of 450-950 nm were used to characterize the Gaussian beam propagation through the imprinted GP elements. Optical trapping experiments were performed with Nd:YVO_4 picosecond laser system (Rapid, Coherent Inc.) operating at a wavelength of 1064 nm with the pulse duration of 10 ps and repetition rate of 640 kHz

(burst of 31 pulses with 50 MHz). Imaging of laser-induced nanogratings was performed with a scanning electron microscope (Zeiss Evo50), after the characteristic topography was revealed during the lapping/polishing and KOH (1 mol/L) etching procedures.

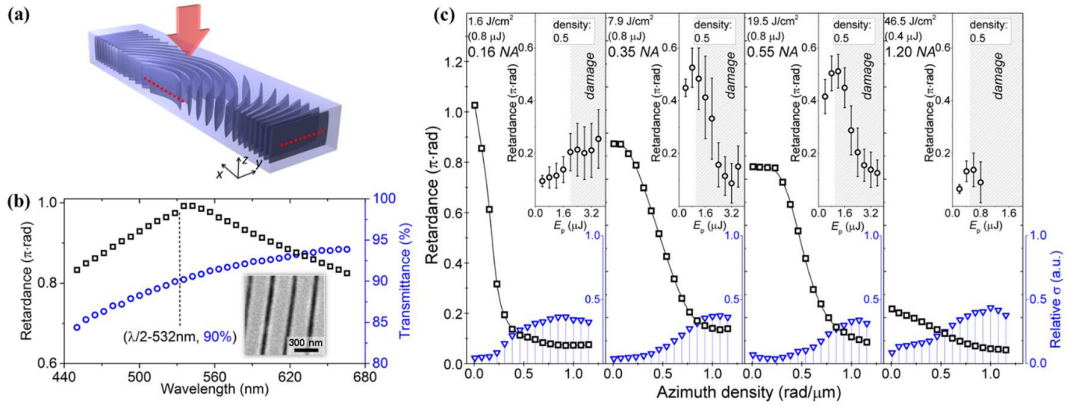

Figure 4. Ultrafast laser nanostructuring of silica glass. (a) Graphical visualization of engineered anisotropy inside a slab of transparent medium. Red dotted lines indicate the azimuth of slow-axis of induced form birefringence. (b) Phase retardation (□) and optical transmission (○) spectra of imprinted half-wave retarder tuned for 532 nm wavelength. Inset: electron microscopy generated image showing the characteristic topography of nanogratings. Scale bar is 300 nm. (c) Induced phase retardation as a function of various processing conditions such as azimuth density of the slow-axis rotation (□), pulse energy (◌̲, insets) and numerical aperture (left to right: 0.16–1.2 NA). Blue open triangles (▽) show the relative standard deviation of the measured retardation value as a function of azimuth density of slow-axis rotation. The azimuth density experiments were performed at a fixed pulse energy of 0.8 μJ for 0.16 NA, 0.35 NA and 0.55 NA, and 0.4 μJ for 1.2 NA; and the pulse energy experiments were performed at a fixed azimuth density of 0.5 rad/μm. The retardation measurement system was operating at 546 nm wavelength.

The dispersion analysis performed in the spectral region from 440 nm to 680 nm revealed a chromatic behavior of the wave plates tuned for 532 nm (Fig. 1(b)). The retardation value varies from 0.8·π to π, and less than 5% variation in retardance is observed in the spectral region from 512 nm to 572 nm wavelength. The transmission coefficient at 532 nm, where the phase retardation is about 0.99π, is roughly of ~0.9 (Fig. 1(b)). Despite the negligible linear absorption of silica, the transmission follows the $\sim\lambda^{-4}$ dependence, which is related to the scattering of subwavelength structure (Fig. 1(b, inset)). The higher transmission can be achieved at longer wavelengths where lower scattering is expected. This gives around 96% of transmission at 1064 nm.

When designing GP elements by laser direct writing, it is important to ensure the continuity of imprinted nanogratings. If the phase gradient is introduced, the local fields as well as the induced structures are perturbed by the previously printed structure. Thus, the induced retardance value drops with the increase of azimuth density of slow-axis rotation (Fig. 1(c)). The effect is strongly dependent on the focusing conditions. If the azimuth density increases up to 0.5 rad/μm, the average retardance value drops by 9.5 times for 0.16 NA, 1.86 times for 0.35 NA, 1.67 times for 0.55 NA, and 1.75 times for 1.2 NA (water immersion), with the corresponding increase in the relative standard deviation by 6 times, 2.8 times, 1.4 times, and 2.5 times, respectively. Even the energy control does not provide a way around this, as the retardance drops due to the material damage observed slightly above the pulse energies of 1.6 μJ for 0.16 NA, 0.8 μJ for 0.35 NA and 0.55 NA, and 0.4 μJ for 1.2 NA. This indicates that to achieve the target retardation the thickness of the structures has to be increased. Therefore, for most of the experiments done in this work a 0.55 NA objective lens in combination with a multilayer printing approach was implemented.

The azimuth density of the slow-axis rotation affects not only the retardance value but also the quality of phase profile. Under the processing conditions reported in this work, the maximum achieved azimuth density, which sufficiently follows the linear-phase profile, is roughly of 0.4π rad/μm (Fig. 2). This corresponds to the phase

density of 0.8π rad/μm, which brings printed optics to the next level allowing high-density GP elements such as vortex retarders with diameter of 10 mm generating optical vortices with topological charge as high as 10k.

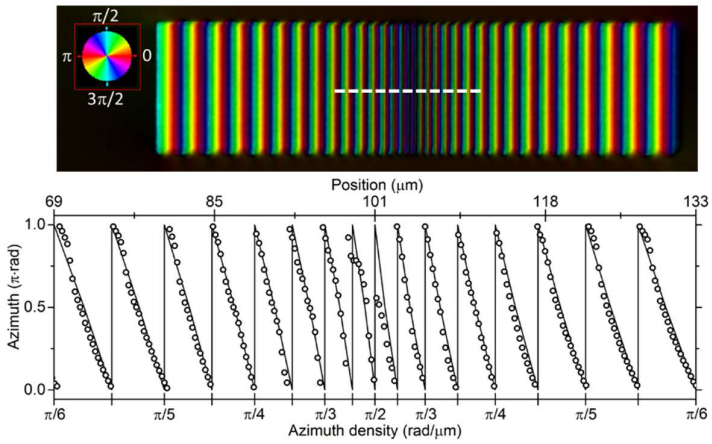

Figure 2. Azimuth of the slow-axis of a laser induced form birefringence dependence on its rotation density. Top image – the azimuth of the slow-axis of the imprinted linear-phase element with the density varying from 0.05π rad/μm to 0.5π rad/μm; bottom graph – the profile (white dashed line in top image) of azimuth of the slow-axis extracted from the birefringence image. Pseudo colours (inset in top image) indicate the local orientation of the slow-axis. The birefringence measurement system was operating at 546 nm wavelength.

RESULTS AND DISCUSSIONS

The laser material processing conditions used to print GP elements were chosen to attain the maximum quality of structures, based on the experimental data from Fig. 1 and Fig. 2. The parameters window for laser-induced nanogratings is very large and is chosen for each application separately according to the target diameter, processing time, required azimuth density and total losses.

The blazed polarization grating (PG) with the geometric phase varying in the x-direction as $\phi(x) = \pm A(x) = \pm(2\pi/a)x|_{\mathrm{mod}\,2\pi}$ was printed inside silica glass (Fig. 3(a, b)). The periodicity of the PG was set to a = 60 μm. For an incident plane wave with the polarization state $|E_{in}\rangle$ the resulting field generated by the PG is $|E_{out}\rangle = \eta_E|E_{in}\rangle + \eta_R e^{i2A(x,y)}|R\rangle + \eta_L e^{-i2A(x,y)}|L\rangle$,[31] where the $\eta_E = 1/2\left(t_x + t_y e^{i\varphi}\right)$, $\eta_R = 1/2\left(t_x - t_y e^{i\varphi}\right)\langle E_{in}|L\rangle$ and $\eta_L = 1/2\left(t_x - t_y e^{i\varphi}\right)\langle E_{in}|R\rangle$ are the complex field efficiencies with $\langle E_{in}|R, L\rangle$ as an inner product of the left-handed $|L\rangle$ and right-handed $|R\rangle$ circular polarizations, φ is the retardation of the imprinted element, and $t_{x,y}$ are the transmission coefficients for light polarized perpendicular and parallel to the optical axis. The imprinted PG with $t_{x,y} \approx 0.9$ and $\varphi \approx 0.99\pi$ at a central wavelength of 532 nm (Fig. 1(b)) is expected to diffract around 0.9 of the total incident light intensity, while the remaining 0.1 would be scattered. Thus, the efficiency expressed as a ratio of first order diffracted light and total transmitted light, $\eta_{1st} = E_{1s}\ /E_{total}^{(T)}$, would be ~100%. However, the characterization of imprinted PG shows ~10% mismatch (Fig. 3(c, d)). This could be related to the non-uniform retardance value across the PG. Averaged phase retardation of the printed element with the corresponding azimuth density possesses the relative standard deviation of around 7%-10% (Fig. 1(c)). Also, the light wave propagating through the large thickness of structure, i.e. from several microns to tens of microns, could be detuned, and additional alignment of the geometry of stacked layers should be performed.[32] Roughly 90% of the transmitted light is projected to the ±1st order and 10% to the 0th and higher orders (Fig. 3(d)). As the handedness of the diffracted circularly polarized beam is flipped, the polarization filtering could be applied in order to completely eliminate the non-diffracted light.

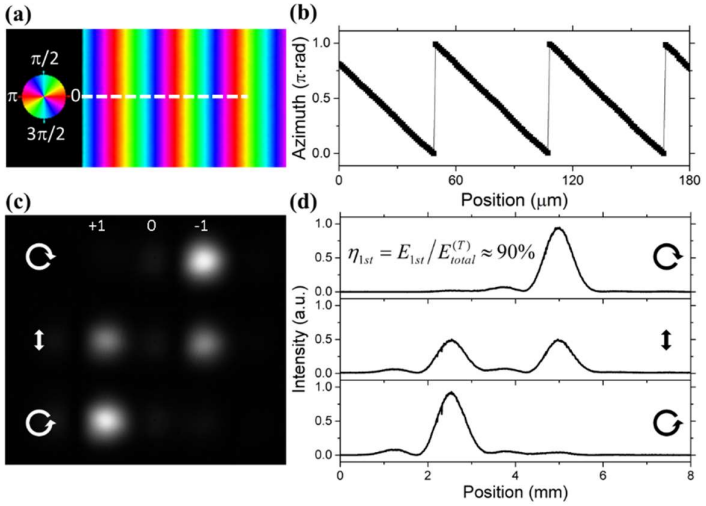

Figure 3. Femtosecond laser direct writing of geometric-phase optical element designed as a blazed polarization grating (PG) with period of 60 μm. (a) Azimuth image of the slow-axis of the imprinted nanogratings; (b) the profile (white dashed line in (a)) of azimuth of the slow-axis extracted from the birefringence image. Pseudo colours (inset) indicate the local orientation of the slow-axis. The birefringence measurement system was operating at 546 nm wavelength. (c) Frequency-doubled Nd:YAG cw laser beam profiles of the transmitted right-handed circular (top), linear (middle) and left-handed circular (bottom) polarizations, and (d) its corresponding intensity profiles with the estimated first order diffraction efficiency. White and black arrows indicate the polarization state of the incident and PG transmitted beams.

High-precision translation and rotation stages synchronized with the laser system enable the complex designs of geometric phase elements such as computer generated Fourier holograms (CGH) that convert the initial Gaussian beam into the target intensity distribution. Using the adapted weighted Gerchberg-Saxton algorithm,[33,34] the 8-bit grayscale CGH element with 0.1 Megapixel and pixel spacing of 1.2 μm was designed to encode the Queen Elizabeth II portrait (Fig. 4). During the continuous writing process, the maximum relative phase change of 0.8π between the two adjacent pixels was achieved. By using the Fourier transforming properties of a positive lens, the target image was reconstructed within the spectral range of 450-950 nm (Fig. 4(c-f)). As it was discussed before, to attain the high-efficiency of an imprinted GP elements, the half-wave retardation must be ensured. However, even if the retardance is below this value, the non-diffracted beam can be completely removed by the means of polarization filtering (Fig. 4(a)). In addition, the geometric phase is independent of wavelength. Therefore, the phase profile for different wavelengths transmitted through the same design will not differ. In this case, the broadband sources can be implemented with a polarization filtering efficiency as high as ~100%.

High-efficiency and independence of wavelength make GP elements attractive for many application areas. For example, taking advantage of sub-micron resolution of ultrafast laser direct writing, vortex half-wave retarders for optical micro-manipulation can be designed.[35] The vortex half-wave retarder, also referred to as polarization converter, which transforms incident linear or circular polarization into radial/azimuthal polarization or optical vortex respectively, was branded as S-waveplate, patented and successfully commercialized several years ago.[7,36] We extend the technology and demonstrate the generation of optical vortices with topological charge of $l = \pm 100$ (Fig. 5). Such elements with the damage threshold being as high as $LIDT_{1\text{-on-}1} = 26.25 \pm 3.15$ J/cm^2 (1064 nm, 3.5 ns, 10 Hz)[36] enable the simultaneous optical manipulation of large number of micro-objects using high-power laser beams.

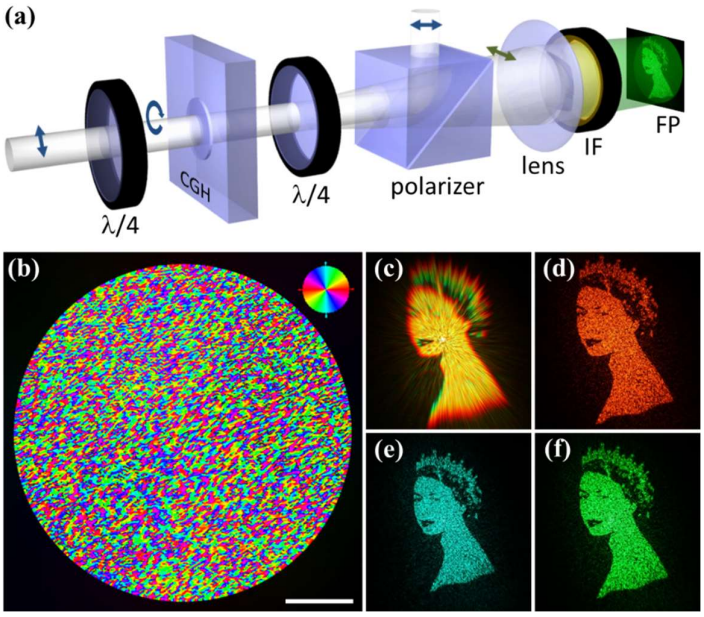

Figure 4. Computer generated geometric-phase Fourier hologram (CGH). (a) Setup for polarization filtering and target image reconstruction: quarter-wave plates (λ/4), laser imprinted 8-bit grayscale CGH, linear polarizer, lens with f = 50 mm, interference filter (IF), Fourier plane (FP). Arrows indicate the state of beam polarization. (b) Orientation of slow-axis of laser-imprinted CGH, and (c-f) it's resulting reconstructed images. Pseudo colours (inset) indicate the local orientation of the slow-axis. The birefringence measurement system was operating at 546 nm wavelength. The hologram was illuminated with (c-f) supercontinuum laser beam, where (c) 450-950 nm, (d) 600 nm, (e) 500 nm and (f) 550 nm filtered wavelengths. Scale bar is 500 μm.

Briefly, the electric field of the linearly or elliptically polarized light can be expressed as a superposition of left- and right-handed circular polarizations. Each photon of circularly polarized light carries spin angular momentum of $S = s\hbar$, where $s = \pm 1$. If these photons are transmitted through the vortex half-wave retarder, the incident spin momentum of S_{in} is changed to $-S_{in}$, and the orbital momentum L is transferred to the light. So, the total angular momentum is contributed by an orbital angular momentum (OAM) with $L = l\hbar$, where l is an integer number (positive or negative). At the output of the retarder, vortices with the two states of opposite handedness circular polarizations and opposite handedness helical phases are generated. Then, the overall state of the beam corresponds to the amplitude ratio of the incident states with the opposite handedness circular polarizations, which can be continuously controlled by the quarter-wave plate. As a result, the retarder generates a circularly polarized vortex beam with the averaged OAM per photon that is controlled by the angle (θ) of the quarter-wave plate:

$$\langle L(\theta) \rangle = c \cdot \langle S(\theta) \rangle = c \cdot sin(2\theta)\hbar, \quad (2)$$

where c is an integer number referred to as a topological charge of the vortex half-wave retarder (corresponds to $q = c/2$), indicating the number of twists in the azimuth of slow-axis by π within the rotation of polar angle by 2π. The sign of the topological charge number is determined by the geometry of the laser processing. If the beam with helical phase $\phi = l\varphi$, where ϕ is phase and φ is polar angle, possesses well-defined OAM with $l\hbar$,[37] then the l can be shown as $l = c \cdot s$, where s is an averaged spin per photon.

Here we demonstrate the printed vortex half-wave retarder with c = -100 (Fig. 5(a)). The retarder is set to have the same topological charge along its radius, thus the azimuth density increases very quickly when the radius is approaching the central point. As a consequence, the relative retardance drops (Fig. 1). Therefore, the center of the element has not been printed and the incident annular vortex beam ($l = \pm 2$) was used to ensure the uniformity

of the phase conversion (Fig. 5(b)). By continuously rotating the quarter-wave, the ring-shaped beams with total OAM from $\langle L \rangle$ = -98$\hbar$ to $\langle L \rangle$ = +98$\hbar$ were generated (Fig. (c)). Thus, continuous control of torque without altering the intensity distribution was implemented in optical trapping demonstration with the total 5 W average laser power (Fig. 5(d)), which would not be possible with alternative beam shaping devices.

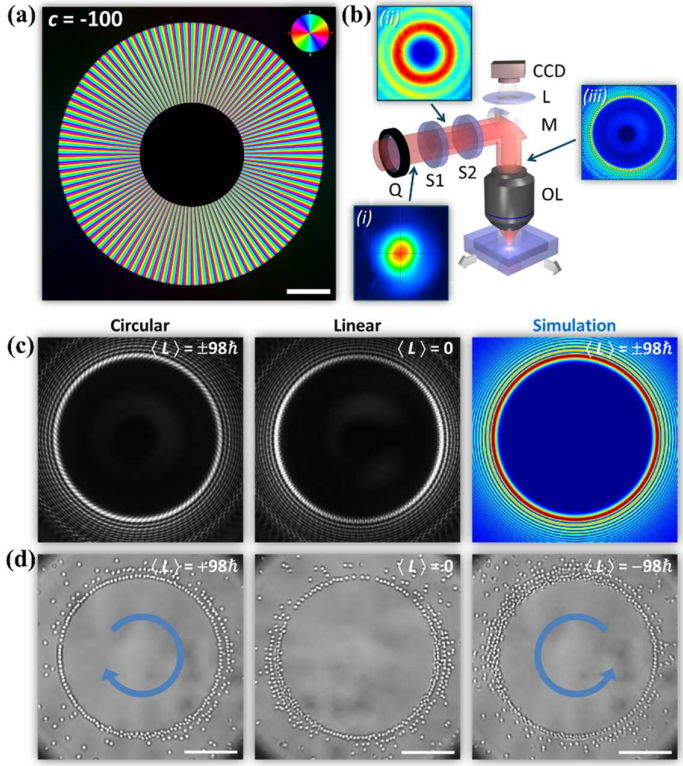

Figure 5. Single beam optical vortex tweezers with continuous control of orbital angular momentum (OAM), where any value from –98$\hbar$ to +98$\hbar$ defined by the angle of quarter-wave plate can be achieved. (a) Geometric-phase based optical vortex retarder with topological charge of c = -100. Scale bar is 200 μm; color bar indicates the orientation of the slow-axis. The birefringence measurement system was operating at 546 nm wavelength. (b) Optical trapping setup. Inset images show the beam profiles measured at the pupil plane of objective lens (OL): (*i*) after the quarter-wave plate (Q); (*ii*) after the Q and vortex retarder (S1) with topological charge of c = –2; and (*iii*) after the Q, S1, vortex retarder (S2) with topological charge of c = -100 and dichroic mirror (M). Micro-manipulation was monitored by projecting the live images via focusing lens (L) on a camera detector (CCD). The trapping setup was tuned for Nd:YVO_4 laser system operating at 1064 nm. (c) Beam intensity distribution measured and simulated at the objective's pupil plane, when the circularly (left and right images) or linearly (middle image) polarized incident Gaussian beam is transmitted through the optical trapping setup. (d) The focused vortex beams with OAM varying from $\langle L \rangle$ = -98$\hbar$ to $\langle L \rangle$ = +98$\hbar$ were used to trap and rotate SiO_2 beads (size of 1μm). Scale bar is 20 μm.

CONCLUSIONS

The high-performance demonstrations of geometric phase elements imprinted in silica glass by direct-write ultrafast laser nanostructuring show the potential of technique for designing functional devices that can be integrated into the real interdisciplinary systems such as high-power lasers, high-resolution microscopy, optical communication systems, polarization sensitive imaging, and consumer electronics. Although the elements demonstrated in this work show slightly poor performance compared to ideal optics, some advantages such as durability and technological flexibility, realizing elements inside transparent solids make the technology

exceptional and free of alternatives. Providing sufficient efficiencies with low losses and high thermal/chemical stability, the printing of multi-layered optical components with different phase profiles embedded in a single slab of silica glass or fiber could enable portable/handheld instruments for many practical applications such as endoscopes, integrated miniature illumination and detection systems.

ACKNOWLEGMENTS

We thank J. Zhang for discussions on computer generated holograms. The study has been supported by EPSRC (grant EP/M029042/1). The data for this work is accessible through the University of Southampton Institutional Research Repository (dx.doi.org/10.5258/SOTON/400343).

AUTHOR CONTRIBUTIONS

RD and PGK conceived, planned, coordinated and supervised the work. RD carried out the experiments and wrote the manuscript. Both authors discussed the results and contributed to the writing of the paper.

REFERENCES

1. Yu N, Capasso F. Flat optics with designer metasurfaces. *Nat Mater.* 2014;**13**:139–150.
2. Khorasaninejad M, Chen WT, Devlin RC, Oh J, Zhu AY, Capasso F. Metalenses at visible wavelengths: Diffraction-limited focusing and subwavelength resolution imaging. *Science* 2016;**352**:1190–1194.
3. Ni X, Emani NK, Kildishev A V, Boltasseva A, Shalaev VM. Broadband Light Bending with Plasmonic Nanoantennas. *Science* 2011;**335**:427.
4. Yu N, Genevet P, Kats M a, Aieta F, Tetienne J-P, Capasso F, et al. Light Propagation with Phase Discontinuities Reflection and Refraction. *Science* 2011;**334**:333–337.
5. Bomzon Z, Biener G, Kleiner V, Hasman E. Space-variant Pancharatnam-Berry phase optical elements with computer-generated subwavelength gratings. *Opt Lett.* 2002;**27**:1141–1143.
6. Miskiewicz MN, Escuti MJ. Direct-writing of complex liquid crystal patterns. *Opt Express* 2014;**22**:12691–12706.
7. Beresna M, Gecevičius M, Kazansky PG. Polarization sensitive elements fabricated by femtosecond laser nanostructuring of glass. *Opt Mater Express* 2011;**1**:783–795.
8. Lin D, Fan P, Hasman E, Brongersma ML. Dielectric gradient metasurface optical elements. *Science* 2014;**345**:298–302.
9. Jahani S, Jacob Z. All-dielectric metamaterials. *Nat Nanotechnol.* 2016;**11**:23–36.
10. Pancharatnam BYS. Generalized theory of interference, and its applications. Part I. Coherent pencils. *Proc Indian Acad Sci A.* 1956;**44**:247–262.
11. Berry M V. Quantal phase factors accompanying adiabatic changes. *Proc R Soc London Ser A*. 1984;**392**:45–57.
12. Anandan J. The geometric phase. *Nature* 1992;**360**:307–313.
13. Bomzon Z, Kleiner V, Hasman E. Pancharatnam-Berry phase in space-variant polarization-state manipulations with subwavelength gratings. *Opt Lett.* 2001;**26**:1424–1426.
14. Meinzer N, Barnes WL, Hooper IR. Plasmonic meta-atoms and metasurfaces. *Nat Phot.* 2014;**8**:889–898.
15. Zheng G, Mühlenbernd H, Kenney M, Li G, Zentgraf T, Zhang S. Metasurface holograms reaching 80% efficiency. *Nat Nanotechnol.* 2015;**10**:308–312.

16. Kim J, Li Y, Miskiewicz MN, Oh C, Kudenov MW, Escuti MJ. Fabrication of ideal geometric-phase holograms with arbitrary wavefronts. **Optica** 2015;**2**:958-964.

17. McManamon PF, Bos PJ, Escuti MJ, Heikenfeld J, Serati S, Xie H, et al. A review of phased array steering for narrow-band electrooptical systems. *Proceeding IEEE* 2009;**97**:1078-1096.

18. Marrucci L, Manzo C, Paparo D. Pancharatnam-Berry phase optical elements for wave front shaping in the visible domain: Switchable helical mode generation. *Appl Phys Lett.* 2006;**88**:221102.

19. Sundaram SK, Mazur E. Inducing and probing non-thermal transitions in semiconductors using femtosecond laser pulses. *Nat Mater.* 2002;**1**:217–224.

20. Gattass RR, Mazur E. Femtosecond laser micromachining in transparent materials. *Nat Photonics* 2008;**2**:219–225.

21. Shimotsuma Y, Kazansky P, Qiu J, Hirao K. Self-Organized Nanogratings in Glass Irradiated by Ultrashort Light Pulses. *Phys Rev Lett.* 2003;**91**:247405.

22. Kazansky P, Inouye H, Mitsuyu T, Miura K, Qiu J, Hirao K, et al. Anomalous Anisotropic Light Scattering in Ge-Doped Silica Glass. *Phys Rev Lett.* 1999;**82**:2199–2202.

23. Bricchi E, Kazansky PG. Extraordinary stability of anisotropic femtosecond direct-written structures embedded in silica glass. *Appl Phys Lett.* 2006;**88**:111119.

24. Bricchi E, Mills JD, Kazansky PG, Klappauf BG, Baumberg JJ. Birefringent Fresnel zone plates in silica fabricated by femtosecond laser machining. *Opt Lett.* 2002;**27**:2200-2202.

25. Cai W, Reber TJ, Piestun R. Computer-generated volume holograms fabricated by femtosecond laser micromachining. *Opt Lett.* 2006;**31**:1836–1838.

26. Papazoglou D, Loulakis M. Embedded birefringent computer-generated holograms fabricated by femtosecond laser pulses. *Opt Lett.* 2006;**31**:1441–1443.

27. Li Y, Dou Y, An R, Yang H, Gong Q. Permanent computer-generated holograms embedded in silica glass by femtosecond laser pulses. *Opt Express* 2005;**13**:2433–2438.

28. Cai W, Libertun A, Piestun R. Polarization selective computer-generated holograms realized in glass by femtosecond laser induced nanogratings. *Opt Express* 2006;**14**:3785–3791.

29. Berlich R, Richter D, Richardson M, Nolte S. Fabrication of computer-generated holograms using femtosecond laser direct writing. *Opt Lett.* 2016;**41**:1752-1755.

30. Gecevičius M, Beresna M, Drevinskas R, Kazansky PG. Airy beams generated by ultrafast laser-imprinted space-variant nanostructures in glass. *Opt Lett.* 2014;**39**:6791–6794.

31. Hasman E, Bomzon Z, Niv A, Biener G, Kleiner V. Polarization beam-splitters and optical switches based on space-variant computer-generated subwavelength quasi-periodic structures. *Opt Commun*. 2002;**209**:45–54.

32. Ng ML, Chanda D, Herman PR. Coherent stitching of light in multilayered diffractive optical elements. *Opt Express* 2012;**20**:23960-23970.

33. Di Leonardo R, Ianni F, Ruocco G. Computer generation of optimal holograms for optical trap arrays. *Opt Express* 2007;**15**:1913–1922.

34. Zhang J, Gecevičius M, Beresna M, Kazansky PG. Seemingly unlimited lifetime data storage in nanostructured glass. *Phys Rev Lett.* 2014;**112**:033901.

35. Gecevičius M, Drevinskas R, Beresna M, Kazansky PG. Single beam optical vortex tweezers with tunable

orbital angular momentum. *Appl Phys Lett.* 2014;**104**:231110.

36. Altechna. S-waveplate (Radial Polarization Converter). Available from: http://www.altechna.com/product_details.php?id=1048

37. Allen L, Beikersbergen MW, Spreeuw RJC, Woerdman JP. Orbital angular momentum of light and the transformation of Laguerre-Gaussian laser modes. *Phys Rev A.* 1992;**45**:8185–8189.

Paper E

J. Zhang, R. Drevinskas, M. Beresna, P. Kazansky

Polarization sensitive anisotropic structuring of silicon by ultrashort light pulses

Applied Physics Letters 107, 041114 (2015)

APPLIED PHYSICS LETTERS **107**, 041114 (2015)

Polarization sensitive anisotropic structuring of silicon by ultrashort light pulses

Jingyu Zhang, Rokas Drevinskas,[a] Martynas Beresna, and Peter G. Kazansky
Optoelectronics Research Centre, University of Southampton, Southampton SO17 1BJ, United Kingdom

(Received 26 May 2015; accepted 24 July 2015; published online 29 July 2015)

Imprinting of anisotropic structures on the silicon surface by double pulse femtosecond laser irradiation is demonstrated. The origin of the polarization-induced anisotropy is explained in terms of interaction of linearly polarized second pulse with the wavelength-sized symmetric crater-shaped structure generated by the linearly polarized first pulse. A wavefront sensor is fabricated by imprinting an array of micro-craters. Polarization controlled anisotropy of the structures can be also explored for data storage applications. © *2015 AIP Publishing LLC*.
[http://dx.doi.org/10.1063/1.4928043]

It is well recognized that tightly focused ultrafast laser pulses can produce localized structural modifications with the precision of tens of nanometers.[1,2] Consequently, femtosecond laser assisted imprinting has been exploited for implementing a high capacity multi-dimensional optical data storage,[3] fabrication of polarization sensitive elements,[4] micro-fluidic channels,[5] and waveguides.[6] The interaction of ultrashort light pulses with materials is defined by multiple parameters, among which polarization plays a significant roles.[7] In particular, the formation of polarization dependent self-assembled periodic nanostructures is commonly observed, either within bulk[8–11] or on surface,[12,13] in the experiments of ultrafast laser direct writing. Another manifestation of the polarization is the anisotropy of near-field distribution produced by the interaction of linearly polarized beam with sub-wavelength structures, which can be revealed via imprinting in photosensitive polymer[14] or ablation of gold nanoparticles.[15] In this letter, we report the polarization sensitive writing with femtosecond double pulse irradiation on the silicon surface. We demonstrate the imprinting of anisotropic near-field pattern, which is produced by the interaction of the linearly polarized second pulse with a symmetric wavelength scale structures generated by the linearly polarized first pulse. The experimental results are supported by numerical simulations of near-field anisotropy of linearly polarized light distribution. We also demonstrate the application of structures imprinted on silicon surface by a single pulse for wavefront sensor fabrication.

Experiments were performed using a mode-locked Yb:KGW ultrafast laser system (Pharos, Light Conversion Ltd.) operating at a wavelength of 1030 nm, 20 kHz repetition rate, and 330 fs pulse duration. Series of dots were printed on the surface of p-type crystalline silicon (111) substrate by either single or double pulse (50 μs time delay between pulses) irradiation with a linear polarization controlled by a zero-order half-wave plate. The laser beam was focused via a 0.65 NA objective lens in the range from 0 to 12 μm above the surface. The pulse energy was varied up to 300 nJ in order to depict a large modification window.

[a]Author to whom correspondence should be addressed. Electronic mail: rd1c12@orc.soton.ac.uk

After laser irradiation, the morphological changes of the surface were characterized using an optical microscope (BX51 Olympus, Inc.), scanning electron microscope (SEM) (Zeiss Evo50), and atomic force microscope (AFM) (Nanonics Multiview 2000).

A smooth and symmetric 150 nm deep crater-shaped structure with a rim was observed after focusing a single 120 nJ (1.35 J/cm^2) pulse 4 μm above the silicon surface (Figs. 1(a)–1(d)). The crater's radius of curvature of 2.69 ± 0.08 μm was estimated from AFM profiles (Fig. 1(c)). Material ejection was not observed at these pulse energies; thus, we assume the structure was formed by a rarefaction (shock) wave, which pushed the molten material from the center to the periphery of the irradiated zone.[16] The light was absorbed by electrons, which afterwards transferred energy to the lattice via electron-phonon coupling resulting in an isotropic heating zone without any collateral damage.[17] During the irradiation with the first pulse, substrate's surface was flat and homogeneous leading to an isotropic near-field distribution. No asymmetry was observed in the crater-shaped structures induced by a single pulse at any of six different orientations of linear polarization.

The isotropic crater structures with their smooth surface can be implemented as a mold for microlens fabrication or itself can be employed as an optical microreflector with a focal length of 1.345 ± 0.04 μm (Fig. 1(c)). To demonstrate this, the sample was examined under an optical microscope in the reflection mode, when the illumination was partly blocked by an aperture. While moving the focal position of the microscope objective, we could clearly see the rectangular aperture imaged by the microreflector (Fig. 1(d)). The array of 5×5 microreflectors was imprinted on the silicon surface (Fig. 2) and implemented as a wavefront sensor.[18] After examining the shape of each crater shown in Fig. 2(a), the position of the geometrical focus was estimated. Tracking the lateral displacement of the imaged aperture (Fig. 2(b)), the map indicating the wavefront of illumination was extracted (Fig. 2(c)).

Unexpectedly, we observed a completely different modification with the double pulse structuring of the sample. Here, an anisotropic transformation of the modified region was observed with the formation of several peculiar features (Figs. 1(e)–1(h)). First, in the middle part of the crater, two enhanced modification zones oriented perpendicular to the

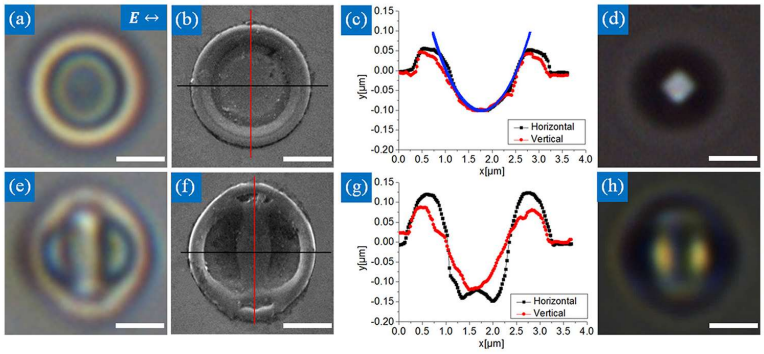

FIG. 1. Silicon structures induced by linearly polarized single pulse (a)–(d) and double pulse (e)–(h) femtosecond laser irradiation. (a) and (e) Optical reflection and (b) and (f) topological SEM images, as well as (c) and (g) AFM profile scans were performed after the first and second pulses; the blue line is the fitting curve for the surface curvature with R = 2.7 μm. Pulses with the energy of 120 nJ were focused 4 μm above the silicon surface (1.35 J/cm^2). *E* indicates the polarization state of the pulse. The images in (d) and (h) represent the microscope aperture imaged using the laser-induced structures shown in (a) and (e), respectively. The scale bars: 1 μm.

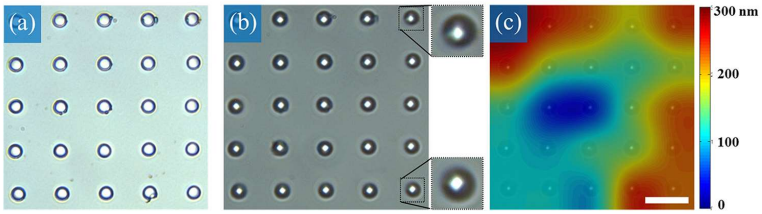

FIG. 2. Silicon microreflectors array induced by single femtosecond laser pulses. Optical reflection images were taken (a) without and (b) with microscope aperture inserted in front of the illumination source. (c) The focal point displacement map caused by the wavefront of illumination was extracted from (a) and (b) images. The scale bar is 10 μm.

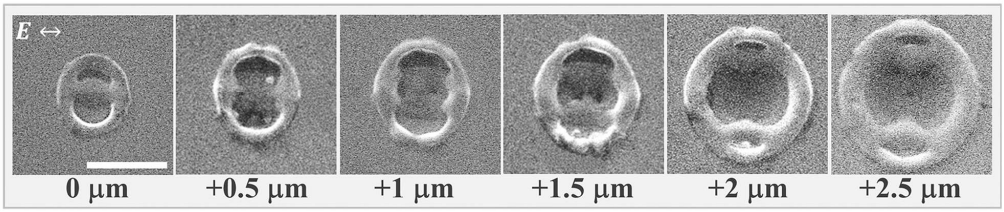

FIG. 3. SEM images of the linearly polarized double pulse modification induced at different focusing positions varying from 0 μm to 2.5 μm above the surface. The pulse energy was fixed at 15 nJ (0.27–0.47 J/cm^2). Scale bar is 1 μm.

light polarization were induced. As a result, a bridge-like structure with a height of roughly 25 nm was formed (Figs. 1(e)–1(g)). The orientation of the bridge was perpendicular to the polarization and located in the center of the modified region (Fig. 1(e)). Second, the rim was deformed at the tips of the bridge slightly elongating the crater shape (Fig. 1(f)). The crater depth along the direction parallel to the beam polarization was increased by more than 80%, while along the perpendicular direction only by 30% (Fig. 1(g)). The two induced lobes located inside the crater were functioning as twin microreflectors (Fig. 1(h)).

The shape of the structure was changing significantly when the laser beam was defocused (Fig. 3). The bridge was either merging or separating depending on the beam focal position. If the double pulse laser beam was focused on the surface, the bridge-shape structure oriented parallel to the polarization direction was produced (Fig. 3, left), whereas the structure similar to the one in Fig. 1(f) emerged when the focus of the beam was above the sample surface (Fig. 3, right).

The wavelength-sized polarization sensitive structures on silicon surface may find applications for the polarization-multiplexed optical memory. The size and orientation of the structure can be independently manipulated by the energy of

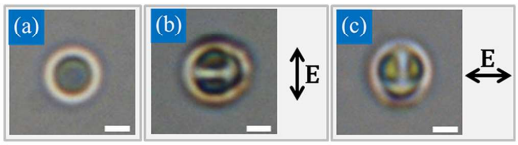

FIG. 4. Optical microscope images of the silicon surface modified with (a) single and (b) and (c) writing pulses with two different polarizations indicated by arrows. Pulses with the energy of 40 nJ (0.77 J/cm^2) were focused at 2.5 μm above the surface. The scale bars: 1 μm.

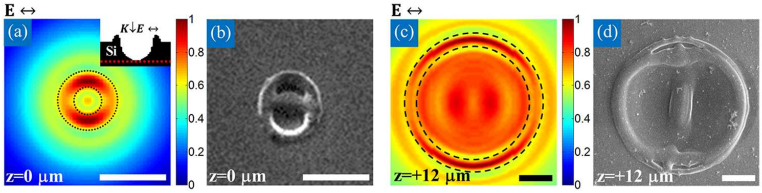

FIG. 5. (a) and (c) Calculated total electric near-field distribution of the light propagating through an isotropic crater-shape silicon structure, and (b) and (d) its subsequent polarization sensitive modification measured by SEM. The double pulse laser beam was focused at (a) and (b) 0 μm and (c) and (d) 12 μm above the substrate surface with the pulse energies of 15 nJ (0.47 J/cm^2) and 300 nJ (0.55 J/cm^2), respectively. The dashed black lines in (a) and (c) indicate the contours of crater-shape pattern used for the calculations. Insets in (a) show the geometry of the pattern used to mimic the conditions during the second pulse irradiation. The dashed red lines—planes of the near-field monitoring. The scale bars: 1 μm.

the first pulse and polarization of the second pulse, respectively. Assuming that the shorter wavelength should produce proportionally smaller structures with the same polarization dependence, we estimated that by recording data with wavelength of 300 nm, a CD-sized disc with the capacity of 36 GB can be achieved (0.5 μm between track pitches, 6 bits polarization-multiplexed data resulting from 64 polarization states between 0° and 180°, and 2 bits power-multiplexed data per structure). The read-out technology could be implemented by monitoring the intensity of the linearly polarized laser beam, when the reflected light is modulated (Fresnel conditions) by the surface morphology. The modulation in intensity and polarization could be detected using a quadrupole detector, which is already exploited in the traditional optical data storage read-out.

In addition, experiments were performed to demonstrate the multilevel polarization sensitive encoding on silicon surface (Fig. 4). First of all, the isotropic craters were imprinted by the single pulse irradiation (Fig. 4(a)). Later, during the encoding stage, the subsequent irradiation with different states of polarization of the writing beam was used to control the orientation of anisotropy of the imprinted structures (Figs. 4(b) and 4(c)). The slight asymmetry of the patterns in the direction perpendicular to the polarization could be explained by the displacement of the focal spot during the polarization rotation.

For the theoretical analysis, the corresponding total near-field distribution was obtained simulating the propagation of the focused second pulse through a symmetric crater-shape structure pre-defined by the first pulse (Fig. 5). A commercial-grade simulator (Lumerical) based on the finite-difference time-domain (FDTD) method was used to perform the numerical calculations of a total near-field distribution. Here, we distinguish between two regimes of polarization dependence for the light propagating through a large size ($d > \lambda$) and a subwavelength size ($d < \lambda$) single circular crater. We can assume that such a structure in the near-field behaves as an aperture. In this case, the explanation may be applied on the basis of an anisotropic near-field distribution dominated for different regions of structure within the surface-wave modes and the field coupling to the wave-guided modes of the aperture.[19] For all conditions, two sets of the lobes of an intense field localized under the rim of the structure are generated with the orientation parallel to the light polarization (Figs. 5(a) and 5(c)). The generated mode in the center of the structure almost vanishes when the crater size is smaller than the excitation wavelength ($d/\lambda = 0.9$) (Fig. 5(a)). Then the strong field generated inside the rim region dominates (Fig. 5(a)). In such a system, it is expected to have a modification localized at the edges of the crater and oriented parallel to the field polarization. When the crater size increases ($d/\lambda = 4.0$), the lobes generated inside the rim are accompanied by the series of perpendicular lobes generated in the central part of the crater (Fig. 5(c)).

The FDTD simulated field patterns (Figs. 5(a) and 5(c)) are in a good agreement with the morphology of re-solidified material (Figs. 5(b) and 5(d)) observed experimentally. Indeed, under the focusing conditions when the modification area is smaller than the laser wavelength, the symmetric structure is slightly elongated, and the bridge-like structure along the polarization is produced (Fig. 5(b)). On the other hand, the bridge-like structure perpendicular to the polarization occurs when the beam is defocused (Fig. 5(d)). At the same time, the regions of the rim perpendicular to the bridge are modified, matching the intensity distribution visualized in numerical analysis (Fig. 5(c)).

In conclusion, we have experimentally demonstrated the polarization sensitive structuring on a silicon surface by the linearly polarized femtosecond double pulses. The distribution of electric near-field becomes asymmetric and polarization dependent when the second pulse propagates through a circular crater structure produced by the first pulse. The phenomenon enables imprinting of optical microreflectors within the single pulse irradiation and is exploited for demonstrating the direct mapping of the near-field distribution within multi-pulse experiments. Polarization sensitive structuring on silicon can be used for the security marking or data storage applications.

This work was supported by the UK Physical Sciences Research Council (EPSRC).

[1]E. N. Glezer, M. Milosavljevic, L. Huang, R. J. Finlay, T.-H. Her, J. P. Callan, and E. Mazur, Opt. Lett. **21**, 2023 (1996).
[2]A. P. Joglekar, H. Liu, G. J. Spooner, E. Meyhöfer, G. Mourou, and A. J. Hunt, Appl. Phys. B: Lasers Opt. **77**, 25–30 (2003).
[3]J. Zhang, M. Gecevičius, M. Beresna, and P. G. Kazansky, Phys. Rev. Lett. **112**, 033901 (2014).
[4]M. Beresna, M. Gecevičius, and P. G. Kazansky, Opt. Mater. Express **1**, 783 (2011).
[5]Y. Bellouard, A. Said, M. Dugan, and P. Bado, Opt. Express **12**, 2120 (2004).

[6]K. Miura, J. Qiu, H. Inouye, T. Mitsuyu, and K. Hirao, Appl. Phys. Lett. **71**, 3329 (1997).
[7]P. Kazansky, H. Inouye, T. Mitsuyu, K. Miura, J. Qiu, K. Hirao, and F. Starrost, Phys. Rev. Lett. **82**, 2199 (1999).
[8]B. Poumellec, M. Lancy, A. Chahid-Erraji, and P. G. Kazansky, Opt. Mater. Express **1**, 766–782 (2011).
[9]Y. Shimotsuma, P. G. Kazansky, J. Qiu, and K. Hirao, Phys. Rev. Lett. **91**, 247405 (2003).
[10]J. Gottmann, D. Wortmann, and M. Hörstmann-Jungemann, Appl. Surf. Sci. **255**, 5641 (2009).
[11]V. Bhardwaj, E. Simova, P. Rajeev, C. Hnatovsky, R. Taylor, D. Rayner, and P. Corkum, Phys. Rev. Lett. **96**, 057404 (2006).
[12]J. Bonse, J. Krüger, S. Höhm, and A. Rosenfeld, J. Laser Appl. **24**, 042006 (2012).
[13]R. Drevinskas, M. Beresna, M. Gecevičius, M. Khenkin, A. G. Kazanskii, I. Matulaitienė, G. Niaura, O. I. Konkov, E. I. Terukov, Yu. P. Svirko, and P. G. Kazansky, Appl. Phys. Lett. **106**, 171106 (2015).
[14]F. H'dhili, R. Bachelot, G. Lerondel, D. Barchiesi, and P. Royer, Appl. Phys. Lett. **79**, 4019 (2001).
[15]A. Plech, V. Kotaidis, M. Lorenc, and J. Boneberg, Nat. Phys. **2**, 44 (2006).
[16]A. Borowiec, M. MacKenzie, G. C. Weatherly, and H. K. Haugen, Appl. Phys. A: Mater. Sci. Process. **76**, 201 (2003).
[17]S. K. Sundaram and E. Mazur, Nat. Mater. **1**, 217 (2002).
[18]J. Ares, T. Mancebo, and S. Bará, Appl. Opt. **39**, 1511 (2000).
[19]J.-M. Yi, A. Cuche, F. de León-Pérez, A. Degiron, E. Laux, E. Devaux, C. Genet, J. Alegret, L. Martín-Moreno, and T. W. Ebbesen, Phys. Rev. Lett. **109**, 023901 (2012).

Paper F

R. Drevinskas, M. Beresna, M. Gecevičius, M. Khenkin, A. G. Kazanskii, I. Matulaitienė, G. Niaura, O. I. Konkov, E. I. Terukov, Y. P. Svirko, and P. G. Kazanksy

Giant birefringence and dichroism induced by ultrafast laser pulses in hydrogenated amorphous silicon

Applied Physics Letters 106(17), 171106 (2015)

APPLIED PHYSICS LETTERS **106**, 171106 (2015)

Giant birefringence and dichroism induced by ultrafast laser pulses in hydrogenated amorphous silicon

Rokas Drevinskas,[1,a)] Martynas Beresna,[1] Mindaugas Gecevičius,[1] Mark Khenkin,[2] Andrey G. Kazanskii,[2] Ieva Matulaitienė,[3] Gediminas Niaura,[3] Oleg I. Konkov,[4] Eugene I. Terukov,[4] Yu. P. Svirko,[5] and Peter G. Kazansky[1]
[1]*Optoelectronics Research Centre, University of Southampton, Southampton SO17 1BJ, United Kingdom*
[2]*Physics Department, M.V. Lomonosov Moscow State University, Moscow, Russia*
[3]*Department of Organic Chemistry, Center for Physical Sciences and Technology, A. Goštauto str. 9, LT-01108 Vilnius, Lithuania*
[4]*A.F. Ioffe Physico-Technical Institute, 194021 St. Petersburg, Russia*
[5]*Institute of Photonics, University of Eastern Finland, P.O. Box 111, FI-80101 Joensuu, Finland*

(Received 18 March 2015; accepted 20 April 2015; published online 28 April 2015)

A femto- and picosecond laser assisted periodic nanostructuring of hydrogenated amorphous silicon (a-Si:H) is demonstrated. The grating structure with the subwavelength modulation of refractive index shows form birefringence ($\Delta n \approx -0.6$) which is two orders of magnitude higher than commonly observed in uniaxial crystals and femtosecond laser nanostructured silica glass. The laser-induced giant birefringence and dichroism in a-Si:H film introduce extra dimensions to the polarization sensitive laser writing with applications that include data storage, security marking, and flat optics. © *2015 AIP Publishing LLC*. [http://dx.doi.org/10.1063/1.4919538]

Form birefringence, which results from spatially inhomogeneous patterns, may exceed the natural birefringence of crystals by several orders of magnitude.[1] The giant birefringence has been developed by the means of chemical material processing or nanolithography techniques in various systems including optical antenna arrays,[2] surface nanogratings,[3–5] ensembles of nanowires,[6,7] photonic crystals,[8] and nanophotonic waveguides.[9] The opportunity to design optically anisotropic surfaces is of special interest because it opens a way to control the light wave front by altering its polarization creating in particular, the geometrical Panchatraman-Berry phase.[10] Theoretically any phase pattern can be achieved solely by means of the geometrical phase with the efficiency reaching 100%.[11] One of the promising techniques for implementing optical elements with a geometrical phase is femtosecond laser assisted nanostructuring.[12] It has been demonstrated that materials irradiated with femtosecond laser pulses undergo the self-assembly process, which results in nanostructures produced on the surface[13,14] or inside the material.[15,16] Recently, this technology was harnessed for producing a series of birefringent optical elements inside silica glass,[12,17–19] while the optical anisotropy produced by laser-induced periodic surface structures (LIPSS) has not been reported. However, as the form birefringence depends on the refractive index modulation,[1] the amount of form birefringence achieved in nanostructured silica glass[20] is of the order of natural birefringence found in crystalline materials such as quartz. In order to enhance the optical anisotropy, a material with a high refractive index is required. A promising candidate is hydrogenated amorphous silicon (a-Si:H), which plays a significant role in the world's production of electronics and is ubiquitous for many applications ranging from liquid crystal displays to medical sensors and solar cells.[21] Transforming amorphous silicon (a-Si) into a nanocrystalline form through ultrafast laser irradiation has already been demonstrated (nc-Si).[22–31] In this letter, we demonstrate that the ultrafast laser assisted nanocrystallization of a-Si:H is accompanied by the formation of a laser-induced periodic structure. The observed pattern with the subwavelength modulation of the complex refractive index exhibits a dichroism and enhanced form birefringence, which is two orders of magnitude higher than commonly observed in uniaxial crystals such as quartz, ruby, sapphire, or femtosecond laser nanostructured silica glass. The proposed technology allows implementing functional optical elements with a sub-micron thickness by exploiting the laser imprinted geometrical phase patterns. Both birefringence and dichroism can be controlled by changing laser writing parameters adding extra dimensions to polarization sensitive printing, which is technologically attractive for flat optics,[11] optical data storage,[32] and security marking.

Experiments were carried out with 300 nm thick a-Si:H films deposited on silica glass by the plasma-enhanced chemical vapour deposition (PECVD) upon the decomposition of the mixture of silane (SiH_4) and argon (Ar) at substrate temperature of 250 °C. The ratio between the gases in the CVD chamber was 25% SiH_4 and 75% Ar.

In the experiments, the a-Si:H films were irradiated with the mode-locked Yb:KGW ultrafast laser system (Pharos, Light Conversion Ltd.) operating at $\lambda_L = 1030$ nm (photon energy ~ 1.2 eV) and delivering pulses with a 100 kHz repetition rate. The pulse duration ranging from 360 fs to 4.8 ps with the pulse energy varying from 0.005 μJ to 0.2 μJ was employed. The laser beam, polarized parallel or perpendicular to the writing direction, was focused onto the film surface via a 0.13 NA-objective lens producing the fluence of 0.0068–0.27 J/cm^2, or intensity of 1.89×10^{10}–7.5×10^{11} W/cm^2 for 360 fs and 1.42×10^{9}–5.6×10^{10} W/cm^2 for 4.8 ps, respectively. The estimated spot size of the laser beam in the

a)Author to whom correspondence should be addressed. Electronic mail: rd1c12@orc.soton.ac.uk

focus was $\omega_o \approx 5\,\mu$m. For all parameters (polarization, pulse duration, and laser energy), 80 μm long lines were written with an interline distance of 30 μm at a 0.2 mm/s translation speed.

Irradiated regions were analysed with a scanning electron microscope (SEM) (Zeiss Evo50) and an optical microscope (Olympus BX51). Raman spectroscopy was performed with a Renishaw inVia system operating at 632.8 nm excitation. The system was calibrated according to the monocrystalline silicon (Si) line at 520.7 cm^{-1}. To avoid heat induced crystallization, the excitation power was restricted to 0.1 mW.

Structural and optical analysis of irradiated regions revealed several modification regimes (Fig. 1). "Type 0" modification occurs at the energies of 0.025–0.03 μJ and is distinguished only for the pulse duration shorter than 2 ps. Optically, this modification manifests as a darkening of the film. According to Zanzucchi *et al.*,[33] "Type 0" regime appears due to enhanced optical absorption in visible spectrum and is attributed to the hydrogen (H) release. The Raman analysis of the wagging vibrations of Si-H studied elsewhere[31] confirms that the H release starts at the energies below 0.02 μJ, and at 0.03 μJ its content drops to 20% of the initial value.

For "Type I" regime, at the energies slightly below 0.07 μJ for 360 fs or 0.05 μJ for 4.8 ps, amorphous silicon with the broad Raman band at 480 cm^{-1} begins to be replaced by the crystalline silicon transverse optical (TO) phonon mode with the peak position at 518.0–519.2 cm^{-1}, which we attribute to the formation of nc-Si (Fig. 2). Using the confinement model,[34] the silicon grain size of 4–6 nm was estimated. The morphology analysis revealed that the nc-Si grains are aggregated into sub-100 nm domains, which are elongated parallel to the beam polarization and organised into high spatial frequency structure with the periodicity defined by the domain width ($\Lambda \approx \lambda_L/10$) (Fig. 3(top)).

Both the energy and pulse duration affect the position and full width at half maximum (FWHM) of nc-Si TO mode (see Fig. 2(b)). The upshift in frequency and the narrowing of the band indicates the formation of larger silicon grains up to 8–9 nm size at higher pulse energies in the case of 360 fs laser pulses. In contrast, the treatment with 4.8 ps pulses always results in development of smaller crystallites reaching ~5 nm size.

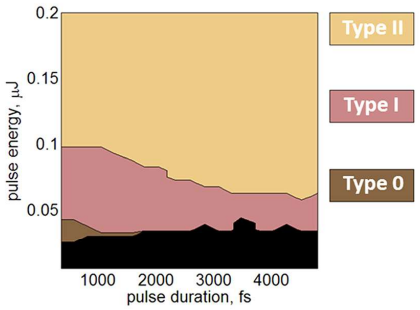

FIG. 1. The threshold energies for a-Si:H modification regimes: Type 0—H release; Type I—silicon crystallization followed by the high spatial frequency structure with low birefringence; Type II—silicon crystallization followed by the nanograting structure that corresponds to the laser-induced dichroism and giant birefringence. Black region indicates the conditions when the change in film structure was not observed.

At high energies (>0.09 μJ for 360 fs, and >0.06 μJ for 4.8 ps) slightly above the ablation threshold, the film starts to crystallize along its depth ("Type II"), periodically organizing into a nanograting oriented perpendicular to the laser beam polarization (Figs. 1–3). The average period of the structure is $\Lambda \approx \lambda_L/3$ that corresponds to λ_L/n_{film}. Such a subwavelength modulation of high-contrast refractive index (n_{air}/n_{film}) originates form birefringence.[1] Simultaneously a non-zero imaginary part of the material's complex refractive index (extinction k) leads to the polarization sensitive absorption coefficient ($\alpha = 4\pi k/\lambda$), i.e., dichroism.

The laser-induced birefringence and dichroism were characterized with the quantitative birefringence measurement system (CRi Abrio; Olympus BX51) operating at $\lambda = 546$ nm. In this system, the dichroism manifests itself as an artificial birefringence added to the system.[35] To recover the absolute values of the birefringence and dichroism, the measured data were additionally processed with a mathematical algorithm.

Figures 4(a) and 4(b) show the retardance and dichroism extracted from the set of 1600 lines imprinted in a-Si:H film. With respect to threshold energy diagram (Fig. 1), the enhanced birefringence corresponds to "Type II" regime, while "Type I" exhibits roughly two orders of magnitude lower birefringence values (Fig. 4(a)). Upon 360 fs, the threshold values of 0.045 μJ for "Type I" regime and 0.1 μJ for "Type II" regime were identified. While for 4.8 ps, these thresholds are reduced to 0.035 μJ and 0.065 μJ, respectively. The laser-induced dichroism follows the "Type II" modification (Fig. 4(b)).

According to the Raman spectra shown in Fig. 2, at the pulse energies higher than 0.1 μJ, irradiation with femtosecond pulses results in larger grains and is 2–3 times more efficient than that with picosecond pulses. Such a pulse duration dependent lattice transformation indicates that the light intensity plays the dominant role, i.e., the lattice transformation starts within the first pulses, when only a-Si:H is present. Specifically, at the initial stage of the irradiation, the intense femtosecond pulses generate more defects (in comparison with picosecond ones) by reducing the hydrogen content in the lattice. Assuming that most of the hydrogen is released before the crystallization and laser-induced nanostructuring,[31] the absorption of the film increases drastically. This is because the absorption coefficient of the produced a-Si (at photon energy of ~1.2 eV) is almost two orders of magnitude higher than the nc-Si and four orders higher than the a-Si:H,[32,35–38] i.e., a-Si defines the efficiency of the subsequent modification regimes. Over the further multi-pulse irradiation, the absorption dependent nc-Si content increase leads to the a-Si:H/a-Si content decrease. As a result, the threshold energy of enhanced retardance and dichroism due to higher absorption starts decreasing with the increase of pulse duration ($\tau > 1$ ps) (Figs. 4(a) and 4(b)).

Although "Type II" threshold energy depends on the pulse duration, the peak values of retardance $R \approx 150$–180 nm (phase shift of $\sim 0.7\pi$, at $\lambda = 546$ nm) and dichroism $D \approx 0.6$–1 remain roughly the same ranging from 360 fs to 4.8 ps at

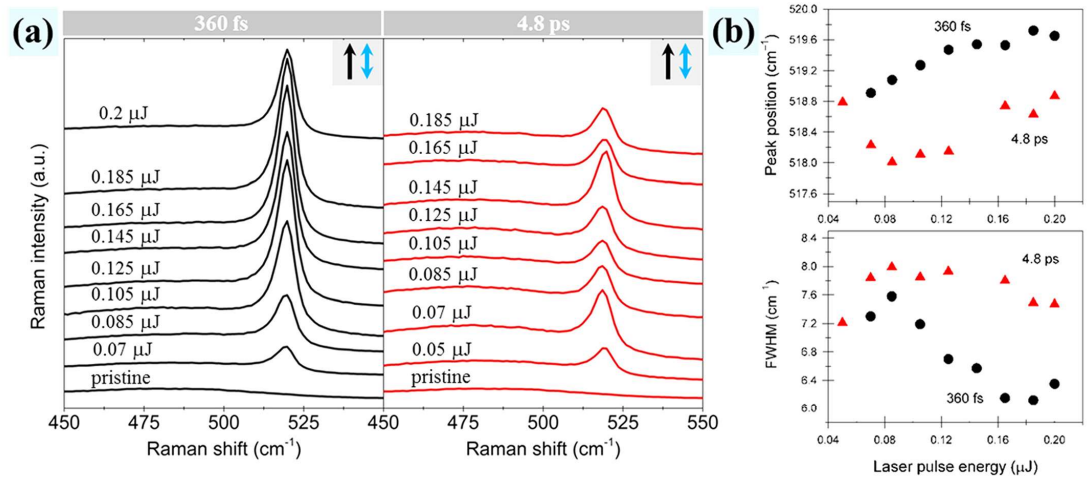

FIG. 2. (a) Raman spectra of a-Si:H treated by 360 fs (black) and 4.8 ps (red) laser pulses with the energy of 0.05–0.2 μJ. The system was operating at 100 kHz with writing speed of 0.2 mm/s. The bottom curves show the Raman spectra of untreated a-Si:H film. Black arrows indicate the laser writing direction, blue arrows—the state of polarization. (b) Effect of laser pulse energy and pulse duration on the peak position (upper panel) and full width at half maximum (FWHM) (bottom panel) of TO mode of produced nc-Si grains.

pulse energies lower than 0.15 μJ (Figs. 4(a) and 4(b)). The retardance is defined as

$$R(\lambda) = d \times (n_e(\lambda) - n_o(\lambda)) = d \times \Delta n(\lambda), \quad (1)$$

where d is the thickness of the film and n_e, n_o—extraordinary and ordinary effective refractive indices. Thus the birefringence of nanograting with $d = 300$ nm and corresponding retardance values is estimated as $\Delta n \approx -0.5$ to -0.6. The birefringence induced by ultrafast laser nanostructuring is comparable to the giant birefringence achieved in amorphous silicon by electron-beam nanolithography.[3] For comparison, the typical values of $n_e - n_o$ imprinted by the femtosecond laser writing inside the silica glass are roughly -5×10^{-3}.[20] However, when the pulse energy is higher than 0.15 μJ, the nc-Si content decreases (Fig. 2(a)). The "Type II" regime is accompanied by the silicon oxidation, apparent due to the enhanced oxygen incorporation into the silicon lattice at high pulse energies.[28,39] As a result, form birefringence is reduced to -0.4 due to the refractive index change from crystalline silicon to silica glass (Fig. 4(a)).

The dispersion of retardance and dichroism was investigated by using a VIS-NIR birefringence measurement system (CRAIC; Olympus BX51). The transmittance of light was measured when the polarizer before the sample was fixed at 45° with respect to the nanograting orientation while the polarizer after the sample was fixed at 45° ($I_{parallel}$) or $-45°$ ($I_{crossed}$). The retardance dispersion $R(\lambda)$ was then calculated as follows:[40]

$$R(\lambda) = \operatorname{acos}\left(\frac{I_{parallel} - I_{crossed}}{I_{parallel} + I_{crossed}}\right) \times \frac{\lambda}{2\pi} = \Delta(\lambda) \times \frac{\lambda}{2\pi}. \quad (2)$$

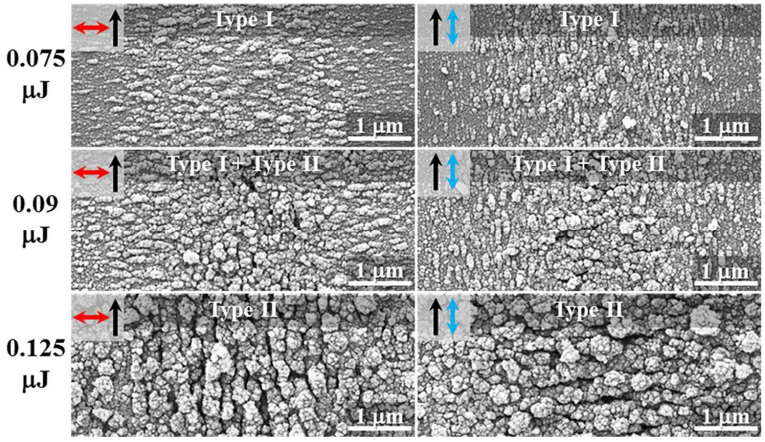

FIG. 3. SEM images of the laser modified a-Si:H film. The shown single lines were written with 0.075 μJ, 0.09 μJ, 0.125 μJ pulse energy. The system was fixed to 100 kHz, 360 fs pulse duration and 0.2 mm/s writing speed. Black arrows indicate the laser writing direction, while red/blue arrows—the polarization state.

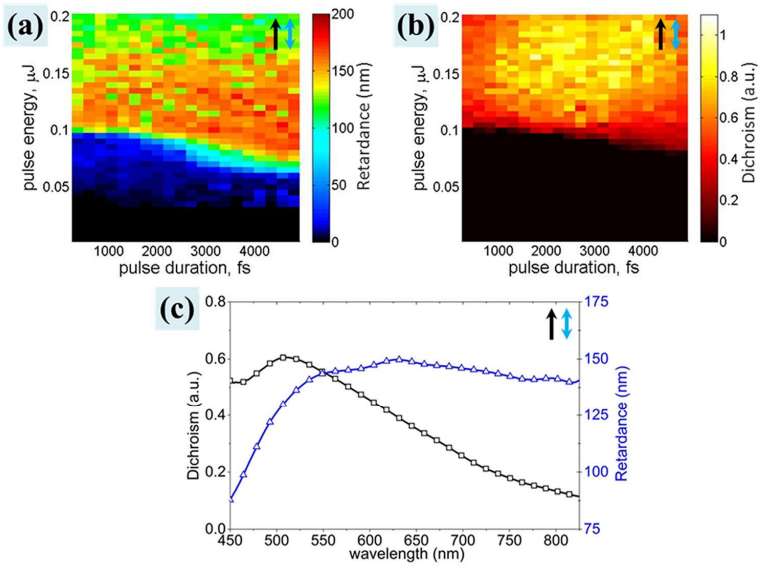

FIG. 4. Laser induced retardance (a) and dichroism (b) in a-Si:H film dependence on pulse duration and energy. The dispersion curves (c) depicted for the structure fabricated with 0.15 μJ energy and 360 fs pulses show its chromatic behavior. The system was operating at 100 kHz with the writing speed of 0.2 mm/s. Black arrows indicate the laser writing direction, blue arrows—the polarization state.

For the dichroism characterization, the transmittance of light polarized parallel ($\|$) and perpendicular ($\perp$) to the orientation of nanograting was measured. Then the dichroism $D(\lambda)$ is defined as

$$D(\lambda) = \left|-\log\left(\frac{T_\perp}{T_\|}\right)\right| = \left|-\log\left(\frac{I_\perp I_{\|o}}{I_\| I_{\perp o}}\right)\right|, \quad (3)$$

where $I_{\perp,\|}$ and $I_{\perp o,\|o}$ are the light intensities transmitted through the system with the sample and without it, respectively.

The dispersion analysis performed in the spectral region from 450 nm to 825 nm for the structure fabricated with 0.15 μJ energy and 360 fs pulses revealed a chromatic behavior of the laser-induced anisotropic material (Fig. 4(c)). The retardance of ~90 nm at 450 nm wavelength steadily increases reaching the peak value of ~150 nm at 550 nm, and then results in an asymptotic decrease to a plateau that corresponds well to the function of refractive index of silicon. At the same time, the extinction coefficient of silicon vanishes in the infrared and increases in the ultraviolet spectral range corresponding to direct band transitions, giving rise to stronger dichroism at the shorter wavelengths.[5] The maximum dichroism of $D \approx 0.6$ was observed at wavelength of 510 nm, while it dropped down to $D \approx 0.1$ at 825 nm.

Both the dichroism and differential phase-shift reach the peak at 510–530 nm (~2Λ) wavelengths enabling the imprinting of polarizing and quarter-wave plate elements with the applications in visible spectrum. The spectral working range of such optical elements can be tuned by the geometry (thickness and duty cycle) and material properties of the grating.[1,41] Thus, the spectral characteristics of phase retardation and transmittance can be changed by controlling the laser processing conditions. Optical components in the range from ultraviolet to near infrared can be fabricated.[3,5]

To demonstrate the application of laser assisted nanostructuring of a-Si:H, we imprinted Einstein's portrait (250 × 250 pixels) by encoding grayscale information via the laser beam's polarization (Fig. 5). Each 5 μm size pixel was written with the 0.2 mm/s translation speed. Rotating the linear polarization, sixteen different states in the range of 0°–90° and 0°–45° for the dichroic and birefringent images, respectively, were imprinted following the grayscale distribution of the portrait.

The portrait was illuminated with four polarization configurations producing the negative (parallel), positive (perpendicular), high contrast (cross-polarized), and weak contrast (unpolarised) images in optical transmission mode (Fig. 5).

In conclusion, we have demonstrated a femto- and picosecond laser assisted nanostructuring of a-Si:H film producing dichroic and birefringent material properties. Within a certain range of pulse energies, distinctive modification regimes are observed identifying hydrogen release from a-Si:H lattice (Type 0); silicon crystallization followed by the periodic surface structures self-organized parallel to the beam polarization (Type I); and silicon crystallization

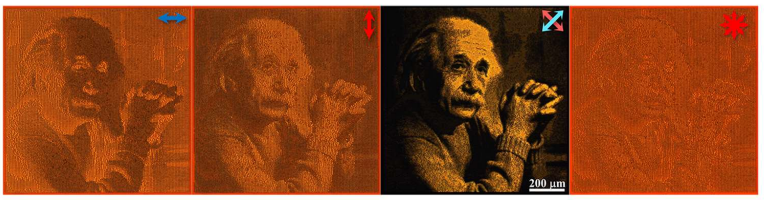

FIG. 5. The polarization sensitive Einstein's portrait imprinted in a-Si:H film by femtosecond laser nanostructuring. Arrows indicate the polarization states used for the optical transmission imaging. (Multimedia view) [URL: http://dx.doi.org/10.1063/1.4919538.1]

followed by the periodic structures organized perpendicular to the beam polarization (Type II). "Type I" regime defines the conditions to produce tandem modules of amorphous and nanocrystalline silicon with potential applications in photovoltaics. While "Type II" regime corresponding to the laser-induced dichroism and enhanced form birefringence is a promising alternative for fabricating functional micro-optical elements with thickness of less than 300 nm.

An anisotropic laser texturing demonstrated in this paper was implemented in the polarization sensitive ultrafast laser printing. The technique enables imprinting of optical elements with the sub-micron resolution and can be used for demonstrating ultrathin optics for complex shaping of phase and polarization, as well as in security marking or data storage applications.

The work was supported by FP7 Marie Curie NANOCOM project.

[1]A. Yariv and P. Yhe, *Optical Waves in Crystals* (Wiley, New York, 1984), pp. 165–174.
[2]M. A. Kats, P. Genevet, G. Aoust, N. Yu, R. Blanchard, F. Aieta, Z. Gaburro, and F. Capasso, Proc. Natl. Acad. Sci. U. S. A. **109**, 12364 (2012).
[3]S. Y. Chou and W. Deng, Appl. Phys. Lett. **67**, 742 (1995).
[4]S.-Y. Hsu, K.-L. Lee, E.-H. Lin, M.-C. Lee, and P.-K. Wei, Appl. Phys. Lett. **95**, 013105 (2009).
[5]T. Weber, S. Kroker, T. Käsebier, E. Kley, and A. Tünnermann, Appl. Opt. **53**, 8140 (2014).
[6]O. L. Muskens, M. T. Borgström, E. P. A. M. Bakkers, and J. G. Rivas, Appl. Phys. Lett. **89**, 233117 (2006).
[7]N. Künzner, D. Kovalev, J. Diener, E. Gross, V. Y. Timoshenko, G. Polisski, and F. Koch, Opt. Lett. **26**, 1265 (2001).
[8]F. Genereux, S. Leonard, H. van Driel, A. Birner, and U. Gösele, Phys. Rev. B **63**, 161101 (2001).
[9]S. Yang, M. L. Cooper, P. R. Bandaru, and S. Mookherjea, Opt. Express **16**, 8306 (2008).
[10]E. Hasman, Z. Bomzon, A. Niv, G. Biener, and V. Kleiner, Opt. Commun. **209**, 45 (2002).
[11]N. Yu and F. Capasso, Nat. Mater. **13**, 139 (2014).
[12]M. Beresna, M. Gecevičius, and P. G. Kazansky, Opt. Mater. Express **1**, 783 (2011).
[13]J. Bonse, J. Krüger, S. Höhm, and A. Rosenfeld, J. Laser Appl. **24**, 042006 (2012).
[14]M. Huang, F. Zhao, Y. Cheng, N. Xu, and Z. Xu, ACS Nano **3**, 4062 (2009).
[15]Y. Shimotsuma, P. Kazansky, J. Qiu, and K. Hirao, Phys. Rev. Lett. **91**, 247405 (2003).
[16]R. R. Gattass and E. Mazur, Nat. Photonics **2**, 219 (2008).
[17]M. Beresna, M. Gecevičius, and P. G. Kazansky, Adv. Opt. Photonics **6**, 293 (2014).
[18]M. Gecevičius, M. Beresna, R. Drevinskas, and P. G. Kazansky, Opt. Lett. **39**, 6791 (2014).
[19]M. Gecevičius, R. Drevinskas, M. Beresna, and P. G. Kazansky, Appl. Phys. Lett. **104**, 231110 (2014).
[20]E. Bricchi and P. G. Kazansky, Appl. Phys. Lett. **88**, 111119 (2006).
[21]R. A. Street, *Technology and Applications of Amorphous Silicon* (Springer-Verlag, Berlin, 2000), p. 417.
[22]J.-M. Shieh, Z.-H. Chen, B.-T. Dai, Y.-C. Wang, A. Zaitsev, and C.-L. Pan, Appl. Phys. Lett. **85**, 1232 (2004).
[23]G. J. Lee, J. Park, E. Kim, Y. Lee, K. M. Kim, H. Cheong, C. S. Yoon, Y.-D. Son, and J. Jang, Opt. Express **13**, 6445 (2005).
[24]G. J. Lee, S. H. Song, Y. Lee, H. Cheong, C. S. Yoon, Y. D. Son, and J. Jang, Appl. Phys. Lett. **89**, 151907 (2006).
[25]B. K. Nayak and M. C. Gupta, Appl. Phys. A **89**, 663 (2007).
[26]X. C. Wang, H. Y. Zheng, C. W. Tan, F. Wang, H. Y. Yu, and K. L. Pey, Opt. Express **18**, 19379 (2010).
[27]A. V. Emelyanov, A. G. Kazanskii, P. K. Kashkarov, O. I. Konkov, E. I. Terukov, P. A. Forsh, M. V. Khenkin, A. V. Kukin, M. Beresna, and P. Kazansky, Semiconductors **46**, 749 (2012).
[28]A. V. Emelyanov, A. G. Kazanskii, M. V. Khenkin, P. A. Forsh, P. K. Kashkarov, M. Gecevičius, M. Beresna, and P. G. Kazansky, Appl. Phys. Lett. **101**, 081902 (2012).
[29]L. Hong, X. C. Wang, H. Y. Zheng, L. He, H. Wang, H. Y. Yu, and Rusli, J. Phys. D: Appl. Phys. **46**, 195109 (2013).
[30]H. Wang, P. Kongsuwan, G. Satoh, and Y. L. Yao, Int. J. Adv. Manuf. Technol. **65**, 1691 (2013).
[31]A. V. Emelyanov, M. V. Khenkin, A. G. Kazanskii, P. A. Forsh, P. K. Kashkarov, M. Gecevičius, M. Beresna, and P. G. Kazansky, Thin Solid Films **556**, 410 (2014).
[32]J. Zhang, M. Gecevičius, M. Beresna, and P. G. Kazansky, Phys. Rev. Lett. **112**, 033901 (2014).
[33]P. J. Zanzucchi, C. R. Wronski, and D. E. Carlson, J. Appl. Phys. **48**, 5227 (1977).
[34]J. Zi, H. Büscher, C. Falter, W. Ludwig, K. Zhang, and X. Xie, Appl. Phys. Lett. **69**, 200 (1996).
[35]S. B. Mehta, M. Shribak, and R. Oldenbourg, J. Opt. **15**, 094007 (2013).
[36]M. H. Brodsky, R. S. Title, K. Weiser, and G. D. Pettit, Phys. Rev. B **1**, 2632 (1970).
[37]S. Veprek, F.-A. Sarott, and Z. Iqbal, Phys. Rev. B **36**, 3344 (1987).
[38]A. V. Shah, J. Meier, E. Vallat-Sauvain, N. Wyrsch, U. Kroll, C. Droz, and U. Graf, Sol. Energy Mater. Sol. Cells **78**, 469 (2003).
[39]K. Hoh, H. Koyama, K. Uda, and Y. Miura, Jpn. J. Appl. Phys., Part 1 **19**, L375 (1980).
[40]M. Beresna, M. Gecevičius, M. Lancry, B. Poumellec, and P. G. Kazansky, Appl. Phys. Lett. **103**, 131903 (2013).
[41]Z. Y. Yang and Y. F. Lu, Opt. Express **15**, 9510 (2007).

Paper G

R. Drevinskas, M. Beresna, J. Zhang, and A. G. Kazanskii, P. G. Kazansky

Ultrafast laser-induced metasurfaces for geometric phase manipulation

Advanced Optical Materials 5, 1600575 (2017)

Ultrafast laser-induced metasurfaces for geometric phase manipulation

Rokas Drevinskas,[1] Martynas Beresna,[1] Jingyu Zhang,[1] Andrey G. Kazanskii,[2] and Peter G. Kazansky[1]

[1] Optoelectronics Research Centre, University of Southampton, Southampton, SO17 1BJ, United Kingdom

[2] Physics Department, M.V. Lomonosov Moscow State University, Moscow, 119991, Russia

Rokas Drevinskas: rd1c12@soton.ac.uk

Martynas Beresna: M.Beresna@soton.ac.uk

Jingyu Zhang: jz2e11@orc.soton.ac.uk

Andrey G. Kazanskii: kazanski@phys.msu.ru

Peter G. Kazansky: pgk@soton.ac.uk

Corresponding author: Rokas Drevinskas rd1c12@soton.ac.uk, +44 23 8059 3924

ABSTRACT

Light waves interacting with inhomogeneous birefringent materials always experience a space-variant phase shift. Engineering the orientation of local optical axis allows implementing continuous phase profiles of nearly any optical element that can be achieved solely by the means of geometric phase. Despite a longstanding expertise in fabrication of anisotropic materials, flexibility still remains a challenging problem. Here we demonstrate a direct-write femtosecond laser nanostructuring of 300-nanometer thick a-Si:H films resulting in space-variant functional metasurfaces with form birefringence of up to $\Delta n \approx -0.5$. The complex designs of geometric phase optical elements including arrays of polarization micro-converters and micro-lenses, polarization gratings and computer generated holograms with continuous phase gradients of ~1 rad/μm were fabricated. In principle, the technique can be extended to any transparent high-index materials that support laser-induced periodic structures, and can be effectively exploited for the integration of metasurfaces into multi-functional photonic systems.

Keywords: Femtosecond phenomena; Materials processing; Form birefringence.

1. INTRODUCTION

The recent advances in flat optics have challenged the limitations of conventional optics by implementing ultrathin planar elements that instead of relying on optical path differences manipulate light waves via optical resonators with spatially varying phase response[1]. In principle, the phase profiles of nearly any optical components including lenses, gratings, vortex phase plates, as well as elements capable of bending light in unusual ways could be designed on the basis of plasmonic metamaterials[2,3] or dielectric gradient metasurfaces[4–7], referred to as geometric phase (Pancharatnam-Berry phase[8–10]) optical elements (GPOEs). The main advantage of such tailored surfaces is that the large phase shifts can be realized by nanostructured thin films within thicknesses smaller than the wavelength of light, and thus can be easily integrated into multifunctional optoelectronic systems[11–13].

Designs of dielectric GPOEs have attracted great interest for being a promising alternative to control light waves. The most common approach for implementing such optical elements is to exploit nanostructured materials which exhibit form birefringence[14]. This means that the desired phase pattern of the wave interacting with an inhomogeneous birefringent element is directly encoded in the optical axis orientation, and is equal to twice the

rotation angle of the locally imprinted wave plate. Although numerous lithography techniques enabling the manufacturing of high efficiency and low scattering optical elements with complex phase gradients have been reported[15–17], the technological flexibility remains a problem; it is still dictated by the material properties, and/or requires a long time to process. Here we propose a direct-write ultrafast laser nanostructuring as an alternative method capable of fabricating GPOEs in various media. One of the most fascinating aspects of this technique is the ability to induce tunable structures[6] with subwavelength periodicities that originate form birefringence[18]. The key advantage of using femtosecond pulses for direct laser writing, as opposed to longer pulses, is that they can rapidly deposit energy in solids with high precision. The light is absorbed and the optical excitation ends before the surrounding lattice is perturbed, which results in highly localized nanostructuring without collateral material damage[19,20].

First observation of laser-induced periodic surface structures (LIPSS) dates back to the 60's, when Birnbaum reported ripple formation on the surface of semiconductors[21]. Since then, this phenomenon was observed on virtually any type of media including metal, semiconductor, dielectric solids and thin films[22–29]. Processing conditions occurred to be broad with wavelengths ranging from the mid-infrared to visible spectrum and from continuous wave operation to femtosecond laser systems. A vast number of applications, including coloration[30], control of surface chemical and mechanical properties[31,32], have been proposed.

More than a decade ago, Bricchi et al. demonstrated that femtosecond laser pulses focused inside silica glass can lead to self-assembled nanogratings, which exhibit birefringence comparable to quartz crystals[33]. Later, the tailored surface nanogratings were introduced showing the three-fold birefringence increase[34]. Thus, a functional birefringent layer should be at least several tens of microns thick. For most applications such a thickness is appropriate. However, this limits the design and integration of miniaturized elements.

To realize the laser-induced nanogratings as functional metasurfaces, the intermediate case between volume and surface periodic structuring has to be implemented when the modification of high-index thin films along its depth would significantly enhance the resulting anisotropy. Here we demonstrate that the interaction of femtosecond laser pulses with hydrogenated amorphous silicon (a-Si:H) thin films induces self-assembled periodic lamellae structures oriented perpendicular to the incident beam polarization. These films with the induced subwavelength modulation of refractive index behave as a uniaxial birefringent material with the slow axis oriented parallel to the imprinted nanogratings. Thus, the form birefringence of two orders of magnitude higher than in silica glass can be achieved[18,33-35]. As a result, large retardation is realized within hundreds of times thinner layers (Figure 1a) that can be deposited on various substrates with different textures.

We leverage the realization of laser-induced periodic thin-film structures as a highly birefringent metasurface to design controllable and high precision GPOEs. Here we report on demonstration of various geometric phase designs including arrays of polarization micro-converters and micro-lenses, polarization gratings and computer generated holograms with phase gradients reaching up to ~1 rad/μm.

2. FEMTOSECOND LASER NANOSTRUCTURING FOR ENGINEERED FORM BIREFRINGENCE

The experiments were carried out with the 300 nm thick a-Si:H films deposited on a silica glass substrate by the plasma-enhanced chemical vapor deposition (PECVD) upon the decomposition of the mixture of silane (SiH_4) and argon (Ar) at substrate temperature of 250°C. The ratio between the gases in the reaction chamber was 25% SiH_4 and 75% Ar.

The film was processed with the mode-locked Yb:KGW ultrafast laser system (Pharos, Light Conversion Ltd.) operating at a wavelength of 1030 nm with the pulse duration fixed at 360 fs. The laser beam was focused to a 4 μm spot on the film via a 0.13 NA-objective lens.

Surface imaging of laser-induced periodic thin-film structures was performed with a scanning electron microscope (SEM) Zeiss Evo50 and optical transmission microscope Olympus BX51. The imprinted elements were optically characterized and/or visualized with the VIS/NIR micro-spectrometer CRAIC (Olympus BX51) and the quantitative birefringence measurement

system CRi Abrio (Olympus BX51) operating at 546 nm wavelength. Nd:YAG cw laser (Spectra-Physics) frequency-doubled to 532 nm and supercontinuum fiber laser (Fianium) emitting a broad optical spectrum in the range of 450-950 nm were used to characterize the Gaussian beam propagation through the imprinted GPOEs.

In order to identify the maximum birefringence of the laser-induced periodic thin-film structures, 80 μm long lines separated by an interline distance of 30 μm were imprinted under different writing conditions. First, the pulse density was varied from 1.25×10^5 pulses/mm to 5×10^6 pulses/mm with various writing speeds to ensure the constant laser repetition rate of 100 kHz. Secondly, the writing speed was varied from 0.05 mm/s to 0.4 mm/s with various laser repetition rates to ensure a constant pulse density of 5×10^5 pulses/mm. From here, the resulting retardance as a function of pulse energy varying from 0.005 μJ to 0.2 μJ was obtained (Figure 1b).

At the pulse energies slightly above the ablation threshold ($> 0.05\mu J$), the film is modified along its depth organizing into periodic structure that is qualitatively dependent on the pulse density (Figure 1b, top graph), while the significant dependence on the laser repetition rate or writing speed is not observed (Figure 1b, bottom graph). At pulse densities higher than $10^5 \mathrm{pulses/mm}$, we detect the formation of birefringent subwavelength periodicity ($\sim \lambda_{\mathrm{laser}}/3$) nanogratings oriented perpendicular to the laser beam polarization. The maximum retardation of $R_{546\mathrm{nm}} \approx 0.55\pi$ is achieved at 5×10^5 pulses/mm with the related writing speed of 0.2 mm/s and repetition rate of 100 kHz. The retardance drops drastically with the further density increase ($> 10^6 \mathrm{pulses/mm}$), and the nanogratings are replaced by non-birefringent wavelength-size ($\sim\lambda_{\mathrm{laser}}$) ripples oriented parallel to the laser beam polarization.

Contrary to the separated lines, the planar wave plate elements were fabricated by partially overlapping the written lines. The calibration of imprinted elements was performed under maximum retardation conditions by changing the pulse energy from 0.005 μJ to 0.2 μJ at a fixed interline distance of 3 μm (Figure 1c), and varying the interline distance from 1 μm to 7 μm at a fixed pulse energy of 0.125 μJ (Figure 1c, inset). The observed retardance linearly grows with the increase of the interline distance reaching the peak value of $\sim0.5\pi$ at 4 μm, which correlates well with the spot size of the focused beam. However, despite the lower retardance value, the most uniform wave plates are fabricated using the interline distance of 3 μm. When the retardance is defined as

$$\varphi = h(n_e - n_o)\, 2\pi/\lambda, \tag{1}$$

where h is the thickness of the film, and n_e, n_o – extraordinary and ordinary effective refractive indices, the birefringence of the imprinted optical elements with h = 300 nm and 0.5π retardation at 546 nm wavelength corresponds to the form birefringence of $\Delta n = n_e - n_o \approx -0.5$.

Optical performance of the fabricated wave plates is strongly dependent on the linear absorption and scattering of the nanostructured material, which can be significantly improved by reducing the value of the complex refractive index. This can be achieved by increasing the laser pulse energy as it triggers the oxidation processes and ultimately enhances the transmission reaching a three-fold value at the pulse energy of 0.2 μJ, while the birefringence remains of the same order (Figure 1c).

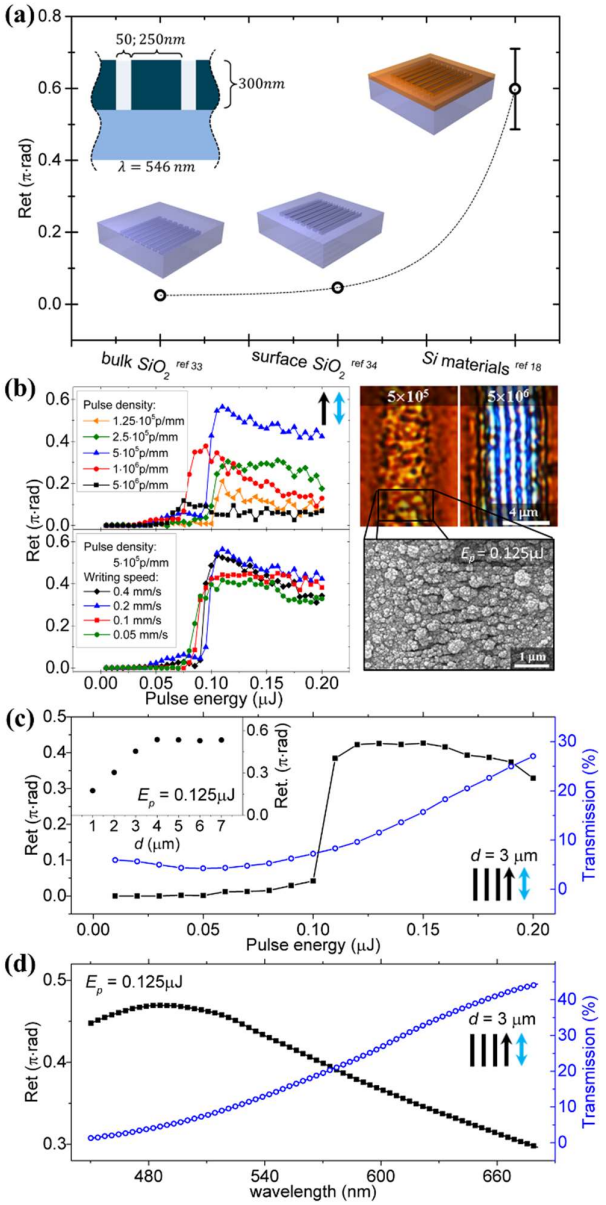

Figure 1. Femtosecond laser-induced periodic a-Si:H film structures. (a) Retardation of nanogratings induced in the bulk of silica; on the surface of silica; and in the thin-film silicon materials (n=3.5-4.5), based on the experimental reports[33-34] and effective medium theory[18]. Both the thickness and the periodicity of structures were set to 300 nm with the duty cycle of 1/6. (b) Separated lines with its retardance dependence on pulse density (top graphs) and writing speed (bottom graphs) as a function of pulse energy. On the right, optical and electron microscopy generated images of periodic structures induced under 5×10^5 (left) and 5×10^6 (right) pulses/mm at pulse energy of 0.125 μJ: identification of subwavelength birefringent structure and wavelength-size non-birefringent ripples formation. Scale bars are 4 μm and 1 μm, respectively. (c) Retardance and transmission of imprinted wave plates as a function of pulse energy. The measurement system was operating at 546 nm wavelength. The dependence of retardance on the interline distance is shown in the inset. (d) Spectra of phase retardation and transmittance for wave plate imprinted at 0.125 μJ. In (c) and (d) the interline distance (*d*) was kept at 3 μm. The system was set to the pulse density of 5×10^5 pulses/mm with corresponding 0.2 mm/s writing speed and 100 kHz repetition rate. Black arrows indicate the laser writing direction; blue arrows – the polarization state.

The dispersion analysis performed in the spectral region from 450 nm to 680 nm revealed a chromatic behavior of the wave plates. In the case of pulse energy of 0.125 μJ and interline distance of 3 μm the retardation value varies from 0.29π to 0.47π

(Figure 1d). Less than 5% variation in retardance is observed in the spectral region from 532 nm to 546 nm wavelength. The transmission coefficient at 532 nm, where the phase retardation is about 0.45π, is roughly of ~0.1. The transmission as high as 50% can be achieved at longer wavelengths (~700 nm) where the lower scattering is ensured, as well as the amorphous silicon band gap is approached (~1.7 eV[36]).

3. THIN-FILM METASURFACES FOR GEOMETRIC PHASE MANIPULATION

The Pancharatnam-Berry phase is a geometric phase achieved by space-variant polarization manipulations[14]. In the next step, we designed GPOEs by controlling the azimuth of the slow axis, $A(x,y)$, of locally imprinted nanogratings. As a result, the circularly polarized light transmitted through the GPOEs experiences the relative phase change equal to $\phi(x,y) = \pm 2A(x,y)$, where the sign is defined by the handedness of the input polarization.

All GPOEs demonstrated in this work were imprinted using the pulse energy of 0.125 μJ and pulse density of 5×10^5 pulses/mm with corresponding 0.2 mm/s writing speed and 100 kHz repetition rate. The interline distance was ranged from 3 μm to 4 μm to balance the homogeneity and magnitude of the laser-induced retardation.

Local orientation of the laser-induced nanogratings was continuously controlled by rotating the half-wave plate mounted before the objective lens. The accuracy of ~0.002 rad is ensured. The resulting geometric phase as a function of rotation of the half-wave plate, $\theta(x,y)$, is expressed as

$$\phi(x,y) = \pm(4\theta(x,y) - \pi), \tag{2}$$

where the orientation of the half-wave plate corresponds to the orientation of the polarization of the linearly polarized laser beam, and the phase-offset of π occurs due to the nanogratings orientation, which is always perpendicular to the incident polarization.

In particular, when designing GPOEs by laser direct writing, it is important to ensure the continuity of the generated nanogratings. If the phase gradient is introduced, the local field as well as the induced structures are perturbed by the previously imprinted structure. Thus, the induced retardance value drops with the decrease of the grating period (a) (Figure 2a).

The efficiency of the GPOEs imprinted in a-Si:H thin films was specified by fabricating the polarization grating (PG) with the geometric phase varying in the x-direction as $\phi(x) = (2\pi/a)x|_{\mathrm{mod}\,2\pi}$ (Figure 2b). The periodicity of the PG was set to 30 μm as the achieved phase retardation shows the value of ~90% of the possible maximum value. For an incident plane wave with the polarization state $|E_{in}\rangle$ the resulting field generated by the PG is[37]

$$|E_{out}\rangle = \eta_E|E_{in}\rangle + \eta_R e^{i2A(x,y)}|R\rangle + \eta_L e^{-i2A(x,y)}|L\rangle, \tag{3}$$

where the $\eta_E = 1/2\left(t_x + t_y e^{i\varphi}\right)$, $\eta_R = 1/2\left(t_x - t_y e^{i\varphi}\right)\langle E_{in}|L\rangle$ and $\eta_L = 1/2\left(t_x - t_y e^{i\varphi}\right)\langle E_{in}|R\rangle$ are the complex field efficiencies with $\langle E_{in}|R,L\rangle$ as an inner product of the left-handed $|L\rangle$ and right-handed $|R\rangle$ circular polarizations, φ is the retardation of the imprinted element, and $t_{x,y}$ is the real-amplitude transmission coefficients for light polarized perpendicular and parallel to the optical axis. From Equation 3, the imprinted PG with $t_{x,y} \approx 0.14$ (Figure 1d) and $\varphi \approx 0.39\pi$ (Figure 2a) at a wavelength of 532 nm is expected to diffract around 5% of the light intensity, while 9% would propagate as a non-diffracting beam. Figure 2c shows good agreement as roughly 64% of the transmitted light is projected to the 0th order and 36% to the ±1st order. Also, the handedness of the diffracted circularly polarized beam is flipped. As the polarization of the generated beams does not vary spatially, polarization filtering could be applied in order to completely eliminate the non-diffracted light. In addition, if the half-wave retarder is fabricated, the ~100% efficiency could be achieved. Potentially, the retardation value could be enhanced by introducing a thicker layer of a-Si:H films.

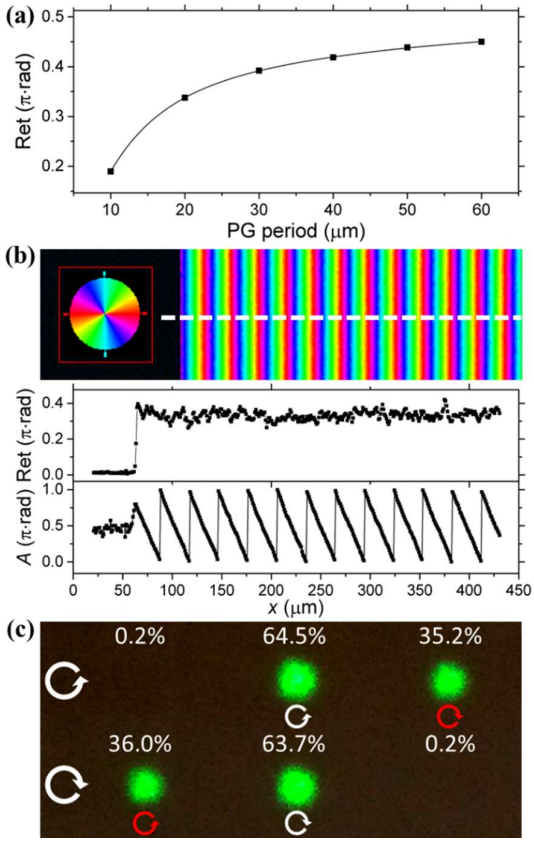

Figure 2. Femtosecond laser direct writing of GPOE designed as a polarization grating (PG). (a) Retardance dependence on the PG periodicity. (b) Imprinted PG with period of 30 μm: top image – the azimuth of the slow axis of the imprinted nanogratings; bottom graphs – the profiles (white dashed line in top image) of retardance and slow axis extracted from the birefringence image. Pseudo colours (inset) indicate the local orientation of slow axis. (c) Frequency-doubled Nd:YAG cw laser beam profiles of the transmitted right-handed circular (top) and left-handed circular (bottom) polarizations, and its corresponding diffraction efficiencies and polarizations states (white and red circular arrows) produced by PG.

The flexibility of the direct-write femtosecond laser nanostructuring technique allows recording of nearly any wavefront as a GPOE. The phase profile of an incident plane wave can be manipulated radially, azimuthally or both simultaneously resulting in complex designs.

Here, we demonstrate GPOEs with azimuthal phase variation serving as polarization and phase converters that generate optical vortices with radial and azimuthal polarizations. Initial experiments were carried out with a radially symmetric 1 mm diameter GPOE (Figure 3a-d). The topological charge of the element was set to $c = -1$, indicating that the resulting orbital angular momentum has opposite sign compared to the input spin momentum[38]. The average value of the induced retardance was $\sim 0.5\pi$ at 532 nm wavelength, which corresponds to the quarter-wave plate value.

The generated radially (azimuthally) polarized vortex with the orbital angular momentum $l = -1$ ($l = 1$) is considered as a superposition of two circularly polarized beams, one possessing the orbital angular momentum $l = -2$ ($l = 2$) and the other having a plane front[39]. The circularly polarized vortex with topological charge 2 can be separated by filtering with a quarter-wave plate and linear polarizer.

To verify the radial/azimuthal polarization optical vortex, the converter was inserted into the path of a left/right handed circularly polarized frequency-doubled Nd:YAG cw laser beam. For comparison the optical test system was modeled using the algorithm based on Jones matrix formalism and Fourier propagation[39]. The

propeller-shaped interference pattern, which is typical for double charged vortex beams, obtained after filtering with a linear polarizer confirms successful realization of the imprinted radially symmetric GPOE (Figure 3e-j).

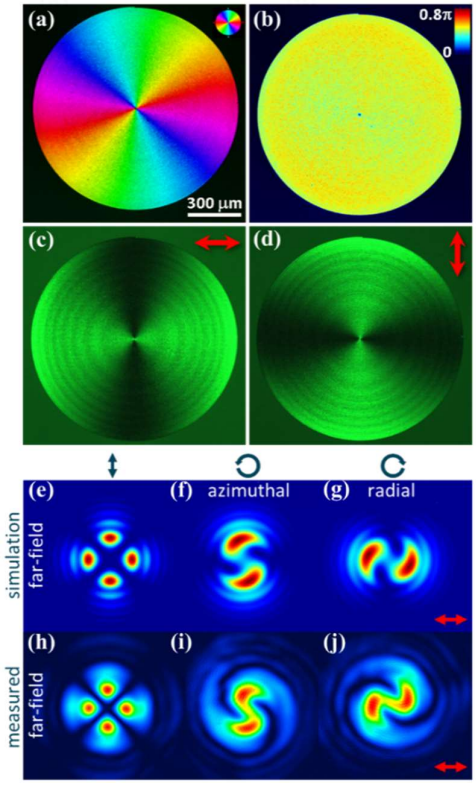

Figure 3. Radial and azimuthal polarization optical vortex converter for circular incident polarization. Imaged (a) azimuth of slow axis orientation and (b) averaged retardance value of roughly 0.5π specifies GPOE as a quarter-wave plate working at wavelength of 532 nm. Pseudo colors indicate the direction of slow axis. Color bar: 0–0.8π rad. (c), (d) Linearly polarized optical transmission images of polarization sensitive element illuminated by circularly polarized light. Scale bar is 300 µm. (e)-(g) Simulated and (h)-(j) measured far-field intensity profiles of frequency-doubled Nd:YAG cw laser beam generated by the radial (azimuthal) polarization vortex converter. Blue arrows indicate the polarization state of the incident beam; and red arrows indicate the polarization state of the light imaged on the camera detector.

In the next step, we imprinted a 2×2 mm array of 100 micron diameter converters (Figure 4). Same as in Figure 3, an intricate swirling interference pattern was observed in the far-field indicating the presence of the orbital angular momentum with l = ±2, where the handedness of the input circular polarization defines both the orientation of the generated whirlpool beams and the resulting polarization state (Figure 4b, c). This shows that the technique enables imprinting of elements with high resolution and can be exploited to develop miniaturized optics for optical manipulation of micro-objects on lab-on-a-chip platform[40], or directly imprint wave-plate arrays for polarization sensitive detectors[41].

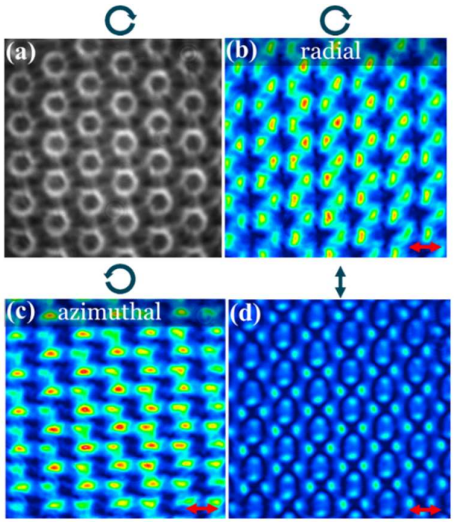

Figure 4. Beam intensity profiles of frequency-doubled Nd:YAG cw laser beam produced by the radial (azimuthal) polarization vortex micro-converters array, where (a) and (b) radially polarized vortices, (c) azimuthally polarized vortices, and (d) circularly/linearly polarized plane wave. Blue arrows indicate the polarization state of the incident beam, and red arrows indicate the polarization state of the light imaged on the camera detector. The light imaged in (a) was not filtered with polarizer. The pattern of the slow axis of the single imprinted converter corresponds to the geometry presented in Figure 3. The diameter of a single element is 100 μm. Far-field patterns were projected via a 20x microscope objective.

To realize the most basic GPOEs with radially varying phase profiles, we fabricated a 9×9 array of 100 μm diameter geometric phase lenses with focal lengths of $f_i = \pm(0.4\text{–}1.2)$ mm (Figure 5). Each lens was repeated nine times to form a 9×9 sub-array (Figure 5a, b). The orientation of the half-wave plate used to control the resulting geometric phase is expressed through the phase function of a conventional aspheric lens:

$$\theta(r) = \pm\frac{1}{4}\left(\pi + \left(\frac{2\pi}{\lambda}\right) R\left(1 - \sqrt{1 - \frac{r^2}{2R^2}}\right)\right), \tag{4}$$

with R as the radius of curvature ($f \approx 2R$), and r as the radial position, which corresponds to $\sqrt{x^2 + y^2}$. Sign of the phase determines the geometry of the imprinted element, which must be chosen according to the handedness of the input circular polarization[42]. Therefore the same geometry works as a converging or diverging lens for left-handed and right-handed circular polarizations, respectively (Figure 5c). These GPOEs were incorporated into the polarization sensitive optical imaging system operating at 546 nm wavelength. By changing the position (z_i) of the microscope objective, the imaged object was projected at different locations on the detector with the corresponding relative magnification of $M_i = f_i/(f_i\text{-}d_0)$, where the distance between the micro-lens array and the object is $d_0 \approx 10$ cm (Figure 5a). It should be noted that the absolute value of position z_i is defined by the overall measurement system, and its relative value is proportional to the focal length of the imaging micro-lens.

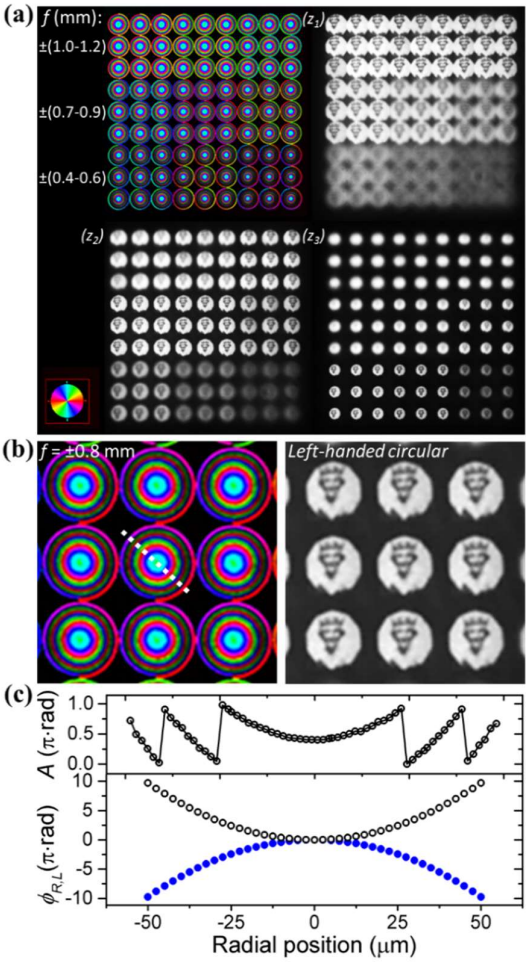

Figure 5. (**a**) GPOEs designed as a micro-lens array with focal lengths varying from f_1= ±0.4 mm to f_9= ±1.2 mm. Top left image, the azimuth of slow axis of imprinted nanogratings. The King John portrait was projected in z_1, z_2, z_3 planes incorporating the GPOEs into the polarization sensitive microscope system operating at 546 nm. The illumination is left-handed circularly polarized. (b) The azimuth of slow axis of zoomed-in nine lenses with the focal length of f = ±0.8 mm and its corresponding image projections using left-handed circularly polarized light. (c) Top graph, the azimuth profile of imprinted single element (dotted line in (b)). Bottom graphs, the estimated phase functions of transmitted plane wave with the right-handed or left-handed circular polarizations. Pseudo colors (inset (a)) indicate the direction of slow axis. The diameter of single element is 100 μm.

The final example of GPOE showing the simultaneous radial and azimuthal phase manipulation is a computer generated geometric phase Fourier hologram (CGH) that converts the initial Gaussian beam into the target intensity distribution. Using the adapted weighted Gerchberg-Saxton algorithm[43], the 8-bit grayscale CGH element with 0.1 Megapixel and pixel spacing of 3 μm was designed to encode the "Light" logo (Figure 6). During the continuous writing process, the maximum relative continuous phase change of π between the two adjacent pixels was achieved.

By using the Fourier transforming properties of a positive lens, the target image was reconstructed within the spectral range of 450-950 nm (Figure 6c-h). As it was mentioned before (Equation 3), to attain the high efficiency of an imprinted GPOE, the half-wave retardation must be ensured. However, even if the retardance is below this value, the non-diffracted beam can be completely removed by the means of polarization filtering (Figure 6a). In addition, the geometric phase is independent of wavelength. Therefore, the phase profile for different wavelengths transmitted through the same GPOE will be the same. In this case, the broadband sources can be implemented with a filtering efficiency, $\eta = I_{1st}/(I_{1st} + I_{0th})$, as high as ~100%

(Figure 6d-h). It also should be mentioned that the same accumulated phase due to the different wave vectors causes each wavelength to diffract at different angles.

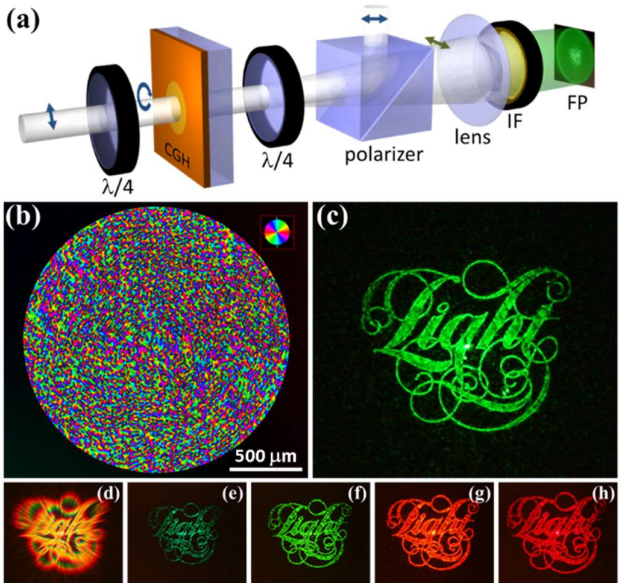

Figure 6. Computer generated geometric phase Fourier hologram (CGH). (a) Setup for polarization filtering and target image reconstruction: quarter-wave plates (λ/4), laser imprinted 8-bit grayscale CGH, linear polarizer, lens with f = 50 mm, interference filter (IF), Fourier plane (FP). Blue arrows indicate the state of beam polarization. (b) Orientation of slow axis of laser-imprinted CGH, and (c-h) it's resulting reconstructed image. The hologram was illuminated with (c) frequency-doubled Nd:YAG cw laser beam, and (d-h) supercontinuum laser beam, where (d) 450-950 nm, (e) 500 nm, (f) 550 nm, (g) 600 nm and (h) 650 nm filtered wavelengths. Scale bar is 500 μm.

4. CONCLUSIONS

In this work, we have demonstrated potential implementations of laser-induced periodic thin-film structures as the geometric phase manipulating elements including polarization gratings, Fourier holograms, micro-lenses and optical vortex micro-converters. The direct-write ultrafast laser nanostructuring is a high precision, flexible and time efficient technique. Through nonlinear light-matter interaction, the subwavelength resolution is ensured providing the possibility of reaching phase gradients higher than 1 rad/μm. As a result, the applicability to any material that supports laser-induced periodic structures including high-index semiconductors and insulators deposited on any substrate with different textures could revolutionize the fields of integrated flat optics and provide new methods of printing. The overall fabrication process of the millimeter-sized elements being on the time-scale of minutes could facilitate innovative solutions in fields such as security marking, data storage, solar cells, sensors & detectors.

ACKNOWLEDGMENTS

We thank C. Pannell and A. Patel for valuable discussions. The study has been supported by EPSRC (grant EP/M029042/1). The data for this work is accessible through the University of Southampton Institutional Research Repository (dx.doi.org/10.5258/SOTON/389785).

AUTHOR CONTRIBUTIONS

RD, MB and PGK conceived, planned, coordinated and supervised the work. RD carried out the experiments and wrote the manuscript. AGK manufactured the thin films, JZ and RD simulated the phase holograms. All authors discussed the results and contributed to the writing of the paper.

REFERENCES

1 Yu N, Capasso F. Flat optics with designer metasurfaces. *Nat Mater* 2014; **13**: 139–150.

2 Ni X, Emani NK, Kildishev A V, Boltasseva A, Shalaev VM. Broadband Light Bending with Plasmonic Nanoantennas. *Science* 2011; **335**: 427.

3 Yu N, Genevet P, Kats M a, Aieta F, Tetienne J-P, *et al.* Light Propagation with Phase Discontinuities Reflection and Refraction. *Science* 2011; **334**: 333–337.

4 Bomzon Z, Biener G, Kleiner V, Hasman E. Space-variant Pancharatnam-Berry phase optical elements with computer-generated subwavelength gratings. *Opt Lett* 2002; **27**: 1141–1143.

5 Miskiewicz MN, Escuti MJ. Direct-writing of complex liquid crystal patterns. *Opt Express* 2014; **22**: 12691–12706.

6 Beresna M, Gecevičius M, Kazansky PG. Polarization sensitive elements fabricated by femtosecond laser nanostructuring of glass. *Opt Mater Express* 2011; **1**: 783–795.

7 Lin D, Fan P, Hasman E, Brongersma ML. Dielectric gradient metasurface optical elements. *Science* 2014; **345**: 298–302.

8 Pancharatnam BYS. Generalized theory of interference, and its applications. Part I. Coherent pencils. *Proc Indian Acad Sci A* 1956; **44**: 247–262.

9 Berry M V. Quantal phase factors accompanying adiabatic changes. *Proc R Soc London Ser A* 1984; **392**: 45–57.

10 Anandan J. The geometric phase. *Nature* 1992; **360**: 307–313.

11 McManamon PF, Bos PJ, Escuti MJ, Heikenfeld J, Serati S, *et al.* A review of phased array steering for narrow-band electrooptical systems. *Proceeding IEEE* 2009; **97**.

12 Kudenov MW, Escuti MJ, Dereniak EL, Oka K. White-light channeled imaging polarimeter using broadband polarization gratings. *Appl Opt* 2011; **50**: 2283–2293.

13 Gecevičius M, Drevinskas R, Beresna M, Kazansky PG. Single beam optical vortex tweezers with tunable orbital angular momentum. *Appl Phys Lett* 2014; **104**: 231110.

14 Bomzon Z, Kleiner V, Hasman E. Pancharatnam-Berry phase in space-variant polarization-state manipulations with subwavelength gratings. *Opt Lett* 2001; **26**: 1424–1426.

15 Meinzer N, Barnes WL, Hooper IR. Plasmonic meta-atoms and metasurfaces. *Nat Phot* 2014; **8**: 889–898.

16 Zheng G, Mühlenbernd H, Kenney M, Li G, Zentgraf T, *et al*. Metasurface holograms reaching 80% efficiency. *Nat Nanotechnol* 2015; **10**: 308–312.

17 Kim J, Li Y, Miskiewicz MN, Oh C, Kudenov MW, *et al*. Fabrication of ideal geometric-phase holograms with arbitrary wavefronts. *Optica* 2015; **2**: 958.

18 Yariv A, Yhe P. *Optical Waves in Crystals*. Wiley: New York, 1984.

19 Sundaram SK, Mazur E. Inducing and probing non-thermal transitions in semiconductors using femtosecond laser pulses. *Nat Mater* 2002; **1**: 217–224.

20 Gattass RR, Mazur E. Femtosecond laser micromachining in transparent materials. *Nat Photonics* 2008.

21 Birnbaum M. Semiconductor surface damage produced by Ruby lasers. *J Appl Phys* 1965; **36**: 3688–3689.

22 Emmony DC, Howson RP, Willis LJ. Laser mirror damage in germanium at 10.6 um. *Appl Phys Lett* 1973; **23**: 598–600.

23 Guosheng Z, Fauchet PM, Siegman AE. Growth of spontaneous periodic surface structures on solids during laser illumination. *Phys Rev B* 1982; **26**: 5366–5381.

24 Van Driel HM, Sipe JE, Young JF. Laser-induced periodic surface structure on solids: A universal phenomenon. *Phys Rev Lett* 1982; **49**: 1955–1958.

25 Nemanich RJ, Biegelsen DK, Hawkins WG. Aligned, coexisting, liquid and solid regions in laser-annealed Si. *Phys Rev B* 1983; **27**: 7817–7820.

26 Bonse J, Krüger J, Höhm S, Rosenfeld A. Femtosecond laser-induced periodic surface structures. *J Laser Appl* 2012; **24**: 042006.

27 Gaković B, Trtica M, Batani D, Desai T, Panjan P, *et al*. Surface modification of titanium nitride film by a picosecond Nd:YAG laser. *J Opt A Pure Appl Opt* 2007; **9**: S76–S80.

28 Miyaji G, Miyazaki K. Origin of periodicity in nanostructuring on thin film surfaces ablated with femtosecond laser pulses. 2008; **16**: 16265–16271.

29 Hashida M, Miyasaka Y, Ikuta Y, Tokita S, Sakabe S. Crystal structures on a copper thin film with a surface of periodic self-organized nanostructures induced by femtosecond laser pulses. *Phys Rev B - Condens Matter Mater Phys* 2011; **83**: 2–6.

30 Vorobyev AY, Guo C. Colorizing metals with femtosecond laser pulses. *Appl Phys Lett* 2008; **92**: 2006–2009.

31 Baldacchini T, Carey JE, Zhou M, Mazur E. Superhydrophobic surfaces prepared by microstructuring of silicon using a femtosecond laser. *Langmuir* 2006; **22**: 4917–4919.

32 Eichstädt J, Römer GRBE, Huis in 't Veld a. JJ. Towards Friction Control using laser-induced periodic Surface Structures. *Phys Procedia* 2011; **12**: 7–15.

33 Bricchi E, Kazansky PG. Extraordinary stability of anisotropic femtosecond direct-written structures embedded in silica glass. *Appl Phys Lett* 2006; **88**: 111113–111119.

34 Drevinskas R, Gecevičius M, Beresna M, Bellouard Y, and Kazansky PG Tailored surface birefringence by femtosecond laser assisted wet etching. *Opt. Express* 2015; **23**: 1428-1437.

35 Drevinskas R, Beresna M, Gecevičius M, Khenkin M, Kazanskii AG, *et al.* Giant birefringence and dichroism induced by ultrafast laser pulses in hydrogenated amorphous silicon. *Appl Phys Lett* 2015; **106**: 171106.

36 Shah A V, Meier J, Vallat-Sauvain E, Wyrsch N, Kroll U, *et al.* Material and solar cell research in microcrystalline silicon. *Sol Energy Mater Sol Cells* 2003; **78**: 469–491.

37 Hasman E, Bomzon Z, Niv A, Biener G, Kleiner V. Polarization beam-splitters and optical switches based on space-variant computer-generated subwavelength quasi-periodic structures. *Opt Commun* 2002; **209**: 45–54.

38 Gecevičius M, Drevinskas R, Beresna M, Kazansky PG. Single beam optical vortex tweezers with tunable orbital angular momentum. *Appl Phys Lett* 2014; **104**: 231110.

39 Beresna M, Gecevičius M, Kazansky PG, Gertus T. Radially polarized optical vortex converter created by femtosecond laser nanostructuring of glass. *Appl Phys Lett* 2011; **98**: 201101.

40 Ladavac K, Grier D. Microoptomechanical pumps assembled and driven by holographic optical vortex arrays. *Opt Express* 2004; **12**: 1144–9.

41 Gecevičius M, Beresna M, Kazansky PG. Polarization sensitive camera by femtosecond laser nanostructuring. *Opt Lett* 2013; **38**: 4096–9.

42 Hasman E, Kleiner V, Biener G, Niv A. Polarization dependent focusing lens by use of quantized Pancharatnam-Berry phase diffractive optics. *Appl Phys Lett* 2003; **82**: 328–330.

43 Di Leonardo R, Ianni F, Ruocco G. Computer generation of optimal holograms for optical trap arrays. *Opt Express* 2007; **15**: 1913–1922.

Paper H

R. Drevinskas, J. Zhang, M. Beresna, M. Gecevicius, A. G. Kazanskii,
Yu. P. Svirko, and P. G. Kazansky

Laser material processing with tightly focused cylindrical vector beams

Applied Physics Letters 108, 221107 (2016)

APPLIED PHYSICS LETTERS **108**, 221107 (2016)

Laser material processing with tightly focused cylindrical vector beams

Rokas Drevinskas,[1,a)] Jingyu Zhang,[1] Martynas Beresna,[1] Mindaugas Gecevičius,[1] Andrey G. Kazanskii,[2] Yuri P. Svirko,[2,3] and Peter G. Kazansky[1]
[1]*Optoelectronics Research Centre, University of Southampton, Southampton SO17 1BJ, United Kingdom*
[2]*Physics Department, M.V. Lomonosov Moscow State University, Moscow 119991, Russia*
[3]*Institute of Photonics, University of Eastern Finland, P.O.BOX 111, FI-80101 Joensuu, Finland*

(Received 27 April 2016; accepted 21 May 2016; published online 3 June 2016)

We demonstrate a comprehensive modification study of silica glass, crystalline silicon, and amorphous silicon film, irradiated by tightly focused cylindrical vector beams with azimuthal and radial polarizations. The evidence of the longitudinal field associated with radial polarization is revealed by second harmonic generation in *z*-cut lithium niobate crystal. Despite the lower threshold of ring-shaped modification of silicon materials, the modification in the center of single pulse radially polarized beam is not observed. The phenomenon is interpreted in terms of the enhanced reflection of longitudinal component at the interface with high-index contrast, demonstrating that the longitudinal component is inefficient for the flat surface modification. Enhanced interaction of the longitudinal light field with silicon nanopillar structures produced by the first pulse of double-pulse irradiation is also demonstrated. *Published by AIP Publishing*. [http://dx.doi.org/10.1063/1.4953455]

The radially polarized beams focused with high numerical aperture optics lead to strong longitudinal electric fields, which are attractive for many applications, including particle acceleration,[1] high capacity optical recording,[2] near-field microscopy,[3] optical trapping of metallic particles,[4] and second-harmonic (SH) generation.[5–7] However, refractive index mismatch at the interface can strongly affect the light field that oscillates perpendicular to the surface.[8,9] Specifically, the field is suppressed when the beam propagates from a low refractive index into a high refractive index medium. This implies that it may be difficult to employ the field component perpendicular to the surface in the laser processing of materials with high refractive indices.

Successful ablation experiments of borosilicate glass by the single or multi-pulse irradiation[10] and modification of silicon with relatively high-index by the multi-pulse irradiation with the pronounced longitudinal field were reported.[11] Furthermore, enhanced modification by an electric field component perpendicular to the surface via a resonant absorption mechanism[12] was suggested to explain the results of the laser-induced nickel ablation.[13] Nevertheless, the direct experimental evidence confirming that the normal field component could produce stronger surface ablation was not demonstrated.

The vectorial distribution of the electric field could be visualized via self-assembled nanogratings, which are always aligned perpendicular to the electric field of the incident beam.[10,14–16] Tailored optical vector beams including radially and azimuthally polarized could be also exploited for complex surface structuring with ultrashort light pulses.[17]

In this letter, using amorphous silicon (a-Si:H), we demonstrate that the longitudinal component of the single pulse tightly focused radially polarized beam is inefficient for modification of flat surface. On the other hand, double pulse experiments indicate that the same vector beams exhibit an improved micromachining performance when employed for processing of pillar-like nanostructures on a crystalline silicon surface. The interaction of tightly focused radially and azimuthally polarized beams at the interfaces with different index contrast is experimentally analyzed for both bulk and thin film materials including silica glass, crystalline silicon and amorphous silicon. The experimental results agree well with the analytical and numerical simulations. In addition, to verify the presence of a strong longitudinal field, the total field of tightly focused radially and azimuthally polarized beams is indirectly visualized by second harmonic patterns generated in a z-cut lithium niobate ($LiNbO_3$) crystal. Moreover, the longitudinal electric field of the focused radially polarized light beam is revealed by the characterization of the self assembled nanogratings inside silica glass.

The experiments were performed with a femtosecond laser system (Pharos, Light Conversion, Ltd.) operating at a wavelength of 1030 nm and delivering pulses of 270 fs at repetition rates of 20 kHz (for silicon materials) and 200 kHz (for silica glass and lithium niobate crystal). The lower repetition rate was used to eliminate any possible heat accumulation in silicon between the first and second pulses. The longitudinal component was generated by tightly focusing radially polarized laser beam, using 0.65 NA dry objectives and 1.2 NA water immersion objectives (Fig. 1).

The Fourier computer generated hologram (CGH) that converts the initial Gaussian beam into the target annular beam was generated using the adapted weighted Gerchberg-Saxton (GSW) algorithm.[18] The beam with

[a)]Author to whom correspondence should be addressed. Electronic mail: rd1c12@soton.ac.uk

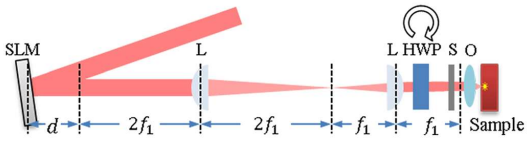

FIG. 1. Setup for femtosecond laser direct writing. Spatial light modulator (SLM), lenses (L), half-wave plate (HWP), S-waveplate (S), objective lens (O); d is the distance necessary for the beam to propagate after the reflection from SLM, and $2f_1$, f_1 correspond to the focal lengths of lenses with $f_1 = 300$ mm.

annular intensity distribution shaped with an electrically addressed spatial light modulator (SLM) (Hamamatsu, LCOS-SLM) was used to enhance the longitudinal component.[2,19,20] The Keplerian beam expander was used to adjust the beam size to match the pupil size of the objective lenses. The cylindrical distribution of the electric field polarization was controlled using a spatially variant polarization converter[21] referred to as S-waveplate. The radially or azimuthally polarized laser beams are generated by rotating the orientation of the incident linear polarization via a half-wave plate placed before the S-waveplate.

The electric field distribution of the focused annular cylindrical vector beams at the focal region is defined as follows:[22]

$$\text{Radial}: E_{transverse}(r,z) = A\int_{\beta}^{\alpha}\sqrt{\cos(\theta)}\sin(2\theta)l(\theta)J_1(kr\sin(\theta))e^{ikz\cos(\theta)}d\theta, \quad (1)$$

$$E_z(r,z) = 2iA\int_{\beta}^{\alpha}\sqrt{\cos(\theta)}\sin^2(\theta)l(\theta)J_0(kr\sin(\theta))e^{ikz\cos(\theta)}d\theta, \quad (2)$$

$$\text{Azimuthal}: E_{transverse}(r,z) = 2A\int_{\beta}^{\alpha}\sqrt{\cos(\theta)}\sin(\theta)l(\theta)J_1(kr\sin(\theta))e^{ikz\cos(\theta)}d\theta, \quad (3)$$

where r and z are cylindrical coordinates, α and β are the focusing angles determined by the outer and inner radius of the annular shaped beam, and $l(\theta)$ is the relative amplitude of the field. If the non-annular shapes are used, the β value becomes zero. In the case of $\beta/\alpha \approx 0.5$ and uniform relative amplitude, the ratio of the generated longitudinal and transverse light intensities in immersion medium is around 0.58 for 0.65 NA dry objective and 2.5 for 1.2 NA water immersion objective. Such focusing conditions were used in all following experiments and simulations.

Longitudinal field does not propagate and is confined to the focal region making its observation very difficult. However, longitudinal component can be visualized via a second harmonic generation. The second harmonic (SH) patterns generated by radially and azimuthally polarized beams can be obtained using the following second-order polarization $P(2\omega)$ generated in the z-cut $LiNbO_3$ crystal[23,24]

$$\begin{pmatrix} P_x(2\omega) \\ P_y(2\omega) \\ P_z(2\omega) \end{pmatrix} = \begin{pmatrix} 0 & 0 & 0 & 0 & d_{31} & -d_{22} \\ -d_{22} & d_{22} & 0 & d_{31} & 0 & 0 \\ d_{31} & d_{31} & d_{33} & 0 & 0 & 0 \end{pmatrix} \begin{pmatrix} E_x^2 \\ E_y^2 \\ E_z^2 \\ 2E_yE_z \\ 2E_xE_z \\ 2E_xE_y \end{pmatrix},$$

for azimuthal:

$$P_x(2\omega) = -2d_{22}E_xE_y,$$
$$P_y(2\omega) = -d_{22}E_x^2 + d_{22}E_y^2,$$

and for radial:

$$P_x(2\omega) = -2d_{22}E_xE_y + 2d_{31}E_xE_z,$$
$$P_y(2\omega) = -d_{22}E_x^2 + d_{22}E_y^2 + 2d_{31}E_yE_z, \quad (4)$$

where $E_{x,y,z}$ are Cartesian components of the electric field of the fundamental beam introduced in Eqs. (1)–(3), and $d_{22} = 2.1$ pm/V, $d_{31} = 4.3$ pm/V, and $d_{33} = 27$ pm/V are the absolute values of components of nonlinear susceptibility tensor.[25]

In order to verify the existence of the longitudinal field, the cylindrical vector beams were focused inside a z-cut lithium niobate crystal via a 0.65 NA microscope objective 100 μm beneath the surface. The generated SH was collected with a 1.2 NA water immersion objective after the sample, imaging the focal plane and far-field intensity distributions of the focusing lens. The SH patterns were observed for both cylindrical radially and azimuthally polarized beams, while the pronounced longitudinal component in the radially polarized beam results in ~70% higher SH power (at 1.5 TW/cm^2 pump intensities) in comparison with that produced by the azimuthally polarized beam. The SH power increase is caused by the $2d_{31}E_xE_z$ and $2d_{31}E_yE_z$ components of the second-order polarization produced by the non-zero longitudinal (E_z) component of the field at the fundamental frequency (Eq. (4)). When the longitudinal field is enhanced, e.g., the ratio with transverse field is 0.58, the contribution of these terms in SH generation increases.

The focal plane SH pattern has the shape of an annular ring for both radial and azimuthal polarizations (see Figs. 2(b-iii) and 2(d-iii)), while in the far-field SH beam profile becomes polarization dependent. Specifically, if the fundamental beam is azimuthally polarized, the far-field SH beam remains ring-shaped (Fig. 2(b-vi)), while the radially polarized fundamental beam in the far-field evolves into a three-lobed pattern (Fig. 2(d-vi)), which is determined by the orientation of the X and Y axes in the z-cut lithium niobate crystal. These experimental observations agree very well with the results of numerical simulation shown in Figs. 2(a) and 2(c), where the polarization component $P_z(2\omega) = d_{31}(E_x^2 + E_y^2) + d_{33}E_z^2$ is not considered because it does not contribute to the transversal SH field measured in our experiments. One can conclude that the difference in the transverse SH patterns generated by the focused radially and azimuthally polarized beams originate from the longitudinal component of the fundamental light field. It should be noted that since the Figure 2 shows only transversal component of the SHG wave, the observable quantitative difference in the

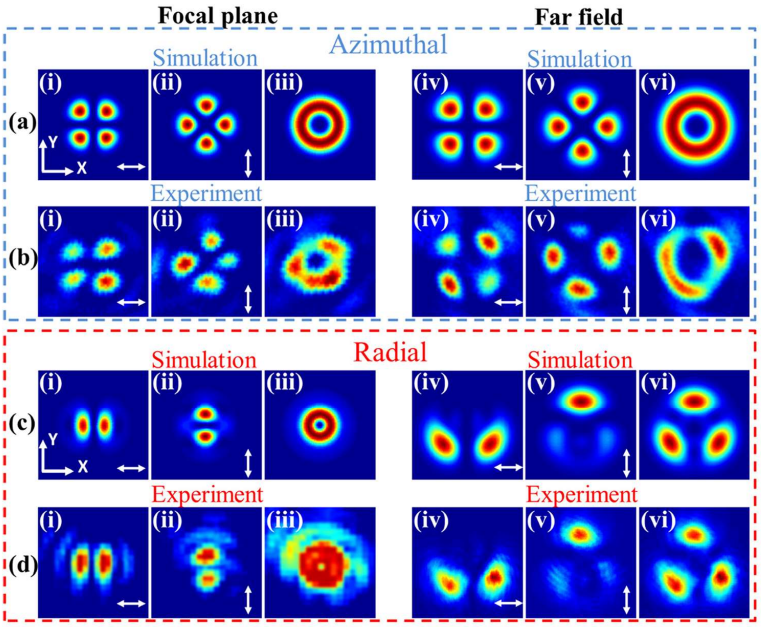

FIG. 2. Second-harmonic patterns generated by focusing ((a) and (b)) azimuthally and ((c) and (d)) radially polarized laser beams, (i, ii, iii) imaged focal plane and (iv, v, vi) the far-field of the focusing lens. In simulations, only the transverse component is shown. White arrows indicate the polarization state of light after the linear analyzer. The x and y axes show the crystal orientation. All intensities are normalized.

SHG intensity calculated (iii-c) and measured (iii-d) originates from the nonzero longitudinal component, which—according to Eq. (4)—is nonzero in the focal plane. As well, the imaging performed with the high numerical aperture optics makes the measurements very sensitive to any minor deviations in the system that can affect the signal.

In further experiments, single dots were imprinted inside silica glass to visualize the vectorial distribution of electric field in the focus. A train of 2000 pulses with 250 nJ pulse energy was focused via a 0.65 NA objective, 120 μm beneath the substrate surface. Under these conditions, the self-assembled nanogratings are induced. The nanostructures with the sub-wavelength periodicity behave as a uniaxial birefringent material where the slow axis is oriented perpendicular to the beam polarization. The slow axis orientation with corresponding vectorial distribution of electric field was mapped using quantitative birefringence measurement system (CRi Abrio; Olympus BX51) (Fig. 3).

The birefringence cannot be observed if the optical axis is oriented perpendicular to the image plane (Fig. 3(a-iii)). Thus, the slow axis induced by the longitudinal field can be visualized only from the side of the structure. One can observe from Fig. 3(b-iii) that the center of the light-induced modification is occupied by an anisotropic structure (light beam) having a slow axis (polarization) oriented perpendicular (parallel) to the beam propagation direction. However, on the sides of the modified region, the nanogratings with orthogonal orientation are induced, which reveals the transverse component of the light polarization (Fig. 3(b-iv)). In contrast, after irradiation with the azimuthally polarized light, the anisotropy associated with longitudinal component is not observed (Fig. 3(b-i)).

Further, to directly imprint the intensity distribution of the tightly focused annular cylindrically polarized beams in high-index material, we carried out the experiments on irradiation of 300 nm thick a-Si:H film. The water immersion microscope objective of 1.2 NA was used for focusing of the beam. The irradiation with pulse energies below 150 nJ were ensured to induce the nanocrystalline type of modification without ablation in amorphous silicon.[26,27] In total, the 21 sets of dots were imprinted by a single pulse irradiation of radially or azimuthally polarized beams at different focusing depths ranging from -10 μm to 10 μm (0.5 μm step), relative to the substrate surface (Fig. 4). By choosing the strongest modification, we ensure that the modification is performed in the focus (Fig. 4(i), (ii)).

Weak dependence of the modification on the focus depth was observed indicating a Bessel-like long Rayleigh length, typical for cylindrically polarized beams (Fig. 4). The threshold energy of modification was more than 40% lower for

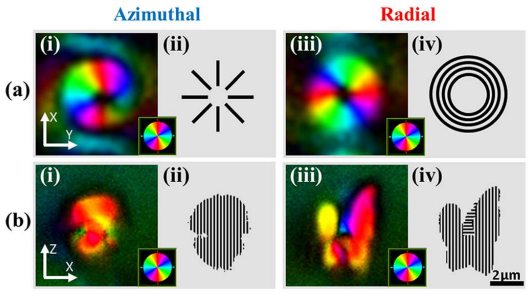

FIG. 3. Slow axis characterization of the birefringent structures inside silica glass induced by azimuthally (left) and radially (right) polarized laser beams. (a) (i, iii) Top view and (b) (i, iii) side view of the slow axis orientation, with (a) (ii, iv), (b) (ii, iv) their corresponding schematics of the possible nanogratings distribution. Pseudo color indicates the direction of slow axis (insets).

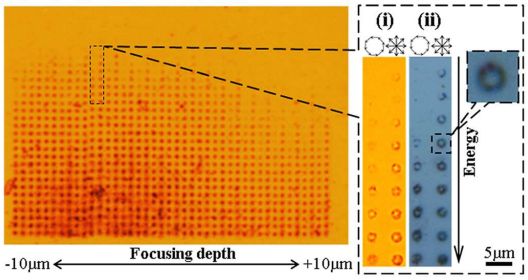

FIG. 4. Optical transmission images of structures imprinted by annular-shape of radially and azimuthally polarized beams in amorphous silicon film at different focus planes, where in the inset the same structures are compared in transmission (i) and reflection (ii) modes. The pulse energy in the inset (right images) varies from 30 nJ to 70 nJ.

radially polarized than for azimuthally polarized beams, 30 nJ versus 50 nJ, respectively. This phenomenon could be explained by the lower Fresnel reflection and different material transformation dynamics for *p*-polarization compared to *s*-polarizations at the interface of modified region.[28] However, in both cases, only the ring-shaped patterns were produced. The modification in the center of annulus, where the strong longitudinal field is present, was not observed. The surface of the film remains flat in the conditions of irradiation below the ablation threshold. Consequently, if the second pulse is fired, modification of the film qualitatively will be the same as by the first pulse and will not reveal the presence of longitudinal component.

Finally, we performed experiments on ablation of *p*-type crystalline silicon (111). The radially and azimuthally polarized beams with pulse energy of 150 nJ were focused on the surface via a 1.2 NA water immersion objective. The irradiation by the single pulse radially polarized beam resulted in a ring-shaped modification with nanopillar structure in the center (Fig. 5 (top-left)). Specifically, the molten silicon is pushed away radially from the region with maximum deposited energy leading to the ring-shaped ablation pattern. The excess material pushed to the center of the ring solidifies forming the nanopillar structure. In the case of azimuthal polarization, the nanopillar structure is not formed due to the lack of deposited energy and possibly the different material dynamics after irradiation.[28] The deposited energy is suppressed by the higher Fresnel reflection for *s*-polarization (azimuthal case) compared to *p*-polarization (radial case) at the interface.

The laser-induced nanopillar, which was emerged along the beam propagation direction, was subsequently ablated during the second pulse irradiation due to the enhanced transmission of the longitudinal field along the distorted interface (Fig. 5 (top-right)). However, the irradiation by double pulse azimuthally polarized beam kept the center untouched partially covering it with the ablated material (Fig. 5 (bottom)). This observation indicates that the needle shaped surface structures aligned along the beam propagation direction are necessary for interaction with the longitudinal field.

Numerical simulations of focused vector beams were performed[29] to understand why the strong effect of

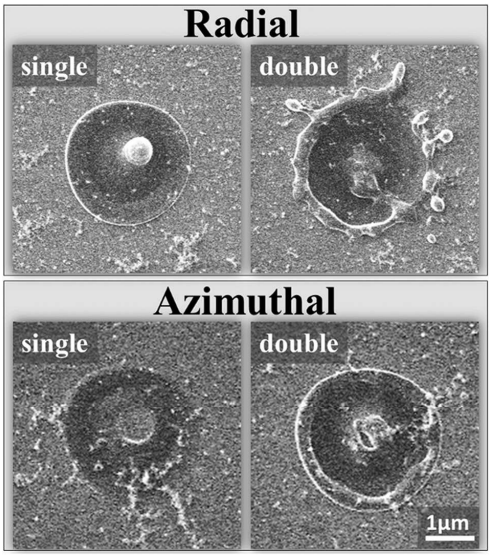

FIG. 5. SEM images of the laser processed crystalline silicon surface. Each spot was irradiated with single (left) and double (right) pulse radially (top) and azimuthally (bottom) polarized beams with energies of 150 nJ.

longitudinal field did not produce modification in amorphous and crystalline silicon. The simulations revealed that the transverse electric field propagates without significant amplitude changes, while the longitudinal electric field is discontinuous through the interface when the incident beam is focused at the *water*/*silicon* interface (Fig. 6 (top)). The magnitude of longitudinal component decreases by a factor of $\varepsilon_2/\varepsilon_1$ ($\sim$7.4), where ε_1 and ε_2 are the dielectric constants of the media. Moreover, the total intensity distribution of radially and azimuthally polarized beams after the transmission through the *water*/*silicon* interface (Fig. 6 (top)) match well with the structures imprinted in the amorphous silicon film (Fig. 4).

On the other hand, inside the silica glass, the magnitude of longitudinal and transverse components are of the same order, since the refractive index contrast at the *air*/*silica* interface is relatively low (Fig. 6 (bottom)). Experimentally, it was confirmed by the nanogratings formation both parallel and perpendicular to the beam propagation direction (Fig. 3).

In conclusion, we have demonstrated the evidence of longitudinal component of tightly focused radially polarized beam by the observation of enhanced second harmonic generation in the *z*-cut lithium niobate crystal and by the laser-induced anisotropy oriented perpendicular to the longitudinal field in silica glass. Despite the lower threshold of ring-shaped modification in amorphous silicon film and the nanopillar formation in crystalline silicon, the longitudinal electric field generated by the single pulse radially polarized beam produces a negligible modification, which can be explained by the discontinuity of longitudinal field at the high-index-contrast interfaces. Thus, the longitudinal electric field is not effective for modifying flat surfaces of materials with high refractive index when irradiating from a low index

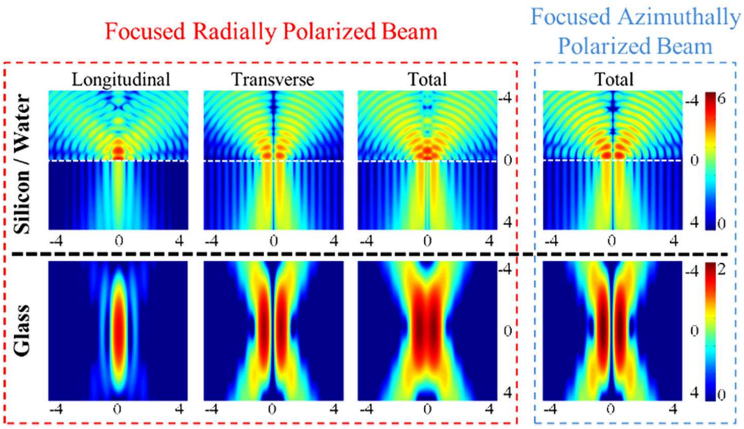

FIG. 6. Simulation of cylindrical vector beams focused on silicon surface ($n = 3.613$) (top) and inside silica glass ($n = 1.458$) (bottom) via a 1.2 NA water-immersion ($n = 1.3265$) microscope objective (top) and via a 0.65 NA dry microscope objective (bottom). Color scales are logarithmic in arbitrary units; axes are in the units of wavelength.

mediums. On the other hand, the effect of the high-index-contrast interface can be eliminated by using high numerical aperture immersion objectives, e.g., solid immersion lenses. Alternatively, the sub-wavelength structures oriented along the beam propagation direction such as nanopillars or enhanced surface roughness could be beneficial for material processing by pronounced longitudinal field.

The study has been supported by EPSRC (Grant No. EP/M029042/1). P.G.K. thanks Ministry of Education and Science of the Russian Federation (Grant No. 14.Z50.31.0009). Y.P.S. thanks Russian Foundation for Basic Research (Grant No. 16-02-00684). The data for this work are accessible through the University of Southampton Institutional Research Repository (http://dx.doi.org/10.5258/SOTON/384580).

[1]Y. Liu, D. Cline, and P. He, Nucl. Instrum. Methods Phys. Res. A **424**, 296 (1999).
[2]X. Li, Y. Cao, and M. Gu, Opt. Lett. **36**, 2510 (2011).
[3]M. R. Beversluis, L. Novotny, and S. J. Stranick, Opt. Express **14**, 2650 (2006).
[4]Q. Zhan, Opt. Express **12**, 3377 (2004).
[5]A. Ohtsu, Y. Kozawa, and S. Sato, Appl. Phys. B Lasers Opt. **98**, 851 (2010).
[6]D. P. Biss and T. G. Brown, Opt. Lett. **28**, 923 (2003).
[7]G. Bautista, M. J. Huttunen, J. Mäkitalo, J. M. Kontio, J. Simonen, and M. Kauranen, Nano Lett. **12**, 3207 (2012).
[8]G. M. Lerman and U. Levy, Opt. Express **16**, 4567 (2008).
[9]W.-C. Kim, Y.-J. Yoon, H. Choi, N.-C. Park, and Y.-P. Park, Opt. Express **16**, 13933 (2008).
[10]C. Hnatovsky, V. G. Shvedov, W. Krolikowski, and A. Rode, Phys. Rev. Lett. **106**, 123901 (2011).
[11]C. Hnatovsky, V. G. Shvedov, N. Shostka, A. V Rode, and W. Krolikowski, Opt. Lett. **37**, 226 (2012).
[12]F. Brunel, Phys. Rev. Lett. **59**, 52–55 (1987).
[13]H. Iwase, S. Kokubo, S. Juodkazis, and H. Misawa, Opt. Express **17**, 4388–4396 (2009).
[14]P. G. Kazansky, H. Inouye, T. Mitsuyu, K. Miura, J. Qiu, K. Hirao, and F. Starrost, Phys. Rev. Lett. **82**, 2199 (1999).
[15]Y. Shimotsuma, P. G. Kazansky, J. Qiu, and K. Hirao, Phys. Rev. Lett. **91**, 247405 (2003).
[16]B. Poumellec, M. Lancry, A. Chahid-Erraji, and P. G. Kazansky, Opt. Mater. Express **1**, 766–782 (2011).
[17]J. Ouyang, W. Perrie, O. J. Allegre, T. Heil, Y. Jin, E. Fearon, D. Eckford, S. P. Edwardson, and G. Dearden, Opt. Express **23**, 12562–12572 (2015).
[18]R. Di Leonardo, F. Ianni, and G. Ruocco, Opt. Express **15**, 1913–1922 (2007).
[19]L. Yang, X. Xie, S. Wang, and J. Zhou, Opt. Lett. **38**, 1331 (2013).
[20]H. Wang, L. Shi, B. Lukyanchuk, C. Sheppard, and C. T. Chong, Nat. Photonics **2**, 501 (2008).
[21]M. Beresna, M. Gecevičius, P. G. Kazansky, and T. Gertus, Appl. Phys. Lett. **98**, 201101 (2011).
[22]K. Youngworth and T. Brown, Opt. Express **7**, 77 (2000).
[23]G. D. Boyd, R. C. Miller, K. Nassau, W. L. Bond, and A. Savage, Appl. Phys. Lett. **5**, 234 (1964).
[24]P. A. Franken, A. E. Hill, C. W. Peters, and G. Weinreich, Phys. Rev. Lett. **7**, 118 (1961).
[25]D. A. Roberts, IEEE J. Quantum Electron. **28**, 2057 (1992).
[26]A. V. Emelyanov, A. G. Kazanskii, M. V. Khenkin, P. A. Forsh, P. K. Kashkarov, M. Gecevicius, M. Beresna, and P. G. Kazansky, Appl. Phys. Lett. **101**, 081902 (2012).
[27]R. Drevinskas, M. Beresna, M. Gecevičius, M. Khenkin, A. G. Kazanskii, I. Matulaitienė, G. Niaura, O. I. Konkov, E. I. Terukov, Yu. P. Svirko, and P. G. Kazansky, Appl. Phys. Lett. **106**, 171106 (2015).
[28]Q. Zhang, Adv. Opt. Photonics **1**, 1–57 (2009).
[29]D. Biss and T. Brown, Opt. Express **9**, 490 (2001).

Paper I

R. Drevinskas, M. Beresna, O. Deparis, and P. G. Kazansky

Laser assisted modification of poled silver-doped nanocomposite soda-lime glass

MATEC Web of Conferences 8, 02008 (2013)

MATEC Web of Conferences **8**, 02008 (2013)
DOI: 10.1051/matecconf/20130802008

Laser assisted modification of poled silver-doped nanocomposite soda-lime glass

Rokas Drevinskas[1,*], Martynas Beresna[1], Olivier Deparis[2] and Peter G. Kazansky[1]
[1]*Optoelectronics Research Centre, University of Southampton, SO17 1BJ, United Kingdom*
[2]*Solid-State Physics Laboratory, University of Namur (FUNDP), 61 rue de Bruxelles, B-5000 Namur, Belgium*
*rd1c12@orc.soton.ac.uk

Abstract: Thermal poling assisted homogenization of polydisperse Ag nanoparticles embedded in the soda-lime glass is demonstrated. The homogenization leads to the narrowing of the localized surface plasmon resonance. The subsequent irradiation with linearly polarized ultrashort laser pulses induces spectrally defined and four times larger dichroism than in non-poled sample.

Metal-doped nanocomposite glasses are of interest for their unique linear and nonlinear optical properties. Simple and low cost fabrication technique of nanocomposite glass is based on ion exchange. In this technique the metal ions are embedded in glass matrix by ion exchange with further annealing in a reducing atmosphere, resulting in randomly distributed metal aggregates with an exponentially decreasing filling factor across the depth [1]. The optical properties of nanoparticles can then be controlled by ultrashort laser pulses with a wavelength close to localized surface plasmon resonance [2]. However, a non-uniform distribution of nanoparticles in the glass matrix complicates any laser assisted modification. In this work we demonstrate the poling assisted homogenization of Ag nanoparticles embedded in soda-lime glass matrix, which improves laser assisted modification of optical properties.

The polydisperse nanocomposite sample prepared from soda-lime float glass by Ag^+-Na^+ ion exchange method was provided by CODIXX AG. The spherical Ag nanoparticles of 30-40 nm mean diameter were distributed in a thin surface layer of several micrometers thickness with the high filling factor close to the surface. The sample was thermally poled in air inside the oven using pressed-contact electrodes, with the anode facing the Ag-doped area. The laser modification of Ag nanoparticles was performed using a regeneratively amplified, mode-locked Yb:KGW based ultrafast laser system (Pharos, Light Conversion Ltd.). The laser system was operating at 515 nm (frequency doubled) and 200 kHz repetition rate. The laser beam was focused on the top of sample via a ×5 (NA=0.13) objective lens. The modification of poled area was carried out using 1 ps pulse duration, linear polarization, 0.5 mm/s writing speed with 5 µm interline distance, 10000 pulses/mm density and the varying laser pulse intensity from 2.2×10^{10} W/cm^2 to 4.4×10^{11} W/cm^2, i.e. below the damage threshold of soda-lime glass. For the modification of pristine area we used 700 fs pulses, linear polarization, 5 mm/s speed with 5 µm interline distance, 40000 pulses/mm density and the intensities from 5.0×10^{10} W/cm^2 to 2.3×10^{11} W/cm^2. For the optical characterization, the absorption spectra of pristine and poled areas were taken with UV-VIS-NIR spectrophotometer (Varian, CARY 500) and optical characterization of modified micro-areas was made with UV-VIS-NIR imaging spectrometer (Andor, Shamrock SR-303i) and VIS microspectrometer system (Olympus BX51, CRAIC). The spectral dependence of modified Ag-doped glass for s- and p-polarizations was measured by inserting linear polarizer before the sample. Images were taken with Olympus BX51 system using ×60 objective lens.

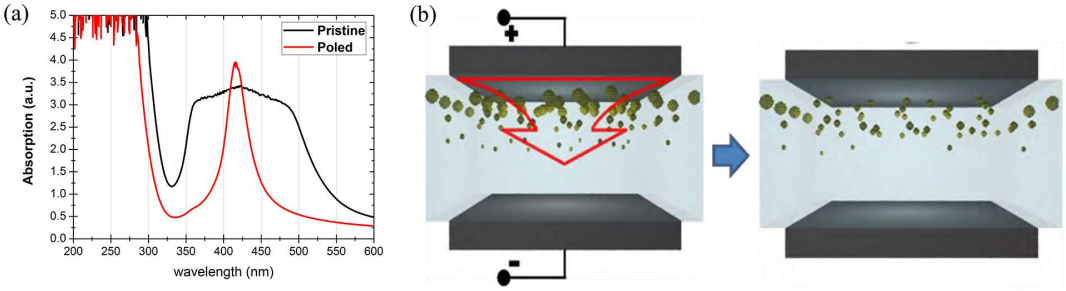

Fig.1. (a) Absorption Spectra of pristine (black) and thermally poled (red) Ag-doped soda-lime glass. (b) Schematic procedure for poling, red arrow indicates the gradient of released Ag ions.

The thermal poling procedure leads to the ionization of Ag clusters. The higher the filling factor of Ag aggregates, the higher the concentration of Ag ions is released [1]. As a result, the top layer is ionized much faster

than the bottom layers reducing the concentration and size of the nanoparticles located close to the surface. After thermal poling procedure we observe narrowing and increase of the absorption band of Ag nanoparticles (Fig.1) indicating that size distribution of the nanoparticles is reduced. This is a clear evidence of homogenization of Ag-doped glass matrix.

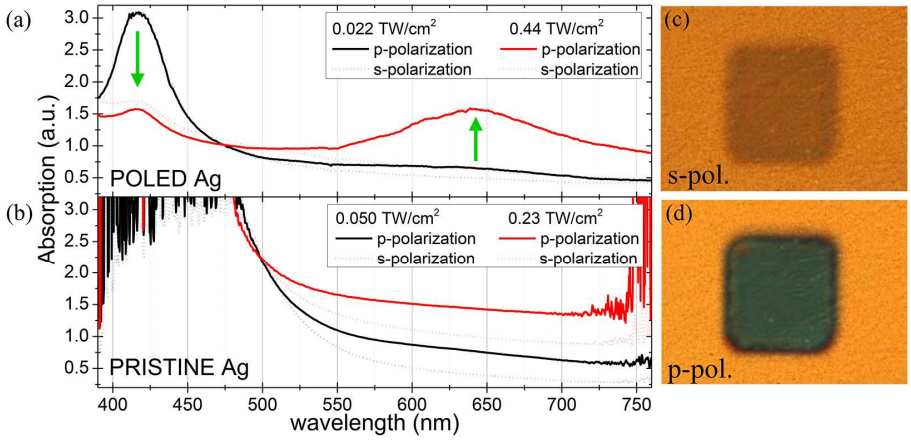

Fig.2. Absorption spectra of (a) poled areas modified with 2.2×10^{10} W/cm^2 and 4.4×10^{11} W/cm^2 laser pulse intensities and (b) pristine areas modified with 5.0×10^{10} W/cm^2 and 2.3×10^{11} W/cm^2, spectra were collected both for s- and p-polarized excitation. (c,d) Images of the poled area modified with the highest energy, for s- and p-polarized illumination, respectively. Green arrows indicate the direction of movement of spectra after the modification.

Ultrashort laser pulse assisted modification of metal-embedded glasses can cause both linear and nonlinear effects due to extremely high peak intensities and the local enhancement of electric field, especially when the irradiated frequency coincides with oscillations of electrons localized on metal surface. As a result Ag clusters in a strong electric field are ionized leading to the shape deformation and dissolution [2, 3]. The deformed Ag nanoparticles exhibit the differential absorption for s- and p-polarizations (Fig. 2). Although the laser pulse frequency is off the peak of SP resonance, we observe strong laser induced dichroism in thermally poled sample. The laser induced dichroism in the poled area was four times larger than in pristine sample at 640 nm. We assume that there is a combination of two states, modified and non-modified Ag clusters, where the interline-unaffected Ag clusters are dominant in the absorption spectra with the peak at 416 nm and elongated Ag clusters responsible for the SP resonance splitting into two peaks, one around 640 nm for p-polarized excitation and another very weak below 416 nm for s-polarized excitation. Combination of thermal poling with ultrafast laser writing can lead to a fine control of optical and structural properties of metal-doped soda-lime glass and can be applied for fabrication of optical components and optical data storage [4, 5].

Acknowledgements

The work was supported by the project FEMTOPRINT, financed by the European Commission Factories of the Future program (FP7/ NMP/Project No 260103), http://www.femtoprint.eu/.

References

[1] O. Deparis, P. G. Kazansky, A. Podlipensky, et al. “Poling-assisted bleaching of soda-lime float glasses containing silver nanoparticles with a decreasing filling factor across the depth”, *Journal of Applied Physics* 2006, Vol.100(4), pp. Art. No. 044318.
[2] M. Kaempfe, et al. “Ultrashort laser pulse induced deformation of silver nanoparticles in glass,” *Appl. Phys. Lett*. 1999, 74, 1200-1202.
[3] M. Kaempfe, et al. “Polarization dependence of the permanent deformation of silver nanoparticles in glass by ultrashort laser pulses,” *Eur. Phys. J*. 2001, D 16, 237-240.
[4] A. Royon, et al. “Silver cluster embedded in glass as a perennial high capacity optical recording medium”, *Advanced materials* 2010, 22, 5282-5286.
[5] A. Podlipensky, et al. “Femtosecond laser assisted production of dichroitic 3D structures in composite glass containing Ag nanoparticles,” *Appl. Phys*. 2005, A 80, 1647-1652.

Paper J

S. Chervinskii, R. Drevinskas, D. V. Karpov, M. Beresna, A. A. Lipovskii, Yu. P. Svirko, and P. G. Kazansky

Revealing the nanoparticles aspect ratio in the glass-metal nanocomposites irradiated with femtosecond laser

Scientific Reports 5, 1-10 (2015)

www.nature.com/scientificreports

OPEN

Revealing the nanoparticles aspect ratio in the glass-metal nanocomposites irradiated with femtosecond laser

Received: 28 April 2015
Accepted: 04 August 2015
Published: 08 September 2015

S. Chervinskii[1,2], R. Drevinskas[3], D. V. Karpov[1,4], M. Beresna[3], A. A. Lipovskii[2,4], Yu. P. Svirko[1] & P. G. Kazansky[3,5]

We studied a femtosecond laser shaping of silver nanoparticles embedded in soda-lime glass. Comparing experimental absorption spectra with the modeling based on Maxwell Garnett approximation modified for spheroidal inclusions, we obtained the mean aspect ratio of the re-shaped silver nanoparticles as a function of the laser fluence. We demonstrated that under our experimental conditions the spherical shape of silver nanoparticles changed to a prolate spheroid with the aspect ratio as high as 3.5 at the laser fluence of 0.6 J/cm². The developed approach can be employed to control the anisotropy of the glass-metal composites.

Ensembles of elongated metal nanoparticles embedded in transparent media are of interest due to their intrinsic anisotropy[1] that results in linear and nonlinear dichroism and birefringence[2,3]. Conventionally, such anisotropic glass-metal nanocomposites (GMNs) are fabricated by stretching glass slabs containing spherical nanoparticles[4]. In particular, this technique is used in commercially available dichroic polarizers, which employ glasses containing elongated silver or copper nanoparticles. However, modern functional devices require control of the birefringence and dichroism with sub-micron spatial resolution when the shape of the nanoparticles varies over the substrate in a prescribed fashion at distances comparable with the wavelength. These devices are of interest for optical encoding, multidimensional data storage and fabrication of complex, polarization-sensitive spectral masks[5]. The required space-selective shaping of metal nanoparticles can be achieved via irradiating GMNs with intense laser[6–9] or ion beams[10,11].

Irradiation of glasses containing spherical silver nanoparticles by femtosecond[12], picosecond[13], nanosecond[9] pulses or even continuous-wave (CW) laser beams[14] results in the formation of metal spheroids with the processing condition-dependent shape. The type—prolate or oblate—and aspect ratio of the spheroidal nanoparticles are usually characterized with transmission electron microscopy (TEM)[3,15,16]. TEM and other characterization techniques, however, cannot be used to examine the shape of the nanoparticles *in-situ* as it is required for fabrication of complex, polarization-sensitive planar plasmonic and photonic systems. At the same time, the laser-induced anisotropy of the metal nanoparticles manifests itself in the polarization sensitivity of the optical absorption spectra; these spectra have been thoroughly studied in silver-based GMN in a wide range of expositions[15]. Although the information on the ensemble-averaged aspect ratio of the nanoparticles is stored in the polarization-sensitive absorption and

[1]Institute of Photonics, University of Eastern Finland, P.O.Box 111 Joensuu, FI-80101 Finland. [2]Institute of Physics, Nanotechnology and Telecommunications, Peter the Great St. Petersburg Polytechnic University, 29 Polytechnicheskaya, St. Petersburg, 195251 Russia. [3]Optoelectronics Research Centre, University of Southampton, Southampton, SO17 1BJ UK. [4]Department of Physics and Technology of Nanostructures, St. Petersburg Academic University, 8/3 Khlopina, St.-Petersburg, 194021 Russia. [5]Advanced Laser Technologies Centre, Mendeleev University of Chemical Technology of Russia, 9 Miusskaya pl., Moscow, 125047 Russia. Correspondence and requests for materials should be addressed to S.C. (email: semen.chervinskii@uef.fi)

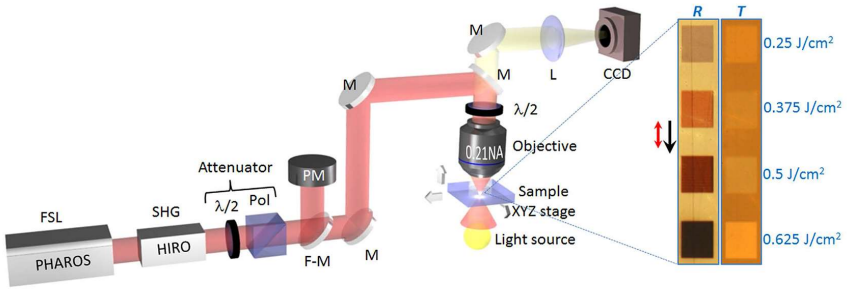

Figure 1. Experimental setup of femtosecond laser modification: femtosecond laser (FSL), second harmonic generator (SHG), half-wave plates (λ/2), polarizer (Pol), power meter (PM), flip-mirror (F-M) allowing to send the radiation to the power meter (PM), dichroic mirrors (M), lens (L), objective lens (0.21 NA), XYZ translation stage. Laser processing was monitored by CCD camera. Inset shows the optical transmission (*T*) and reflection (*R*) images of laser-modified regions of GMN (of $1 \times 1\,mm^2$) irradiated with various laser fluences. Black arrow indicates the laser writing direction, red arrow—the state of polarization. Drawn by Rokas Drevinskas.

reflection spectra, the problem of revealing the nanoparticles aspect ratio from the linear dichroism of the laser processed GMN is still unresolved.

In this paper, we report an investigation of the linear dichroism spectra of silver-based GMN irradiated with intense femtosecond laser pulses at a wavelength of 515 nm. Using an effective media approximation for ellipsoidal inclusions[17], we analyze the measured differential transmission spectra for the light polarized parallel (*s*) and perpendicular (*p*) to the polarization azimuth of the femtosecond laser beam used for the GMN modification, and depict the dependence of the aspect ratio of nanoparticles in laser-exposed GMN on the processing conditions.

Methods

GMN layer fabrication. GMN samples were prepared from soda-lime float glass by Ag^+-Na^+ ion exchange method described in details elsewhere[18]. Ion exchange process was carried out at 325 °C immersing the soda-lime glass slides into $Ag_{0.5}Na_{0.95}NO_3$ solution for 20 minutes, when the subsurface of the glass was enriched with silver ions. Later, the sample was annealed in hydrogen atmosphere at atmospheric pressure for 10 minutes at 250 °C. During the annealing, the silver ions in the glass were reduced and then aggregated into nanoparticles[19]. Finally, we made two roughly 100 nm thick layers of several nanometers sized silver nanoparticles (Ag NPs) embedded in the glass beneath both surfaces of the slide[20]. Our TEM measurements showed that the procedure we use results in step-like concentration profile of Ag NPs in the glass. According to the evaluations from Ref. 20 for similarly manufactured GMN, the volume fraction of spherical nanoparticles is about 0.1 for 2 nm particles radii. This size was taken from the best fit of the measured optical absorption spectrum, supposing the width of the Ag NPs size distribution was below 15%[20].

Femtosecond laser modification of glass-silver nanocomposites. In order to investigate the laser modification of the GMN, the sample was irradiated with 330 fs pulses generated by regeneratively amplified, mode-locked Yb:KGW based ultrafast laser system (Pharos, Light Conversion Ltd.) operating at 515 nm (frequency doubled) at a 20 kHz repetition rate. We irradiated the series of $1 \times 1\,mm^2$ square regions of the sample by writing 1 mm lines with 2 μm interline distance. The writing speed was 0.5 mm/s, and the laser pulse energy was controlled by a half-wave plate and linear polarizer (Fig. 1) and varied in the range of 0.01–0.065 μJ for different squares. The laser beam was polarized parallel to the writing direction. The beam was focused inside the substrate via a 0.21 NA objective lens providing a net fluence of 0.25–1.625 J/cm² (0.76–4.9 TW/cm²), each point under the beam was irradiated with ~60 laser pulses. For a set of laser energies the series of squares were written (Inset in Fig. 1).

Laser induced linear dichroism measurements. Optical characterization of the pristine and irradiated GMN regions was performed with UV-VIS-NIR microspectrometer system (Olympus BX51, CRAIC). The absorbance spectrum of the pristine GMN was measured using a non-polarized light (Fig. 2). The dichroism of the irradiated regions of the GMN was studied by measuring differential optical density $\Delta D = \log_{10}\left(T_{\parallel}/T_{\perp}\right)$, where $T_{\parallel}$ and $T_{\perp}$ are the transmittances of light polarized along (*s*-polarization) and perpendicular (*p*-polarization) to the writing beam polarization, respectively (Fig. 2).

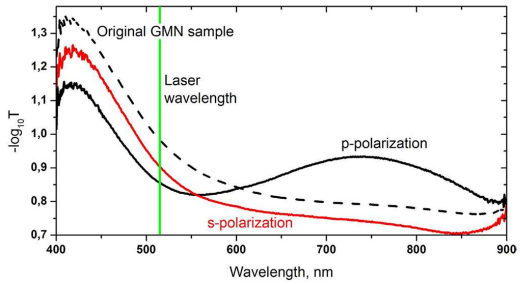

Figure 2. Absorbance spectra of original GMN (dashed), and after laser irradiation with 0.5 J/cm^2 fluence (solid) in *s* (red) in *p* (black) polarized light. Green line denotes the wavelength of the modifying laser.

We controlled the polarization of the probe light beam by inserting a linear polarizer before the sample.

Results

Figure 3 demonstrates the difference in optical densities $\Delta D = \log_{10}\left(T_{\parallel}/T_{\perp}\right)$ of the modified GMN for orthogonally polarized probe beams. One can see two strong bands in the vicinity of 450 nm and 750 nm that dominate the linear dichroism spectrum of the processed GMN substrate. The linear dichroism originates from the splitting of the surface plasmon resonance (SPR) when spherical silver nanoparticles are elongated by the femtosecond laser irradiation[2]. In other words, the SPR position in the transmittance spectrum is different for *s* and *p*-polarized probe beams.

Figure 3 shows that the linear dichroism of the modified GMN is non-monotonous function of the laser fluence. Specifically, the SPR associated with $T_{\perp}$ (i.e. when ΔD is negative) becomes stronger when the fluence increases up to 0.625 J/cm^2 (Fig.3(a)), and its strength decreases for higher fluences (Fig. 3(b)). Figure 4 shows the spectral position of the differential optical density minimum as a function of laser fluence. The dependence behaviour can be due to the heat accumulation at higher laser intensities that prevents complete solidification of silver spheroids between two subsequent femtosecond pulses and partial destruction of nanoparticles[15].

Discussion

The reshaping of silver nanoparticles under laser irradiation is caused by the enhancement of the local electric field in the vicinity of metal inclusion in dielectric. At high laser intensities, the local field gives rise to the ejection of electrons from metal nanoparticle into the glass matrix and drastically increases the local temperature[15] driving the system out of equilibrium. This provokes the transformation of spherical nanoparticles to spheroids with rotation axis along the polarization azimuth of the laser beam and eventually leads to the optical dichroism.

For the analysis of the GMN modification, it is instructive to consider optical properties of the homogeneous composite medium consisting of identical metal spheroids with permittivity ϵ_m, embedded into a host matrix with permittivity ϵ. We assume that the spheroids size is much less than light wavelength and that they all have the same shape and orientation prescribed by the polarization of the processing femtosecond laser beam. Since we studied silver-based GMN with the metal concentration less than 15 vol.%, we employ Maxwell Garnett approach (MGA)[21] by describing the permittivity tensor of the composite in terms of the polarizability tensor of the spheroids[1].

The polarizability tensor of an isolated spheroid with the radii of a and c (rotation axis) can be presented in the following form: $\alpha_{ij} = v_0\beta_{ij}$, where $v_0 = 4\pi ca^2/3$ is the volume of the spheroid. If z axis is directed along the rotation axis c of the spheroid, tensor β_{ij} is diagonal one, $\beta_{xx} = \beta_{yy} = \beta_{\perp}$ and $\beta_{zz} = \beta_{\parallel}$, and[1]

$$\beta_{\parallel,\perp} = \frac{\epsilon_m - \epsilon}{\epsilon + N_{\parallel,\perp}(\epsilon_m - \epsilon)} \quad (1)$$

Here $N_{\parallel,\perp}$ are depolarization factors of the spheroid[1],

$$N_{\parallel} = \frac{a^2 c}{2}\int_0^{\infty} \frac{ds}{(s+c^2)^{3/2}(s+a^2)},$$

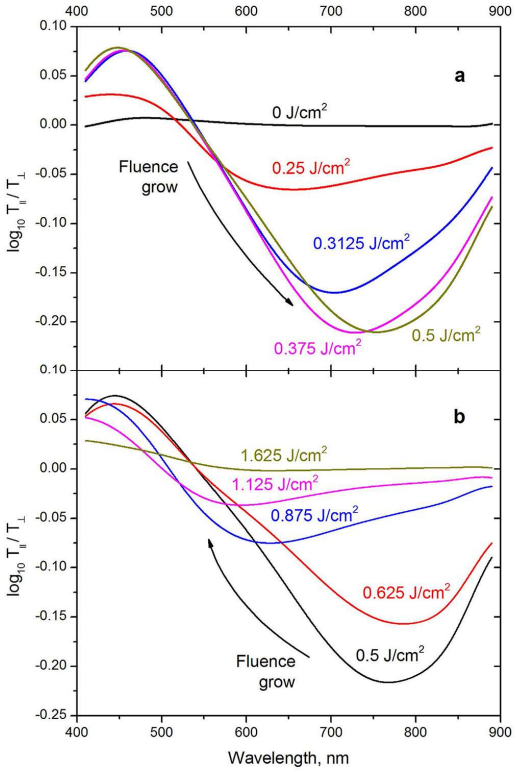

Figure 3. Differential optical density of the modified GMN. (**a**) Low power regime: the resonance band shifts towards longer wavelengths, and its strength increases as the laser power increases. (**b**) High-power regime: the resonance band shifts towards shorter wavelengths, and its strength decreases as the laser power increases.

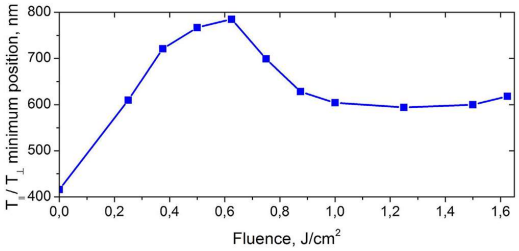

Figure 4. The position of the differential optical density minimum as a function of laser fluence. The data are extracted from the spectra shown in Fig. 3.

and $N_\perp = \left(1 - N_\parallel\right)/2$. For a sphere $N_\perp = N_\parallel = 1/3$, while for prolate and oblate spheroids the depolarization factor is $\frac{1}{3} < N_\parallel < 1$ and $0 < N_\parallel < 1/3$, respectively.

The dielectric permittivity of silver in the visible spectral range can be well described in the Drude model framework[22]:

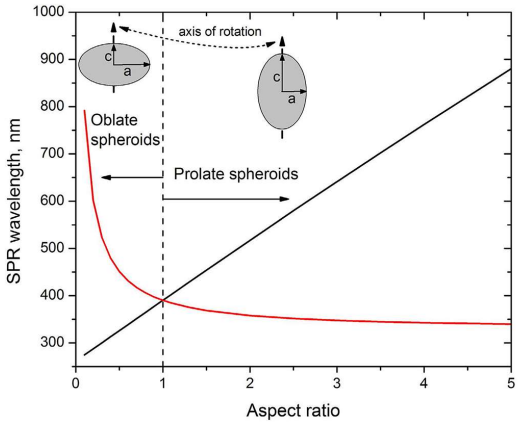

Figure 5. Surface plasmon resonance wavelengths calculated for oblate and prolate silver spheroids of different aspect ratios in the glass matrix. Red and black solid line show SPR wavelength for the light polarized along *a*- and *c*-axis, respectively. The following parameters were used for the numerical simulations: $\epsilon_\infty = 4$, $\lambda_p = 135\,nm$, $\gamma/\omega_p = 0.1$[23], $\epsilon = 2.72$.

$$\epsilon_m = \epsilon_\infty - \frac{\omega_p^2}{\omega(\omega + i\gamma)}, \tag{2}$$

where ϵ_∞ is the high frequency permittivity, ω_p is the plasma frequency, and γ is the electron scattering rate[23]. The model[1] allows calculating SPR for a silver spheroid for the plasmonic oscillation along *a*-axis and *c*-axis. The dependence of SPR wavelengths on the spheroid aspect ratio is illustrated in Fig. 5. It is worth noting that in Fig. 5, the electron scattering at the surface of the spheroid is not taken into consideration, i.e. the size of the spheroid is not accounted for.

When the *c*-axes of the spheroids are aligned in the same direction, the composite possesses the properties of uniaxial material. Thus the dielectric permittivity tensor of the composite is diagonal, $\epsilon_{xx} = \epsilon_{yy} = \epsilon_\perp$ and $\epsilon_{zz} = \epsilon_\parallel$, where[17]

$$\epsilon_{\parallel,\perp} = \epsilon\left(1 + \frac{f\beta_{\parallel,\perp}}{1 - fN_{\parallel,\perp}\beta_{\parallel,\perp}}\right), \tag{3}$$

and f is the volume fraction of the spheroidal inclusions.

It is convenient to express $\epsilon_\parallel$ and $\epsilon_\perp$ in terms of $\Delta N = N_\parallel - 1/3$, a quantitative measure of the spheroidicity of nanoparticles that constitute the composite:

$$\epsilon_\parallel = \epsilon\frac{3(1 + \Delta N\beta_0) + (2 - 3\Delta N)f\beta_0}{3(1 + \Delta N\beta_0) - (1 + 3\Delta N)f\beta_0}, \tag{4}$$

$$\epsilon_\perp = \epsilon\frac{3(2 - \Delta N\beta_0) + (2 + 3\Delta N)f\beta_0}{3(2 - \Delta N\beta_0) - (2 - 3\Delta N)f\beta_0}. \tag{5}$$

Here

$$\beta_0 = \frac{3(\epsilon_m - \epsilon)}{\epsilon_m + 2\epsilon} \tag{6}$$

represents the polarizability $\alpha_0 = v_0\beta_0$ of a sphere with volume v_0. One can see that at $\Delta N = 0$, Eqs (4,5) give the permittivity of the isotropic composite consisting of spherical nanoparticles, $\epsilon_\parallel = \epsilon_\perp = \epsilon(3 + 2f\beta_0)/(3 - f\beta_0)$. When $\Delta N \neq 0$, i.e. when nanoparticles are spheroids, the GMN is anisotropic. However, the optical anisotropy of the composite can be controlled not only by the particle spheroidicity ΔN, but also by the volume fraction f. In particular, Eqs (3,4) yield $\epsilon_\parallel - \epsilon_\perp$

$\propto \Delta N\,(\epsilon_m - \epsilon) f\,(1-f)$, i.e. in the Maxwell Garnett composite ($f \ll 1$), the anisotropy is proportional to the product of $\Delta N f$. This implies that the change of particles shape and metal volume fraction provides us two independent channels for the GMN optical response control.

The anisotropy of the composite comprising of metal spheroids embedded into the dielectric matrix manifests itself in the linear dichroism contrary to almost pure birefringence observed in glasses without nanoparticles after ultrashort pulse irradiation[24]. Specifically, in the irradiated nanocomposite the position and the width of the SPR are different for the light polarized along *c*- and *a*-axis of the spheroid. The SPR wavelength in a spherical particle can be determined within the conditions of vanishing the real part of the denominator in Eq. (6), $\mathrm{Re}\{\epsilon_m + 2\epsilon\} = 0$. However, in the composites comprised of spheroids, the SPR resonances for the light polarized along *c*- and *a*-axes take place at different frequencies that can be found from the following equations:

$$Re\left\{\epsilon_m + \epsilon\frac{2 - 3\Delta N + f\,(1 + 3\Delta N)}{(1 + 3\Delta N)\,(1-f)}\right\} = 0, \tag{7}$$

$$Re\left\{\epsilon_m + \epsilon\frac{4 + 3\Delta N + 2f\,(2 - 3\Delta N)}{(2 - 3\Delta N)\,(1-f)}\right\} = 0. \tag{8}$$

It is instructive to obtain an analytical formula for the SPR resonance in the composite using Drude model. By using Eqs (7,8) and taking into account that in the visible spectral range $\omega_p \gg \gamma$, one can obtain the following equations for the surface plasmon wavelengths for light polarized along and perpendicular rotation axis of metal spheroids comprising the composite:

$$\lambda_{\parallel}^{SPR} = \lambda_p\sqrt{\epsilon_\infty + \epsilon\frac{2 - 3\Delta N + f\,(1 + 3\Delta N)}{(1 + 3\Delta N)\,(1-f)}}, \tag{9}$$

$$\lambda_{\perp}^{SPR} = \lambda_p\sqrt{\epsilon_\infty + \epsilon\frac{4 + 3\Delta N + 2f\,(2 - 3\Delta N)}{(2 - 3\Delta N)\,(1-f)}}, \tag{10}$$

where $\lambda_p = 2\pi c/\omega_p$ is the plasma wavelength. At $f \ll 1$, $\lambda_{\perp}^{SPR}$ and $\lambda_{\parallel}^{SPR}$ depend on the aspect ratio similarly to resonant wavelengths of the isolated spheroid (see Fig. 5).

By using Eqs (9,10) we can show that with ω_p, $\omega \gg \gamma$, the SPR has Lorentzian shape,

$$\mathrm{Im}\left\{\epsilon_{\perp,\parallel}(\lambda)\right\} \propto \left[\left(\lambda - \lambda_{\perp,\parallel}^{SPR}\right)^2 + \left(\Delta\lambda_{\perp,\parallel}^{SPR}\right)^2\right]^{-1}, \tag{11}$$

where the linewidth is determined by the electron scattering rate,

$$\Delta\lambda_{\perp,\parallel}^{SPR} \approx \frac{\gamma}{2\omega_p}\lambda_{\perp,\parallel}^{SPR}. \tag{12}$$

It is necessary to mention that electron scattering rate γ in a nanoparticle can be considerably higher than that in a bulk metal. Specifically, for silver spherical nanoparticle with radius *r*, the scattering rate is $\gamma = 1/\tau + AV_F/r$ where $\tau \cong 30$ fs and $V_F = 1.4 \times 10^8$ cm/s are the electron collision time and Fermi velocity in the bulk silver, respectively, and *A* is the parameter of the order of one[23]. Since in our experiment, the GMN was comprised of silver nanoparticles with radius less than 10 nm[22], one may expect that in our experimental conditions, the collisions of free electrons with the particle's surface dominates γ.

From Eqs (9,10) we observe that SPR can be shifted by changing the metal volume fraction. In particular, for prolate spheroids $0 < \Delta N < 2/3$, $\lambda_{\parallel}^{SPR}$ varies in the spectral region $\lambda_{\parallel}^{SPR} > \lambda_o^{SPR}$ while $\lambda_{\perp}^{SPR}$ changes in the region $\lambda_{\perp}^{SPR} < \lambda_o^{SPR}$. Here

$$\lambda_o^{SPR} = \lambda_p\sqrt{\epsilon_\infty + \epsilon\frac{2+f}{1-f}}$$

is the SPR wavelength for the nanocomposite comprised of spherical nanoparticles.

It is worth noting that modification of the particle shape also affects the electron scattering rate γ in Eq. (8). Specifically, in spheroids, the collision rate, which is the function of radius in spherical metal nanoparticles[23], depends on whether electron moves along *c*- or *a*-axis[25]. If we assume that the particle volume $v_0 = 4\pi r^3/3$ does not change under its transformation from a sphere to a spheroid, the scattering rates for electrons oscillating along *c*- and *a*- axis can be expressed as $\gamma_{\parallel} = \gamma\,(a/c)^{2/3}$ and $\gamma_{\perp} = \gamma\,(c/a)^{1/3}$, respectively.

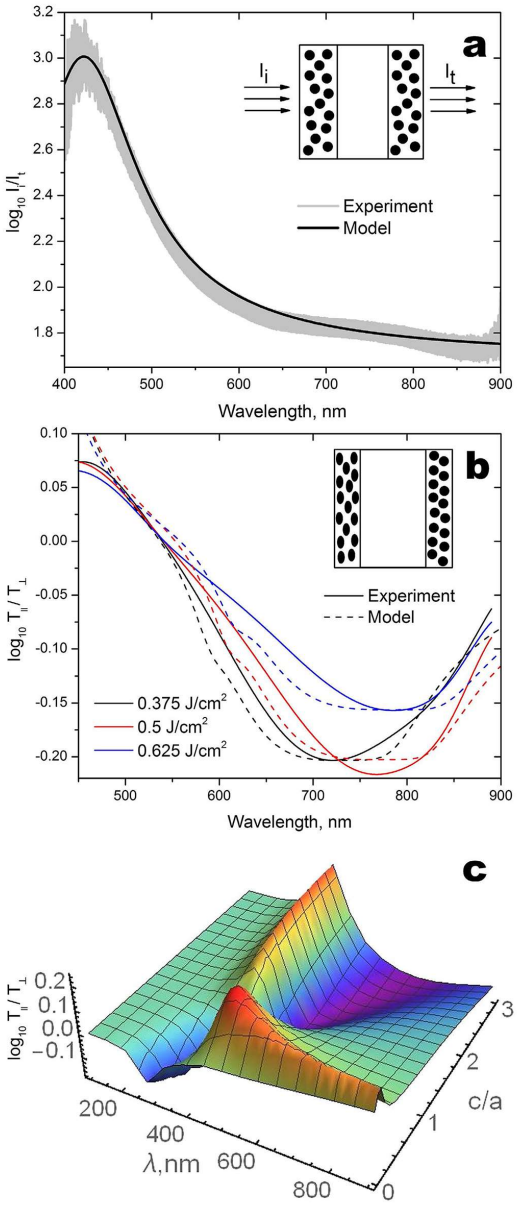

Figure 6. (**a**) Absorbance of the non-modified GMN calculated using MGA (black solid line) and obtained in the experiment (wide grey line). (**b**) Solid lines represent differential optical density of the GMN after laser irradiation with fluence of 0.375 J/cm^2 (black), 0.5 J/cm^2 (red), and 0.625 J/cm^2 (blue). Dash lines represent differential optical density of the GMN calculated using MGA upon $c/a = 3.32$, $\xi = 0.37$ (black); $c/a = 3.61$, $\xi = 0.38$ (red), and $c/a = 3.74$, $\xi = 0.31$ (blue). Inset shows nanoparticles inside the laser modified sample. (**c**) Simulated spectrum of the differential optical density vs aspect ratio and resonance wavelength for $\xi = 0.31$. The following parameters were used for the numerical simulations: $\epsilon_\infty = 4$, $\lambda_p = 135$ nm, $\gamma/\omega_p = 0.09$, $L = 10$ nm, $f = 0.06$, $\alpha_s = 0.016$ nm^{-1}, the refractive indices of the bare and silver-enriched glass are 1.5 and 1.65, respectively.

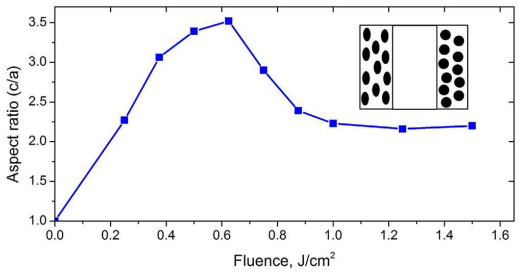

Figure 7. Aspect ratio, *c/a*, of prolate silver spheroids as a function of the modification laser fluence. The relation between the peaks of differential optical density and the aspect ratio of spheroids were extracted from the processed transmission spectra partly shown in Figs 3 and 6(b). The inset schematically show nanoparticles shape and location inside the laser irradiated sample.

Equations (4,5) allow us to model polarized transmission spectra of the structure consisted of a layer of the modified GMN, bare glass substrate, and a layer of the pristine GMN comprising spherical nanoparticles. The latter should be taken into account because the ion exchange technique (see Section 2) results in the formation of nanoparticles beneath both surfaces of the glass plate, while the tight focusing of the femtosecond laser beam leaves the back surface of the sample unmodified.

In order to reveal the parameters of nanocomposite we performed fitting of measured linear absorption spectrum of the non-modified GMN. In the fitting, we used conventional Drude model parameters for silver, $\epsilon_\infty = 4$, $\lambda_p = 135\,nm$, $\gamma/\omega_p = 0.09$[23], and assumed that the refractive indices of the bare and silver-enriched glass are 1.5 and 1.65. This difference in the refractive indices originates both from the ion exchange and increase of silver ions concentration in the subsurface region of glasses in the course of the hydrogen processing[19,20]. The scattering losses in the subsurface layer were taken into account phenomenologically by introducing extinction coefficient $\alpha_s = 0.0016\,nm^{-1}$. One can observe from Fig. 6(a) that we obtain a good agreement between the calculated (solid line) and measured (broad grey line) spectra upon the $f = 0.06$ and the thickness of silver-enriched layer $L = 100$ nm.

The obtained parameters of the non-modified composite allow us to reproduce the spectra measured after the femtosecond laser irradiation (Section 2.2). We assume that the laser processing results in the transformation of spherical metal nanoparticles into spheroids only beneath the front surface of the sample. However, it is worth noting that in our experiments, the distance between lines is 2 μm, with the spot diameter of 1.6 μm. According to the lower intensity in the periphery of the focal spot and the periodicity of the inscribed lines, considerable area of the processed region remains unmodified. Despite the fact that only modified regions of the sample possess linear dichroism, both modified and non-modified areas contribute to the transmittance: $I_t/I_i = \xi T_M + (1 - \xi)\, T_N$. Here T_M and T_N are transmittances of the modified and non-modified regions, while ξ describes relative area of the modified region. That is from Fig. 6(b), where we presented experimental and calculated spectra of differential optical density $\Delta D = \log_{10}\left(T_\parallel / T_\perp\right)$, one may conclude that in our experimental conditions more than 30% of the nanoparticles beneath the front surface of the glass were modified. We also simulated the spectrum of the differential optical density as a function of the spheroids aspect ratio and plot it in coordinates of *c*/*a* and resonance wavelength (Fig. 6(c)).

The fitting of the experimental spectra shown in Fig. 6(b) allows us to obtain the aspect ratio of reshaped particles as a function of the fluence of the processing laser beam (Fig. 7). By comparing Figs 4 and 7, one can conclude that $\lambda_\perp^{SPR}$ is a nearly linear function of the aspect ratio the same way as for isolated spheroids in Fig. 5. In our experimental conditions, this function takes the following form: $\lambda_{SPR}[\mathrm{nm}] \approx 145(c/a) + 275$ nm. This is in a good agreement with the estimations made for the isolated spheroids[26].

One can observe from Fig. 7 that in our experiment, we obtained the maximum aspect ratio of $c/a \approx 3.5$ at the fluence of about 0.625 J/cm^2. It is worth noting however that increasing laser fluence results in the drop of the aspect ratio down to ~2.6. The observed phenomenon can be understood if one recall that elongation of nanoparticles within focal area of the writing beam is accompanied by their rapid heating due to the relatively slow (0.5 mm/s) translation of the sample and relatively high (20 kHz) repetition rate. Since each pulse increases the nanoparticle temperature by $\Delta T \simeq \nu_0 I/\lambda\kappa_g$, where I is the laser pulse intensity, $k_g \approx 1\,W/mK$ is the thermal conductivity of the glass, ν_0 is the nanoparticle volume[27], even at moderate intensities melting of the nanoparticle and softening the surrounding glass occur[28]. These thermal effects influence the electric and surface tension forces, whose balance determines the shape of the nanoparticle. In our experimental conditions, one may expect the elongation of the nanoparticles caused by electrical forces at fluences above 0.625 J/cm^2 results in their partition with the

formation of less elongated nanoparticles, which gives rise to the decreasing of aspect ratio at fluences between 0.625 J/cm^2 and 1 J/cm^2. When we increase fluence higher a strong local electric field eventually destroys nanoparticles[15,29] similarly to their destruction by strong DC electric field[30].

Conclusion

By comparing the experimental and theoretical differential transmittance spectra of the femtosecond laser processed silver-based GMN we demonstrated that in the wide range of the laser fluences the aspect ratio of the reshaped silver nanoparticles comprising GMN is a linear function of the fluence. This result opens avenues towards the control of shape and optical properties of metal nanoparticles essential for a variety of plasmonic and nanophotonic applications. In particular, this is important for modification of GMN with high spatial resolution in order to create a plasmon enhanced gratings and widely tunable surface components. Spectral separation between the SPR peaks of orthogonally polarized light as high as 400 nm was obtained, that corresponds to transformation of the spherical silver nanoparticles into prolate spheroids with the aspect ratio up to 3.5. This light-induced anisotropy can be increased even further by using GMN substrates with larger metal particles and by controlling the overall modification process.

References

1. Landau, L. D. & Lifshitz, E. M. *Electrodynamics of Continuous Media, Volume 8 of "A Course of Theoretical Physics"* (Pergamon Press, 1960).
2. Seifert, G., Kaempfe, M., Berg, K.-J. & Graener, H. Production of "dichroitic" diffraction gratings in glasses containing silver nanoparticles via particle deformation with ultrashort laser pulses. *Appl. Phys. B* **73,** 355 (2001).
3. Rangel-Rojo, R. *et al.* Linear and Nonlinear Optical Properties of Aligned Elongated Silver Nanoparticles Embedded in Silica in *Silver Nanoparticles* (Ed. Perez D. P.) Ch. 2 (InTech, 2010).
4. Berger, A., Drost, W.-G., Hopfe, S., Steen, M. & Hofmeister, H. Stress state and twin configuration of spheroidal silver nanoparticles in glass. Nanostructured and Advanced Materials for Applications in Sensor, Optoelectronic and Photovoltaic Technology: Proceedings of the NATO Advanced Study Institute on Nanostructured and Advanced Materials for Applications in Sensors, Optoelectronic and Photovoltaic Technology, Sozopol, Bulgaria, 6–17 September 2004.
5. Baraldi, G., Gonzalo, J., Solis, J. & Siegel, J. Reorganizing and shaping of embedded near-coalescence silver nanoparticles with off-resonance femtosecond laser pulse. *Nanotechnology* **24**, 255301 (2013).
6. Kaempfe, M., Rainer, T., Berg, K.-J., Seifert, G. & Graener, H. Ultrashort laser pulse induced deformation of silver nanoparticles in glass. *Appl. Phys. Lett.* **74,** 1200 (1999).
7. Kaempfe, M., Rainer, T., Berg, K.-J., Seifert, G. & Graener, H. Erratum: Ultrashort laser pulse induced deformation of silver nanoparticles in glass. *Appl. Phys. Lett.* **77,** 459 (2000).
8. Podlipensky, A., Abdolvand, A., Seifert, G. & Graener, H. Femtosecond laser assisted production of dichroitic 3D structures in composite glass containing Ag nanoparticles. *Appl. Phys. A* **80,** 1647 (2005).
9. Fleming, L., Tang, G., Zolotovskaya, S. A. & Abdolvand, A. Controlled modification of optical and structural properties of glass with embedded silver nanoparticles by nanosecond pulsed laser irradiation. *Opt. Mat. Express* **4,** 969–975 (2014).
10. Oliver, A. *et al.* Controlled anisotropic deformation of Ag nanoparticles by Si ion irradiation. *Phys. Rev. B* **74,** 245425 (2006).
11. Mishra, Y. K. *et al.* Synthesis of elongated Au nanoparticles in silica matrix by ion irradiation. *Appl. Phys. Lett.* **91,** 063103 (2007).
12. Stalmashonak, A., Seifert, G. & Graener, H. Optical three-dimensional shape analysis of metallic nanoparticles after laser-induced deformation. *Opt. Lett.* **32**(21), 3215–3217 (2007).
13. Tyrk, M. A., Gillespie, W. A., Seifert, G. & Abdolvand, A. Picosecond pulsed laser induced optical dichroism in glass with embedded metallic nanoparticles. *Opt. Express* **21**(19), 21823–8 (2013).
14. Destouches, N. *et al.* Dichroic colored luster of laser-induced silver nanoparticle gratings buried in dense inorganic films. *JOSA B* **31**(11), C1–C7 (2014).
15. Stalmashonak, A., Seifert, G. & Abdolvand, A. *Ultra-Short Pulsed Laser Engineered Metal-Glass Nanocomposites*, Springer Briefs in Physics, 59–67 (Springer, 2013).
16. Seifert, G., Stalmashonak, A., Hofmeister, H., Haug, J. & Dubiel, M. Laser-Induced, Polarization Dependent Shape Transformation of Au/Ag Nanoparticles in Glass. *Nanoscale Res Lett.* **4**(11), 1380–1383 (2009).
17. Sihvola, A. & Kong, J. A. Effective Permittivity of Dielectric Mixtures. *IEEE Trans. Geosciences and Remote Sensing* **26(4),** 420–429 (1988).
18. de Marchi, G. *et al.* Silver nanoclusters formation in ion-exchanged waveguides by annealing in hydrogen atmosphere. *Appl. Phys. A* **63**(4), 403–7(1996).
19. Kaganovskii, Yu., Lipovskii, A., Rosenbluh, M. & Zhurikhina, V. Formation of nanoclusters through silver reduction in glasses: The model. *Journal of Non-Crystalline Solids* **353,** 2263–2271 (2007).
20. Afrosimov, V. V. *et al.* M. I. Mass Transfer in Thermo Electric Field Modification of Glass–Metal Nanocomposites. *Techn. Phys.* **55**(11), 1601–1609 (2010).
21. Garnett, J. C. M. Colours in metal glasses and in metallic films. *Philos. Trans. R. Soc. Lond. A* **203,** 385–420 (1904).
22. Maier, S. A. *Plasmonics: Fundamentals and Applications* (Springer, 2007).
23. Kreibig, U. & Vollmer, M. Optical Properties of Metal Clusters. *Springer Series in Materials Science*, **25,** 535 (1995).
24. Poumellec, B., Lancry, M., Chahid-Erraji, A. & Kazansky, P. G. Modification thresholds in femtosecond laser processing of pure silica: review of dependencies on laser parameters. *Opt. Mat. Express* **1(4),** 766–782 (2011).
25. Uskov, A. V., Protsenko, I. E., Mortensen, N. A. & O'Reilly, E. P. Broadening of plasmonic resonance due to electron collisions with nanoparticle boundary: a quantum-mechanical consideration. *Plasmonics* **9,** 185–192 (2014).
26. Noguez, C. Surface Plasmons on Metal Nanoparticles: The Influence of Shape and Physical Environment. *J. Phys. Chem. C* **111,** 3806–3819 (2007).
27. Tribelsky, M. I., Miroshnichenko, A. E., Kivshar, Yu. S., Luk'yanchuk, B. S. & Khokhlov, A. R. Laser Pulse Heating of Spherical Metal Particles. *Phys. Rev. X* **1,** 021024 (2011).
28. Kaganovskii, Yu., Lipovskii, A. & Rosenbluh, M. Mechanism and kinetics of particle motion and coalescence in quantum dot glass under pulsed laser irradiation. *Functional materials* **6**(2), 221–228 (1999).
29. Petrov, M. I., Melehin, V. G. & Lipovskii, A. A. On the stability of elastic particles. *Phys. Status Solidi B* **249**(11), 2137–2139 (2012).
30. Deparis, O. *et al.* Poling-assisted bleaching of metal-doped nanocomposite glass. *Appl. Phys. Lett.* **85(6),** 872–874 (2004).

Acknowledgements

The study has been supported by EU (Marie Curie FP7 project #269140), Academy of Finland (grant #288151 and #265015), EPSRC (grant EP/M029042/1), and Russian Science Foundation (grant no. 14-22-00136). P.G.K. thanks Ministry of Education and Science of the Russian Federation (Grant No. 14.Z50.31.0009). Authors are grateful to Amin Abdolvand for valuable comments on the manuscript.

Author Contributions

S.Ch. made GMN sample, performed spectra measurements and processing, and wrote the main manuscript text. R.D. assembled the modification setup and performed the modification experiments. D.K. and Yu.P.S. made numerical EMA calculations. M.B. supervised the modification experiments. A.A.L. supervised GMN fabrication and processing of the data. P.G.K. supervised the whole work.

Additional Information

Competing financial interests: The authors declare no competing financial interests.

How to cite this article: Chervinskii, S. *et al.* Revealing the nanoparticles aspect ratio in the glass-metal nanocomposites irradiated with femtosecond laser. *Sci. Rep.* **5**, 13746; doi: 10.1038/srep13746 (2015).